Diluted Combustion of Methanol
in Spark-Ignition Engines with On-Board Fuel Reforming

Verdunde verbranding van methanol
in vonkontstekingsmotoren met brandstofreforming aan boord

Duc-Khanh Nguyen

Promotoren: prof. dr. ir. S. Verhelst, dr. ir. L. Sileghem
Proefschrift ingediend tot het behalen van de graad van
Doctor in de ingenieurswetenschappen: werktuigkunde-elektrotechniek

UNIVERSITEIT
GENT

Vakgroep Mechanica van Stroming, Warmte en Verbranding
Voorzitter: prof. dr. ir. P. De Baets
Faculteit Ingenieurswetenschappen en Architectuur
Academiejaar 2018 - 2019

ISBN 978-94-6355-222-6
NUR 977, 978
Wettelijk depot: D/2019/10.500/30

Supervisors:

Prof. Sebastian Verhelst
Dr. Louis Sileghem

Members of the examination board:

Chairman:

Prof. Patrick De Baets - Ghent University

Secretary:

Dr. Steven Lecompte - Ghent University

Reading committee:

Prof. Mark Saeys - Ghent University
Prof. Per Tunestål - Lund University
Prof. James Turner - University of Bath
Dr. Jeroen Vancoillie - DAF Trucks N.V.

Other members:

Prof. Sebastian Verhelst - Ghent University
Dr. Louis Sileghem - Ghent University

“A people without a positive history is like a vehicle without an engine.”

STEVEN BIKO

Acknowledgments

I have been waiting to write this section to express how thankful I am to everyone who has provided me with a chance, knowledge and motivation to finish my Ph.D.

First and foremost, I would like to express my sincere gratitude to my first supervisor Prof. Sebastian Verhelst for accepting me, an international student with limited English skill, to be a Ph.D. student in his research group. Since the day of acceptance (July 16, 2015), he has always provided me with remarkably strong and continuous support throughout my studies while giving me a magnificent amount of freedom, responsibility and flexibility.

Secondly, I am thankful to my second supervisor, Dr. Louis Sileghem for his scientific input to my work in the last two years of my Ph.D. Many valuable discussions and suggestions from him have helped me to grow in many aspects.

I wish also to thank all committee members for their interest in my thesis, for being my co-examiners and for a meticulous reading of this book. Their comments, corrections and suggestions certainly lead to a significant improvement in my work.

Special thanks go to my "godfather" Stijn Broekaert for his support and guidance at the beginning of my Ph.D., to Jeroen Dierickx for helping me to translate a part of my work into Dutch, and to other (ex-)colleagues Thomas De Cuyper, Roel Verschaeren, Jakob Coulier, Ahmed Melo Espinosa, Gilles Decan and Haohan Li for sharing knowledge and for the enjoyable environment you create in the laboratory.

In addition, many thanks go to the technicians, Koen Chielens, Patrick De Pue, and Yves Maenhout, who had helped me to solve the mechanical, electrical, and IT problems. I am also thankful for the administration supports that Griet Blondé, Annie Harri and Annick De Coster gave me. A special thanks go to master thesis students for their excellent work during their theses under my supervision.

Thank you so much my dear friends in the Vietnamese Combustion Group, Minh-Bau Luong, Lam K. Huynh, Thuong Nguyen, Manh-Vu Tran, Dinh-Thi

Luong and Tien Nguyen, for all of the discussions and your answering a massive of questions from me.

Last but not least, I would like to express my sincerest gratitude to my family, my friends for their unconditional love and support. This work would not have been possible without you.

Ghent, April 2019
Duc-Khanh Nguyen

Table of Contents

Nomenclature

Symbols

A	area	m^2
c_p	specific heat at constant pressure	$J/kg.K$
c_v	specific heat at constant volume	$J/kg.K$
h_f	enthalpy of formation	kJ/mol
h	heat transfer coefficient	–
p	pressure	Pa/bar
Q_{fuel}	fuel energy	J
Q	heat transfer rate	W
T	temperature	K
$T_{c,90}$	catalyst light-off temperature	$^{\circ}C$
U_p	mean piston speed	m/s
u	burning velocity	m/s
u'	turbulent intensity	m/s
V	volume	m^3
W	work	J
X	molar fraction	–
x_b	burned mass fraction	–
Y	mass fraction	–

Greek symbols

α	temperature power exponent	–
β	pressure power exponent	–
ε	exponential function of dilution term	–
δ_{F}	flame thickness	m
η	efficiency	–
γ	specific heat ratio	–
λ	lambda (air-to-fuel equivalence ratio)	–
μ_{imep}	mean IMEP	bar
ϕ	fuel-to-air equivalence ratio	–
ϕ'	fuel-to-charge equivalence ratio	–
σ_{imep}	standard deviation of IMEP	bar
τ_{ID}	autoignition delay time	second
τ_{RES}	residence time	CAD
τ_{F}	chemical time scale	second
θ	combustion duration	CAD

Subscripts

blend	fuel blend
comb	combustion
comp	compression
EGR	exhaust gas recirculation
emiss	emissions
end	end of compression
exp	experiment
ht	heat transfer
i	component i
ID	ignition delay
imep	indicated mean effective pressure
ini	initial
IVC	intake valve closure
max	maximum
MeOH	methanol
NA	naturally aspirated
pump	pumping
RES	residence
res	residual
SG	syngas
st	stoichiometric
0	reference condition
b	burned
f	firing
g	gas
L	laminar
t	turbulent
u	unburned

Acronyms

2-MF	2-methylfuran
aBDC	after bottom dead center
AFR	air-to-fuel ratio
aTDC	after non-firing top dead center
$aTDC_f$	after firing top dead center
ATR	auto-thermal reforming
bBDC	before bottom dead center
BEV	battery electric vehicles
BMEP	brake mean effective pressure
bTDC	before non-firing top dead center
BTE	brake thermal efficiency
CA	crank angle
CAD	crank angle degree
CD	combustion duration
CFD	computational fluid dynamics
CoV	coefficient of variance
CR	compression ratio
CVC	constant volume chamber
DBE	double bond equivalence
D-EGR	dedicated-exhaust gas recirculation
DF	downsizing factor
DI	direct-injection
DMC	dimethyl carbonate
DoE	design of experiment
ECU	engine control unit
EFR	external fuel reforming
EGR	exhaust gas recirculation
EtOH	ethanol
FCV	fuel cell vehicles
FMEP	friction mean effective pressure
FTP	federal test procedure
GPF	gasoline particulate filter
HCCI	homogeneous charge compression ignition
HoV	heat of vaporization
HP	high pressure
ICE	internal combustion engine
ICEV	internal combustion engine vehicles
ID	ignition delay
IMEP	indicated mean effective pressure
ITE	indicated thermal efficiency

IVC	intake valve closure
KLSA	knock-limited spark advance
LBV	laminar burning velocity
LHV	lower heating value
MAP	manifold absolute pressure
MBT	minimum spark advance for best torque
MeOH	methanol
MER	molar expansion ratio
MON	motor octane number
NA	naturally aspirated
NO_x	nitrogen oxides
NTP	normal temperature and pressure
OI	octane index
PFI	port fuel injected
PM	particle matter
PMEP	pumping mean effective pressure
PMI	particle matter index
POX	partial oxidation
PtG	power-to-gas
PtL	power-to-liquid
R-EGR	reformed-exhaust gas recirculation
RMSE	root mean square error
r-WGS	reverse-water gas shift
RON	research octane number
RPM	engine revolution speed
SACI	spark assisted compression ignition
SG	syngas
SOFC	solid-oxide fuel cell
SR	steam reforming
S-VVT	simultaneous variable valve timing
TCR	thermochemical recuperation
TD	thermal decomposition
TDC	top dead center
TPA	three pressure analysis
TPRF	toluene primary reference fuel
TWC	three-way catalyst
VGT	variable geometry turbine
VP	vapour pressure
WGS	water gas shift
WHR	waste heat recovery
WOT	wide open throttle

List of publications

Publications directly related to the Ph.D. topic

Publications in peer reviewed international journals

1. **Nguyen, D. K.**, and Verhelst, S. (2017). Computational Study of the Laminar Reaction Front Properties of Diluted Methanol-Air Flames Enriched by the Fuel Reforming Product. *Energy & Fuels*, 31(9), 9991-10002.

2. **Nguyen, D. K.**, Sileghem, L., and Verhelst, S. (2019). Exploring the potential of reformed-exhaust gas recirculation (R-EGR) for increased efficiency of methanol fueled SI engines. *Fuel*, 236, 778-791.

Publications in proceedings of international conferences

3. **Nguyen, D. K.**, and Verhelst, S. (2016). The temperature dependence of laminar burning velocities of methanol-syngas-air flames. *FISITA 2016 World Automotive Congress*. Busan, South Korea.

4. **Nguyen, D. K.**, and Verhelst, S. (2017). Development of laminar burning velocity correlation for the simulation of methanol fueled SI engines operated with onboard fuel reformer. *SAE Technical Paper* 2017-01-0539.

5. **Nguyen, D. K.**, Van Craeynest, T., Pillu, T., Coulier, J., and Verhelst, S. (2018). Downsizing Potential of Methanol Fueled DISI Engine with Variable Valve Timing and Boost Control. *SAE Technical Paper* 2018-01-0918.

6. **Nguyen, D. K.**, Stepman, B., Vergote, V., Sileghem, L., and Verhelst, S. (2019). Combustion Characterization of Methanol in a Lean-burn Direct Injection Spark Ignition (DISI) Engine. *SAE Technical Paper* 2019-01-0566.

Other publications

Publications in peer reviewed international journals

7. **Nguyen, D. K.**, Sileghem, L., and Verhelst, S. (2018). A quasi-dimensional combustion model for spark ignition engines fueled with gasoline-methanol blends. *Proceedings of the Institution of Mechanical Engineers, Part D: Journal of Automobile Engineering*, 232(1), 57-74.

Publications in proceedings of international conferences

8. De Cuyper, T., Broekaert, S., **Nguyen, D. K.**, Chana, K., De Paepe, M., and Verhelst, S. (2017). Studying the Effect of the Flame Passage on the Convective Heat Transfer in a SI Engine. *SAE Technical Paper* 2017-01-0515.

Nederlandse samenvatting –Summary in Dutch–

Verbranding gaf mensen gezond voedsel, bescherming, hitte, licht, enzovoort. Verbranding gaf ook de kracht voor een auto om van punt A naar punt B te gaan. Het grootste deel van de voertuigen in de wereld worden op dit moment aangedreven door verbrandingsmotoren. Een interne verbrandingsmotor zet chemische energie opgeslagen in de reactanten, d.w.z. het mengsel van brandstof en lucht, om in thermische energie door verbranding. Vervolgens wordt die thermische energie omgezet in mechanische energie door een gecontroleerde expansie. Op dit moment gebruiken de meeste motoren fossiele brandstoffen (diesel en benzine) en produceert de verbranding een enorme hoeveelheid CO_2 en andere vervuilende emissies. De energiezekerheid, de vervuilende uitstoot van auto's en de opwarming van de aarde als gevolg van het broeikasgaseffect, waarbij CO_2 een van de belangrijkste oorzaken is, hebben geleid tot het besluit om voertuigen met een interne verbrandingsmotor in verschillende steden of landen te verbieden. Elektrificatie wordt beschouwd als een oplossing voor het decarboniseren van transport op de weg. Hoewel elektrische voertuigen geen emissies uitstoten, gebeurt dit wel tijdens de productie van elektriciteit, batterijen, voertuigen en het recycleren van deze auto's. Vandaar dat een voertuig zonder emissies een politieke aanduiding is, geen wetenschap. Bovendien zijn de lage energiedichtheid van een batterij en de beschikbaarheid van zeldzame materialen zoals kobalt of lithium de twee andere uitdagingen voor elektrische voertuigen met batterijen. Daarom zijn interne verbrandingsmotoren nog steeds de belangrijkste energiebron voor de huidige en toekomstige transportsystemen.

Motoren en brandstoftechnologie zijn schaalbaar en compact, wat belangrijk is voor transport. De motoren en brandstoffen kunnen ook op een duurzame manier worden geproduceerd (via een gesloten CO_2-cyclus). De CO_2-uitstoot kan worden opgevangen en gebruikt voor de productie van synthetische brandstoffen (ook elektrofuels of e-fuels genoemd). Duurzaam transport vereist synthetische brandstoffen en de eigenschappen van synthetische brandstoffen kunnen worden geoptimaliseerd om de efficiëntie van de motor te vergroten. Methanol is de meest eenvoudige vloeibare synthetische brandstof, en heeft daardoor een voordeel in de productie in vergelijking met andere meer complexere brandstoffen. Dankzij zijn

eigenschappen is methanol meer geschikt voor motoren met vonkontsteking. De eigenschappen van methanol zorgen bovendien ook voor lagere CO_2-emissies in vergelijking met motoren op diesel en benzine.

Het huidige werk begint met een evaluatie van de vereisten voor brandstofeigenschappen om de CO_2-emissies van motoren te verminderen. De brandstof moet een lage koolstofintensiteit hebben en verschillende interessante eigenschappen om het rendemenet van motoren te verbeteren. De koolstofintensiteit wordt gedefinieerd als de hoeveelheid geproduceerde CO_2 voor een bepaalde hoeveelheid warmte van de verbranding van die brandstof. In termen van koolstofintensiteit laat de verbranding van H_2 geen CO_2 vrij. CH_4 is de koolwaterstof die de laagste koolstofintensiteit heeft. Zowel H_2 als CH_4 zijn echter gasvormig bij omgevingsdruk en -temperatuur. Methanol is de vloeibare brandstof met de laagste koolstofintensiteit. Een vloeibare brandstof heeft de voorkeur vanwege zijn hoge energiedichtheid, en de eenvoud voor opslag en distributie met behulp van huidige infrastructuren.

Met het oog op het rendement van een benzinemotor te verhogen, moet de brandstof een hoog research-octaangetal hebben, een laag motor-octaangetallen, een hoge laminaire vlamsnelheid, een hoge verdampingswarmte, een hoge zuurstofmassafractie, een lage fijn stof index en een lage katalysator aanschakeltemperatuur of een korte opwarmingsduur voor het nabehandelingsysteem. Met een hoog research-octaangetal en een laag motor-octaangetal heeft de brandstof een betere klopvastheid, de motor kan met een hogere compressieverhouding werken, het rendement neemt toe. Een hogere verdampingswarmte veroorzaakt een verlaging van de onverbrande gastemperatuur en klop wordt uitgesteld. Bovendien leidt de afname van de verbrande gastemperatuur ook tot een vermindering van warmteverliezen naar de cilinderwand. De lagere verbrandingstemperatuur vraagt aan de andere kant een langere opwarmperiode voor het nabehandelingssysteem. Een hogere laminaire vlamsnelheid genereert een meer isochore verbranding, de motor heeft een hogere effectieve expansieverhouding, wat leidt tot een hogere rendement. Een snellere verbranding veroorzaakt ook een toename van het wrijvingswerk en de neiging tot klop. Een brandstof met een hogere zuurstofmassafractie leidt tot een verhoging van het verbrandingsrendement. Als de emissies worden verwaarloosd, zorgen deze eigenschappen voor een hoger motorrendement. Een lage fijn stof index zorgt voor minder roet, het pompwerk vermindert dankzij de afwezigheid van een benzinedeeltjesfilter. Methanol heeft een hoge klopkweerstand, een hoge vlamsnelheid, een hoge verdampingswarmte, een hoge zuurstofmassafractie en een bijna roetvrije verbranding. Daarom is het motorrendement (tank-to-wheel) voor methanol hoger dan voor andere vloeibare brandstoffen. Samen met zijn lage koolstofintensiteit is methanol de meest veelbelovende brandstof voor een lage CO_2-uitstootmotor. In vergelijking met andere synthetische vloeibare brandstoffen heeft de productie van methanol het hoogste (well-to-tank) rendement. Daarom is het well-to-wheel-rendement voor methanolmotoren het hoogst. Het rendement

van well-to-wheel voor voertuigen met een inwendige verbrandingsmotor is echter nog steeds veel lager dan voor elektrische voertuigen met batterijen.

Het potentieel van methanol als brandstof voor een direct-injectie-verbrandingsmotor met vonkontsteking wordt vervolgens bestudeerd. Metingen bij volledige belasting hebben het downsizingpotentieel van methanol in vergelijking met benzine aangetoond. De motor kan worden verkleind met 10.7% ten opzichte van benzine. De vermindering van de onverbrande gastemperatuur werd ook duidelijk waargenomen. Dit helpt om klop te voorkomen. Bij dezelfde motorbelasting (maximale belasting voor benzine) heeft de methanol-aangedreven motor een hoger thermisch rendement (7-8%-punten) en een lagere uitstoot vergeleken met benzine. De arme werking van methanol werd ook onderzocht en vergeleken met benzine. Dankzij de hoge laminaire vlamsnelheid kan de motorbelasting worden geregeld door middel van de lean-burn-strategie in een breder bereik voor methanol voordat de verbranding onstabiel wordt. Het maximale rendement voor methanol werd bereikt met lambda in het bereik van 1.2-1.4, en bedraagt 41%, 20% hoger dan bij benzine. De vroege vlamontwikkeling is de verbrandingsduur die het meest nauw samenhangt van de variatiecoëfficiënt van de aangegeven gemiddelde effectieve druk. De CA0-10 van 26.5 graden krukhoek en laminaire vlamsnelheid bij ontstekingstijdstippen van 0.4 m/s kunnen worden gebruikt om de arme verbrandingsgrens voor wijd geopende gasklep weer te geven.

Om het rendement van methanolmotoren verder te verhogen, werd gezocht om de warmte in de uitlaatgassen te recupereren. Een kort overzicht van de technologieën voor de recuperatie van restwarmte werd uitgevoerd met als resultaat dat de conversie van uitlaatenergie in chemische energie door thermochemische recuperatie (of endotherme brandstofreforming) in dit werk gekozen werd. Methanol wordt bij hoge temperatuur omgezet in een waterstofrijk gas (of syngas). Vijf soorten methanolreformingsmethodes werden geanalyseerd. De Gibbs-vrije-energie-minimalisatiemethode werd gebruikt om het reformproduct te voorspellen als een functie van de reactortemperatuur. Omdat de computersimulatie een reactor met een oneindig volume gebruikt, heeft het reactant een lange verblijftijd. Hierdoor is de reformingtemperatuur van de simulatie veel lager dan met experimenten mogelijk zou zijn. Het reformingrendement van methanol werd vergeleken met andere motorbrandstoffen met vonkontsteking, namelijk ethanol en iso-octaan (benzinesurrogaat). Hoewel de absolute reformingstemperatuur niet kan worden voorspeld, kan het relatieve verschil tussen brandstoffen en reactanten worden ingeschat. Ethanol en vooral iso-octaan vereiste een hogere temperatuur om dezelfde brandstofomzetting als methanol te bereiken. Daarom heeft methanol reforming bij lage temperatuur een hogere energieverhouding (producten/reactanten) dan ethanol en iso-octaan. Bij hoge temperatuur (brandstofconversie van 100%) neemt de energieverhouding toe naarmate de temperatuur stijgt. Dit kan worden verklaard door de aanwezigheid van CO in de producten als gevolg van de initiatie van de water-gas-shift-reactie.

Om een hogere energieverhouding te hebben dan voor methanol, moet de temperatuur voor ethanol en iso-octaan hoog genoeg zijn om meer dan 80% brandstofomzetting te hebben. Dankzij de snelle reactie en lage neiging tot vorming van cokes, had de methanol-reformering met stoom de voorkeur. Voor een betere water-gas-shift-reactie werd een koper-gebaseerde katalysator gekozen. Het gereformeerde uitlaatgasrecirculatieconcept (R-EGR) werd ook gekozen vanwege een betere warmteoverdracht en geen behoefte aan een extra watertank.

Vervolgens werd het theoretische rendement van de motor met het R-EGR-concept berekend. Het rendement van de Otto-cyclus werd eerst berekend voor methanol, daarna werd de vergelijking met ethanol en iso-octaan geanalyseerd. Een kleine toename in Otto cyclus-rendement met methanolreforming werd waargenomen, maar niet zo veel als toename van de onderste verbrandingswaarde van de reactanten. Een verlaging van de molaire expansieverhouding veroorzaakt een afname in de uitvoer. De lagere onderste verbrandingswaarde heeft de vermindering van de mol-expansieverhouding gecompenseerd. De rendementstoename ligt meer voor de hand bij sterk verdunde omstandigheden als gevolg van het feit dat de verlaging van de mol-expansieverhouding kleiner is. Als de warmteoverdracht in rekening wordt genomen, is het verschil in het bruto aangegeven rendement onzichtbaar tussen conventionele EGR- en R-EGR-verdunning. De vergelijking van Otto cyclus-rendement tussen methanol en ethanol/iso-octaan werd uitgevoerd bij dezelfde reformingfractie, dezelfde verbrandingsstabiliteitslimiet en dezelfde katalysatortemperatuur. Bij een lage reformingfractie (<30%) heeft methanol een hoger Otto-cyclusrendement. Bij een hogere reformfractie is het Otto-rendement voor ethanol en iso-octaan echter hoger als gevolg van een significante verbetering in energie/exergie van de producten in vergelijking met methanol. De berekening bij dezelfde katalysatortemperatuur toont een groot verschil in Otto-rendement tussen methanol en ethanol/iso-octaan bij lage temperatuur als gevolg van het verschil in de brandstofomzetting. De hogere temperatuur zorgt voor een toename in het Otto-rendement dankzij de aanwezigheid van CO in de reformingproducten.

De laminaire vlamsnelheid van methanol-syngas-mengsels werd voorspeld met behulp van een eendimensionale vlamcode. Verschillende mixregels zijn geëvalueerd en het Hirasawa-model geeft de beste resultaten. Het is echter niet beter dan de regel van Le Chatelier. De impact van syngasfractie op de exponent van de temperatuurkracht is erg klein bij een equivalentieverhouding in een bereik van 0.5-1.5. De laminaire vlamsnelheidscorrelatie werd vervolgens ontwikkeld voor het methanol-syngasmengsel. De correlatie komt goed overeen met de gesimuleerde resultaten en de bestaande correlatie voor methanol. De laminaire vlamsnelheid bij dezelfde verdunningsverhouding en dezelfde reformeringsfractie voor het R-EGR-concept was sneller. Dit is een extra reden voor de selectie van dat concept. Hoewel de verdunningsverhouding identiek is, is de laminaire verbranding in het R-EGR-concept hoger dan de conventionele EGR vanwege de aanwezigheid van waterstof in de reactanten. Voor beide soorten verdunningen

werd een universele verdunningsterm ontwikkeld.

De eigenschappen van het vlamfront voor verdunde methanol-vlammen werden geanalyseerd. Het stabiele verbrandingsregime werd gevonden voor verschillende soorten verdunning (lucht, conventionele EGR en R-EGR). Vergeleken met conventionele EGR heeft de R-EGR-verdunning een breder stabiel regime vanwege een snellere laminaire vlamsnelheid en een hogere klopvastheid. Met de verdunning van EGR en R-EGR is de molaire fractie CO en H_2 in de uitlaat hoger in vergelijking met luchtverdunning. De neiging tot klop neemt toe met de toename van EGR. Bij een hogere verdunningsverhouding heeft R-EGR een lagere klopintensiteit in vergelijking met de conventionele EGR-verdunning en een lagere neiging tot klop in vergelijking met luchtverdunning.

Ten slotte werd de volledige motorsimulatie uitgevoerd met behulp van GT-Power. Het reactiemechanisme voor methanolreforming werd gemodificeerd en gevalideerd met experimentele gegevens. Vergelijkbaar met de bevindingen van het Otto-cyclusrendement, is het verschil in bruto rendement zeer klein tussen R-EGR en conventionele EGR. De verbetering in effectief rendement is voornamelijk te wijten aan de vermindering van het pompwerk. Met een snellere laminaire vlamsnelheid heeft de R-EGR een kortere vlamontwikkelingsperiode, wat betekent dat deze een stabielere verbranding heeft. Er komt meer warmte vrij in het R-EGR-concept, wat leidt tot een hogere vlamtemperatuur en een hoger warmteverlies naar de wanden. Het absolute verschil in effectief rendement tussen de twee werkingspunten is ~0.3%. Bij de verdunningslimiet neemt het rendement toe met respectievelijk ~4% en 6.9% ten opzichte van de basislijn met de verdunning van EGR en R-EGR.

Als conclusie kan men stellen dat het huidige werk erin geslaagd is om het potentieel aan te tonen van methanol als brandstof in een motor met directe injectie en vonkontsteking. Dit werk bewees ook het belang van de molaire expansieverhouding op het motorrendement. De mogelijkheid om de energie van de brandstof aan de inlaat te verbeteren door middel van reforming en om het motorrendement met die technologie te vergroten, werd geëvalueerd.

English summary

Flame or combustion gave humans healthy food, protection, heat, light, and so on. Combustion also gave the power for a car to move from point A to point B. Most of the vehicles in the world now are powered by internal combustion engines. The engine converts the chemical energy stored in the reactant, i.e. a mixture of fuel and air, into thermal energy through combustion. Then, thermal energy is converted into mechanical energy via constrained expansion. Currently, most engines use fossil fuels (diesel and petrol/gasoline), and combustion produces a huge amount of CO_2 and other pollutant emissions. The energy security, polluting emissions from cars and global warming due to the greenhouse effect, to which CO_2 is one of the main contributors, lead to a decision of banning internal combustion engine vehicles in several cities or countries. Electrification is considered as a solution to decarbonizing transports. Although the electric vehicles do not release any emissions to the environment, the production of electricity, batteries, vehicles and the recycling of these cars after their backwards produce a significant amount of harmful emissions. Hence, "zero-emissions vehicle" is a political designation, not science. Furthermore, the low energy density of a battery, long charging time and the limitation of rare-earth materials such as cobalt or nickel are the other two challenges for battery electric vehicles. Therefore, internal combustion engines are still the main power source for the current and for future transport systems.

Engines and fuel technology are scalable and compact, which is important for transportation. The engines and fuels can also be produced in a sustainable way (closed CO_2 cycle). The CO_2 emissions can be captured and employed to produce synthetic fuels (or electrofuels, e-fuels). Sustainable transport requires synthetic fuels and synthetic fuel properties can be optimized to increase engine efficiency. Methanol is the most simple type of liquid synthetic fuel, so it has an advantage in production compared to other complex fuels. Thanks to its properties, methanol is more suitable for spark-ignition engines. The properties of methanol also support a potential of decreasing CO_2 emissions from spark-ignition engines.

The present work started with a review of the requirements of fuel properties to reduce CO_2 emissions from engines. The fuel should have a low carbon intensity and several interesting properties to improve the efficiency of engines. The carbon intensity is defined as the amount of produced CO_2 for a certain amount of heat

from the combustion of that fuel. In terms of carbon intensity, combustion of hydrogen does not release any CO_2. Methane is the hydrocarbon which has the lowest carbon intensity. However, both hydrogen and methane are gaseous at ambient pressure and temperature. Methanol is the liquid fuel which has the lowest carbon intensity. Liquid fuel is preferred due to its high energy density, ease of storage and distribution using current infrastructures.

In order to increase the efficiency of a spark-ignition engine, the fuel should have high research octane number, low motor octane number, high laminar burning velocity, high heat of vaporization, high oxygen mass fraction, low particle matter index, and low catalyst light-off temperature or short warm-up duration for the aftertreatment system. With high research octane number and low motor octane number, the anti-knock quality of that fuel increases. The engine is able to operate at a higher compression ratio, thus efficiency increases. Higher heat of vaporization causes a reduction in the unburned gas temperature, the knock is suspended. Furthermore, the decrease of burned gas temperature also leads to a reduction in heat losses to the wall. However, the lower combustion temperature makes a longer warm-up period for the aftertreatment system.

Higher laminar burning velocity generates more isochoric combustion, the engine has a higher effective expansion ratio, leading to higher efficiency. Fuel with higher oxygen mass fraction leads to an increase in combustion efficiency. If the emissions are neglected, these properties support higher engine efficiency. Low particle matter index represents less-soot combustion, the pumping work decreases thanks to the absence of a gasoline particle filter. Methanol has high anti-knock quality, high burning velocity, high heat of vaporization, high oxygen mass fraction, and almost soot-free combustion. Therefore, the engine efficiency (tank-to-wheel) for methanol is higher than for other liquid fuels. Together with the lowest carbon intensity, methanol is the most promising fuel for a low CO_2 emissions engine. Compared to other synthetic liquid fuels, the production of methanol has the highest (well-to-tank) efficiency. Therefore, the well-to-wheel efficiency for methanol engines is the highest. However, the well-to-wheel efficiency for internal combustion engine vehicles is still much lower than for battery electric vehicles.

The potential of methanol as a fuel for a direct-injection spark-ignition engine was studied. The measurements at full load have proved the downsizing potential of methanol compared to gasoline. The engine can be further downsized by ~10.7% against gasoline. The reduction of unburned gas temperature was also clearly seen. This helps for the suspension of knock occurring. At the same engine load (maximum load for gasoline), the methanol-fueled engine has higher thermal efficiency (7-8% points) and lower emissions compared to gasoline. The lean operation with methanol was also investigated and compared with gasoline. Thanks to a higher laminar burning velocity, the engine load can be controlled by lean-burn strategy in a wider range for methanol before the combustion becomes

unstable. The maximum efficiency for methanol was reached with lambda in range of 1.2-1.4, it reaches ~41%, 20% higher than for gasoline. The early flame development period is the combustion duration most closely related to coefficient of variance of indicated mean effective pressure. The CA0-10 of 26.5 degree crank angle and laminar burning velocity at ignition timing of 0.4 m/s can be used to represent the lean-burn limit for wide open throttle operations.

In order to further increase the efficiency of methanol engines, the recovery of engine exhaust heat was considered. A brief overview of the waste heat recovery technologies was performed, and the conversion of exhaust energy into chemical energy through thermochemical recuperation (or endothermic fuel reforming) was chosen in this work. Methanol is converted into hydrogen-rich gas (or syngas) at high temperature. Five types of methanol reforming were analyzed. The Gibbs free energy minimization method was used to predict the reforming product as a function of reactor temperature. Because the simulation uses a reactor with infinite volume, the reactant has a long residence time. This causes the reforming temperature from the simulation is much lower than what would be possible with experiments.

The reforming performance of methanol was compared to other spark-ignition engine fuels, ethanol and iso-octane (gasoline surrogate). Although the absolute reforming temperature cannot be predicted, the relative difference between fuels and reactants can be estimated. Ethanol and especially iso-octane required a higher temperature to achieve the same fuel conversion as methanol. Therefore, at low temperature, methanol reforming has a higher energy ratio (products/reactants) than ethanol and iso-octane. At high temperature (fuel conversion of 100%), the energy ratio increases as temperature increases. This can be explained by the presence of CO in the products because of the initiation of the reverse-water gas shift reaction. In order to have a higher energy ratio than for methanol, the temperature for ethanol and iso-octane should be high enough to have over 80% fuel conversion. Thanks to the fast reaction and low propensity for coke formation, the methanol steam reforming was preferred. For a better water gas shift reaction rate, a copper-based catalyst was selected. The reformed-exhaust gas recirculation (R-EGR) concept was also chosen due to a better heat transfer and no need for an additional water tank.

Then, the theoretical efficiency of the engine with R-EGR concept was calculated. The Otto cycle efficiency was calculated for methanol first, then the comparison with ethanol and iso-octane was analyzed later. A small increase in Otto cycle efficiency with methanol reforming was observed, not as much as the improvement in the lower heating value of reactants. A reduction in molar expansion ratio causes a small improvement in the piston work. The lower heating value has compensated for the reduction of molar expansion ratio. The improvement in efficiency is more obvious at highly diluted condition due to the reduction in the molar expansion ratio being smaller. If the heat transfer is taken into account, the difference in

the gross indicated efficiency is invisible between conventional EGR and R-EGR dilution.

The comparison of Otto cycle efficiency between methanol and ethanol/iso-octane was performed at the same reforming fraction, same combustion stability limit, and the same catalyst temperature. At low reforming fraction (< 30%), methanol has a higher Otto cycle efficiency. However, at a higher reforming fraction, the Otto efficiency for ethanol and iso-octane is higher due to a significant improvement in energy/exergy of products compared to methanol. The calculation at the same catalyst temperature shows a big difference in Otto efficiency between methanol and ethanol/iso-octane at low temperature due to the difference in the fuel conversion. The higher temperature causes an increase in Otto efficiency thanks to the presence of CO in the reforming products.

The laminar burning velocity of methanol-syngas blends was predicted using a one-dimensional flame code. Several mixing rules were evaluated, and Hirashawa's model gives the best results. However, it does not outperform compared to Le Chatelier's rule. The impact of syngas fraction on the temperature power exponent is very small at an equivalence ratio in a range of 0.5-1.5. A laminar burning velocity correlation was then developed for the methanol-syngas mixture. The correlation has a good agreement with the simulated data and the existing correlation for methanol. The laminar burning velocity at the same dilution ratio and the same reforming fraction for the R-EGR concept was faster. This is an additional reason for the selection of that concept. Although the dilution ratio is identical, the laminar burning in the R-EGR concept is higher than the conventional EGR due to the presence of hydrogen in the reactants. A universal dilution term was developed for both types of dilution.

The reaction front properties for diluted methanol flames were analyzed. The stable combustion regime was found for different kinds of dilution (air, conventional EGR, and R-EGR). Compared to conventional EGR, the R-EGR dilution has a wider stable regime due to a faster laminar burning velocity and higher knock resistance. With the dilution of EGR and R-EGR, the molar fraction of carbon monoxide and hydrogen in the exhaust is higher compared to the air dilution. The knock tendency increases with the increase of the EGR ratio. At a higher dilution ratio, R-EGR has a lower ringing intensity compared to the conventional EGR dilution and a lower knock tendency compared to air dilution.

Finally, the full engine simulation was performed using GT-Power. The reaction mechanism for methanol reforming was modified and validated with experimental data. Similar to the finding with Otto cycle efficiency, the difference in gross indicated efficiency is very small between R-EGR and conventional EGR. The improvement in brake thermal efficiency is mainly due to the reduction of pumping work. With a faster laminar burning velocity, the R-EGR has a shorter flame development period, this means it has more stable combustion. More heat is released in the R-EGR concept, causing a higher flame temperature and a

higher heat loss to the walls. The absolute difference in brake thermal efficiency between the two cases is ~0.3% at 15% EGR. At the dilution limit, the efficiency increases ~4% and 6.9% against the baseline with the dilution of EGR and R-EGR, respectively.

In conclusion, the current work succeeded in demonstrating the potential of methanol as a fuel in a direct-injection spark-ignition engine. This work also proved the importance of molar expansion ratio on engine efficiency. The possibility to enhance the inlet fuel energy through reforming and to increase engine efficiency with that technology was evaluated.

1 Introduction

1.1 Why spark-ignition (SI) engines?

Although internal combustion engines (ICEs) had a big contribution to the development of the modern society, some governments have been planning to reduce the number of ICE powered vehicles because they consume around 42 million barrels of crude oil each day [1] and produce a huge amount of polluting emissions. Recently, four big cities (Paris, Mexico City, Madrid and Athens) have decided to ban cars and trucks that run on diesel from 2025 [2]. A larger quantity of particulate matter (PM) and nitrogen oxides (NO_x) emissions are the key reasons for that decision. PM, NO_x and other pollutants have contributed to the deaths of over three million people each year [3]. In SI engines (or gasoline/petrol engines), fuel and air are premixed at stoichiometric condition before the ignition, producing a homogeneous mixture which results in less PM than the diesel engines. Although the SI engine produces more engine-out NO_x than the diesel engine, that emission can be easily treated by a cheap and robust after-treatment system, the three-way catalyst (TWC). However, low fuel economy is a challenge of the SI engines. With a stoichiometric operation, high throttling losses at low load and low compression ratio, the SI engine is less efficient than the diesel engine. The compression ratio is limited by the auto-ignition of the end gas (knock phenomena) during the flame propagation. Although diesel engines have a higher tank-to-wheel efficiency

(less engine-out CO_2) than SI engines, the well-to-tank (including fuel refining) efficiency of diesel cars are lower than petrol cars. In summary, the well-to-wheel efficiency of a petrol car is higher than a diesel car. Figure 1.1 compares the lifecycle CO_2 emissions of diesel and petrol cars [4]. Due to the larger amounts of manufacturing materials, higher emissions to produce biodiesel compared to ethanol, and a longer moving distance, a diesel car produces 3.65 tonnes more CO_2 emissions than petrol car over its timelife [4]. A diesel car produces about 23.43 kg CO_2 and a petrol car produces about 22.29 kg CO_2 on average per 100 kilometers.

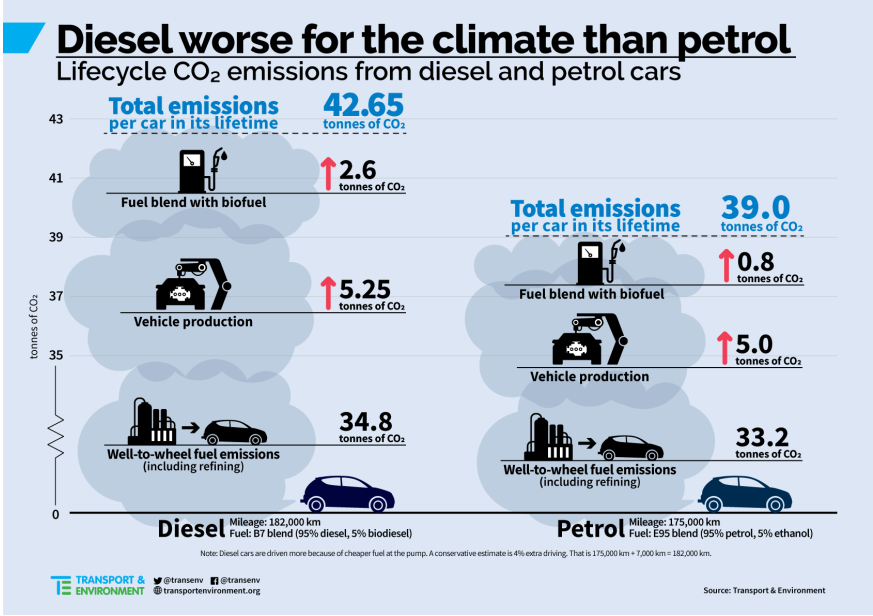

Figure 1.1: Life cycle CO_2 emissions from diesel and petrol cars [4].

The SI engines still have potential to further increase the tank-to-wheel efficiency to be comparable with the diesel engines with several technologies such as cylinder deactivation, variable compression ratio, diluted by air (lean-burn) or exhaust gas recirculation (EGR), Miller/Atkinson cycle, water injection, etc. [5]. Figure 1.2 shows a typical brake thermal efficiency (BTE) curve as a function of load for a port fuel injected (PFI) naturally aspirated (NA) SI engine. The efficiency increases as load increases and then it reaches a peak before decreasing at higher loads. At high load, the BTE decreases because of retarded combustion phasing to avoid engine knock and the enrichment strategy. Depending on the engine load, different methodologies can be used to increase the efficiency. As can also be seen in Figure 1.2, the dilution technology (with air or EGR/cooled EGR) could

be employed to increase the engine BTE for different engine load ranges.

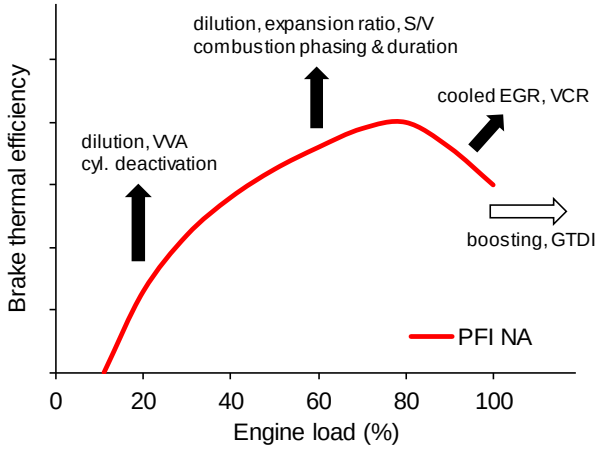

Figure 1.2: Typical brake thermal efficiency profile for a PFI NA SI engine and technologies to increase efficiency [6].

Both air and EGR dilution strategies are promising approaches to mitigate knock [7] as well as to enhance the efficiency of SI engines [8]. The efficiency improvement can be explained by the decrease of combustion temperature, thus lower heat losses, reduced pumping work and increased specific heat ratio. With the enhancement of knock resistance, a higher compression ratio can be used. However, the cycle-by-cycle variation increases with both types of dilution [7]. Another challenge of lean operation is the NO_x emissions due to the low conversion efficiency of the TWC in that condition. Therefore, the current direction for SI engines development is reducing CO_2 emissions at stoichiometric condition. This chapter is devoted to the optimum fuel properties and importance of synthetic fuel for future sustainable mobility.

1.2 Fuel selection for SI engines

In this section, the fuel for a low CO_2 emissions SI engine will be selected. The selection will be performed based on the tank-to-wheel efficiency/emissions. The well-to-tank efficiency/emissions will be discussed in section 1.3. The equation $CO_2 = CO_2$ can be rewritten by multiplying and dividing the same values, Q_{fuel} and W_{engine}, as in equation 1.1 (when Q_{fuel} and W_{engine} do not equal zero).

$$CO_2 = \frac{CO_2}{Q_{fuel}} \times \frac{Q_{fuel}}{W_{engine}} \times W_{engine} \tag{1.1}$$

where Q_{fuel} and W_{engine} are the fuel energy (or lower heating value, LHV) and the engine work, respectively.

Based on that equation, to reduce CO_2 emissions at a certain engine work W_{engine}, the ratio of CO_2 to Q_{fuel} and the ratio of Q_{fuel} to W_{engine} need to be decreased. The first ratio (CO_2/Q_{fuel}) represents the carbon intensity of the fuel with an unit of g-CO_2/MJ. The second ratio shows an inverse of engine thermal efficiency. Therefore, to reduce the CO_2 emissions, the selected fuel should have a low carbon intensity and the engine efficiency be as high as possible. The engine efficiency is also influenced by the fuel properties. Table 1.1 presents key properties of six fuels for SI engines. The properties of typical gasoline were compared with alternatives such as methanol, ethanol, 2-methylfuran (2-MF), dimethyl carbonate (DMC), and hydrogen. In this section, the first part will consider the CO_2 intensity for the fuel selection. Important properties for increased efficiency will then be analyzed in the second and third sections.

*Table 1.1: Properties of typical gasoline, methanol, ethanol, 2-methylfuran (2-MF), dimethyl carbonate (DMC) and hydrogen relevant to internal combustion engines [9–21]. *Includes atmospheric nitrogen. **Atmospheric pressure. ***Calculated with fuel energy. NA: not available.*

Property	**Gasoline**	**Methanol**	**Ethanol**	**2-MF**	**DMC**	**Hydrogen**
Chemical Formula	Various	CH_3OH	C_2H_5OH	C_5H_6O	$C_3H_6O_3$	H_2
Oxygen Content by Mass [%]	0	49.9	34.7	20.5	53.3	0
Density at NTP [kg/l]	0.74	0.79	0.79	0.91	1.079	0.00008
Lower Heating Value (LHV) [MJ/kg]	42.9	20.09	26.95	30.37	15.8	120
Volumetric Energy Content [MJ/l]	31.7	15.9	21.3	27.63	17.05	0.010
Stoichiometric Air-to-Fuel Ratio [kg/kg]	14.7	6.5	9	10.08	4.64	34.2
Energy per Unit mass of air [MJ/kg]	2.92	3.09	2.99	3.01	3.41	3.51
Research Octane Number (RON) [-]	92-98	109	109	103	109	130 (λ=2.5)
Motor Octane Number (MON) [-]	85	89	90	86	102	NA
Sensitivity (S = RON-MON) [-]	10	20	19	17	7	NA
Boiling point at 1 bar [^{o}C]	25-215	65	79	64	90	-253
Heat of vaporization (HoV) [kJ/kg]	180-350	1100	838	358	418	-
Heat of vaporization, λ=1 [kJ/kg Air]	18.0	169.2	93.1	35.52	90.09	-
HoV/LHV ratio [-]	0.0042-0.0082	0.0548	0.0311	0.0118	0.0265	-
Reid Vapour Pressure [psi]	7	4.6	2.3	2.68	NA	-
Molar expansion ratio (MER) [-]*	0.937	1.061	1.065	1.016	1.13	0.852
Ratio of triatomic to diatomic products [-]*	0.35	0.53	0.44	0.35	0.53	0.53
Flammability Limits in Air [vol%]	1.3-7.6	6.7-36	3.3-19	NA	4.2-12.9	4-75
Flammability Limits in Air [λ]	0.26-1.60	0.23-1.81	0.28-1.91	NA	NA	0.15-10.57
Minimum Ignition Energy in Air [mJ]	0.25	0.14	0.23	NA	NA	0.02
Laminar flame speed at 358 K, λ=1 [cm/s]**	46.0	54.8	53.3	57.58	39.01	~290
Specific CO_2 Emissions [g/MJ]***	73.95	68.75	71.22	85.34	92.83	0.00

1.2.1 Carbon intensity

Figure 1.3 shows the carbon intensity of different fuels under stoichiometric condition. The fuel exergy is employed to calculate specific CO_2 emissions instead of fuel energy (as in Table 1.1). Fuel exergy provides the potential work, and it is a better indicator than the fuel energy (or lower heating value, LHV) [22]. Due to the lack of exergy data for 2-MF and DMC, these candidates were not considered in this selection. Hydrogen was not considered as well because its combustion does not produce CO_2. Fuels were separated in four groups: alcohols, alkanes, olefins, and aromatics. The carbon intensity was calculated for three alcohols (C1 to C3), ten alkanes (C1 to C10), four olefins (C2 to C5), and three aromatics (C6 to C8). The chemical formula of these fuels were presented in that Figure.

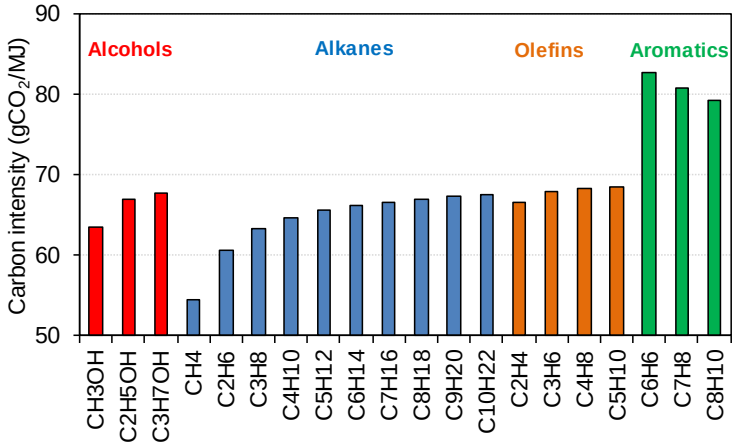

Figure 1.3: Comparison of carbon intensity from stoichiometric combustion of different fuel candidates.

As can be seen, methane (CH_4), ethane (C_2H_6), propane (C_3H_8), and methanol (CH_3OH) are the four fuels which have the lowest carbon intensity. Methane, ethane, and propane are gaseous, only methanol is liquid at ambient temperature and pressure. Hence, in these four groups, methanol is the liquid fuel which has the lowest CO_2 emissions. Compared to other liquid fuels, 2-MF and DMC in Table 1.1, methanol produces less CO_2 than 2-MF and DMC (lower heating value based) due to a higher H/C ratio. A liquid fuel has higher energy density, it is easily stored and distributed using current infrastructures with a few modifications. Furthermore, the latent heat of liquid fuel is an important property for a highly efficient engine, which will be discussed in the following section.

1.2.2 Fuel properties for highly efficient SI engines

An engine is a complex power system, which includes the gas exchange, thermodynamics, heat transfer, combustion, friction, etc. Therefore, the total energy losses is the combination of all losses by these factors. The engine efficiency can be expressed by several efficiencies, as in equation 1.2 [23].

$$\eta_{th} = \eta_{ideal} \times \eta_{glh} \times \eta_{comb} \times \eta_{pump} \times \eta_{ht} \times \eta_{emiss} \times ... \tag{1.2}$$

where

- η_{th} is the indicated thermal efficiency
- η_{ideal} is the ideal Otto cycle efficiency
- η_{glh} is the combustion phasing efficiency (degree of constant volume combustion)
- η_{comb} is the combustion efficiency
- η_{pump} is the pumping efficiency
- η_{ht} is the heat transfer efficiency
- η_{emiss} is the emissions efficiency

The ideal efficiency (or Otto cycle efficiency) can be expressed as in equation 1.3. It is a function of engine compression ratio (CR) and the specific heat ratio γ (c_p/c_v). A higher value of CR and γ leads to an increase in η_{ideal}.

$$\eta_{ideal} = 1 - \frac{1}{CR^{\gamma-1}} \tag{1.3}$$

As mentioned previously, the CR in SI engines is limited by knock. The CR can be increased with a fuel which has high anti-knock quality [24]. Normally it is indicated by the fuel's octane numbers like Research Octane number (RON) and Motor Octane number (MON). Remmert et al. confirmed that the octane number remains an important factor for improving power and efficiency in emerging engine technologies [25]. With higher octane number fuels, further downsizing or higher compression ratios are possible [25]. If two fuels have the same RON, a lower MON fuel has a better performance on the mitigation of knock and better

engine efficiency [26–28]. Remmert et al. did the measurements with seven fuels to investigate the octane appetite on the Ultraboost SI engine [25]. They found that for a fixed RON, better knock resistance is achieved with a fuel which has a lower MON. Szybist and Splitter [29] also confirmed that a fuel which has high RON and high octane sensitivity (S - the difference between RON and MON) helps to resist knock.

Kalghatgi [30] used an octane index (OI) to present the anti-knock quality of a fuel at a given engine condition. Equation 1.4 shows the calculation of OI as a function of RON, S and K. K is a weighting factor between RON and MON, and it depends on the engine operating condition. OI equals RON and MON with K equals 0 and 1, respectively. A higher OI represents a better anti-knock quality.

$$OI = RON - K \times S \tag{1.4}$$

In the RON measurement, the air temperature was controlled at 52 °C and the mixture temperature was set to 149 °C in the MON test [31]. Both tests were performed with an inlet pressure of 1 atm. Recent SI engines are equipped with turbochargers and direct injection system. Therefore, the unburned mixture in modern SI engines has a higher pressure and a lower temperature than in the RON test, or "beyond RON" condition [32]. K is negative in beyond RON condition, so a fuel with high RON and high S is preferred to achieve higher ideal efficiency. Recently, Ratcliff et al. [33] developed a correlation to predict K as a function of unburned gas temperature at a cylinder pressure of 15 bar (T_{comp15}) and lambda (λ) as in equation 1.5. Thus K is not only a function of engine condition, but it is also affected by fuel property, the heat of vaporization (HoV). A fuel with high HoV results in a lower T_{comp15}, so K decreases. Therefore the anti-knock quality improves with high HoV fuel.

$$K = 0.00497T_{comp15} - 0.135\lambda - 3.67 \tag{1.5}$$

The CR is not only limited by the "normal" knock, but it is also restricted by the pre-ignition. It is the auto-ignition of reactant at high pressure and temperature before the spark plug onsets. It usually occurs at low speed and high load condition. A fuel with low minimum ignition energy causes a higher chance for the pre-ignition by hot spots. Although the pre-ignition is unpredictable, the propensity can be reduced by employing ceramic for the spark electrode and sodium filled exhaust valves. Split injection strategy is also used. It reduces the temperature of hot spots and increases in-cylinder turbulence near the spark plug [34].

The specific heat ratio γ in equation 1.3 strongly depends on the gas temperature, it increases as temperature decreases. To reduce the gas temperature, a liquid fuel with high HoV can be used. If that fuel has a low stoichiometric air-to-fuel ratio (AFR), the inlet temperature further decreases. Charge cooling also is one of the reasons why ethanol-gasoline blends allow for an advanced spark timing without knock [35–37]. Lower initial temperature by the evaporation of the fuel also can mitigate knock. Therefore, a fuel which has a higher heat of vaporization is better to have a higher ideal efficiency in SI engines. The challenge with that fuel is the cold start and catalyst light-off behaviors.

The second efficiency, η_{glh}, represents the impact of combustion phasing and combustion duration. It presents the ratio of cycle work with non-isochoric combustion to the work with constant volume combustion. To first order, efficiency increases with a more isochoric combustion. Fast combustion also leads to an increase in the friction and heat losses due to the increase in peak pressure and combustion temperature. However, shorter combustion duration is better to improve the fuel economy [38], thus a fuel with a high laminar burning velocity (LBV) is recommended.

The "inherent" combustion efficiency, η_{comb}, is defined as the ratio of heat released by the fuel to the heat input by the fuel. It can be predicted by the oxygen mass fraction in the fuel's molecule. A fuel with high oxygen fraction might help to improve the combustion efficiency [15, 39]. However, the energy density decreases with higher oxygen mass fractions.

The pumping efficiency (η_{pump}) and heat transfer efficiency (η_{ht}) show the ratio of the cycle work with theses losses divided by the work without losses. The pumping work relies on the difference between exhaust and intake pressure. A lower intake pressure will increase the pumping work. A lower intake gas temperature causes an increase in intake charge density, so it requires a lower inlet pressure to maintain the output [40]. A lower intake gas temperature also reduces the final (combustion) temperature, so heat losses decrease. Therefore, the pumping work increases and heat transfer decreases with a higher HoV fuel. This means that pumping efficiency decreases and heat transfer efficiency increases. In general, the BTE increases as HoV increases. Jung et al. [40] quantified the impact of HoV on the increase of BTE based on the experimental data. Approximately half of the improvement was accounted by the ratio of HoV to LHV due to the fact that the fuel HoV detracts from the measured LHV, however that is available for free in engines. Therefore, the impact of HoV on the increase of BTE (ΔBTE) can be expressed as in equation 1.6.

$$\Delta BTE\% \approx 2 \times \left(\frac{HoV}{LHV} \right) \times 100\% \tag{1.6}$$

For instance, the difference between BTE of methanol and ethanol due to this effect is ~2×(0.0548-0.0311)×100% = 4.74% (see Table 1.1).

The emissions efficiency, η_{emiss}, considers the fuel penalty to reduce the PM emission and to warm up the TWC during the cold-start. For PM emission, it presents the fuel mass ratio over driving cycle of an engine with to without a Gasoline Particulate Filter (GPF). The combustion of a fuel with low particle matter index (PMI) produces less PM, so that a GPF might not be needed. With the presence of GPF, the back pressure increases. Thus the pumping work increases, also leading to a higher propensity for knock. This means a fuel with low PMI will potentially have a higher efficiency.

Equation 1.7 proposes a relation to calculate the PMI. The PMI is a function of DBE - double bond equivalence, $VP(433K)$ - vapour pressure at 443 K, and Wt - the mass fraction of that species in the fuel blend [41]. PMI decreases as DBE decreases and $VP(443K)$ increases (at the same Wt). DBE is defined as in equation 1.8, it depends on the number of carbon, hydrogen, and nitrogen atoms in the fuel molecule. $VP(443K)$ is represented by a relationship with boiling temperature using a polynomial formula. A lower boiling temperature causes a higher vapour pressure [41].

$$PMI = \sum_{i=1}^{n} \left[\frac{DBE_i + 1}{VP\left(443K\right)_i} \times Wt_i \right] \tag{1.7}$$

$$DBE = \frac{2C + 2 - H + N}{2} \tag{1.8}$$

where C, H, and N are the number of carbon, hydrogen and nitrogen atom in fuel molecule, respectively. Hence, alcohol and alkanes (or paraffins) have DBE equals 0. The effect of chain length on soot formation has not been taken into account.

A shorter warm-up period for the TWC causes a lower fuel penalty during the cold start. Therefore, a fuel with low catalyst light-off temperature $T_{c,90}$ is recommended. The catalyst light-off temperature $T_{c,90}$ is defined as the temperature where 90% of unburned hydrocarbons were converted by the TWC. Unburned hydrocarbons contain paraffin, olefin, etc., and different gases have different catalytic reactivities. Hence, the $T_{c,90}$ is dependent on fuels.

In conclusion, a fuel needs the following properties to boost engine efficiency:

- high Research Octane number (RON)
- high octane sensitivity (S)
- high heat of vaporization (HoV)
- high oxygen mass fraction
- high laminar burning velocity (LBV)
- low particle matter index (PMI): low *DBE* and low boiling temperature
- low catalyst light-off temperature ($T_{c,90}$)

As can be seen in Table 1.1, methanol has a similar RON as ethanol and DMC, it equals 109. However, the octane sensitivity of methanol is the largest, 20 compared to 19 for ethanol and 7 for DMC. The RON of 2-MF is 103, lower than other alternatives. The HoV/LHV ratio of methanol is also the highest one. This means methanol has the potential of highest ideal efficiency. Methanol has a comparable oxygen mass fraction as DMC, so the combustion efficiency is more or less the same. The laminar burning velocity at atmospheric pressure, temperature of 358 K is also presented in the Table. As shown, 2-MF is the fuel which has the fastest LBV, and methanol is the second. Methanol has a similar boiling temperature as 2-MF and has a lower *DBE* (0 versus 3 for 2-MF), which means the combustion of methanol produces less soot, so that a GPF might not be needed. Methanol however has low LHV and high HoV, which means the duration for catalyst warm-up is much longer than for gasoline, which leads to a higher fuel penalty during the cold start. From this analysis, methanol seems the most promising fuel for SI engines, especially for steady state operations.

Recently, Miles has developed a merit function to calculate the relative efficiency benefit compared to gasoline [42]. The purpose of that work is finding the most promising fuel to blend with gasoline. The RON, S, HoV, LBV, PMI and $T_{c,90}$ of fuel blends were taken into account. A higher value of the merit function score presents for a higher relative improvement of engine efficiency against conventional gasoline. Figure 1.4 shows the distribution of merit function values for different blending candidates at 10% volume in the mixture with conventional gasoline. 10,000 samples of the engine dependent factor K between -1.25 to 0.5 were used. As can be seen, methanol and 2-MF are the two candidates which have the highest merit score. Although (pure) methanol has higher RON, higher S, higher HoV, and lower PMI than 2-MF, the engine efficiency with 10% methanol

and 10% 2-MF in the gasoline blend are comparable. 2-MF is a prospective octane booster [43], the RON value for low blending levels of 2-MF/gasoline is higher than methanol/gasoline. This explains for a similar merit function score of 2-MF and methanol in Figure 1.4. However, methanol has a lower specific CO_2 emissions than 2-MF (see Table 1.1). Thus, the amount CO_2 emissions for a methanol/gasoline blend (10% methanol by volume) will be the lowest.

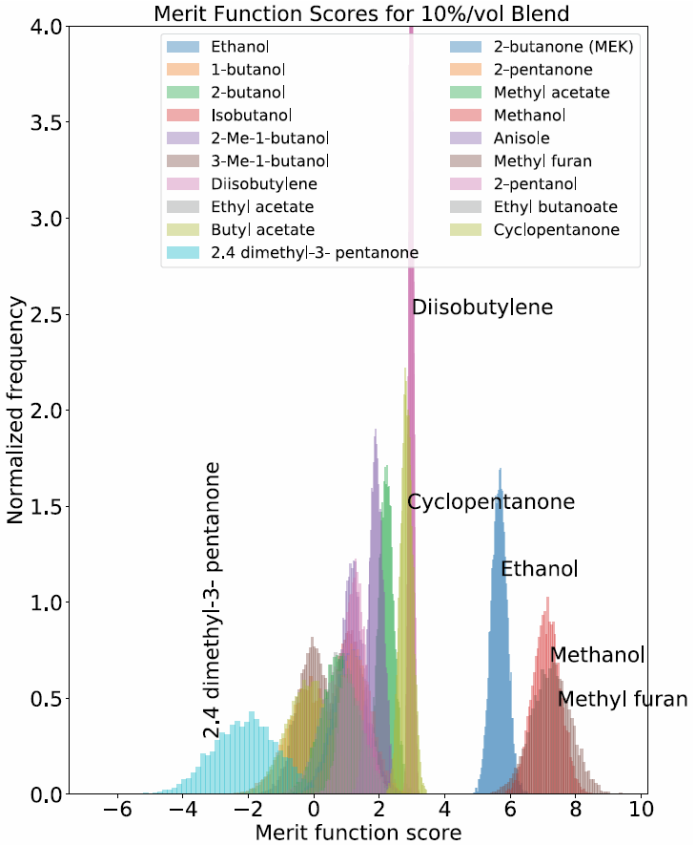

Figure 1.4: Distribution of merit function values for different blending candidates at 10% volume with conventional gasoline [44].

If 100% fuel is used, methanol has the highest merit function score thanks to its interesting properties compared to other fuels. Figure 1.5 shows the merit function score of four pure fuels (methanol, ethanol, 2-MF, and DMC) as a function of K factor. Due to the lack of catalyst light-off temperature, the score was calculated without the impact of emissions (PMI and $T_{c,90}$). The effect of RON, S, HoV and LBV were taken into account [42]. As can be seen in Figure 1.4, 2-MF is a good fuel to blend with gasoline at low volumetric level. However, using 100% 2-MF is

not a good choice because of the lowest RON and HoV compared to other fuels.

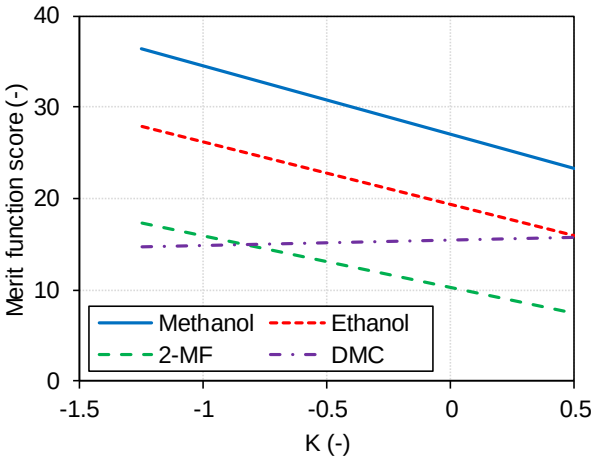

Figure 1.5: Merit score as a function of K factor for methanol, ethanol, 2-MF and DMC.

1.2.3 Molar expansion ratio

In the previous section, chemical and physical fuel properties for a highly efficient SI engine were reviewed. This section analyzes another fuel property, the molar expansion ratio or MER. The MER is defined as the ratio of number of moles of products to the reactants. This is a less explored fuel property, however, it is an important one. Szybist et al. [22] concluded that an engine is able to produce higher output with a fuel that has higher MER. The impact of MER on engine efficiency will be investigated in detail here.

First, the combustion reaction of a "general fuel" $C_xH_yO_z$ with air and EGR dilution is presented in reaction (R1.1). The combustion reaction was written for stoichiometric and lean cases (equivalence ratio $\phi \leq 1$). Assuming the fuel is completely burnt, the products include carbon dioxide (CO_2), water vapour (H_2O), nitrogen (N_2) and the oxygen left in the lean cases.

$$C_xH_yO_z + \frac{d}{\phi}\left(O_2 + 3.76N_2\right) + Y_{EGR}\left[aCO_2 + bH_2O + cN_2 + d\left(\frac{1}{\phi} - 1\right)O_2\right]$$

$$\longrightarrow \; aCO_2 + bH_2O + cN_2 + d\left(\frac{1}{\phi} - 1\right)O_2 \qquad \text{(R1.1)}$$

After balancing reaction R1.1, coefficients a, b, c, and d were calculated as a

function of x, y, z, ϕ, and Y_{EGR} (see Appendix B). The MER is then calculated as in equation 1.9.

$$MER = \frac{4.76\left(x+\frac{y}{4}-\frac{z}{2}\right)+\left(\frac{y}{4}+\frac{z}{2}\right)\left[\phi+Y_{EGR}\left(1-\phi\right)\right]}{4.76\left(x+\frac{y}{4}-\frac{z}{2}\right)+\left[1-Y_{EGR}\left(1-\frac{y}{4}-\frac{z}{2}\right)\right]\left[\phi+Y_{EGR}\left(1-\phi\right)\right]} \tag{1.9}$$

As can be seen, there are two methodologies to change MER: change fuel (change x, y, z), and dilution (change ϕ and/or Y_{EGR}). With the increase of dilution (air and EGR), the MER tends towards unity. The impact of MER by increasing the dilution fraction is not a focus of this part, so the equivalence ratio and EGR ratio were kept at 1 and 0% in this section, respectively.

In order to estimate the link between MER and efficiency, a simulation approach using GT-Power is employed. The simulation was performed from -180 degree crank angle (CAD) to +180 CAD after firing top dead center ($aTDC_f$) without gas exchange. Thus, the pumping work equals 0. The compression ratio and expansion ratio were fixed at 10:1. The initial pressure and temperature at -180 CAD $aTDC_f$ were 1 bar and 343 K, respectively. The GT-Power recommended values for combustion chamber wall temperatures were employed: 550 K for cylinder head and piston, 400 K for cylinder liner [45]. A Wiebe heat release profile was used, and the heat release is described as below

$$x_b = 1 - exp\left[-a\left(\frac{\theta-\theta_0}{\Delta\theta}\right)^{w+1}\right] \tag{1.10}$$

where $\Delta\theta$ and θ_0 are set by matching the desired combustion duration CA10-90 (10-90% burn duration) and combustion phasing CA50 (crank angle at 50% burn). The efficiency factor a equals 5 and the Wiebe exponent w equals 1.422 to have the best match with the engine experiment, presented in Chapter 2. Combustion efficiency is taken to be 100%.

To simulate the Otto cycle efficiency, CA50 was set at top dead center, and CA10-90 of 2 CAD was employed [46], without heat transfer and friction. To analyze the impact of heat transfer and friction, these losses were added step by step. First, Morel's heat transfer model was employed [47], so the gross indicated thermal efficiency (ITE) can be predicted. Then, the Chen and Flynn expression [48] was used to calculate the friction mean effective pressure (FMEP). Thus, the

gross BTE can be estimated. The FMEP is described as a function of mean piston speed U_p (in m/s) and peak cylinder pressure P_{max} (in bar), as in equation 1.11. The engine speed is set at 1500 rpm (revolutions per minute), giving a mean piston speed of 4.07 m/s.

$$FMEP = 0.4 + 0.005P_{max} + 0.09U_p + 0.0009U_p^2 \tag{1.11}$$

Wissink et al. [49] concluded that the efficiency improves with decreased CA10-90 and CA50 closer to TDC. However, the peak pressure and temperature are high, which leads to an increase in heat transfer and friction. Thus, this combustion phasing and combustion duration are not optimized. The optimum CA50 and CA10-90 were then employed. In practice, the CA50 is controlled easily by changing the ignition timing. The CA10-90 strongly depends on the fuel's LBV, in-cylinder turbulence, combustion chamber geometry, etc. It is not easy to control in practice; however, the optimum value for the combustion duration was employed to present the highest efficiency that the engine can achieve.

The test was performed with standard fuels in GT-Power fuel database first. All fuels have the same chemical formula of C_nH_{2n+2}, with "n" varying between 0 (H_2) and 8 (C_8H_{18}). The fuel was mixed with air at stoichiometric condition without combustion products. Thus, the MER increases from ~0.852 to ~1.058. However, the air-to-fuel ratio, lower heating value, specific heat ratio γ, mixture density, etc. also change.

To minimize the impact of other properties, user-defined fuels then were employed. The properties of n-heptane were used for all fuels including the lower heating value, critical temperature/pressure, transport properties, enthalpy coefficients, etc. The number of C, H, and O atoms in a fuel molecule are changed to have different MER. The formula of olefins (C_nH_{2n}) is employed for user-defined fuels because the AFR for olefins is a constant, it equals ~14.7. In this case, the number of O atoms is 0.

Figure 1.6 shows the resulting efficiency as a function of MER. The filled symbols represent the efficiency with CA50 at TDC and CA10-90 of 2 CAD. Due to isochoric combustion, peak pressure and maximum temperature increase. Therefore, heat loss and friction loss are higher than the case with optimum combustion. The opened symbols illustrate the efficiency with optimum combustion parameters, CA50 and CA10-90, for each fuel. With optimum CA50 and CA10-90, the maximum engine efficiency (without heat and friction losses) is lower than the Otto cycle efficiency due to the presence of combustion phasing loss. However, if the heat transfer and friction are taken into account, the optimum

gross ITE and optimum gross BTE increase due to the reduction of relative heat transfer and friction work. As clearly be seen, the efficiencies increase as MER increases.

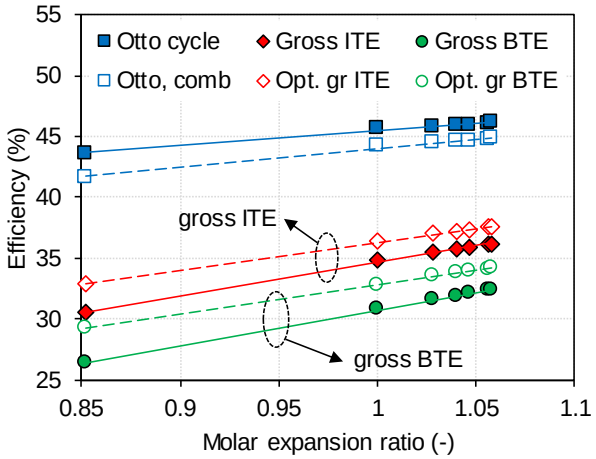

Figure 1.6: The relationship between efficiency and MER. "Opt." represents the simulation results with optimized CA50 and CA10-90 for different fuels.

Figure 1.7 presents the in-cylinder pressure profiles of four fuels with their optimum combustion phasing and combustion duration. As can be seen, the motored pressure decreases and the peak pressure increases as MER increases. The decrease of motored pressure (or compression work) is due to the reduction of γ with a higher MER fuel [22]. The peak pressure is influenced by the fuel's lower heating value, combustion duration, initial pressure and MER. Higher peak pressure leads to an increase in temperature, so the absolute heat loss increases. The FMEP also increases with the increase of MER due to a higher P_{max} (see equation 1.11).

Figure 1.8 presents the key efficiency losses as a function of MER. These losses were calculated based on the data in Figure 1.6. The filled symbols represent the losses for the TDC isochoric combustion (CA50 at TDC and CA10-90 of 2 CAD). The heat loss and friction loss decrease as MER increases. The reduction in friction work is significantly less with increased MER due to a smaller impact of P_{max} on FMEP (see equation 1.11). With optimized combustion phasing and duration, the efficiency decreases because of three losses: retarded combustion phasing and prolonged combustion duration, heat transfer and friction. Although the absolute values for the heat loss and FMEP increase, the relative energy losses are lower than for the TDC isochoric combustion cases. The optimum CA50 gets closer to TDC and the optimum CA10-90 becomes shorter with increased MER. This

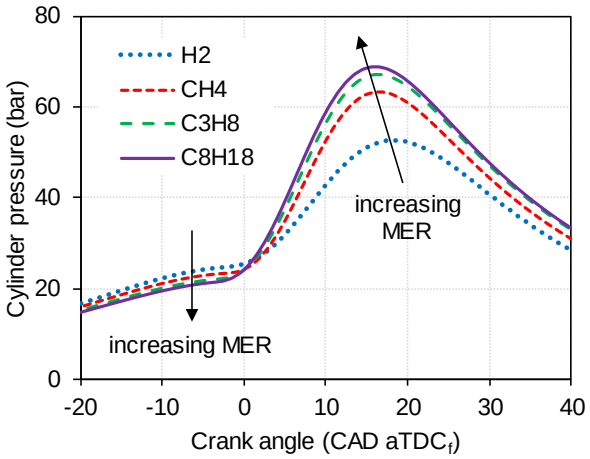

Figure 1.7: The in-cylinder pressure histories of H_2, CH_4, C_3H_8, and C_8H_{18} at optimum condition.

explains the decrease of the combustion loss with a higher MER (square symbols in Figure 1.8).

In order to quantify the impact of MER on the gross BTE, user-defined fuels were employed. The simulation was done at two initial conditions: at -180 CAD $aTDC_f$ with pressure of 1 bar and temperature of 343 K; and at -5 CAD $aTDC_f$ with pressure and temperature taken from the simulation of n-heptane in the previous simulation. In the former case, the impact of γ on the compression process is taken into account. In the latter case, the pre-combustion condition is identical. Figure 1.9 shows the relative improvement of gross BTE with the increase of MER (normalized to C_2H_4 which has MER of 1). As can be seen, the gross BTE increases ~1% relatively with an increase of MER of 0.02. The improvement in the second case (identical pre-combustion condition) is smaller as the impact of γ was ignored.

In conclusion, a fuel with higher MER is preferred to improve engine efficiency. As shown in Figure 1.4, 2-methylfuran and methanol are the two best fuels to blend with gasoline at 10% by volume. The score was calculated with a variety of fuel properties without MER. Methanol has the MER value of 1.061, and the MER of 2-methylfuran is 1.016. This means methanol has the potential to achieve a higher merit score if the MER is taken into account (higher tank-to-wheel efficiency). If pure fuels are used, the benefit of using methanol as a fuel is further increased. Methanol is the simplest type of liquid synthetic fuel [50], and therefore has production advantages compared to more complex fuels (higher well-to-tank

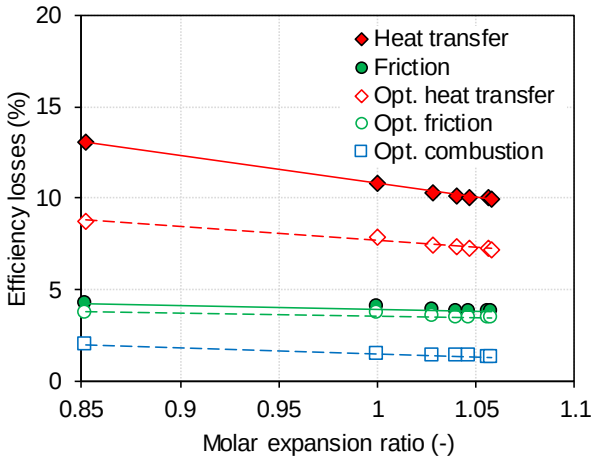

Figure 1.8: The efficiency losses as a function of MER. "Opt." represents the losses with optimized CA50 and CA10-90.

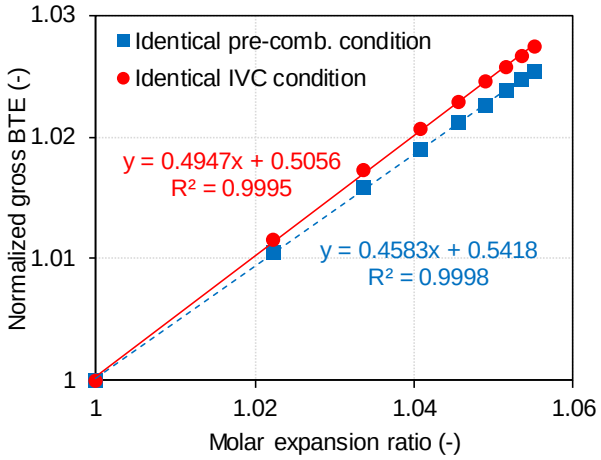

Figure 1.9: The relative improvement of gross BTE as a function of MER.

efficiency). More information about synthetic fuels will be presented in the next section.

1.3 Synthetic fuels for internal combustion engines

In the previous section, methanol was selected to have a higher tank-to-wheel efficiency. In this section, the well-to-tank efficiency of synthetic fuels will be discussed. Synthetic fuels are produced from the synthesis of hydrogen and carbon-based gases (CO or CO_2) through a Fischer-Tropsch process, methanation or methanol synthesis. If H_2 is produced by water electrolysis using electricity, this is called Power-to-Gas (PtG) or Power-to-Liquid (PtL). Sometimes, the resulting product is called an electro-fuel (or e-fuels) because the fuel is produced using electricity. Methane (CH_4) is considered to be the main product of PtG through the methanation process. For PtL, the liquid fuel can be produced through methanol synthesis between H_2 and CO_2 or through a Fischer-Tropsch process between H_2 and CO which was produced from CO_2 using the reverse water gas shift reaction (r-WGS). As mentioned in the previous section, a liquid fuel is preferred because it has higher energy density, is easier for storage and distribution, and the HoV contributes to the engine efficiency, so only PtL is considered in this part. Figure 1.10 presents an example of the closed carbon cycle for PtL (methanol) production and use. As can be seen, the electricity conversion efficiency depends on the efficiency of three main processes: water electrolysis, fuel production, and fuel conversion in engines.

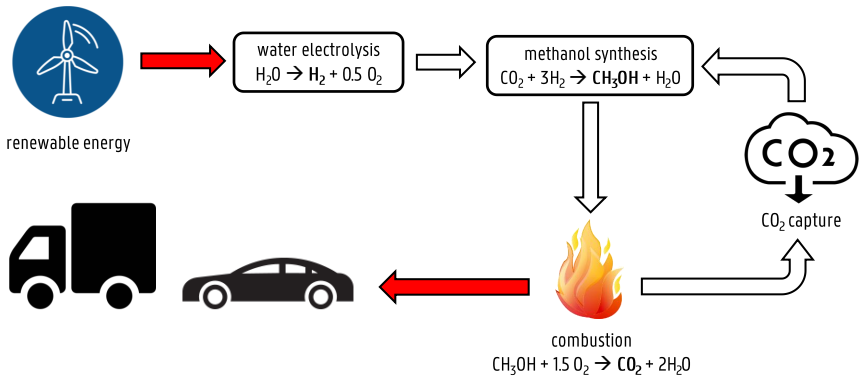

Figure 1.10: Neutral-CO_2 cycle for synthetic methanol production and use.

Figure 1.11 compares the efficiency of different pathways for the use of electricity in transportation. There are three pathways to use the electricity: directly with

battery-electric vehicles (BEV), fuel cell vehicles (FCV) with renewable H_2 from water electrolysis, and internal combustion engine vehicles (ICEV) with renewable synthetic fuels. The synthetic fuel in this study is e-diesel or e-gasoline. As can be seen, the well-to-tank efficiency of BEV is the highest (86%), the second is FCV with 53.6% (compressed hydrogen, 67%×80%) and the last is ICEV with only 44%. To the wheel, BEV has the highest overall efficiency (69%), much higher than FCV (26%) and ICEV (13%). For FCV and ICEV, energy is lost significantly in the water electrolysis process for hydrogen production (33%). Then, the hydrogen is compressed to use in FCV or is employed to produce synthetic liquid fuels. Additionally, ICE has a low efficiency (30% in this study), the total efficiency of ICEV is very low, around one fifth of BEV efficiency.

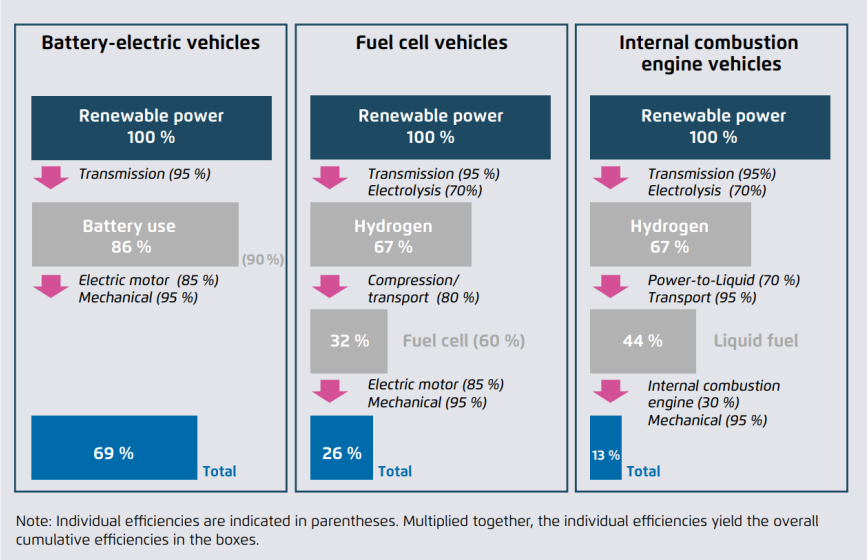

Figure 1.11: Efficiency comparison between BEV, FCV, and ICEV [51].

According to Tremel et al. [52], the efficiency of hydrogen-to-methanol is higher, around 80% compared to 69-70% of hydrogen-to-diesel/gasoline. Therefore, the well-to-tank efficiency of fuel (methanol) production can increase to ~50.5% (=95%×70%×80%×95%). Another study by Bongartz et al. showed a simple synthetic fuel like methanol or dimethyl ether has fuel production efficiency of around 55-57% [53]. The PtL efficiency can be further improved by using co-electrolysis with a waste heat recovery system [54]. Thanks to a higher tank-to-wheel efficiency for methanol, the well-to-wheel efficiency of the methanol-fueled ICEV is higher than for other fuels.

Bongartz et al. concluded that the total CO_2 emissions from a methanol fueled SI

engine can be reduced to 23.8 gCO_2-eq./km if renewable energy is used for the electrolysis. It is much lower than 124 gCO_2-eq./km for conventional gasoline vehicles (tank-to-wheel). However, if the grid electricity is used (with 53% renewable), well-to-wheel CO_2 emissions per km of vehicles with e-fuels are higher than with fossil fuels [53]. To produce enough e-fuels for future ICEV, a huge amount of renewable electricity is needed.

Although the well-to-wheel efficiency of the methanol-fueled ICEV is the highest, it is still much lower than the BEV. However, the well-to-wheel efficiency is not the sole criterion to take into account. Key challenges of batteries include low energy density, long charging time and limited resources of metals such as cobalt and nickel [55]. Even for air quality, the negative health consequences of BEVs seem likely to be at least those of ICEVs [56]. This means the synthetic fuel powered ICE may still play an important role in decarbonizing the transport sector.

1.4 Scope and outline

Within the author's research group, the use of methanol as a fuel or a blended fuel with gasoline in SI engines have been investigated [11, 12]. As explained above, (synthetic-)methanol was considered as the most promising e-fuel for future SI engines in terms of fuel properties (high tank-to-wheel efficiency) and fuel production (high well-to-tank efficiency), which leads to a higher overall efficiency compared to other liquid fuels. Together with the improvement in the fuel production, increasing engine efficiency is necessary. Engine efficiency can be further improved by recovering the exhaust heat. Fuel reforming is a type of waste heat recovery system which converts thermal energy into chemical energy. The goal of this work is to investigate the possibility of fuel reforming for increased efficiency of methanol SI engines. Extending the validity of the quasi-dimensional model to methanol with the addition of reforming products is also an additional goal of this study.

Chapter 2 focuses on the use of methanol in a production DISI engine. The possibility to increase efficiency and to extend the lean burn limit will be considered. Chapter 3 gives some information about fuel reforming and the reforming concept. Chap 4 presents the theoretical efficiency of a methanol-fueled SI engine with an on-board fuel reformer using an Otto cycle efficiency analysis. The losses (heat transfer, combustion duration, and friction) will be added to give an idea about the gross efficiencies. The effect of fuel reforming on combustion has not been investigated in this chapter. Hence, the laminar burning velocity of methanol-syngas blends will be studied in Chapter 5. The effect of syngas

addition on the LBV will be examined. The development of a LBV correlation with a "universal" dilution term also will be presented in this chapter. Chapter 6 is devoted to reaction front properties with different kinds of dilution. Chapter 7 focuses on the full cycle engine simulation. The final chapter summarizes the main findings of this work and some recommendations for future work.

2

Methanol as a fuel for a direct-injection SI engine

2.1 Introduction

In Chapter 1, methanol is considered as the future fuel for SI engines to reduce CO_2 emissions. A number of studies compared the engine performance and emissions between methanol and gasoline. All of the investigations showed a better engine efficiency due to some interesting properties of methanol (as mentioned in section 1.2.2), as well as lower regular exhaust emissions compared to gasoline [57–62]. Most of the studies compared gasoline and methanol on PFI engines. Because the fuel is evaporated outside the combustion chamber, the benefit of methanol's high latent heat is not fully utilized. Direct-injection (DI) engines could make even better use of the heat of vaporization of methanol. This chapter will present the downsizing and the lean-burn potential of methanol compared to conventional gasoline on a DISI engine. These works were published previously in SAE Technical Papers [63, 64]. The measurements were performed by master thesis students (Tim Van Craeynest, Thomas Pillu, Bram Stepman and Viktor Vergote) at Ghent University under guidance of the author [65, 66]. The analysis, simulation, writing, preparation of figures and tables were accomplished by the author Duc-Khanh Nguyen. The author Jakob Coulier contributed with

work on the engine setup. The authors Louis Sileghem and Sebastian Verhelst contributed corrections, discussions and proof-reading.

2.2 Experimental setup

2.2.1 Test engine

The experiments are performed on a Volvo T3 engine. This is a four cylinder in-line, turbocharged DISI engine. The engine specifications from the manufacturer are listed in Table 2.1. The engine is equipped with a high-pressure solenoid injector, Bosch HDVE5. In this research, the delivery pressure and the start of injection are maintained as in the standard settings, 150 bar and 300 CAD before firing top dead center ($bTDC_f$) respectively. The engine is equipped with a fixed geometry turbocharger, BorgWarner KP39, as well as a boost control system to control the intake pressure. The original opening (gauge) pressure of the wastegate is 34 kPa, and the maximum boost pressure can increase up to 1.2 bar.

Table 2.1: Volvo T3 engine specifications

Engine type	Turbocharged DISI engine
Cylinders	4 in-line
Valves	16
Valvetrain	Double overhead camshaft
Bore × Stroke	79 × 81.4 mm
Total displacement	1596 cc
CR	10:1
Standard intake valve phase	26 CAD aTDC - 50 CAD aBDC
Standard exhaust valve phase	14 CAD bBDC - 4 CAD bTDC
Injection timing	300 CAD $bTDC_f$
Injection pressure	150 bar

There are four valves per cylinder in this engine, two intakes and two exhausts. The timing of all valves is controlled by rotating the camshafts. The valve lift and the opening duration are fixed, only the phasing of the valve is adjustable. As can be seen in Table 1, the standard valve overlap is -30 CAD. The intake valve can advance by 45 CAD, and the exhaust valves can retard by 50 CAD. Therefore, the maximum valve overlap that can be obtained is 65 CAD. Here, the opening and closing times are defined at a valve lift of 1 mm.

2.2.2 Equipment and measurement uncertainty

The engine is coupled to a G-type water brake manufactured by Froude through a universal joint. The schematic of the experimental setup is shown in Figure 2.1. The MoTeC M142 engine control unit (ECU) can read some engine data such as the engine speed, the intake pressure (manifold absolute pressure - MAP), the throttle position, the exhaust lambda, etc. and control some parameters like the boost pressure, the valve timings, the ignition timing, and the injection timing/pressure/duration. Other data, not used for direct engine control, e.g. the engine output torque, intake/in-cylinder/exhaust instantaneous pressures, exhaust gas temperatures, are read through a data acquisition system in a LabVIEW environment.

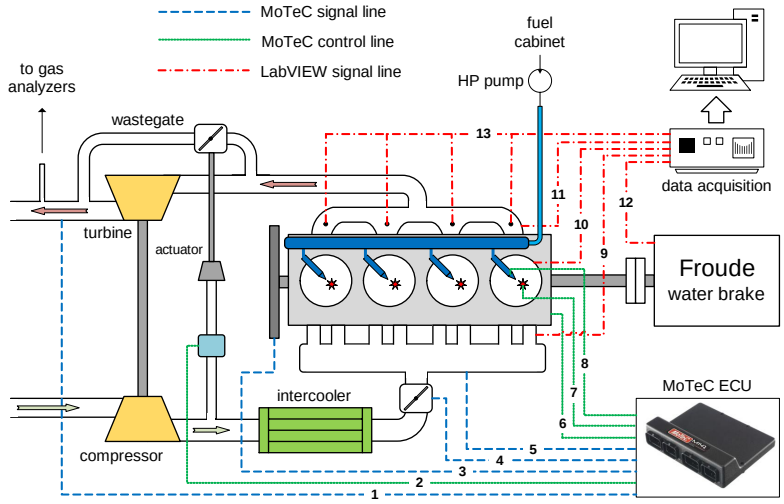

Figure 2.1: Schematic of the experimental setup. Signal/control lines: 1-exhaust lambda, 2-boost control, 3-engine speed, 4-throttle position, 5-manifold absolute pressure (MAP), 6-camshaft position, 7-ignition timing, 8-injection timing/pressure/duration, 9-intake pressure, 10-cylinder pressure, 11-exhaust pressure, 12-output torque, 13-exhaust gas temperatures.

The exhaust lambda is read by a Bosch LSU 4.9 lambda sensor. It measures the proportion of oxygen in the exhaust gases and converts this to a lambda value. The in-cylinder pressure measurements were conducted with a piezo-electric high temperature pressure sensor, Kistler model 6118BCD27. The maximum relative error of the measurement is 0.16% of the full scale, leading to an absolute error of 0.32 bar. The intake and exhaust pressures were measured by a Kistler 4007C005FDS and Keller PAA-M5-HB sensor, respectively. The maximum absolute errors of the measurement are 1% and 0.053% of the full

scale, respectively. These pressure sensors are installed on the fourth cylinder of the engine. The pressures were saved over 50 cycles, and the cycle-averaged pressure is presented and used for analysis. Cylinder pressure was pegged by intake pressure. The pressure offset between mean intake pressure and mean measured cylinder pressure at the end of the intake stroke, 160 CAD aTDC to 180 CAD aTDC, was employed to calculate the cylinder pressure.

The exhaust gas temperature for each cylinder was measured by a K-type thermocouple. The engine output torque was measured by an Omega load cell (type LCM101-25). For the emissions, CO, CO_2 and NO_x were measured with a Maihak Multor 610 (non-dispersive infra-red). The exhaust gas was sampled before the TWC. The fuel consumption was calculated from a gravimetric fuel flow measurement with a Mettler Toledo type ICS429 scale with a relative error of 1%. The water dynamometer used to load the engine did not allow to maintain the engine speed at a constant value. It fluctuated around the desired speed by ~50 rpm. Furthermore, due to the unstable of the water brake, the most stable engine speed in each test campaign was chosen. The uncertainty for the torque sensor is 0.25%. The BMEP is calculated from the measured torque and engine displacement. Therefore the relative uncertainty of BMEP is similar to the uncertainty of the torque, 0.25%. The brake thermal efficiency (BTE) is calculated from the measured torque, engine speed, mass flow rate of fuel, and fuel's lower heating value. The resulting uncertainty for the BTE is 3.2%. The uncertainties of NO_x, CO_2 and CO emissions are 6%, 5.3%, and 35%, respectively.

2.3 Downsizing potential

Downsizing the SI engine is one of the current directions to enhance the engine efficiency [67]. A smaller engine with lower weight helps to improve the fuel economy of vehicles [26]. Additionally, with a smaller size, the engine can operate near full throttle opening at low load, close to the high-efficiency region. However, to achieve a similar power output with a smaller engine displacement, several technologies have to be applied, such as direct injection and turbocharging or supercharging. Because the air is compressed to a higher pressure to increase the volumetric efficiency, thus the intake temperature increases. Higher initial temperature leads to an increase in the mixture temperature, and knock can occur more easily, damaging the engine. To reduce the mixture temperature, direct injection can be employed to cool down the intake charge [67, 68]. Lower temperatures also allow an increase in the compression ratio [68], making the engine more efficient. To investigate the downsizing potential of methanol experimentally, boost control and variable valve timing were applied to improve

the engine performance. Simulation with GT-Power is performed to understand the behavior inside the combustion chamber at these conditions.

2.3.1 Research methodology

Experiment

To determine the downsizing potential of methanol, first, the maximum output torque of the engine with gasoline was tested through the test matrix following a design of experiment (DoE) approach. Two control parameters were selected, the valve timing and the intake boost pressure. To calculate the downsizing potential, the displacement of two engines which have the same engine power output is required [67]. In this study, tests were performed on a multi-cylinder engine, therefore the output (BMEP) is used to predict the downsizing potential. Based on the improvement of BMEP with methanol fuel, the downsizing possibility of the engine is calculated. The BMEP is further increased with higher boost pressure and different valve timing, therefore the maximizing potential can be estimated with a constraint of the maximum in-cylinder pressure. All of the tests were performed at an exhaust lambda of 1 for a high conversion efficiency of the TWC and minimum spark advance for best torque (MBT) or knock-limited spark advance (KLSA) ignition timing is used. The ignition timing was also limited by an exhaust gas temperature of 850 °C, to protect the turbine blades. The sweep tests of these two parameters then were carried out on methanol. For this sweep test, the ignition timing is fixed at the MBT ignition timing for the baseline case.

To achieve different valve overlap period, retarding exhaust valves or advancing intake valves or combined shifting of two valves can be used. For simplicity, simultaneous shifting of the two valves was performed in this research (which is called simultaneous variable valve timing, S-VVT). The intake valves are advanced, and the exhaust valves are retarded by the same valve shifting angle. Because the original valve overlap is -30 CAD, the valve overlap with different valve shifting angle is calculated as:

$$\text{valve overlap} = 2 \times \text{valve shifting angle} - 30 \tag{2.1}$$

Figure 2.2 shows four examples of the valve strategies, baseline, S-VVT 10, S-VVT 25 and S-VVT 40. The number presents the valve shifting angle (advancement angle of the intake valves and retardation angle of the exhaust valves). The valve overlap in the case S-VVT 40 is 2×40 - 30 = 50 CAD.

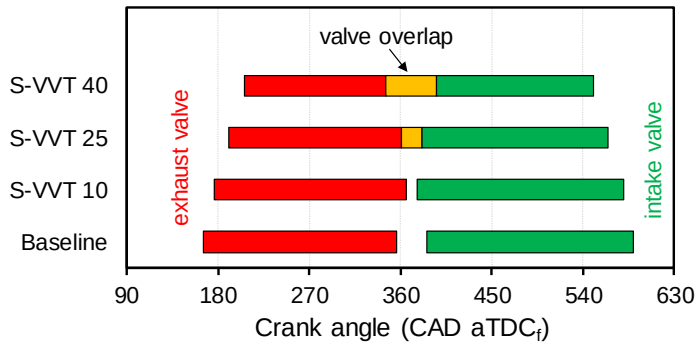

Figure 2.2: Valve events with different shifting strategies.

The influence of intake boost pressures was also studied. The actuating (gauge) pressure of the wastegate is 34 kPa. If the boost control system is deactivated, the maximum absolute pressure of the intake air is 1.34 bar. The MoTeC ECU can control to a higher value of the intake pressure; gauge pressures of 40 kPa, 60 kPa and 70 kPa were tested.

Numerical simulation

To determine the knock limit, the auto-ignition delay is needed. In this research, the auto-ignition delay of mixtures is predicted through a chemical kinetic simulation using Cantera [69]. The simulation was performed with a homogenous mixture in a constant volume reactor, and the auto-ignition delay is defined as the time when the maximum temperature rise rate is observed. The mechanism developed by Li et al. was used for methanol-air mixtures [70], and Mehl's mechanism was used for gasoline-air mixtures [71]. A blend of iso-octane, n-heptane, and toluene with volumetric ratios of 35%, 15%, and 50% respectively was used to simulate gasoline. With that fraction, the toluene primary reference fuel (TPRF) has a similar RON and MON to the tested gasoline, 96.3 and 87.3 respectively [72].

The ignition delay ID (mass fraction burned 0-2%), combustion duration (10-75% and 10-90% mass fraction burned, CA10-75 and CA10-90), unburned gas temperature, etc. were predicted through a three pressure analysis (TPA) in GT-Power [73]. The instantaneous intake, in-cylinder, and exhaust pressures were implemented into the model for the gas dynamic simulation. The mass flow rate of fuel was controlled to have the overall exhaust lambda of 1 and identical to the measured fuel flow rate (±2%). The TPRF in the prediction of ignition delay is

also used to simulate gasoline.

Because the engine in this study is a direct injection engine, a cylinder evaporation model is required. Similar to the previous research on methanol [74], the mass fraction of the injected liquid fuel that vaporizes immediately after injection is 3%, and the duration for 50% fuel evaporated at 4000 rpm and liquid temperature of 600 K is 60 CAD. A shorter evaporation duration (20 CAD) is used for gasoline. Because of methanol's high latent heat, the evaporation is slower compared to gasoline surrogate fuel [75]. n-Heptane has a similar behavior in the mass fraction of vapour as gasoline at high temperature (T_{gas} = 353 K) [76], therefore the evaporation rate of n-heptane can be used to represent the evaporation of gasoline. According to Lee and Law [77], the evaporation rate in a dry environment of n-heptane is 1.5 times higher than that of methanol. With the same mass, the evaporation duration for n-heptane (or gasoline) should be 40 CAD. Because the lower heating value of methanol is around half that of gasoline, the mass flow rate of gasoline is around 50% that of methanol. Therefore, the evaporation duration was taken to be 20 CAD. However, the vaporization heat taken from the walls was changed to 50% (from 75%). The reason is the injector location/direction. In the previous research, the fuel was injected from the side; thus it can be expected that more fuel impinges on the cylinder wall, and more heat is taken from the walls than in an engine which has direct injection from the centre of the pent-roof shaped cylinder head like the Volvo T3 engine.

The wall temperature is also an important parameter for the prediction of engine volumetric efficiency as well as the unburned gas temperature. One value was used for the cylinder head, cylinder liner, and the piston. Because no wall temperature measurement was available for this engine, a basic calculation for the wall temperature as a function of IMEP was performed, as follows [78]:

$$T_{wall}(K) = \frac{200}{23} IMEP(bar) + 83 + 273.15 \tag{2.2}$$

It is a primary estimation of the wall temperature, so makes no difference between fuels if the engine works at the same load. A constant temperature is used because a very small fluctuation of the wall temperature during the combustion (~10 K) is typically found over the cycle [79]. The heat transfer model of Morel [47] was employed to calculate the heat losses to the wall. In order to match the cylinder pressure profile to the experiment, a heat transfer multiplier table for methanol was made for the baseline case. This heat transfer multiplier table then was used for other simulations of methanol. A different table for gasoline was also created.

2.3.2 Results

In this part, the results from the experimental and simulation studies are presented and analyzed. First, a basic comparison between gasoline and methanol was performed. Then, the maximum torque of the gasoline-fueled engine was found. Later on, the measurement results with variable valve timing and boost pressure were analyzed to understand the change in engine BMEP. The downsizing factor of the methanol-fueled engine is then calculated. Finally, the comparison between methanol and gasoline is performed at the same load (maximum BMEP for gasoline) with boost and valve timing controls.

Comparison between methanol and gasoline

Figure 2.3 presents BTE versus engine BMEP at 2500 rpm, exhaust lambda of 1. The measurements were done with the standard valve timing. At two similar loads (equivalent to BMEP of 7 and 11 bar), the MBT ignition timings for each fuel were applied. To achieve the same BMEP, the throttle opening is smaller for methanol. For the comparison at wide open throttle (WOT) and boost pressure of 1.34 bar, the same ignition timing (MBT ignition timing for gasoline, 15 CAD bTDC$_f$) was used.

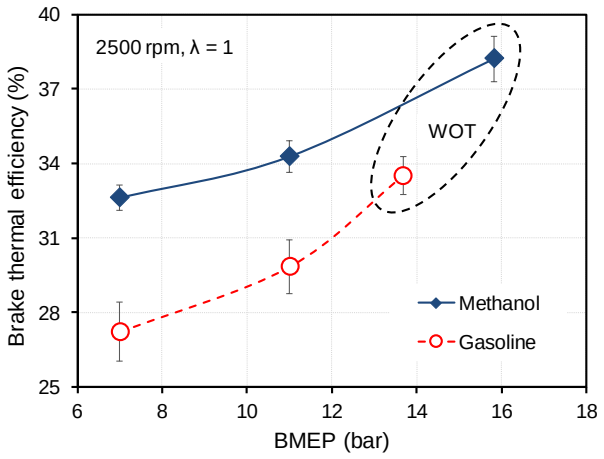

Figure 2.3: Comparison of brake thermal efficiency versus engine BMEP, with gasoline and methanol, at 2500 rpm and exhaust lambda of 1. At BMEP of 7 and 11 bar, MBT ignition timing was used; at WOT, ignition timing was 15 CAD bTDC$_f$ for both fuels.

As can be seen in this figure, the BTE of methanol is higher. This can be explained by a variety of interesting properties of methanol compared to gasoline

[57]. With a higher heat of vaporization, the in-cylinder mixture is cooler, so the volumetric efficiency increases. Furthermore, the combustion temperature of methanol is lower than gasoline, the heat losses therefore decrease. Another reason is a faster burning velocity of methanol compared to gasoline; the combustion is more isochoric, closer to the ideal Otto cycle. At the same load, the difference between BTE of gasoline and methanol is smaller as the BMEP increases. At WOT condition, not only the BTE, but the maximum BMEP of gasoline is also lower than that of methanol, by around 2 bar. At that point, if the MBT ignition timing for methanol is used, the maximum BMEP and BTE of the engine can be further increased.

Figure 2.4 illustrates the in-cylinder pressures at BMEP of 11 bar and WOT condition, two conditions which were presented in Figure 2.3. At the same engine settings (WOT condition), the in-cylinder pressure at ignition timing of methanol is a bit higher than gasoline due to the fuel evaporation. Methanol has a higher heat of vaporization, the volumetric efficiency increases; therefore the in-cylinder pressure at the end of the compression stroke improves. Because the flame speed of methanol is faster than gasoline, both ignition delay and combustion duration are shorter. Therefore, the combustion starts earlier and the pressure reaches peak sooner. Due to the combustion being more isochoric, the peak in-cylinder pressure increases, the engine BMEP improves. Thanks to these properties, to maintain the BMEP (11 bar) with methanol, a smaller throttle opening angle was used. Therefore, the pressure at the sparking condition is lower for methanol. However, due to the faster burning rate of methanol, the peak in-cylinder pressure is still higher.

Optimum point of gasoline

To find the optimum point of gasoline, first the S-VVT and boost pressure sweep tests were done to know how BMEP changes at a lower engine speed, 1650 rpm. The baseline point (without valve shifting and boost control) is used as the reference. The BMEP at that point (with knock limit spark advance-KLSA ignition timing, 9 CAD $bTDC_f$) is 13.72 bar. In all of these sweep tests, this ignition timing was maintained. The valve shifting angle and boost pressure for these sweep test points are presented as the triangular symbols in Figure 2.5. The maximum valve shifting angle and boost pressure is limited at 25 CAD and 49 kPa due to knock, respectively.

The engine BMEP increases with a larger valve shifting angle and a higher intake boost pressure. It can be explained by the reduction of burned gas mass fraction in the combustion chamber due to scavenging and a richer combustion when positive

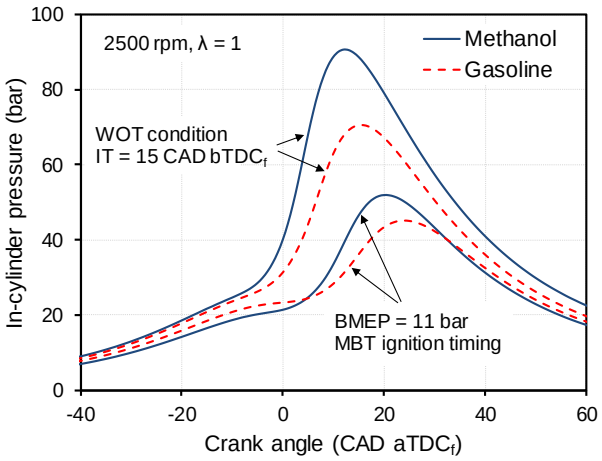

Figure 2.4: In-cylinder pressure curves of methanol and gasoline at BMEP of 11 bar and WOT condition, engine speed of 2500 rpm and exhaust lambda of 1.

valve overlap is applied [80]. With a positive valve overlap, the fresh air from the intake manifold can push the burned gases out of the cylinder and follow the flow to go to the exhaust manifolds during the valve overlap period. As the lambda sensor is an oxygen sensor, therefore it will show $\lambda > 1$. The injection duration is then prolonged to achieve the overall exhaust lambda of 1, i.e. the in-cylinder mixture is richer than what is indicated by the lambda sensor. With a lower mass fraction of burned gases and a richer combustion (faster burning velocity, more heat is absorbed during the fuel evaporation), the BMEP improves. The BMEP is also raised with a higher intake boost pressure due to the increase of the engine volumetric efficiency.

Then the measurement matrix following the DoE approach was tested to understand the interaction between the two settings. The boost pressure varied from ~38 kPa to ~50 kPa, and the valve shifting angle from 5 to 25 CAD; with steps of 5 CAD. The conditions of these 13 test points are presented in Figure 2.5 (diamond symbols). At each point, the KLSA ignition timing is used. A similar trend was found: BMEP improves with a larger valve overlap period and a higher boost pressure. However, the improvement of the engine BMEP is less significant with the increase of boost pressure when S-VVT is applied. Furthermore, a significant improvement of engine BMEP is found when the valve shifting angle is larger than 20 CAD. Therefore, the test was continued with a higher value of valve shifting angle and higher boost pressure to find the maximum BMEP. Three extra points were tested, located at the top right corner of the test matrix.

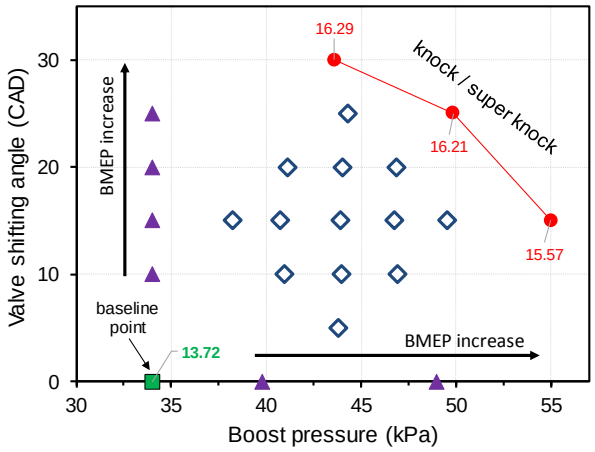

Figure 2.5: The valve shifting angle and boost pressure of the matrix test points at WOT, 1650 rpm, and exhaust lambda of 1. The values present the BMEP (in bar) at that point. Square symbol: baseline point; triangular symbols: sweep test points; diamond symbols: DoE matrix test points; circular symbols: extra points.

The first one is at S-VVT of 15 CAD, and a boost pressure that is raised to achieve the maximum BMEP. The maximum BMEP with S-VVT of 15 CAD was 15.57 bar with a boost pressure of 55 kPa. The second point is at a boost pressure of 44 kPa, and the valve shifting angle increase before knock onset. The maximum valve shifting angle at this boost pressure is 30 CAD with KLSA of -0.5 CAD. The BMEP at this point was ~16.3 bar. The third point is at the maximum boost pressure and valve shifting angle in the test matrix, 50 kPa and 25 CAD, respectively. The BMEP at this point is ~16.2 bar. In theory, the BMEP can be further increased if we increase both valve shifting angle and boost pressure; however, heavy knock will occur. Therefore, no more extra points were tested. The conditions at these three points present the knock/super knock border for this engine speed. Finally, the maximum BMEP achievable for gasoline at this speed was ~16.3 bar, improved by ~19% compared to the baseline case. In order to achieve this BMEP, valve shifting angle of 30 CAD (positive valve overlap of 30 CAD) and boost pressure of 44 kPa were employed. Thus, the in-cylinder mixture is richer than the stoichiometric, and engine efficiency decreases. The potential of achieving higher BMEP with methanol will be tested in the following section.

Methanol sweep tests

In the previous section, the increase of valve overlap, as well as the intake boost pressure, have a positive effect on the improvement of engine BMEP. A similar approach was applied for methanol: three valve strategies (S-VVT 10, S-VVT 25, and S-VVT 40), and three boost pressure (40 kPa, 60 kPa, and 70 kPa) were tested. When one of these two techniques is applied, the second one is kept at its original setting (boost pressure of 34 kPa for S-VVT sweep tests and valve overlap of -30 CAD for boost pressure tests).

Figure 2.6 presents the BTE as a function of engine BMEP with different valve strategies and boost pressures. The MBT ignition timing of the baseline case (10 CAD $bTDC_f$) is used for all measurements. The baseline and the optimum points for gasoline (from the previous section) are also illustrated in this Figure. As can be seen, the BMEP improves with a longer valve overlap duration and a higher boost pressure, similar to the findings on gasoline in the previous section. In the S-VVT sweep tests, the BTE is maintained at around 37% in the first three cases (baseline, S-VVT 10 and S-VVT 25), but a significant reduction of BTE is found when the valve shifting angle increases to 40 CAD (down to ~34%). In the boost control sweep tests, the BMEP increases from 15.5 bar (baseline BMEP for methanol) to over 20 bar. The baseline BMEP for methanol is lower than the maximum BMEP for gasoline. With higher boost pressure or more extended valve overlap period, the engine BMEP increases to over the maximum value for gasoline. No knock was detected during the measurement. Therefore, the maximum BMEP of the engine can be extended with methanol.

However, due to a faster and more advanced combustion, the peak in-cylinder pressure is over 100 bar in some cases. As the engine was designed to work with gasoline, if the engine is to operate with methanol at higher BMEPs a stronger engine block, cylinder head, piston, etc. are needed. Figure 2.7 presents the relationship between peak in-cylinder pressure and engine BMEP. With boost control, the peak in-cylinder pressure increases linearly with the improvement of BMEP. Therefore, the maximum BMEP can be easily estimated, ~18.2 bar if the peak in-cylinder pressure is to be constrained to 100 bar. The maximum BMEP with valve timing control is ~17.5 bar. Therefore, the boost control has a higher downsizing potential.

Because the change of maximum torque (or BMEP) is inversely proportional to the change of engine displacement, the downsizing factor (DF) can be calculated as [67]:

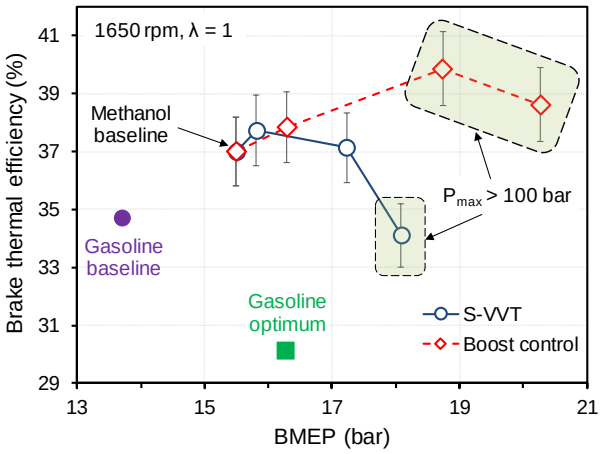

Figure 2.6: Brake thermal efficiency of methanol engine as a function of BMEP with different valve timings and boost pressure. Test conditions for methanol: WOT, 1650 rpm, exhaust lambda of 1, ignition timing of 10 CAD bTDC$_f$.

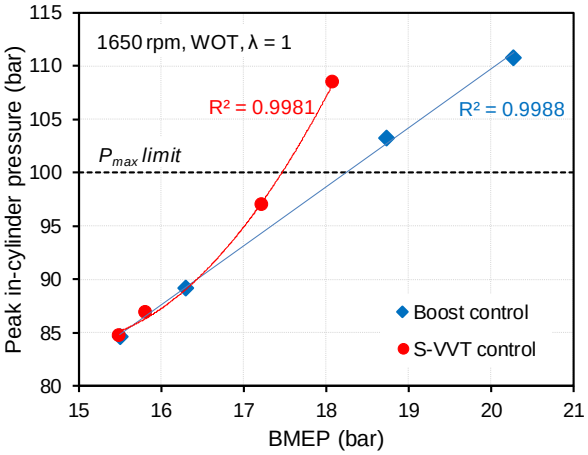

Figure 2.7: The relationship between the peak in-cylinder pressure and engine BMEP for boost control and S-VVT control sweep tests. Test conditions: WOT, 1650 rpm, exhaust lambda of 1, ignition timing of 10 CAD bTDC$_f$.

$$\begin{aligned} DF &= \frac{V_{swept,gasoline} - V_{swept,methanol}}{V_{swept,gasoline}} \\ &\approx \frac{1/BMEP_{gasoline,max} - 1/BMEP_{methanol,max}}{1/BMEP_{gasoline,max}} \\ &= \frac{1/16.29 - 1/18.244}{1/16.29} \times 100\% \approx 10.7\% \end{aligned} \tag{2.3}$$

The maximum pressure also constrains the compression ratio. Based on the relationship between boost pressure versus peak pressure, the maximum boost pressure is 57 kPa if the peak pressure is limited to 100 bar. A basic calculation to predict the maximum compression ratio for a NA SI engine is performed. The end pressure P_{end} and the initial pressure P_{ini} is related as a function of the compression ratio CR and the specific heat ratio γ, as in equation (5). The subscript "NA" indicates the naturally aspirated condition.

$$\frac{P_{end}}{P_{ini}} = CR_{NA}{}^{\gamma_{NA}} \tag{2.4}$$

Assuming the initial pressure is 1 bar, and the specific heat ratio remains constant during the compression stroke. The value of γ at boost pressure of 57 kPa and 0 kPa (intake boost pressure in NA SI engines, WOT condition) is predicted through the relationship between the intake stroke averaged γ versus boost pressures. The intake-stroke averaged γ at each boost pressure is derived from a TPA simulation. The γ for the boost pressure of 57 kPa and 0 kPa is ~1.3059 and 1.3 respectively. Hence the maximum compression ratio for the NA SI engines when it works with methanol is calculated as follows:

$$\begin{aligned} CR_{NA} &= \left(\frac{P_{end}}{P_{ini}}\right)^{1/\gamma_{NA}} = \left(\frac{P_{boost} \times CR_{boost}{}^{\gamma_{boost}}}{P_{ini}}\right)^{1/\gamma_{NA}} \\ &= \left(\frac{1.57 \times 10^{1.3059}}{1}\right)^{1/1.3} \approx 14.3 \end{aligned} \tag{2.5}$$

In conclusion, if the maximum pressure is limited to 100 bar, using methanol the engine could be further downsized by ~10.7%. If the engine hardware would be stronger, the downsizing factor could be further improved. However, the weight of the engine would then increase. For NA SI engines, the maximum compression ratio when the engine works with methanol (at $\lambda = 1$) is around 14:1. In this calculation, the influence of CR on turbulent flame speed and residual mass

fraction is ignored, assuming the flame speed is similar to the case which has an intake boost pressure of 57 kPa. To explain the improvement of BMEP by changing the boost pressure and valve timing, a more in-depth investigation into the operating cycle will be presented in the following sections.

S-VVT sweep tests

Figure 2.8 shows the in-cylinder pressure profiles in log(P)-log(V) diagram at different valve strategies. As is shown clearly, the peak in-cylinder pressure increases with a more prolonged valve overlap duration, especially with a positive valve overlap. There are two reasons for that change: lower residual gas mass fraction and a richer in-cylinder mixture. Both improve the burning velocity, so the pressure rises more sharply. As can be seen, the crank angle when the in-cylinder pressure reaches peak gets closer to TDC with a longer valve overlap period.

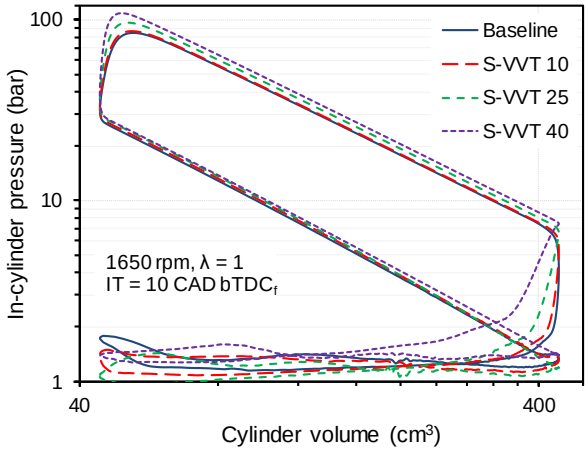

Figure 2.8: In-cylinder pressure profiles in log(P)-log(V) diagram with different valve strategies. Test condition: WOT, 1650 rpm, λ = 1, IT = 10 CAD bTDC$_f$, boost pressure of 34 kPa.

When the valve shifting angle further increases, the residual mass fraction decreases due to the scavenging resulting from positive valve overlap. The intake air pushes the burned gases out of the cylinder at the end of the exhaust stroke. A part of the intake air follows the flow to the exhaust manifold. Therefore, the lambda sensor will show a value greater than 1. The injection duration is then controlled to be longer to increase the amount of fuel. Figure 2.9 presents the instantaneous exhaust lambda in the S-VVT 40 case from a TPA simulation. The exhaust lambda increases during the valve overlap because of the presence of fresh

air in the exhaust. The in-cylinder lambda should be rich, $\lambda_{in-cylinder}$ = 0.95, to achieve the overall exhaust lambda of 1. In the S-VVT 25 case, the exhaust lambda also reaches a peak during valve overlap. However, only a small amount of fresh air is then present in the exhaust, so the overall exhaust lambda does not change significantly, remaining around 1. For the four cases, only the S-VVT 40 case has a significant rich combustion. This explains the reduction of BTE in that case, as shown in Figure 2.6.

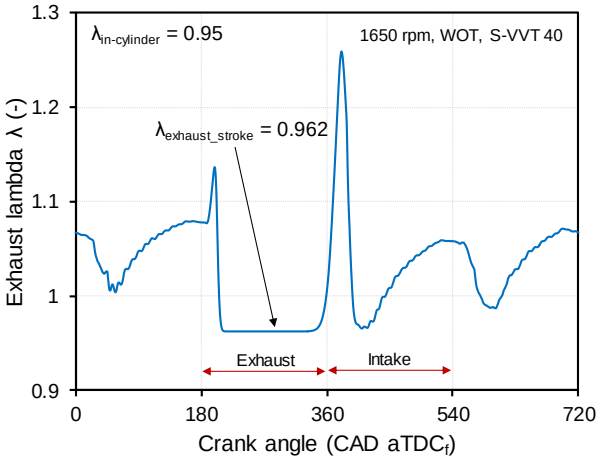

Figure 2.9: Instantaneous exhaust lambda in the case S-VVT 40, WOT, engine speed of 1650 rpm, overall exhaust lambda of 1.

Figure 2.10 presents the ignition delay ID, crank angle when 50% mass is burned (CA50), combustion duration CA10-75 and CA10-90, and residual gas mass fraction in the four cases. These parameters are derived from the TPA simulation in GT-Power. As can be seen, the residual gas fraction first increases and then decreases with the prolongation of the valve overlap period. ID, CA50, CA10-75 and CA10-90 decrease when the valve shifting angle increases from 0 to 40 CAD. Although the residual fraction is higher in the S-VVT 10 case, a small reduction of ID, CA50, CA10-75 and CA10-90 can be observed when the valve shifting angle increases from 0 to 10 CAD. Higher mixture temperature can explain this behavior (see Figure 2.11). In the case of S-VVT 25, less residual gas is the main reason, whereas, in the S-VVT 40 case, the combination of a lower residual gas fraction and a richer combustion leads to the decrease of ID, CA50, and combustion duration.

The ignition timing is maintained at 10 CAD bTDC$_f$ in this sweep test, this is the MBT timing of the baseline case. With different valve timings, the MBT timing will actually change. As shown in Figure 2.10, the CA50 is closer to the TDC with

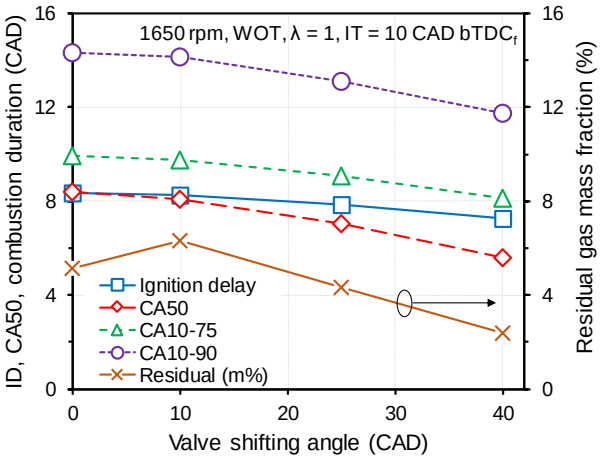

Figure 2.10: The ignition delay, CA50, CA10-75, CA10-90, and residual gas mass fraction versus valve shifting angle at 1650 rpm, IT = 10 CAD bTDC$_f$.

a larger valve shifting angle, this means the combustion phasing is too advanced using the fixed ignition timing. A later spark timing is required to keep the CA50 at around 8 CAD aTDC$_f$ as with the baseline case. Therefore, in these cases, the ignition timing is too advanced, compared to the MBT timing.

With a shorter combustion duration, the unburned mixture has less time for auto-ignition. However, it also leads to a sharp increase of pressure as well as unburned gas temperature, reducing the auto-ignition delay time of the mixture. Therefore there is a trade-off of faster combustion versus knock. Figure 2.11 presents the pressure-unburned gas temperature trajectories for different valve strategies. The grey lines show the constant auto-ignition delay contours of the undiluted stoichiometric methanol-air mixture which is derived from a simulation with Li's mechanism [70]. Because the amount of burned gas in the mixture is small, and the difference in residual mass fraction between the four cases is limited, the results from the simulation of an undiluted methanol-air mixture are used to present the auto-ignition delay contours for all situations. The "knock limit" line is the auto-ignition delay contour of 1.36 ms, which was calculated from equation 2.6 [81].

$$\tau_{RES} = \frac{13.5 \times 1000}{6 \times RPM} \tag{2.6}$$

This is a very rough approach to define the knock limit in an SI engine. At 1650 rpm, the residence time is 1.36 ms. As can be seen, the end gas state is still far

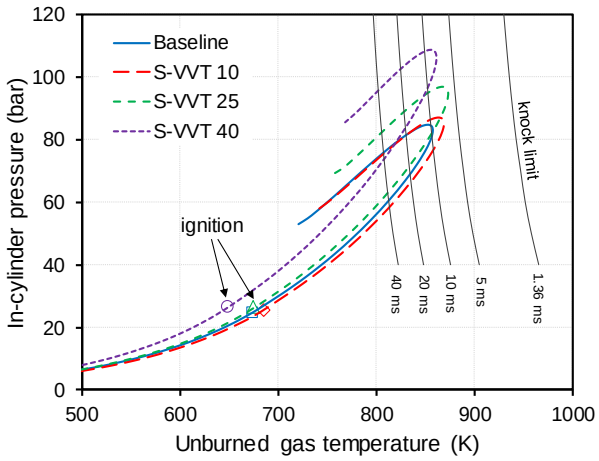

Figure 2.11: In-cylinder pressure-unburned gas temperature trajectories for different valve strategies at 1650 rpm, IT = 10 CAD bTDC$_f$. Grey lines: simulated auto-ignition delay contours for stoichiometric methanol-air mixture.

from the "knock limit". From this figure, the S-VVT 25 is the case which has the highest chance to experience knock. In the S-VVT 40 case, due to the cooling effect of the fuel evaporation (rich mixture), the peak in-cylinder temperature is lower than the S-VVT 25 and S-VVT 10 cases. These peak temperatures are still far from the knocking temperature, ~955 K, for methanol (see Chapter 6).

Intake boost pressure sweep tests

Figure 2.12 presents the in-cylinder pressure curves with different boost pressures at 1650 rpm; the ignition timing is maintained at 10 CAD bTDC$_f$. With a higher intake boost pressure, the pressure is higher over the entire cycle. The crank angle when the in-cylinder pressure reaches the peak is not advanced as was the case in the variable valve timing sweep test. This means the combustion speed does not change much when the intake pressure increases.

Four combustion parameters, the ID, CA50, CA10-75, and CA10-90 are presented in Figure 2.13. As can be seen, there is an insignificant change in these parameters when the boost pressure increases. This can be explained by the gas exchange processes being similar with different boost pressure as the valve timing is fixed. Therefore the mass fraction of the residual gases is almost constant (~5%), as shown in Figure 2.13. A very small decrease in CA50, CA10-75, and CA10-90 is found. It can be explained by the increase of intake mass flow rate; the turbulence

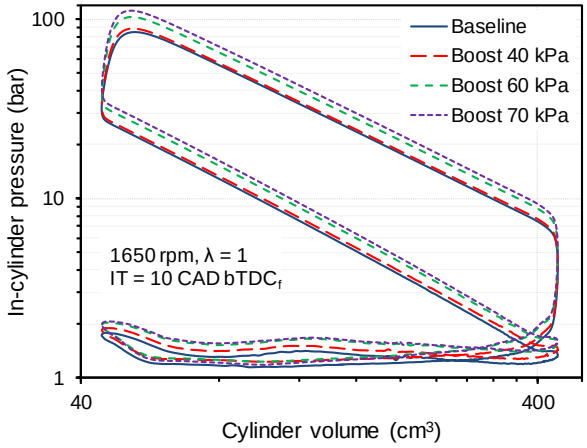

Figure 2.12: In-cylinder pressure profiles in log(P)-log(V) diagram with different boost pressure at 1650 rpm, IT = 10 CAD bTDC$_f$.

is slightly enhanced, and the turbulent flame speed improves. Because the change in CA50 is insignificant with higher boost pressure, the ignition timing in the boosted cases is close to the MBT timing.

In this sweep test, the mixture is stoichiometric. Because more fuel is injected in the high boost pressure cases, the heat generation during combustion is greater, so a higher peak temperature of the end gas is observed. That peak temperature is still lower than the "knock limit" curve, τ_{ID} = 1.36 ms, as shown in Figure 2.14. With a higher boost pressure, the end gas condition is closer to the knock limit. Therefore, there is a limit for the maximum boost pressure. However, there is another limit for the combustion of methanol; it is the peak in-cylinder pressure, as mentioned above. If 100 bar is the limit for the maximum in-cylinder pressure, the boost pressure should be lower than 57 kPa.

Comparison at maximum BMEP

Figure 2.15 compares the in-cylinder pressure profiles in log(P)-log(V) diagram at the maximum BMEP of gasoline, 16.3 bar. The ignition timing for gasoline is 0.5 CAD bTDC$_f$, which is KLSA. For methanol, the MBT ignition timings were used, 10 CAD bTDC$_f$ for the boost 40 kPa case and 11 CAD bTDC$_f$ for the S-VVT 17 case. Because of the lower knock resistance property of gasoline compared to methanol, the combustion phasing is retarded, resulting in a substantially lower peak in-cylinder pressure.

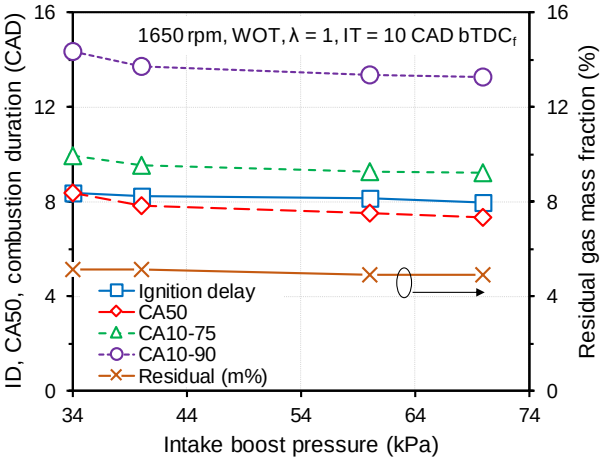

Figure 2.13: The ignition delay, CA50, CA10-75, CA10-90, and residual gas mass fraction versus boost pressure at 1650 rpm, IT = 10 CAD bTDC$_f$.

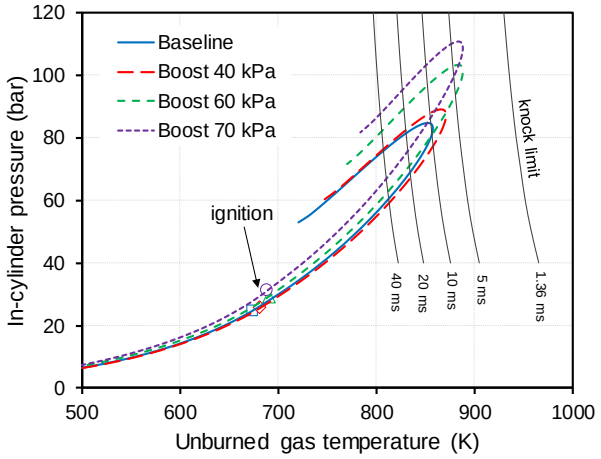

Figure 2.14: In-cylinder pressure-unburned gas temperature trajectories for different boost pressures at 1650 rpm, IT = 10 CAD bTDC$_f$. Grey lines: simulated contour lines of the auto-ignition delay of stoichiometric methanol-air mixture.

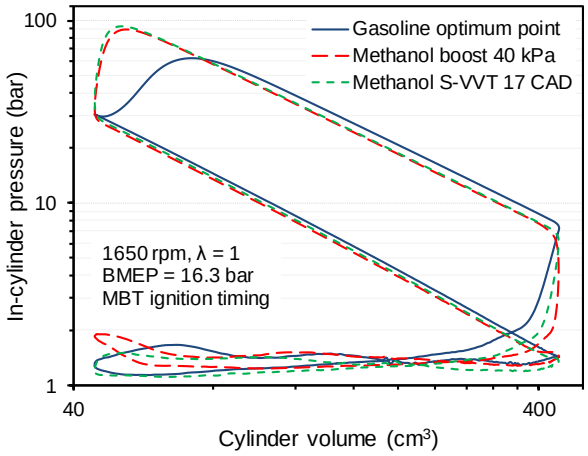

Figure 2.15: Comparison of the in-cylinder pressure at BMEP of 16.3 bar, engine speed of 1650 rpm.

Figure 2.16 shows the pressure-temperature trajectories at the same BMEP of 16.3 bar. Therefore the in-cylinder wall temperature in the TPA simulation is the same. From this figure, the effect of fuel vaporization is seen. Higher temperature at the same pressure is observed with gasoline. However, peak end gas temperature for gasoline is lower than methanol. This is due to a lower combustion pressure with gasoline. As can be seen, although the ignition timing is the KLSA, the end gas condition for gasoline is far off the knock limit for that fuel. A possible explanation is that there was no knocking cycle during the experiment, and the in-cylinder pressure-temperature trajectory presents the cycle-averaged value. The end gas pressure and temperature for methanol are much higher than for gasoline, and passes the "knock limit" of gasoline. The auto-ignition delay contour, τ_{ID} = 1.36 ms, of the undiluted TPRF-air mixture is also presented. Szybist et al. confirmed that the burned gas has a very small effect on the knock suppressor at high loads [82]. Therefore, the auto-ignition delay contour of the undiluted mixture is used to present the knock limit for gasoline. If the TPRF-air mixture is compressed to the same pressure and temperature as methanol, knock would occur. Thanks to the high knock resistance of methanol, the ignition delay is longer at the same pressure and temperature, therefore no knock takes place.

The BTE and three main emissions (NO_x, CO_2, and CO) were compared and presented in Figure 2.17, for a BMEP of 16.3 bar and at 1650 rpm. The methanol-fueled engine has a higher thermal efficiency and lower emissions compared to gasoline. Although the peak unburned gas temperature is lower for gasoline, the burned gas temperature is higher because of the higher flame

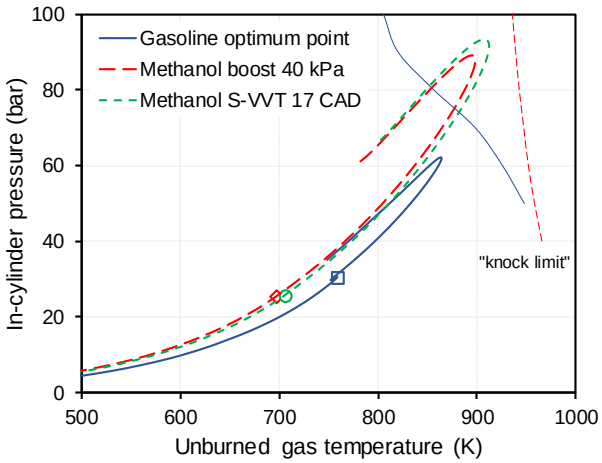

Figure 2.16: In-cylinder pressure-unburned gas temperature trajectories at BMEP of 16.3 bar, engine speed of 1650 rpm. Knock limit lines: dash line is for methanol, solid line is for gasoline.

temperature as well as the higher initial gas temperature. The increase of unburned gas temperature after ignition in Figure 2.16 is mainly due to the rising of in-cylinder pressure, not due to the heat transfer from the burned zone to the unburned region.

2.4 Lean combustion

Lean combustion is a promising method to increase the engine efficiency due to the decrease of combustion temperature, lower heat losses, reduced pumping work and increased specific heat ratio [8, 83, 84]. The challenge for lean-burn SI engines is the combustion stability and low conversion efficiency of the TWC. The engine out NO_x decreases with lean combustion; however, the conversion of NO_x to N_2 and O_2 in the TWC decreases [85]. This leads to a higher concentration of NO_x at the exhaust tailpipe. An extremely lean condition ($\lambda \geq 1.8$) is needed to have a lower raw NO_x compared to a stoichiometric SI engine with a TWC [86]. To extend the dilution limit, several methods were applied such as the use of tumble intake ports [87, 88], new ignition systems [89–91], or increasing the flame speed. Higher LBV fuels such as H_2 were employed as an additive fuel to increase the dilution limit [22]. The disadvantage of this technique is that the engine needs an additional storage tank for hydrogen. Another method is using fuel reforming technology to produce H_2-rich gas onboard [92–95] and use this gas to extend the

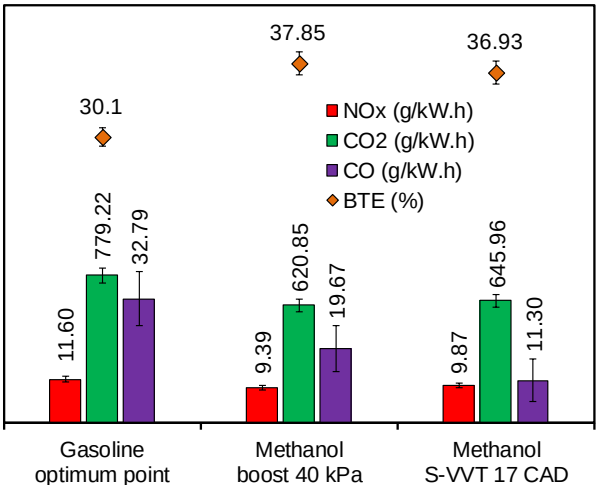

Figure 2.17: Comparison of the BTE and emissions between gasoline and methanol at BMEP of 16.3 bar, engine speed of 1650 rpm.

dilution limit.

From literature, a slow burning velocity leads to an increase in the combustion instability. However, a limit for that combustion process is not well understood, especially for methanol. In order to answer this question, the engine was tested with a diluted mixture under WOT condition. Due to engine failure, there are no measurements on EGR dilution. The results of lean combustion of methanol at WOT condition will be used. The engine load was controlled by a lean-burn strategy up to the stability limit. The potential of an engine control load strategy using lean combustion was first evaluated. Then the combustion characteristics were analyzed to find the parameter most related to the combustion instability. The laminar burning velocity was also studied. A critical laminar burning velocity was employed to determine the dilution limit. Finally, the potential of using these parameters for the determination of dilution limit at low loads was investigated.

2.4.1 Research methodology

Similar to the previous section, the standard delivery pressure (150 bar) and the start of injection (300 CAD $bTDC_f$) are maintained in this work. Two engine speeds (1750 rpm and 2250 rpm) were tested. As in previous research [60], the load control potential of the lean-burn strategy was evaluated at wide open throttle (WOT). The injection duration was controlled to achieve the desired exhaust

lambda (increasing from 1 to a higher value in steps of 0.05 until the CoV_{imep} reaches the dilution limit). The CoV_{imep} can be calculated by dividing the standard deviation of the IMEP σ_{imep} with the mean of IMEP μ_{imep} (over 50 cycles), as in equation 2.7.

$$CoV_{imep} = \frac{\sigma_{imep}}{\mu_{imep}} \times 100\% \tag{2.7}$$

The CoV_{imep} limit can be taken at 3% or 5% [38], or even 10% [60]. In order to see a wider range of load controlled by lean-burn strategy, and enable comparison with earlier work, a CoV_{imep} limit of ~10% was used. The maximum CoV_{imep} during the testing period (2-3 minutes) was employed to represent the combustion instability. The potential for load control using the lean-burn strategy was assessed for both methanol and gasoline. MBT ignition timing was used for every operating point. After testing the lean-burn strategy, the conventional stoichiometric throttled load control was used to compare the efficiency.

In order to estimate the in-cylinder conditions, the TPA simulation using GT-Power was employed. The settings for fuel evaporation, wall temperature, heat transfer model, and heat transfer multiplier were set the same as in the previous section. The model can be tuned in order to have the lower heating value multiplier (ratio of predicted total burned fuel mass and experimental total burned fuel mass) of the TPA simulation close to 1 (±2%).

2.4.2 Results

General comparison

Figure 2.18 represents the engine BMEP as a function of exhaust lambda λ for methanol and gasoline at WOT. As can be seen, BMEP decreases linearly with the increase of λ. The measurements were stopped when the CoV_{imep} reached ~10%, so the largest values of λ for each fuel and each engine speed represent the lambda limit. The CoV_{imep} reaches its limit at exhaust lambda of ~1.2 and ~1.5 for gasoline and methanol, respectively. Similar to the previous study [60], the lean-burn limit for methanol is much higher than for gasoline due to the faster burning velocity of methanol. As can be seen, at lambda 1, the BMEP for methanol is higher than for gasoline. Thanks to a high HoV of methanol, the volumetric efficiency increases. Furthermore, methanol has a lower stoichiometric air-to-fuel ratio (see Table 1.1), which leads to a significant reduction in the unburned gas temperature, thus decreasing the heat losses. This also causes the energy per

unit mass of air for methanol to be higher. Together with a more isochoric combustion due to a faster combustion with methanol, the BMEP at stoichiometric operation for methanol is higher compared to gasoline, ~15.5 bar versus ~13 bar, respectively.

Thanks to a higher maximum BMEP at lambda 1 and a higher lambda limit for methanol, the load range that can be controlled by a lean-burn strategy for methanol is wider than for gasoline. For gasoline, the BMEP can be controlled from ~13 bar (stoichiometric) to ~11 bar (dilution limit). Therefore, the engine load can be controlled from 85% load to 100% load with this lean-burn strategy. The load range for the methanol-fueled engine is much wider than for gasoline. The BMEP for methanol can be controlled from ~15.5 bar (stoichiometric) to ~9 bar (combustion stability limit). This means the engine load can be controlled from 58% load to 100% load with this technique.

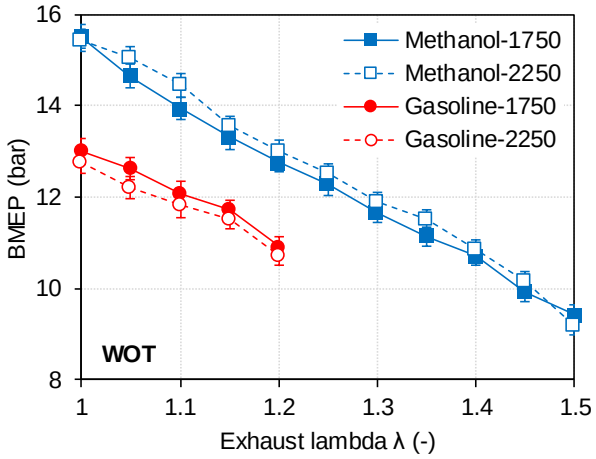

Figure 2.18: Engine BMEP as a function of exhaust lambda for lean-burn of methanol (square symbols) and gasoline (circular symbols) at 1750 rpm (filled symbols) and 2250 rpm (open symbols), WOT, MBT ignition timing.

Figure 2.19 shows the measured CoV_{imep} as a function of engine BMEP for lean-burn of methanol and gasoline at two speeds, 1750 rpm and 2250 rpm. The CoV_{imep} increases slightly and linearly with the decrease of BMEP before reaching the "turning point". After passing the "turning point" (BMEP of ~11.7 bar for gasoline and ~10.7 bar for methanol), CoV_{imep} increases dramatically with decreased BMEP. Compared to methanol, gasoline has a higher CoV_{imep} at the same load and it increases faster as load decreases. Again, faster burning velocity of methanol is the reason for this extension. Faster burning velocity not only supports higher engine performance [96], it also is an important parameter

to extend the dilution limit in SI engines [38, 97]. If the intake port and the combustion chamber geometry are designed for highly turbulent combustion [98], the dilution limit could be further increased.

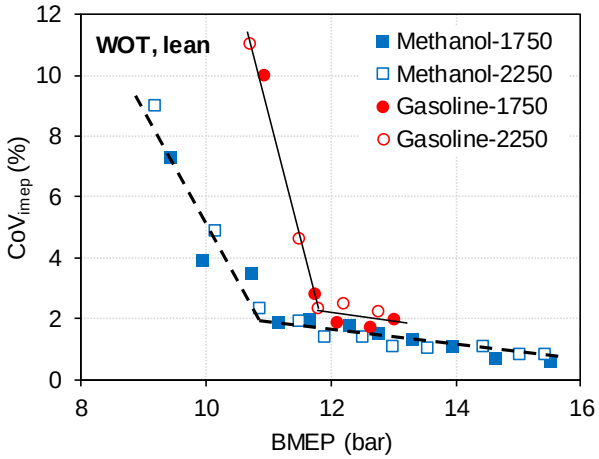

Figure 2.19: CoV_{imep} as a function of engine BMEP for lean-burn of methanol (square symbols) and gasoline (circular symbols) at 1750 rpm (filled symbols) and 2250 rpm (open symbols), WOT, MBT ignition timing.

Figure 2.20 compares the BTE between gasoline and methanol over a range of engine BMEP at two speeds and two methods for load control, WOT lean-burn and throttled stoichiometric. In general, the BTE for methanol is much higher compared to gasoline for both throttled stoichiometric operation and the WOT lean-burn strategy. Thanks to a higher HoV and a faster LBV, the engine efficiency increases due to the reduction of heat and pumping losses, as well as a more isochoric combustion. Comparing throttled and lean-burn operation, lean-burn normally has the potential for higher efficiencies due to the reduction of heat transfer, lower pumping loss, higher specific heat ratio, and increased oxygen availability. However, the difference in measured BTE between lean-burn and throttled conditions for gasoline is limited whereas the BTE difference between lean-burn and throttled conditions is obvious for methanol. The maximum BTE for lean-burn methanol is ~41%, much higher than the maximum BTE for gasoline, ~34%. The relative improvement in the maximum BTE of methanol is ~20% against gasoline. The BTE increases as lambda increases and reaches its peak at a lambda of ~1.2-1.4. At highly diluted conditions (λ >1.4), the friction outweighs the benefits of lean operation [46], so the BTE decreases as lambda further increases. As can be seen in equation 1.11 (on page 15), FMEP does not decrease proportionally with the peak pressure (or load). At higher engine speeds, the BTE reaches its maximum for a richer mixture (smaller lambda) because the

peak pressure becomes less important than the mean piston speed.

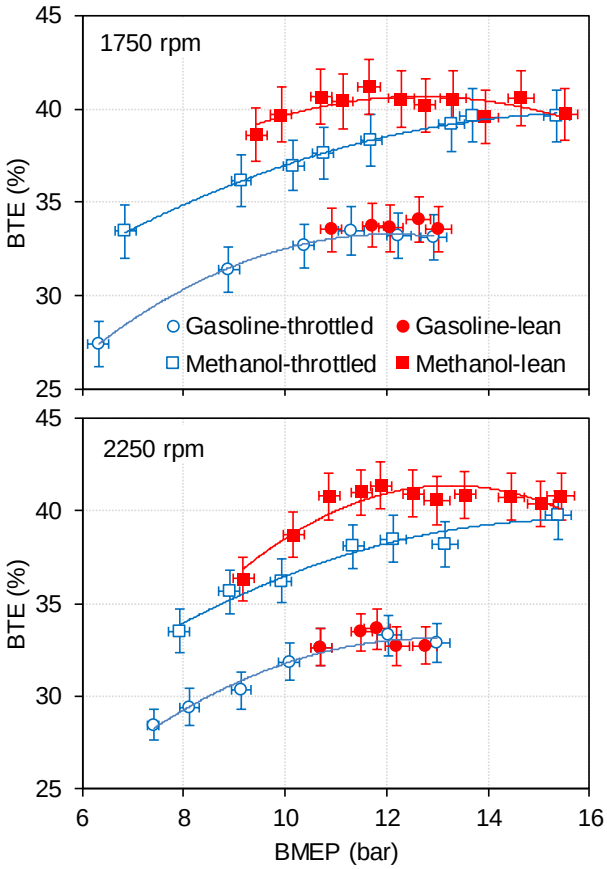

Figure 2.20: BTE as a function of engine BMEP for methanol (square symbols) and gasoline (circular symbols); lean-burn (filled symbols) and throttled (opened symbols) at 1750 rpm and 2250 rpm.

At 2250 rpm, BMEP of ~9 bar, the lean-burn and throttled case have a comparable BTE. The cycle mean in-cylinder pressure profiles at that load are plotted in Figure 2.21. As can be seen, the initial pressure in the lean-burn case is higher because the throttle is fully opened. Although the pre-combustion pressure is lower in the throttled case, the pressure rises fast after ignition with a stoichiometric mixture to have a comparable peak pressure as in the lean-burn case. The peak pressure and its location over 50 cycles are also added in this Figure. For the lean-burn case, the CoV_{imep} is ~9% (see Figure 2.19), and the CoV_{imep} for the throttled case is 2% (stoichiometric mixture). Therefore, the peak pressure and its location vary significantly in the lean-burn case.

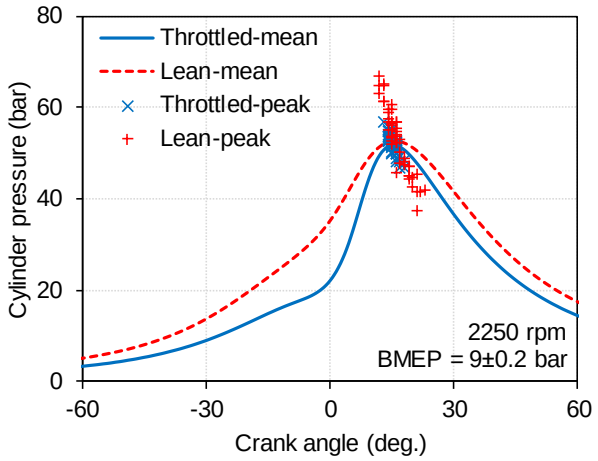

Figure 2.21: Comparison of mean cylinder pressures with its peak and its location over 50 cycles for throttled and lean-burn of methanol at BMEP of ~9 bar, 2250 rpm.

Combustion characterization

The potential of load control using a lean-burn strategy was tested in the previous section. The purpose of this part is analyzing the combustion process of methanol under lean conditions, and looking for a relationship between the combustion process and CoV_{imep}. If such a relationship could be found, the combustion stability limit can be determined by other combustion parameters. The CoV_{imep} is very difficult to predict in engine simulation, therefore finding another parameter to represent the dilution limit is necessary.

In the stoichiometric cases, the mixture is also diluted to some extent, but in this case by residuals (internal exhaust gas recirculation). In order to quantify the dilution ratio, the fuel-to-charge equivalence ratio ϕ' is employed. The fuel-to-charge equivalence ratio is calculated as in equation 2.8 [99].

$$\phi' = \frac{F/(A+R)}{F/A_{st}} = \phi\left(\frac{1-Y_{EGR}}{1+\phi Y_{EGR}(F/A)_{st}}\right) \cong \phi(1-Y_{EGR}) \tag{2.8}$$

where, F, A and R are the masses of fuel, air and residual gas, respectively. The subscript st indicates the stoichiometric condition. For example, at $\phi = 1$, if the EGR ratio is 20% by mass, the fuel-to-charge equivalence ratio is 0.8.

Both lean-burn and throttled cases have in-cylinder residual, i.e. $Y_{EGR} > 0$; therefore, ϕ' is lower than ϕ. Figure 2.22 presents the mixture condition

(equivalence ratio and residual mass fraction) for lean-burn and throttled cases at two engine speeds. The residual mass fraction was determined from the TPA simulation. As can be seen, ϕ is maintained and the residual increases with a decreased load for the throttled cases. For the lean-burn cases, ϕ decreases and the residual mass fraction slightly increases as lambda increases. Although the throttle is fully opened, a reduction in the pressure difference between cylinder and exhaust explains the small increase in residual with increasing lambda. With the equivalence ratio and residual mass fraction from this Figure, ϕ' can be computed using equation 2.8. The constant ϕ' contours are also plotted in Figure 2.22.

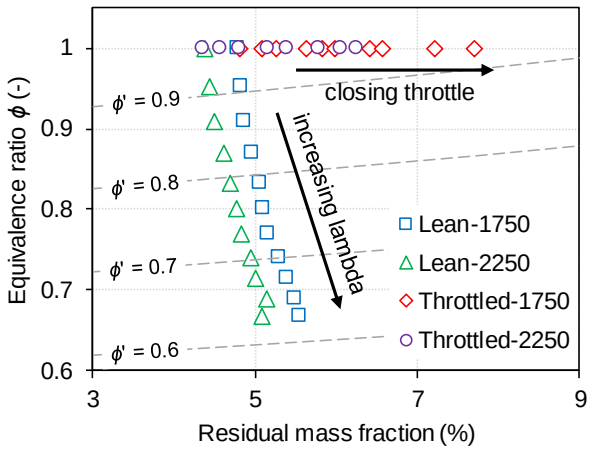

Figure 2.22: The equivalence ratio and residual mass fraction of the reactants for lean-burn and throttled conditions. Grey dashed lines: constant ϕ' contours.

Figure 2.23 illustrates the basic timing of the combustion process as a function of ϕ' for two engine speeds. The MBT ignition timing is represented as "spark" timing in this Figure. The timing of 2%, 10%, 50% and 90% mass fraction burned are presented as CA2, CA10, CA50 and CA90, respectively. These timings were found through the analysis of measured cylinder pressure traces. The results for throttled conditions are also plotted in this Figure, as filled symbols. As shown in Figure 2.22, the residual increases a few percent in the throttled cases, so ϕ' slightly decreases as load decreases. Thus, the range of ϕ' for throttled cases is much smaller than the range for lean combustion.

In order to achieve the maximum brake torque, the spark timing has to be advanced for highly diluted cases. The timing of CA50 almost does not change for different ϕ'. At 1750 rpm, the CA50 is maintained around 8.2 CAD aTDC$_f$, and CA50 is maintained around 9.5 CAD aTDC$_f$ at 2250 rpm. Due to the reduction of laminar burning velocity, the combustion process elongates with decreased ϕ', especially

during the initial flame propagation. The combustion starts with a laminar flame front after ignition, and then the flame is wrinkled by the in-cylinder turbulence to form a turbulent flame. Thus the impact of turbulence is more important in the second phase of combustion.

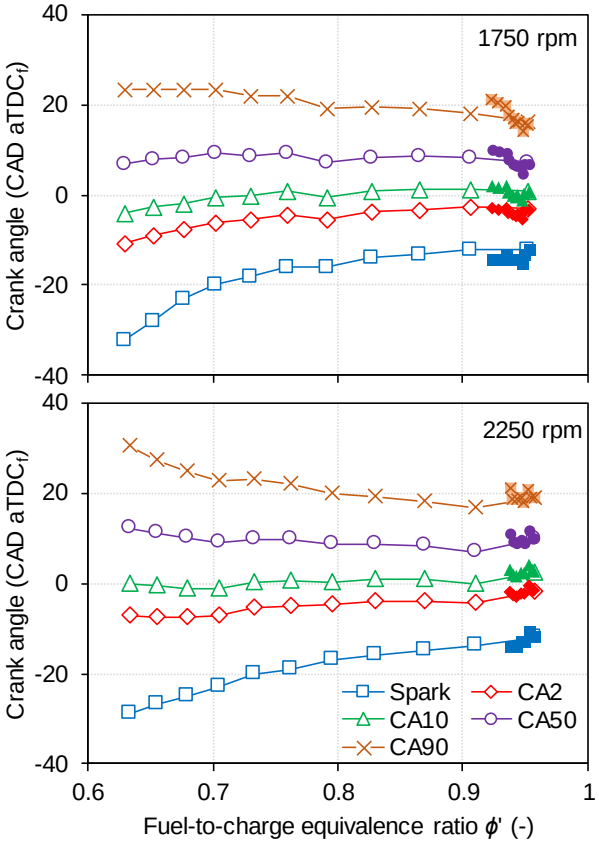

Figure 2.23: Timing of the combustion process as a function of ϕ' for lean-burn of methanol (opened symbols) and throttled conditions (filled symbols).

Previously, Lee et al. used the combustion duration CA10-90 as a CoV_{imep}-related parameter [100]. Other research employed the early flame development period CA0-5 to represent the dilution limit [92]. In this study, in order to find the combustion duration that is most related to CoV_{imep}, the relative change (compared to stoichiometric operation) of combustion durations are plotted against the relative change of CoV_{imep} in Figure 2.24. For a certain relative change of CoV_{imep}, the duration which has a higher relative change versus the stoichiometric case is the most CoV_{imep}-related parameter.

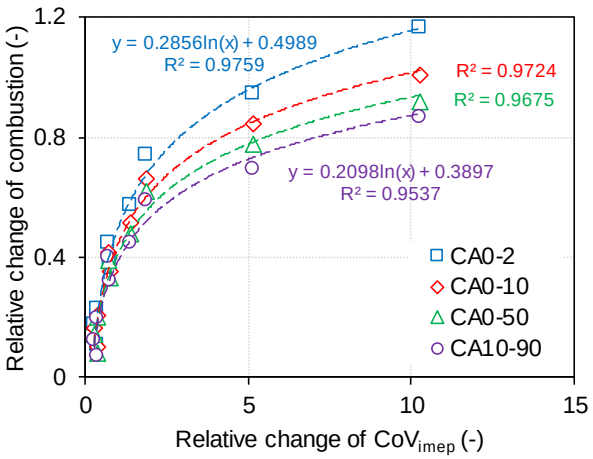

Figure 2.24: The relationship between the relative change of combustion durations and the relative change of CoV_{imep} at 2250 rpm.

As can be seen, the CA0-2 is the combustion duration most closely related to CoV_{imep}. The second most related duration is CA0-10, and the least related duration is CA10-90. This means that the CoV_{imep} is the most sensitive to a change of CA0-2. Therefore, the changing behavior of CA0-2 is the most closely related to the nature of CoV_{imep}. However, in this study, CA0-10 is used instead of CA0-2 because the CA0-10 is widely used and it is easier to determine from the experiment. Furthermore, the CA0-10 has a linear relationship with the change of CA0-2, as shown in Figure 2.25.

The relationship between CoV_{imep} and CA0-10 is shown in Figure 2.26. As can be seen, the CoV_{imep} increases with a longer flame development period. Although the variation of CoV_{imep} at the two speeds are not identical, a value of CA0-10 can be used to represent the stable combustion limit. If 5% CoV_{imep} is employed as limit, combustion becomes unstable with a CA0-10 larger than 26.5 CAD. The results from a correlation which was developed by Schiffmann et al. [101] was also added in this Figure. As can be seen, the CA0-10 limit is comparable between the two studies. Based on the relationship between CA0-10 and CA0-2 in Figure 2.25, the CA0-2 limit can be calculated, it equals ~19.8 CAD. A shorter CA0-2 and CA0-10 duration have to be used if a lower CoV_{imep} limit is employed (e.g. 3%). The requirement of a short flame development period to achieve a stable combustion explains the importance of engine ignition systems for diluted combustion.

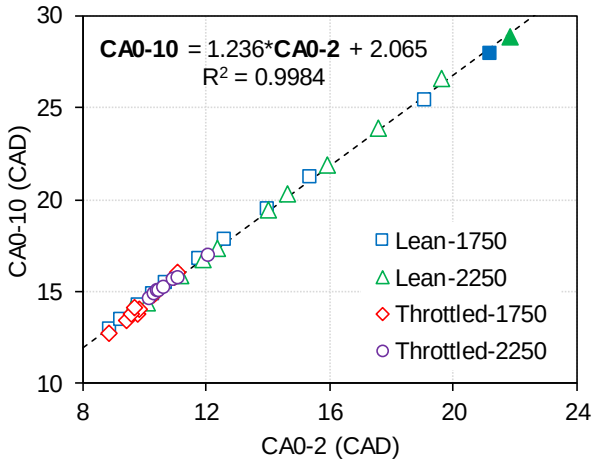

Figure 2.25: The relationship between CA0-10 and CA0-2 for lean-burn and throttled condition at 1750 rpm and 2250 rpm. Filled symbols: CoV_{imep} over 5%.

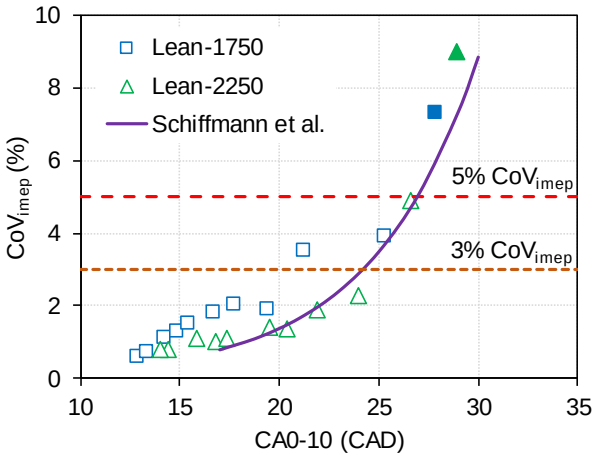

Figure 2.26: The relationship between CoV_{imep} and CA0-10 for the lean-burn combustion of methanol at 1750 rpm (square symbols) and 2250 rpm (triangular symbols). Solid line: correlation from Schiffmann et al. [101]. Filled symbols: CoV_{imep} over 5%.

Laminar burning velocity

In the previous section, the combustion duration was employed to define the dilution limit on this engine. The combustion duration is strongly influenced by laminar and turbulent burning velocities. The laminar burning velocity is the dominant one during early flame development period, so the LBV will be investigated in this part. The LBV was calculated using a correlation (discussed future in Chapter 5) with the unburned gas temperature and the residual mass fraction derived from the TPA simulation. Similar to the previous section, finding a value for LBV to demonstrate the combustion stability limit is the main purpose of this part. Previously, a constant LBV was employed to define the combustion stability limit [99]. The LBV is influenced by equivalence ratio, residual gas fraction, as well as the end-gas state, pressure and temperature. Assuming the mixture is homogeneous, the equivalence ratio and residual fraction of the unburned gas are maintained during the combustion.

The end-gas state at ignition timing, CA2, CA10, and CA50 for the lean-burn cases with methanol at 1750 rpm and 2250 rpm is presented in Figure 2.27. The pressure-unburned temperature (P-T_u) trajectory at full load (λ=1) is also plotted in this Figure. As can be seen, the unburned gas temperature in the lean-burn cases (symbols) is a bit higher compared to the full load condition (at the same pressure). It can be explained by the reduction of absorbed heat from the fuel evaporation. Less fuel is injected into the combustion in the lean case, this leads to a slight increase in the unburned gas temperature.

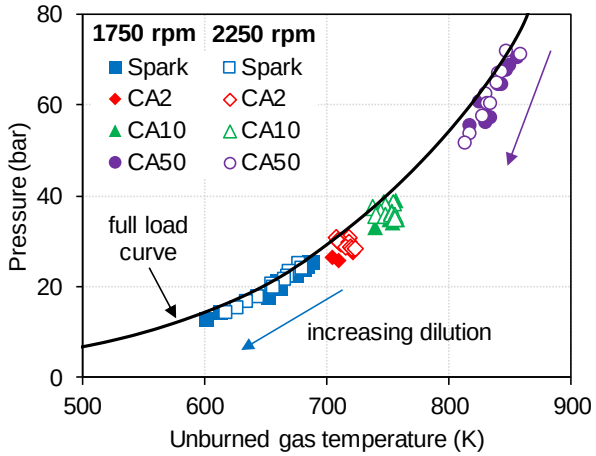

Figure 2.27: Unburned gas state (pressure and temperature) for lean-burn cases of methanol at 1750 rpm (filled symbols) and 2250 rpm (opened symbols).

Because the ignition timing has to be advanced for the lean-burn case (see Figure 2.23), the pressure and unburned temperature at spark timing for highly diluted cases are lower than for the richer cases. However, there is only a small difference in the state of unburned gas at CA2 and especially at CA10. The pressure and temperature at CA10 vary around 35 bar and 750 K, respectively. However, the pressure and temperature at CA50 clearly decrease with a leaner mixture. Although the timing of CA50 is maintained, the reduction of flame speed leads to a decrease in the cylinder pressure at CA50. The T_u at CA50 also slightly decreases as lambda increases. Therefore, at ignition timing and CA50, the end-gas state and the fuel-to-charge equivalence ratio are the two parameters influencing the LBV.

Figure 2.28 presents the LBV (u_L) at four end-gas states as a function of ϕ' with a fixed residual mass fraction of 5%. Although the residual mass fraction changes with varied ϕ (see Figure 2.22), an averaged value of residual mass fraction was employed for simplicity. Therefore, for each end-gas state, the LBV is influenced by ϕ only. For $\phi \leq 1$, the LBV decreases as ϕ decreases (same pressure and temperature). The impact of pressure and temperature are also presented in this Figure. The laminar burning velocity decreases as temperature decreases from 690 K to 600 K (at a fixed pressure of 25 bar), and it increases as pressure decreases from 25 bar to 12.4 bar (at a fixed temperature of 690 K). Because the temperature has a stronger influence, the LBV at 12.4 bar and 600 K is lower than the LBV at 25 bar and 690 K. The end-gas state at ignition timing for the stoichiometric case and the most diluted case at 1750 rpm are ~25 bar/690 K (solid line) and ~12.4 bar/600 K (dash-dotted line), respectively. So, the end-gas state has an impact on the LBV. An earlier ignition timing leads to a decrease in the initial LBV. Additionally, the ϕ' for stoichiometric operation is 0.95, and for the most diluted case is ~0.64, so the LBV decreases further, as shown by the diamond and the circle symbols in the Figure.

In order to identify the most relevant LBV to a change of CoV_{imep}, the relative change of LBV was plotted against the relative change of CoV_{imep} in Figure 2.29. The LBV is calculated using the correlation which will be presented in Chapter 5. Negative values mean the CoV_{imep} increases as LBV decreases. Larger absolute value means a strong relation of this parameter to a change of CoV_{imep}. At ignition timing and CA50, the end-gas state influences the LBV, so the absolute relative change of LBV against the stoichiometric condition is larger than at CA10 and CA2. The LBV at CA10 is mostly influenced by the equivalence ratio only, this explains the lower sensitivity to a change of CoV_{imep}. Therefore, the LBV at spark timing is the LBV most related to CoV_{imep}, similar to the conclusion in the previous study [97].

Figure 2.30 presents the relationship between CA0-10 and LBV at spark timing for

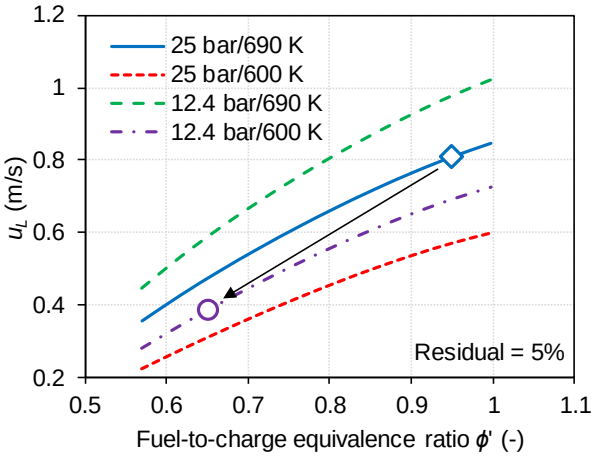

Figure 2.28: The influence of ϕ' and unburned gas states on LBV. Diamond symbol: stoichiometric condition, circle symbol: most diluted case.

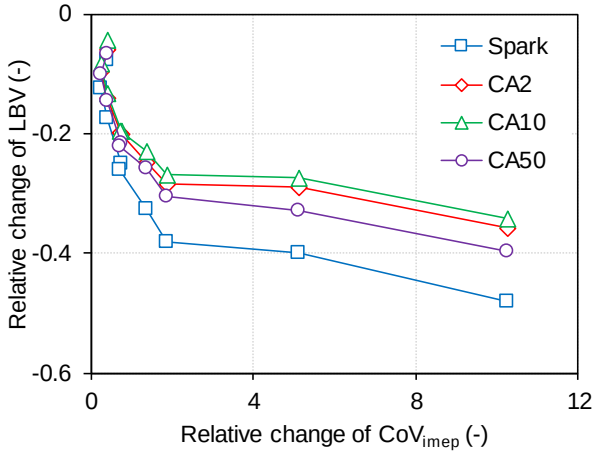

Figure 2.29: The sensitivity of CoV_{imep} to a change of laminar burning velocity at ignition timing, CA2, CA10 and CA50 at 2250 rpm.

two engine speeds. With a decreased LBV, the CA0-10 increases. The combustion becomes unstable with CA0-10 larger than 26.5 CAD, which was represented by filled symbols. Based on the correlation, the limit for LBV at ignition timing can be estimated; it equals ~0.4 m/s.

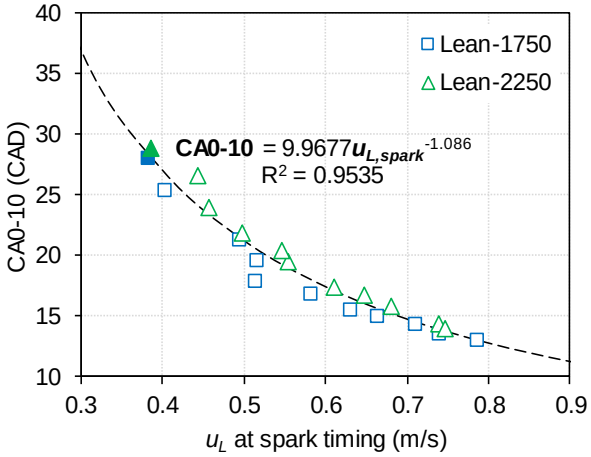

Figure 2.30: The relationship between CA0-10 and LBV at ignition timing at two engine speeds. Filled symbols: CoV_{imep} over 5%.

Lower loads

As explained in the previous analysis, the LBV strongly depends on the end-gas state. Therefore, a single value of LBV cannot represent the dilution limit for different engine conditions. For example, Figure 2.31 illustrates the end-gas state at ignition timing, CA2, CA10, and CA50 for the throttled cases at 1750 rpm. The solid line presents the full load pressure-temperature trajectory of the end gas. With a smaller throttle position, the pressure drops significantly. However, the end gas temperature does not change much at the beginning of combustion. Only at CA50, the temperature decreases as the load decreases. Because pressure has a negative effect on the LBV, the LBV increases as pressure decreases with a fixed temperature, equivalence ratio and residual fraction. Because the residual mass fraction is not constant, so averaged values are employed. LBV contours are also shown in the P-T_u diagram, for a stoichiometric mixture with a residual fraction of 6.5%. As can be seen, the LBV at all conditions increases as load decreases. However, the engine becomes unstable at lower loads, as shown in Figure 2.32.

The increase of CoV_{imep} with reduced engine load can be explained by the reduction of mean IMEP, see equation 2.7. Therefore, the dilution limit for lower

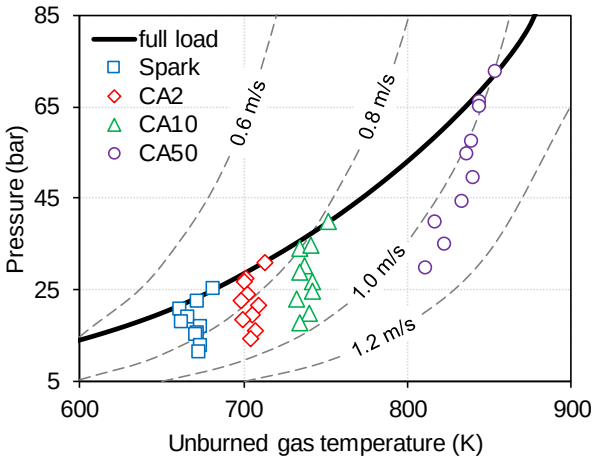

Figure 2.31: Unburned gas state (pressure and temperature) for throttled conditions of methanol at 1750 rpm. Dashed lines: constant laminar burning velocity contours at stoichiometric with 6.5% residual.

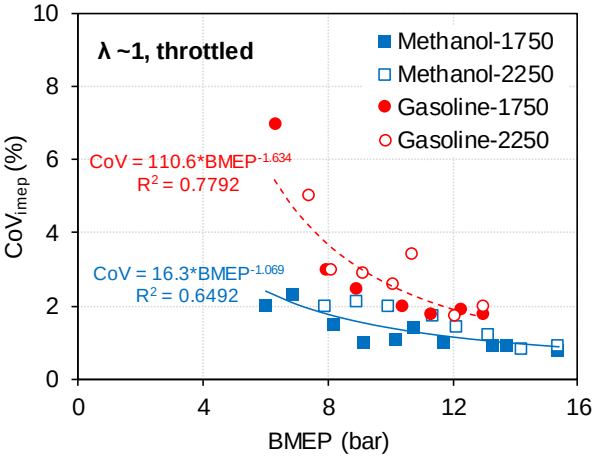

Figure 2.32: CoV_{imep} as a function of engine BMEP for throttled cases of methanol (square symbols) and gasoline (circular symbols) at 1750 rpm (filled symbols) and 2250 rpm (opened symbols).

load will be decreased. At a lower load, the intake gas temperature decreases, and cylinder wall temperature reduces. Furthermore, less fuel is injected into the combustion chamber, and since the fuel is mainly evaporated by the heat of the intake charge, the gas temperature drops significantly. The residual mass fraction also increases as load decreases. Therefore, the laminar burning velocity decreases. In this simulation, 50% of the heat for fuel spray evaporation is from the intake charge and 50% of the heat is from cylinder walls (see section 2.3.1). It was kept the same for all simulations. The throttling effect on inlet gas temperature was also not considered in this simulation. With a positive Joule-Thomson coefficient, air temperature decreases after the throttle (pressure drops). The generated turbulence downstream the throttle might result in a decrease in inlet temperature. Additional measurements with lean-burn (and EGR dilution) at lower load are needed to identify the CoV_{imep}-related parameter and its limit.

2.5 Closure

The present chapter gave insights into the downsizing and lean-burn extension potential with methanol. Experiments and TPA simulations using GT-Power were conducted. The potential of downsizing and lean combustion of methanol were compared to conventional gasoline.

In order to estimate the downsizing potential of methanol, the maximum output torque for gasoline was first found through a test matrix following a DoE approach. The engine BMEP increased by ~19% compared to the original settings, to 16.3 bar. Sweep tests with different intake boost pressure and valve timing were then conducted on methanol. Much higher BMEP was observed with a positive valve overlap and a higher boost pressure. Faster combustion was observed with a larger valve shifting angle, especially at the cases which have positive valve overlap. A lower residual gas fraction was the reason for the significant improvement of combustion speed. In the case of S-VVT 40, the in-cylinder lambda was 0.95. The combination of rich combustion and lower residual gas mass fraction explains the enhancement of combustion speed and engine BMEP. However, lower BTE was observed. The engine BMEP improved with higher intake pressure. The combustion speed was similar with different intake pressure. Because the valve timing was fixed, the gas exchange process was similar in all cases. However, the peak in-cylinder pressure increased due to the increase of initial pressure. A linear relationship between the peak in-cylinder pressure and BMEP was found in the boost control cases.

Based on that relationship, the maximum allowed BMEP of the engine could

be found with the peak in-cylinder pressure constrained at 100 bar. Then the downsizing factor of methanol compared to gasoline could be calculated. With methanol, the engine can be further downsized by ~10.7%. The downsizing factor can be improved if the engine hardware is stronger, however, this will increase the engine mass. The maximum compression ratio for the NA SI engines was also estimated. At $\lambda = 1$, the maximum allowable compression ratio for a methanol fueled NA SI engine is around 14:1. At the same maximum BMEP for gasoline, the peak unburned gas temperature and pressure is higher with methanol, and in the knocking region of gasoline. However, due to the high knock resistance of methanol compared to gasoline, no knock occurs. Although the unburned gas temperature is higher with methanol, the NO_x (as well as CO and CO_2) emissions are lower than gasoline. This can be explained by the lower burned gas temperature of methanol and a higher combustion efficiency compared to gasoline.

For the lean-burn potential of methanol, a basic comparison between two load control strategies, WOT lean-burn and throttled stoichiometric, was done for both methanol and gasoline. In the throttled cases, methanol had a higher efficiency than gasoline over a wide range of loads. The efficiency was further increased with the use of a lean-burn strategy for the load control. The maximum BTE for methanol was ~20% higher than for gasoline. Due to a faster laminar burning velocity compared to gasoline, the lean-burn limit could be extended for methanol. The lambda limit for methanol was ~1.5, much higher than for gasoline, ~1.2 (with a CoV_{imep} limit of ~10%). With methanol the engine was able to operate at lower load compared to gasoline before the combustion became unstable.

The ignition delay (CA0-2), flame development period (CA0-10), and combustion duration (CA10-90) are prolonged with the decrease of fuel-to-charge equivalence ratio ϕ'. CA0-2 and CA0-10 are the parameters most related to the change of CoV_{imep}. A CA0-10 duration of 26.5 CAD could be used as a limit for the combustion stability if 5% CoV_{imep} is employed. A limit for the laminar burning velocity at ignition timing for lean combustion was proposed. The combustion became unstable with LBV at ignition timing less than ~0.4 m/s. That LBV limit could be used to present the dilution limit for this engine at WOT condition. However, the same limit proved not to be applicable for low load conditions. The CoV_{imep} increases with decreased load. Whereas, the LBV increases as load decreases. Therefore, a certain value of LBV could not be used to represent the combustion stability limit for both WOT lean-burn strategy and stoichiometric throttled condition.

In both cases, the efficiency for methanol is always higher than for gasoline thanks to the interesting properties of methanol mentioned in the first Chapter. The efficiency can be further increased with advanced engine technologies. The

exhaust heat contains a significant fuel energy, therefore, the system efficiency could increase if a part of the exhaust heat is recovered. The next chapter is devoted to engine exhaust heat recovery by methanol reforming.

3

Methanol reforming using engine exhaust heat

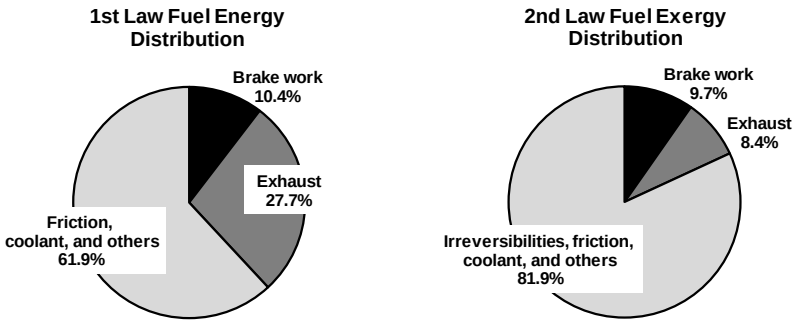

Figure 3.1: The first law fuel energy and the second law fuel exergy distribution in an SI engine [102].

Figure 3.1 shows data that were collected at the Oak Ridge National Laboratory chassis dynamometer for a 2007 Saab Biopower under the federal test procedure (FTP) driving cycle [102]. As can be seen, **the exhaust contains 8.4% fuel exergy**, which is nearly as high as the brake work. Thus, recovery of the waste exhaust heat can help to increase the overall system efficiency. In this chapter,

first an overview of waste heat recovery (WHR) systems will be provided and then more details about fuel reforming will be presented in the following parts.

3.1 Waste heat recovery systems

There are several technologies that have been investigated and applied to recover the engine exhaust heat. The main approaches can be summarized as follows:

1. Conversion of exhaust energy into mechanical energy through turbocharging.
2. Conversion of exhaust energy into mechanical/electrical energy by means of an additional turbine: turbo-compounding.
3. Conversion of exhaust energy into electrical energy by means of thermoelectric generator.
4. Conversion of exhaust energy into acoustic energy by means of thermoacoustic engines.
5. Conversion of exhaust energy into mechanical energy or electricity by means of thermal power generation: Rankine cycle and Brayton cycle.
6. Conversion of exhaust energy into chemical energy by means of thermochemical recuperation.

The first is the most well known technology to recover exhaust energy. The exhaust gas drives a turbine which is connected to an air compressor. It pushes extra air into the cylinder, thus increasing the specific power of engines. The engine can deliver a similar power with a lower speed (downspeeding) or a smaller displacement volume (downsizing). It has been used since 1905, and turbochargers are often major component in modern engines. The second technology uses the same principle as the first one with an additional turbine. It converts the exhaust energy into mechanical/electrical energy. The advantages of this technology include simplicity, compactness and low cost. However, it has challenges such as the increase of back pressure in the exhaust system and a small benefit at low speed/load conditions.

The third method generates electricity based on the temperature difference across a thermoelectric device. The advantage depends on the efficiency of the heat exchange and the efficiency of the thermoelectric generator [103]. The challenges

of thermoelectric conversion include the durability of thermoelectric material, as well as the weight and cost. The fourth technique converts heat into a high energy acoustic wave which transports energy to an electric generator. It is still in the early stages of development.

The fifth one is the use of a Rankine cycle or a Brayton cycle to convert waste heat into mechanical energy or electricity using an expander or a turbine. In the Rankine cycle, heat is utilized to heat up a boiler which contains working fluid at high pressure. The (high pressure) vapour is used to drive a turbine for generating mechanical power or electricity. The low pressure vapour is then condensed and pumped back into the boiler to make a closed cycle. It is widely employed in heavy-duty diesel engines, especially in diesel generators. The expander and working fluid are the two parts which have the biggest influence on the system performance [104]. Similar principle to the Rankine cycle, high temperature and high pressure working fluid expands in a turbine and generates additional work in the Brayton cycle. The major difference between these two cycles is the working fluid. Gas is employed in the Brayton cycle.

The last methodology is using engine exhaust heat to convert (reform) the original fuel into a H_2-rich gas through an endothermic reaction. The energy of the reforming products can be higher than the original fuel [95], thus it is called a thermochemical recuperation (TCR) method. This is the main topic of this Ph.D. research, and this approach will be presented in the following section.

3.2 Methanol reforming

In the first Chapter, methanol was shown to be a very promising liquid fuel for future SI engines. Furthermore, the low reforming temperature and high H/C ratio of methanol are advantages compared to other fuels when it comes to reforming [105]. Thus, this section will focus on the reforming of methanol and its application in SI engines. There are several kinds of methanol reforming, including steam reforming, thermal decomposition, dry reforming, auto-thermal reforming, and partial oxidation. Some kinds of fuel reforming produce heat, so they are not a kind of TCR (endothermic process). The five types of methanol reforming to produce H_2-rich gas are described below.

- **Partial oxidation (POX)**

  This is rich combustion of methanol. Normally, one mole of methanol requires 1.5 moles of oxygen for complete combustion. In reaction R3.1,

only 0.5 mole of oxygen is used. The products include H_2 and CO_2. Because this is the oxidation of methanol, so the reaction releases heat. Therefore, the heating value (or energy) of the products is lower than the input.

$$CH_3OH + 0.5O_2 \xrightarrow{\text{catalyst}} 2H_2 + CO_2 \quad \text{(R3.1)}$$

- **Auto-thermal reforming (ATR)**

  The reaction includes not only methanol and oxygen like with POX, but also water vapour, as in reaction R3.2. It is the combination of POX and steam reforming reaction (which will be discussed later). The enthalpy of formation for that reaction equals 0.

$$CH_3OH + 0.2O_2 + 0.6H_2O \xrightarrow{\text{catalyst}} 2.6H_2 + CO_2 \quad \text{(R3.2)}$$

- **Steam reforming (SR)**

  In this case, methanol reacts with water to form H_2 and CO_2, as shown in reaction R3.3. It is an endothermic reaction, so the energy of products is higher than the input. One mole methanol requires at least one mole of water for 100% fuel reforming. If the water to methanol molar ratio is less than unity, a part of methanol will be reformed following the steam reforming reaction, the rest will follow the thermal decomposition reaction.

$$CH_3OH + H_2O \xrightarrow{\text{catalyst}} 3H_2 + CO_2 \quad \text{(R3.3)}$$

- **Thermal decomposition (TD)**

  Thermal decomposition is a split reaction of methanol to produce a mixture of H_2 and CO (reaction R3.4). Methanol does not require any co-reactant to reform it into H_2-rich gas. It is a highly endothermic reaction, the energy of the product is higher than the methanol steam reforming case.

$$CH_3OH \xrightarrow{\text{catalyst}} 2H_2 + CO \quad \text{(R3.4)}$$

- **Dry reforming (Dry)**

  This is the most highly endothermic reaction to reform methanol. Methanol reacts with CO_2 to form a mixture of H_2, CO and H_2O, as in reaction R3.5. From the thermodynamic point of view, it is the combination of the thermal decomposition reaction and the reversed-water gas shift reaction (which will be explained later).

$$CH_3OH + CO_2 \xrightarrow{\text{catalyst}} H_2 + 2CO + H_2O \quad \text{(R3.5)}$$

The five mentioned reforming strategies for methanol are presented in Figure 3.2, indicating the reaction with their energy ratio and enthalpy of formation. The cases with an energy ratio lower than unity or a negative enthalpy of formation

are exothermic processes. Note that, the enthalpy of formation for these reactions was calculated with the reactants in the gas phase. The enthalpy of formation increases if the liquid phase is employed. However, the energy ratio does not change. As can be seen, POX is an exothermic process. All cases here are presented with theoretical reactions. However, the products can change with increased temperature. H_2 and CO_2 in the products of POX, ATR and SR can react together to form CO and H_2O following the reverse-water gas shift (r-WGS) reaction (reaction R3.6). It is an endothermic reaction, thus, the products of POX, ATR, and SR will have a higher fraction of CO at a higher temperature. The equilibrium reforming products and energy ratio as a function of temperature will be calculated in the following section.

$$H_2 + CO_2 \longrightarrow CO + H_2O \qquad \Delta h_f = 41 \text{ kJ/mol} \tag{R3.6}$$

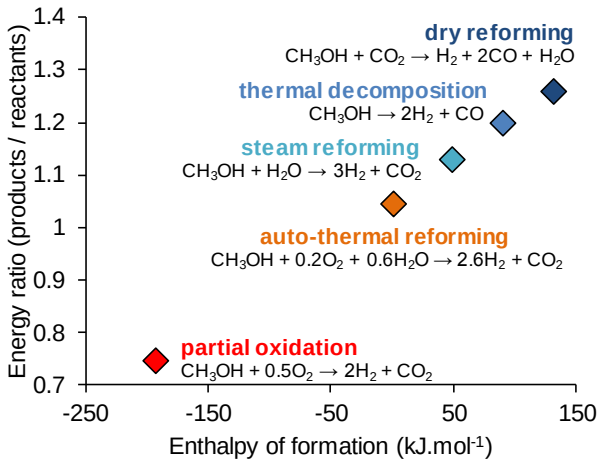

Figure 3.2: Reforming reactions of methanol, shown with their enthalpy of formation and energy ratio of products to reactants.

3.2.1 Equilibrium products

To predict the impact of temperature on the equilibrium products and to calculate the energy ratio, the Gibbs free energy minimization method was employed. For a mixture of ideal gases, the Gibbs free energy (G_{mix}) can be calculated as follows [106]:

$$G_{mix} = \sum N_i \bar{g}_{i,T} = \sum N_i \left[\bar{g}^o_{i,T} + R_u T ln\left(P_i/P^o\right) \right] \tag{3.1}$$

where N_i is the number of moles, R_u is the gas constant, P^o is the standard-state pressure (1 atm), P_i is the partial pressure of the i^{th} species. $\bar{g}_{i,T}$ is the Gibbs function at a certain temperature T, $\bar{g}^o_{i,T}$ is the Gibbs function of pure species at the standard-state pressure.

To find the equilibrium chemical products, the total Gibbs free energy is minimized, i.e. $dG_{mix} = 0$. The RGibbs reactor in ASPEN PLUS was used to predict the equilibrium products of different types of methanol reforming. The model in ASPEN PLUS includes the inlet, the RGibbs reactor, and the outlet. The inlet contains methanol and co-reactants (except for the case of the thermal decomposition) as in reactions R3.1-R3.5. The temperature of the reactor was varied from 200 °C to 600 °C. The simulation was performed at ambient pressure, it closes to the reforming condition in the selected engine concept (see Section 3.4). The concentrations of products were analyzed at the outlet.

The equilibrium products are a result of the Gibbs free energy minimization and the reaction pathways to achieve the equilibrium condition are not considered in the model. The effect of space velocity (ratio of reactant volumetric flow rate to the volume of the catalyst) and catalyst material are not taken into account. In this simulation, a reactor with an infinite volume was employed, thus reactants have a long residence time for reforming. As a result, the fuel conversion will reach 100% at a lower temperature than what would be possible with experiments [107]. According to Palo et al. [108], operation at low temperature without a catalyst at a long residence time will lead to high levels of methane (CH_4). In practice, with the presence of a catalyst and high space velocity, methane formation is not a concern. The formation of carbon, C, was also neglected in this calculation. Therefore, to simulate the real products, only six species were considered in this simulation, including CH_3OH, O_2, CO_2, H_2O, CO and H_2.

Figure 3.3 shows the energy ratio of the four main reforming strategies (POX, SR, TD and Dry). The ATR is a mix between POX and SR, so the energy ratio of ATR was not presented in this Figure. As can be seen, the energy ratio of POX and SR increases as temperature increases. This can be explained by the reaction between H_2 and CO_2 in the products to form CO and H_2O, which has a higher energy. In the SR, the water is "re-formed" through the r-WGS reaction at high temperature. The energy ratio of SR tends toward to the energy ratio of the TD reaction at high temperature. For the TD reaction, the energy ratio is maintained because H_2 and CO do not react together to form other species. For the dry reforming, the energy ratio at 200 °C is comparable to the TD. This can be explained by the high required temperature for the dry reforming. At this temperature, the methanol splits into H_2 and CO (following the TD reaction), and CO_2 does not have any impact on the reforming. Then the H_2 in the products reacts with CO_2 following the r-WGS

reaction. To achieve a high energy product like in reaction R3.5, the required temperature is very high.

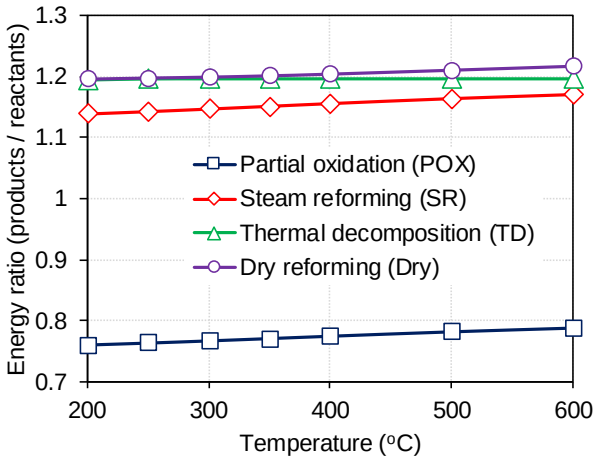

Figure 3.3: Energy ratio as a function of temperature.

Figure 3.4 presents the normalized moles of products (normalized to moles of methanol in the reactant) for four kinds of methanol reforming as a function of temperature. It is clear that the CO and H_2O fractions increase as the temperature increases in the POX and SR cases, whereas H_2 and CO_2 decrease with an increased temperature. A similar behavior was observed for the dry reforming. For the thermal decomposition case, the reaction is maintained over a wide range of temperatures.

3.2.2 Comparison with other fuels

In the previous part, the equilibrium products for different methanol reforming reactions were calculated. In this part, methanol will be compared to other SI engine fuels. As mentioned in the previous section, the required temperature for 100% fuel reforming from ASPEN PLUS simulation is much lower than in experiments. Although the Gibbs free energy minimization method cannot predict the absolute temperature for 100% fuel conversion, the difference in required temperature for different fuels for the same fuel conversion can be estimated with this simulation (same space velocity for all fuels). Two SI engine fuels were selected for this comparison: ethanol and iso-octane (gasoline surrogate). The steam reforming case was chosen for the comparison (see section 3.4). Theoretically the steam reforming of methanol produces a mixture of H_2 and CO_2

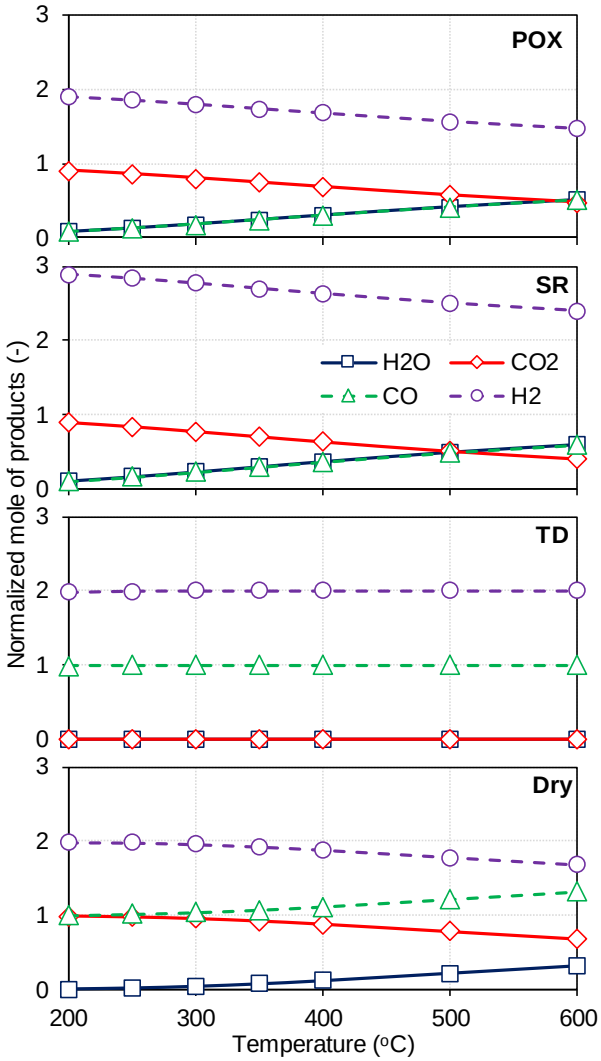

Figure 3.4: Normalized moles of reforming products as a function of temperature.

(reaction R3.3). The reactions for ethanol and iso-octane steam reforming with the same products as methanol steam reforming process are presented in reactions R3.7 and R3.8, respectively.

$$C_2H_5OH + 3H_2O \longrightarrow 2CO_2 + 6H_2 \qquad \Delta h_f = 173 \text{ kJ/mol} \tag{R3.7}$$

$$C_8H_{18} + 16H_2O \longrightarrow 8CO_2 + 25H_2 \qquad \Delta h_f = 930 \text{ kJ/mol} \tag{R3.8}$$

In order to simulate the reforming of iso-octane (in primary reference fuels), 2,2,4-Trimethylpentane $(CH_3)_3CCH_2CH(CH_3)_2$ was used. It is one of several isomers of C_8H_{18}. Similar to the previous simulation, the inlet contains fuel and water vapour. The water to fuel molar ratio was set as in reactions R3.3, R3.7 and R3.8. This means the water to fuel molar ratio was 1, 3 and 16 for methanol, ethanol and iso-octane, respectively. The products include non-reacted fuel, H_2O, CO_2, CO and H_2. The reactor temperature was varied with steps of 50 °C to see the impact of temperature on the fuel conversion and the product concentrations.

Figure 3.5 shows the fuel conversion as a function of reactor temperature for methanol, ethanol and iso-octane. Because the reactor volume is infinite, the fuel starts reforming at a very low temperature. Although steam reforming is an endothermic reaction, methanol conversion was ~3% at -100 °C. As shown in this Figure, the fuel conversion increases as temperature increases for all fuels. To achieve the same fuel conversion, methanol requires a much lower temperature compared to ethanol and iso-octane. For instance, to have 90% fuel conversion, the required temperature for methanol was lower than ethanol by ~180 °C, and lower than iso-octane by ~290 °C. However, the absolute temperature for 90% fuel conversion cannot be predicted with this simulation. The required temperature in a real test depends not only on temperature, but also space velocity, co-reactants, and catalyst materials.

Figure 3.6 presents the energy ratio for methanol, ethanol and iso-octane reforming as a function of the reactor temperature. At low temperature (less than 250 °C), the energy ratio of methanol reforming is higher than ethanol because of a higher fuel conversion. That value versus iso-octane is 350 °C. At these temperatures (250 °C for ethanol and 350 °C for iso-octane), the fuel conversion equals ~80% for both fuels (see Figure 3.5). This means at least ~80% of ethanol and iso-octane have to be reformed to have a higher energy ratio than in the methanol case. If 100% fuel was reformed, the products of ethanol and especially iso-octane reforming have higher energy ratio compared to methanol. Similar to the results in Figure 3.3, the energy ratio continues to increase after 100% fuel is reformed due to the initiation of the r-WGS reaction.

Figure 3.7 illustrates the normalized amount of moles of products of ethanol steam

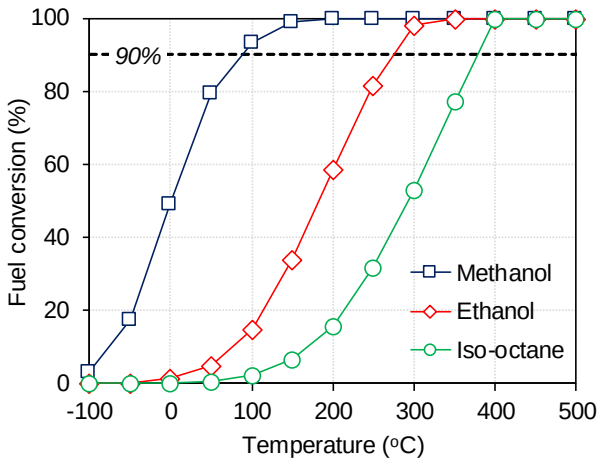

Figure 3.5: Fuel conversion for methanol, ethanol and iso-octane reforming as a function of temperature.

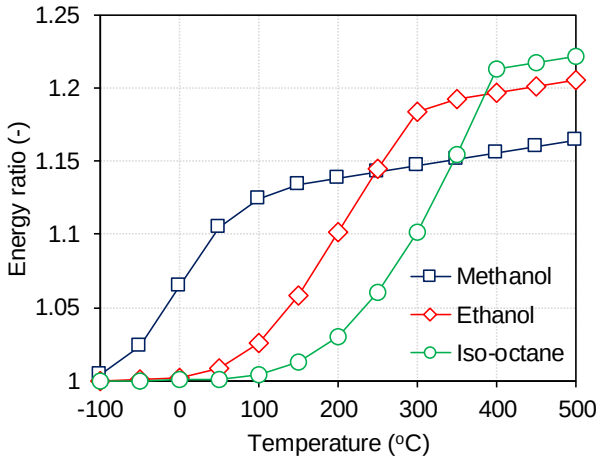

Figure 3.6: The energy ratio for methanol, ethanol and iso-octane reforming as a function of temperature.

reforming (normalized to moles of ethanol in the reactant). At low temperature, fuel conversion is equal to 0, the outlet contains one mole of ethanol and three moles of water (the reactants in reaction R3.7). The number of moles of water and ethanol decreases as temperature increases. There is almost no ethanol molecule in the outlet when the temperature is higher than 300 °C. However, water is not fully consumed at that temperature, its concentration starts rising with the increase of temperature from that temperature onwards because H_2O is a product of the r-WGS reaction. The reaction starts at ~200 °C, indicated by the increase of CO. At 300 °C, the fuel conversion equals ~100%, however, the energy ratio in Figure 3.6 is 1.184, higher than the theoretical energy ratio in reaction R3.7 (1.165). This is due to the presence of CO in the product, which has a higher mole-based energy than H_2. Similar behavior is observed for iso-octane, the energy ratio at 400 °C is 1.213, higher than the energy ratio with a mixture of H_2 and CO_2 in reaction R3.8, 1.183. Again, remember that the temperature from this simulation does not correspond with the real temperature. For a finite volume reactor, higher temperatures will be needed.

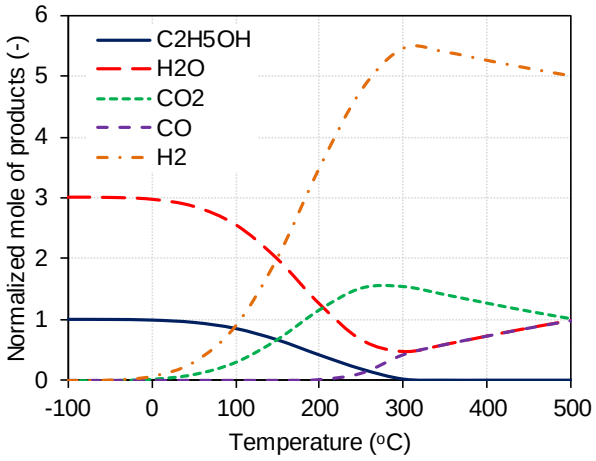

Figure 3.7: The normalized moles of products for ethanol reforming as a function of temperature.

The temperature increases depends on the catalyst material, space velocity, and the pressure drop over that catalyst. In order to have an idea about the temperature increase, a simulation using ASPEN PLUS was performed with the inlet taken from experiments [109]. Mixtures of CH_3OH, H_2O and helium (He) with two reactant concentrations were simulated. These mixtures have the same water to methanol molar ratio of 1.5. The first mixture contains 87.5% He, and the second mixture contains 20% He [109]. Helium is used as a diluted gas. As explained previously, the fuel starts to reform into H_2-rich gas at a very low temperature in

the Gibbs free energy simulation. A temperature increase of 260 °C was used to match the temperature for 50% fuel conversion from the experiment. Figure 3.8 presents the comparison of methanol conversion between experiment [109] and the ASPEN PLUS simulation with this temperature increase. As can be seen, the fuel conversion is higher at the same temperature with a highly diluted mixture (87.5% He). Although the temperature for 50% fuel conversion is matched, the conversion rate in the experiment is more sensitive to a change of temperature.

Also shown in this figure, one value of temperature increase can be used for the two mixtures. The temperature difference to have the same fuel conversion between the two mixtures is predicted well. Therefore, the temperature difference between methanol and ethanol/iso-octane in Figure 3.5 seems correct. If this temperature increase is employed, the required temperature to have 90% fuel conversion for methanol, ethanol and iso-octane is ~350 °C, ~530 °C and ~640 °C, respectively. The range of these values is similar to the temperature range for steam reforming of methanol (~500-600 K), ethanol (~800-1000 K) and gasoline (~1000-1150 K) [105]. Remember that, the required catalyst temperature in practice depends on the reactants (water-to-fuel ratio, dilution), catalyst materials, and space velocity. If that temperature increase is used, the temperature for ethanol and iso-octane to have a higher energy ratio than methanol can be estimated, and equals 510 °C and 610 °C, respectively.

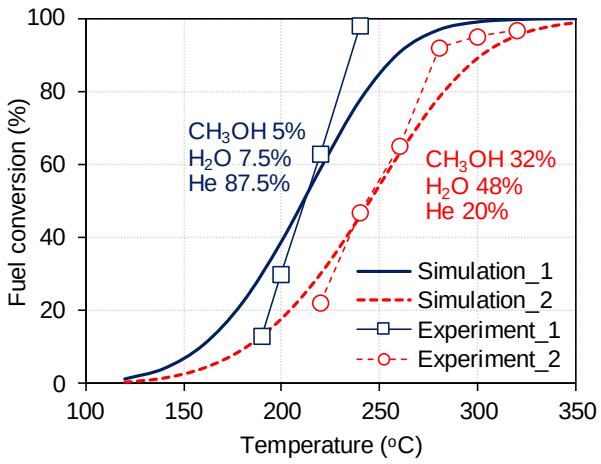

Figure 3.8: Comparison of fuel conversion of methanol steam reforming over Cu-Mn-O metal-foam based catalyst. Simulation: ASPEN PLUS simulation with a temperature increase of 260 °C, experiment: from [109].

Although the simulation using ASPEN PLUS cannot predict the absolute temperature for fuel reforming, the trends with different fuels and different

reactants can be predicted well with this tool. From the simulation results, methanol seems the most suitable fuel for fuel reforming because it requires a much lower reforming temperature. Using ethanol or iso-octane will only have a higher benefit than methanol if the temperature is sufficient for over 80% fuel conversion.

3.3 Fuel reforming research on SI engines

Although partial oxidation is an exothermic process, the presence of H_2 in the products might help stabilization of diluted combustion. The fuel can be reformed through in-cylinder reforming. The cylinder works as a reactor for partial oxidation to produce syngas [110, 111]. The dedicated-exhaust gas recirculation (D-EGR) engine concept has been built [112] based on that principle. One of four cylinders operates with a rich mixture, and the exhaust gas of that cylinder returns back to the intake to mix with the intake air. The EGR ratio is almost fixed at 25%, and the engine can be operated at a higher CR. Because of the rich combustion in the dedicated cylinder, the combustion produces H_2 and CO. The amount of H_2 and CO strongly depends on the enrichment in the dedicated cylinder. Richer combustion generates a higher concentration of H_2 and CO, which supports the combustion in the other cylinders. Shorter combustion duration was observed in those cylinders, leading to a reduction in fuel consumption by enabling diluted combustion. The rich limit of methanol combustion is higher than with gasoline, causing the dedicated cylinder to be able to operate at an equivalence ratio of 2.67 (versus 1.6 for gasoline) [113], so more hydrogen can be produced. The brake thermal efficiency of the D-EGR engine with methanol was shown to improve by 1-3% compared to gasoline.

Steam reforming is an endothermic process, hence this kind of reforming can be used as a thermal recuperation system in SI engines. Recently, Poran et al. have built the first prototype of a direct-injection SI engine with a high-pressure thermal recuperation [114]. Methanol is converted to syngas at high pressure through steam reforming. The product is injected directly in the combustion chamber, allowing the volumetric efficiency of the engine to be maintained. The occurrence of back-fire and pre-ignition can also easily be solved then. The experiments with methanol reformate from the reformer [114] and from compressed gas bottles [115–117] both showed a significant improvement in efficiency (18-39%) and lower emissions (up to 94% in NO_x, 96% in CO, 97% in HC, and 25% in CO_2), albeit compared to the original gasoline engine equipped with carburetor.

Auto-thermal reforming is the combination of partial oxidation and steam

reforming which requires no heat for reforming. A change in the O_2 and H_2O fraction results in a difference in enthalpy of formation. To date, no investigation on the use of auto-thermal reforming of methanol for SI engines was published. A study with iso-octane was done previously with POX and SR combination [92, 118, 119]. To have oxygen in the exhaust, one (of four) cylinder was operated with a lean mixture. The catalyst was located inside the exhaust system of that cylinder. Additional fuel was injected at the end of the expansion stroke, to provide a fuel rich mixture (with oxygen left from the combustion) and feed it into the catalyst during the exhaust stroke. The fuel reacts with lean combustion products (O_2, H_2O and CO_2) over a 2% wt Rh on Al_2O_3 catalyst [118] to form H_2-rich gas. The products then recirculate back to the intake to mix with the air of the other cylinders. For a given engine load and speed, the catalytic EGR-loop can stabilize the combustion with a volumetric equivalent of 45-55% EGR, and the fuel consumption was shown to decrease by 8% compared to the baseline case [92].

Thermal decomposition is a highly endothermic process. During the 1980s, several tests with dissociated/decomposed methanol on SI engines were performed and a large relative improvement in engine efficiency versus gasoline was found [120–122]. However, the enhancement was small (3-7%) if it was compared to the efficiency that could be obtained with an engine operated on pure methanol, which itself is smaller than the change in LHV of dissociated methanol [123]. Work was also done on decomposed methanol at lean conditions, and showed a significant improvement (15-25%) in efficiency compared to neat methanol [124, 125].

The dry reforming (or CO_2 reforming) is the most highly endothermic process to reform methanol into H_2-rich gas. In terms of thermodynamics, using the dry reforming products produces the highest efficiency. Because it requires a very high enthalpy for the formation, this reforming type has not been investigated on engines. Normally, in order to have the thermodynamic benefit from fuel reforming, steam reforming and thermal decomposition are considered. Compared to thermal decomposition, the steam reforming process reacts faster [126] and has less propensity for a coking problem [127]. Based on these criteria, steam reforming is chosen as the topic for detailed investigation (producing H_2-rich gas using engine exhaust heat).

3.4 Selection of reforming concept

A part of the fuel or 100% fuel can be reformed and used in SI engines. Using 100% reformate will have a higher efficiency. However, the liquid fuel is needed

for a fast response under transient conditions, for increasing the volumetric efficiency, and for operating at high load modes [128, 129]. In this study, two reforming concepts were considered and compared: external fuel reforming (EFR) shown in Figure 3.9a and reformed-exhaust gas recirculation (R-EGR) shown in Figure 3.9b. In the first concept, a small amount of fuel (methanol) is injected into the catalyst which is heated up by the hot exhaust gases through a heat exchanger and reacts with water from another tank to form syngas. For steam reforming, to convert one mole of methanol, one mole of water is needed. Normally the water to methanol molar ratio is controlled to be higher than unity to ensure ~100% fuel conversion, so there is water vapour left in the product after reforming. The wet syngas is then condensed, after which the dry mixture is recirculated to the intake and mixed with the fresh air before entering the combustion chamber. Methanol is also injected directly into the combustion chamber. The molar ratio of methanol to syngas in the chamber is controlled by the mass fraction of methanol which is supplied to the catalyst. The EGR system is added to dilute the combustion.

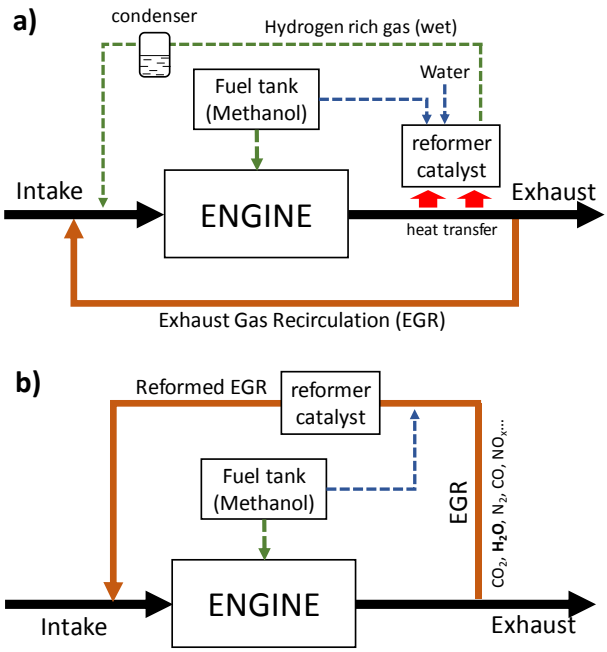

Figure 3.9: Schematic diagram of two reforming concepts: (a) external fuel reforming (EFR), and (b) reformed-exhaust gas recirculation (R-EGR).

In the second concept, the water vapour contained in the EGR is utilized to react with fuel (methanol) which is injected and vaporized upstream of the catalyst to produce syngas. The catalyst is installed inside the EGR system. This concept

looks similar to the invention of Turner [130]. However, the EGR system does not comprise an air introduction for the partial oxidation of the fuel. With the absence of oxygen, fuel reacts with water vapour following the steam reforming. Therefore, this concept is preferred for stoichiometric operation. For lean operation, the fraction of O_2 in the exhaust increases and the fraction of H_2O decreases as lambda increases. This results in a more POX reaction. The reforming reaction with the presence of both O_2 and H_2O is presented in R3.9.

$$CH_3OH + xO_2 + (1\text{-}2x)H_2O \xrightarrow{\text{catalyst}} (3\text{-}2x)H_2 + CO_2 \qquad \text{(R3.9)}$$

As is shown clearly, high x causes a decrease in H_2 in the reforming products, thus the energy ratio reduces and laminar burning velocity decreases. The fuel also can be reacted with CO_2 in the exhaust to follow a dry reforming process. However, as mentioned previously, dry reforming is normally neglected due to a high requirement in catalyst temperature. The amount of methanol is controlled on the basis of the water vapour concentration in the exhaust gas (or the EGR rate) to achieve the desired water-to-methanol molar ratio. The mixture of syngas, excess water vapour and inert gases (CO_2 and N_2) in the combustion products then follows the EGR path to recirculate back to the intake manifold. In this concept, an extra water tank is not needed. This concept was investigated with other fuels such as bio-ethanol, gasoline, dimethyl ether, diesel, biodiesel and gas-to-liquid fuel [131–141].

Comparing these two reforming concepts, the second one looks more “simple”: no additional water tank, no syngas condenser, and no heat exchanger. Because the catalyst contacts the hot exhaust gases directly, it provides a better heat transfer. Furthermore, the reactants (CH_3OH and H_2O) will be diluted by other combustion products such as N_2, CO_2, etc., and the fuel conversion is higher (if the space velocity is maintained). The drawback of the R-EGR concept is the increase of pressure drop in the EGR system. A back pressure valve in the exhaust might be needed to increase the EGR ratio. Additionally, direct contact with exhaust gas might lead to a deposit of particle matter on the catalyst surface (on DISI engines). Methanol has low PMI, so the PM emission can be ignored. Therefore, the R-EGR concept was selected to evaluate the potential of increased efficiency for methanol fueled SI engines.

3.5 Selection of metal-based catalyst

As shown in Figure 3.4, the steam reforming products can contain CO. The CO selectivity is used to evaluate the steam reforming performance. It is the volume

fraction of CO to the sum of CO and CO_2. A different catalyst material leads to a change in the CO selectivity. Reaction R3.10 presents the overall steam reforming reaction of one mole of methanol. If the CO selectivity (X_{CO}) is high, this means methanol is not fully reformed by the steam.

$$CH_3OH + \left(1\text{-}X_{CO}\right)H_2O \longrightarrow X_{CO}CO + \left(1\text{-}X_{CO}\right)CO_2 + \left(3\text{-}X_{CO}\right)H_2 \qquad \text{(R3.10)}$$

Figure 3.10 shows the influence of CO selectivity on the molar fraction of reforming products and its lower heating value. The reaction changes from steam reforming to thermal decomposition when the CO selectivity increases from 0% to 100%. In terms of energy, the product with a larger CO selectivity has higher energy, which would be better for engine performance. The lower heating value increases from ~14 MJ/kg to ~24 MJ/kg. However, in terms of catalyst durability, it is not good due to the absence of water vapour in the reaction, leading to coking problems that can deactivate the catalyst [127].

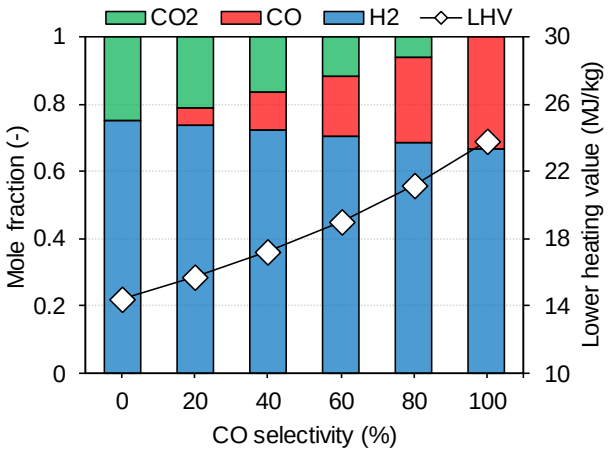

Figure 3.10: The molar fraction of methanol reforming products and their lower heating value as a function of CO selectivity.

Higher CO means higher possibility for catalyst deactivation. CO can be converted to CO_2 through the water-gas shift (WGS) reaction ($CO + H_2O \longrightarrow CO_2 + H_2$). To prevent coke formation, the selected material should have a high WGS reaction rate. Figure 3.11 compares the relative rate of the WGS reaction for several metals. As can be seen, copper (Cu) has the highest rate for the WGS reaction. Although Cu has some drawbacks including deactivation, pyrophoricity, and high-temperature sintering, it is cheap and has a good thermal conductivity. Group VIII materials such as rhodium (Rh) and platinum (Pt) have a lower WGS reaction rate, which means these metals are more suitable for the thermal decomposition

reaction. These materials were most resistant to coke formation [142]. In term of product energy and durability, Rh and Pt are the two most suitable metals for the catalyst. However, Rh or Pt is very expensive, so the Cu-based catalyst is selected for methanol steam reforming.

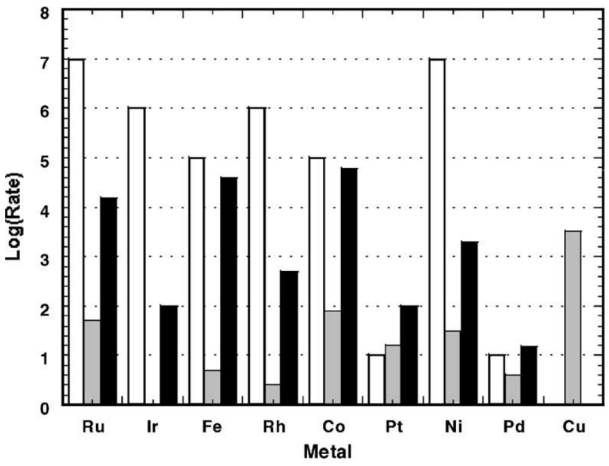

Figure 3.11: Relative rates of C-C bond breaking reaction (white), water-gas shift reaction (grey), and methanation reaction (black) for different catalyst materials [143].

The Cu-Mn-O metal-foam based catalyst was selected for this investigation [109]. Metal foam has high porosity, high specific area (ratio of surface area to volume) and tortuous structure resulting in better mixing as well as enhanced gas-wall interaction [144]. Four catalysts with the same dimension of 10×50×350 mm (H×W×L) were ordered, so the total volume of the catalyst is 4×10×50×350 = 700,000 mm^3, or 0.7 liter.

3.6 Closure

This chapter started with an overview of waste heat recovery systems for internal combustion engines. There are several ways to convert the exhaust energy into different kinds of energy. The conversion to chemical energy by means of thermochemical recuperation, called fuel reforming, was chosen. There are five main types of methanol reforming, and steam reforming was chosen because of high reaction rate, being an endothermic process, and reduced coke formation. Steam reforming of methanol produces a higher energy ratio than ethanol and iso-octane at low temperature. The energy ratio increases as temperature increases

due to the reaction between two products of steam reforming process (H_2 and CO_2) into CO and H_2O through the reversed-water gas shift reaction.

Two reforming concepts were compared, and the reformed-exhaust gas recirculation (R-EGR) concept was selected. The metal-based catalyst was also chosen, copper. Cu-Mn-O metal-foam based catalyst was ordered for the next studies. In the following chapter, the theoretical engine efficiency will be calculated with the R-EGR concept. The laminar burning velocity and the reaction front properties will be analyzed with products from this catalyst. Later on, the chemical kinetic mechanism for this catalyst will be developed and implemented into a GT-Power engine model to simulate the whole engine.

4

Theoretical efficiency with fuel reforming

4.1 Introduction

As explained in the previous Chapter, the R-EGR concept was selected to produce H_2-rich gas on-board for supporting diluted combustion. The potential of this concept for methanol will be studied theoretically in this chapter. The Otto cycle efficiency of methanol fueled R-EGR engines will be calculated. The change of combustion duration due to the addition of syngas is not considered here. The effect of syngas addition on the laminar burning velocity of methanol-air mixtures will be presented in the next Chapter. In this Chapter, only engine thermodynamics will be analyzed, i.e. the comparison was performed at the same combustion duration. This chapter includes figures and tables which were published previously in the Fuel journal [93]. The author Duc-Khanh Nguyen did all calculations and simulations, wrote the paper and prepared all figures and tables. The authors Louis Sileghem and Sebastian Verhelst contributed corrections, proof-reading and discussions.

4.2 Otto cycle efficiency

4.2.1 Methodology

The R-EGR concept is complex, thus it requires a significant effort to predict the system efficiency. In a first step, we use the simplification of an Otto cycle as an approximation, to get an initial idea of the impact of fuel reforming on engine efficiency. This efficiency is computed using the extracted work and the fuel energy, similar to the methodology of Szybist et al. [22]. Figure 4.1 shows the pressure-volume diagram of the Otto cycle. The area enclosed by the graph is used to calculate the Otto mean effective pressure (Otto MEP).

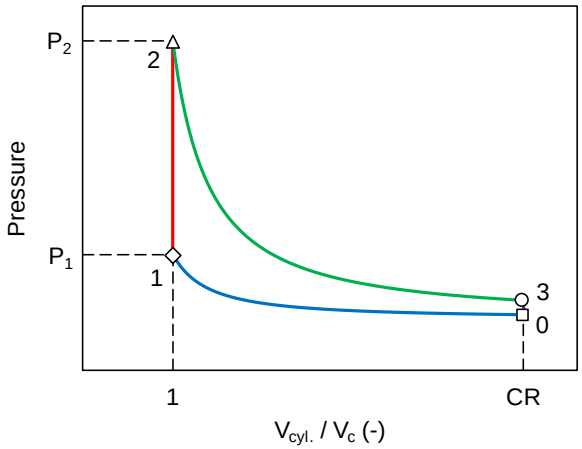

Figure 4.1: The pressure-volume diagram of the Otto cycle.

The Otto cycle was calculated with the initial pressure P_0 of 1 bar, and the initial temperature T_0 of 343 K. The compression ratio (CR) and the expansion ratio was 9:1. That CR is lower than the geometric CR of current production SI engines; however, with a late intake valve closure (IVC) as used in a number of high-efficiency concepts, the effective compression ratio is comparable to 9:1. In practice, fuel evaporates during the intake and the compression strokes, with the evaporation rate being strongly dependent on the in-cylinder condition. For a simplification of this calculation, the influence of heat of vaporization (HoV) was ignored. The liquid fuel was assumed to be fully vaporized at a constant temperature before compression. A difference in the specific heat ratio (γ) causes a change in the post-compression state (P_1 and T_1). The γ for the compression and the expansion process was calculated at 800 K and 2000 K, respectively. Variation in the γ during the compression and expansion was neglected. After

an isochoric combustion, the pressure and the temperature rise to P_2 and T_2. The reactant is burned stoichiometrically, completed combustion products include carbon dioxide CO_2, water vapour H_2O, and nitrogen N_2. The dissociation of completed combustion products at high temperatures to produce CO and H_2 [22] was ignored. The combustion product then expands to a lower pressure and temperature, P_3 and T_3. The cycle work can then be calculated.

In the R-EGR cases, a portion of fuel is injected into the EGR loop. The fuel can react with water vapour (steam reforming) or with carbon dioxide (dry reforming) or split (thermal decomposition) to produce H_2-rich gas. The required energy for thermal decomposition and especially for dry reforming is much higher than for steam reforming. Therefore, the reforming follows the steam reforming reaction which has a minimum-energy barrier to produce H_2 and CO_2. The combustion reaction can be written as below:

$$\mathrm{CH_3OH} + d\left(\mathrm{O_2} + 3.76\mathrm{N_2}\right) + \left(Y_{res} + Y_{EGR}\right)\left(a\mathrm{CO_2} + b\mathrm{H_2O} + c\mathrm{N_2}\right)$$

$$- X_{fuel}\mathrm{H_2O} + X_{fuel}\mathrm{CO_2} + 3X_{fuel}\mathrm{H_2} \longrightarrow a\mathrm{CO_2} + b\mathrm{H_2O} + c\mathrm{N_2} \qquad \text{(R4.1)}$$

where Y_{res} is the residual mass fraction in the combustion chamber (internal EGR), Y_{EGR} is the external EGR mass fraction, and X_{fuel} is the normalized amount of reformed fuel to the unconverted fuel. Coefficients a, b, c and d were calculated as a function of Y_{res}, Y_{EGR} and X_{fuel} to balance the reaction, see Appendix B. The number of moles in reaction R4.1 was normalized to one mole of CH_3OH. X_{fuel} mole of methanol was injected to the catalyst, it consumed X_{fuel} mole water, produced X_{fuel} mole CO_2 and $3X_{fuel}$ mole H_2. The reforming fraction (fraction of the reformed fuel to the total fuel) can be calculated as below

$$Y_{reforming} = \frac{X_{fuel}}{1 + X_{fuel}} * 100(\%) \qquad (4.1)$$

In this study, Y_{res} was set at 0.04 (4% mass), Y_{EGR} ranged from 0 to 0.5 (no EGR to EGR 50% by mass, with steps of 10%), and X_{fuel} varied from 0 to 1 (no reforming to reforming fraction of 50%). The purpose of fuel reforming is to support the combustion of liquid fuel, so the fuel fraction for the reforming is less than or equal to the fuel injected directly in the combustion chamber. The reforming started at EGR ratio $\geqslant$ 20%, which is when the water vapour in the EGR loop is sufficient for steam reforming.

4.2.2 Results

Figure 4.2 presents the post-combustion pressure versus post-combustion temperature for different EGR ratios and different reforming fractions. The upper line shows the relationship between P_2 and T_2 of conventional EGR. At high EGR levels, a significant decline in P_2 and T_2 can be seen. Due to the replacement by the burned gases, the amount of air and fuel decrease because of the maintained initial pressure P_0. The reactants thus have less energy than the non-EGR case, leading to a reduction in P_2 and T_2. Three lines for reforming fractions of 13%, 33% and 50% are also plotted in this figure. Compared to the conventional EGR, the R-EGR cases have a lower pressure and a higher temperature.

Thanks to the presence of H_2, the combustion temperature increases, whereas a reduction in molar expansion ratio (MER) of the reformates and a lower reactant energy (maintained P_0) results in a decline of the post-combustion pressure. In the R-EGR cases, the decrease of the inlet energy is likely due to the reduction of fuel and air provided by a molar expansion of the reforming products. In a constant volume combustion chamber and constant temperature, if the heat release is neglected, the post-combustion pressure equals MER (in bar) if the initial pressure is 1 bar. Thus the fuel which has MER greater than unity is able to produce more work. MER of hydrogen is around 0.852, much lower than methanol, ~1.061 (see Table 1.1), therefore the combustion of hydrogen produces a lower work than is indicated by its LHV. As reforming fraction increases, pressure decreases and temperature enhances.

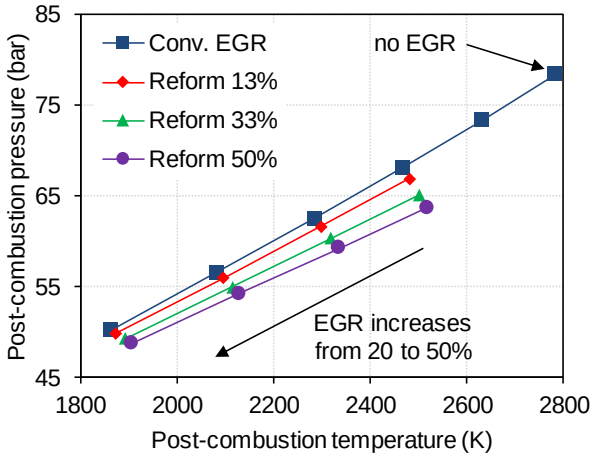

Figure 4.2: Post-combustion pressure and temperature at different EGR ratios and different reforming fractions.

The lower post-combustion pressure points to the cycle work of the R-EGR cases potentially being lower than with conventional EGR. This is confirmed in Figure 4.3 which compares conventional EGR with R-EGR in terms of normalized cycle work plotted against the EGR ratio. In the case of conventional EGR (reforming fraction of 0%), increased EGR level reduces the cycle work. Note that the heat transfer is not taken into account, if it is, the cycle work further decreases. To maintain the work, the intake pressure should be increased in the R-EGR cases. Thus, the pumping loss would decrease. In a naturally aspirated SI engine, the intake pressure is limited to 1 bar. Therefore, the engine output with the R-EGR system will be low. The comparison between the non-diluted case, the conventional EGR and the R-EGR should be done at low loads. At those loads, the pumping work of the non-EGR case would be high, so an improvement in BTE with the R-EGR concept might be seen.

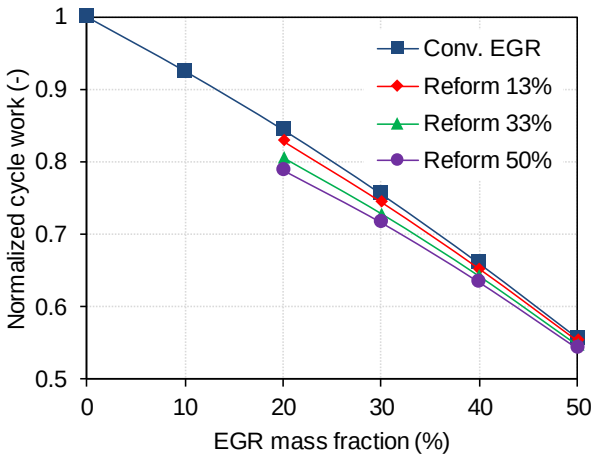

Figure 4.3: Normalized cycle work at different reforming fractions versus EGR ratio.

Figure 4.4 illustrates the Otto cycle efficiency, plotted as a function of the reforming fraction. It can be seen that the efficiency improves significantly with the rise of EGR ratio (at reforming fraction of 0%). Although the cycle work decreases (Figure 4.3), a significant reduction in inlet energy due to the displacement effect of the burned gases is the main reason for that efficiency improvement. The influence of the reforming fraction is presented at EGR ratio $\geqslant$ 20%. As the reforming fraction increases, Otto cycle efficiency improves slightly compared to the conventional EGR. It can be explained by a small enhancement in exergy of the methanol steam reforming product compared to methanol, see Table 4.1. The LHV has to compensate for the reduction of MER, thus the increase in efficiency is not as high as the increase in the LHV. At higher EGR ratios, the increase is more obvious.

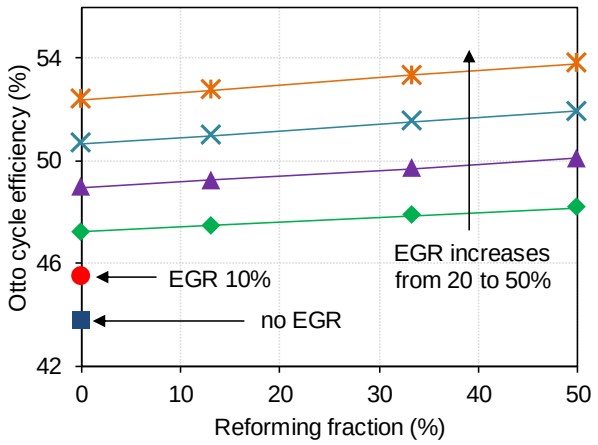

Figure 4.4: Influence of reforming fraction on the Otto cycle efficiency at different EGR ratios.

Figure 4.5 demonstrates the relationship between the Otto cycle efficiency and the MER. In the case of conventional EGR (square symbols), the MER decreases as the dilution level rises. This is due to the MER of the combustion products being 1, lower than methanol. Different reforming fractions (13%, 33% and 50%) are also plotted in this Figure. In the cases of reformed fractions 33% (triangular symbols) and 50% (circular symbols), the MER increases thanks to the dilution. H_2 has a MER less than unity (~0.85), thus a mixture with high H_2 concentration has MER less than 1. Therefore, the MER in the cases of reformed fraction of 33% and 50% increases as EGR ratio increases.

A smaller change in MER with fuel reforming can be seen at high EGR ratios. For example, the MER decreases from 1.046 to 0.958 at EGR ratio of 20% and from 1.027 to 0.974 at EGR ratio of 50%. This explains a visible improvement in the Otto cycle efficiency at 50% EGR (see Figure 4.4). There is a strong correlation between the Otto cycle efficiency and the MER at a certain reforming fraction. The MER approaches unity with increasing EGR ratio (see the linear trend lines for different reforming fractions). At MER of 1 (EGR ratio of 100%), the end of each trend line shows the theoretical efficiency that can be achieved with a certain reforming fraction. The absolute difference in the efficiency between reforming 50% and conventional EGR cases is ~3%. In practice, the engine is obviously not able to operate at that EGR ratio, meaning the improvement in engine efficiency with the R-EGR concept is limited. The change in the MER explained the small improvement in engine efficiency with the dissociated methanol compared to the neat methanol at λ close to 1 [123]. A bigger difference in the efficiency can be

seen at a highly diluted condition (lean burn or EGR dilution), as in [124, 125].

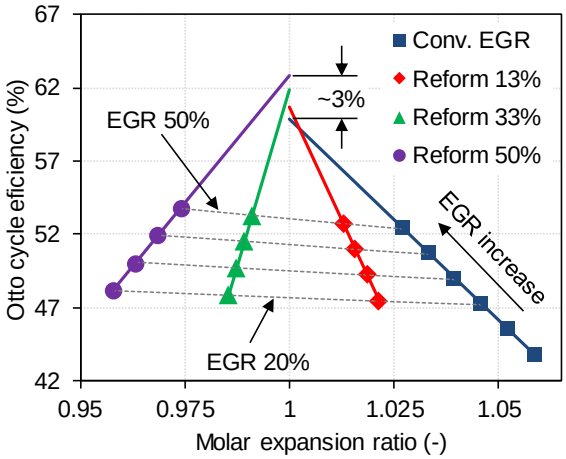

Figure 4.5: The relationship between molar expansion ratio and the Otto cycle efficiency.

The Otto cycle efficiency calculation indicated the efficiency rises only very slightly with fuel reforming at equal EGR fractions due to the limited change in exergy of the reformate. A bigger increase could come from enhanced EGR tolerance due to an improved combustion stability of the reformed products which will be investigated in section 4.4.2. The Otto cycle however only considers the thermodynamic part, other impacts such as heat transfer, pumping work, friction work, combustion duration, etc. are not taken into account. A simple estimation of these losses will be performed and the results will be presented in the following section.

4.3 Analysis of energy losses

4.3.1 Methodology

In the previous section, the idealized Otto cycle was employed. That cycle does not take the effect of combustion duration, heat transfer, and friction into account. In this part, these idealizations were removed one-by-one to estimate their effect on the efficiency. Some engine parameters are needed to calculate these impacts. The specifications of a production engine, a Volvo T3, was employed. More information about the engine can be found in section 2.2.1. At the standard valve timing, the effective compression ratio and the effective expansion ratio was 8.8

and 9.9, respectively (see Table 2.1). The ideal gas law was employed to calculate the intake mass. The impact of HoV was neglected again, and all calculations were performed at T_0 of 343 K.

In the theoretical Otto cycle, the combustion duration (CD) is 0 degree crank angle (CAD). The impact of combustion duration of 10 and 20 CAD were first investigated. For simplicity, the combustion duration is defined here as the duration to reach the maximum pressure from the TDC. It means the pressure reaches its peak at 10 CAD and 20 CAD after TDC. Although the total combustion duration (CA0-100) of 10 CAD or 20 CAD is too short, a peak pressure location between 10 CAD to 20 CAD after firing top dead center ($aTDC_f$) is representative for conventional SI engines. The optimum combustion phasing (CA50) was not considered in this section. Figure 4.6a presents an example of in-cylinder pressure profiles for different CD. The peak pressure is the adiabatic combustion pressure for the pre-combustion pressure and temperature at a crank angle of 10 CAD and 20 CAD $aTDC_f$. At 10 CAD and 20 CAD $aTDC_f$, the unburned gas pressure is lower than at TDC, leading to a reduction in post-combustion pressure. It was assumed that the pressure rises linearly as a function of the cylinder volume from the post-compression pressure at TDC (P_1) to the post-combustion pressure at 10 CAD or 20 CAD $aTDC_f$ (P_2). Figure 4.6b shows the cylinder pressure versus normalized volume ratio. As can be seen, a linear increase of cylinder pressure from P_1 to P_2 was presented.

The compression starts at the volume ratio of 8.8, which represents the effective CR. Then, the product expands to a higher volume ratio, 9.9 (effective expansion ratio). As can be seen, there is a small reduction in the cycle work with the CD of 10 CAD, and the decline in the cycle work is higher with a longer CD. The input energy is maintained, so this means there is a reduction in the Otto efficiency as CD increases.

Next, the influence of heat transfer is studied. The heat loss can be estimated as follows

$$Q = Ah(T_{gas} - T_{wall}) \tag{4.2}$$

where A is the heat transfer area, h is the heat transfer coefficient, T_{gas} is the in-cylinder gas temperature, and T_{wall} is the wall temperature. According to Broekaert et al. [145], a heat transfer model based on the Pohlhausen equation can predict the heat loss accurately. That equation includes the Nusselt number, the Reynolds number and the Prandtl number. Therefore, the heat transfer coefficient is a function of characteristic length, characteristic velocity, thermal

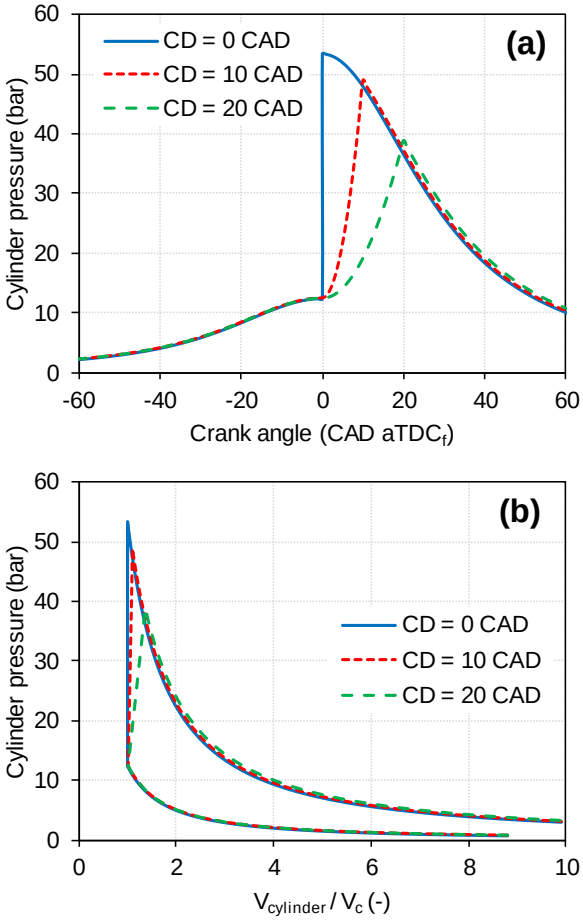

Figure 4.6: Impacts of combustion duration on the in-cylinder pressure. (a) Pressure-degree crank angle diagram, (b) Pressure-compression ratio diagram,

conductivity, dynamic viscosity and density of the combustion gases. In this work, the heat transfer coefficient from Hohenberg's model [146] was employed due to its simplicity. Therefore, the heat transfer is related as follows

$$Q \sim AP^{0.8}T_{gas}^{-0.4}V^{-0.06}(T_{gas} - T_{wall}) \tag{4.3}$$

where P is the cylinder pressure, and V is volume of the combustion chamber. The wall temperature was calculated as a function of Otto MEP instead of IMEP (see equation 2.2). Because the Otto MEP is greater, so the calculated T_{wall} is higher than the wall temperature which is predicted with IMEP. Based on equation 4.3, the relative change of Q against the baseline case (P_0 of 0.6 bar, combustion duration of 0 CAD, no EGR, and no reforming) can be calculated. In the baseline case, the relative heat transfer was assumed to be 15% of the total fuel energy [147, 148]. Therefore, the heat loss in another cases can be estimated.

For simplification, the relative change of Q is based on the relative change of Q_{max}. The heat transfer rate reaches its peak at the end of combustion, i.e. Q_{max} occurs at 0, 10, and 20 CAD $aTDC_f$. Because the combustion efficiency equals 100%, the burned gas temperatures at these crank angles (T_2) were used for the calculation. The piston and cylinder head were assumed to be flat (pan cake combustion chamber) to calculate A and V in equation 4.3. With a longer combustion duration, A and V increase, while P and T_{gas} decrease. A test matrix was computed for the conventional EGR case, varying P_0 (from 0.6 bar to 1.4 bar, steps of 0.2 bar), combustion duration (from 0 CAD to 20 CAD, steps of 10 CAD), and EGR ratio (no EGR, EGR ratio of 20, 30 and 40%). For the R-EGR case, the reforming fraction was fixed at 20%, and the EGR ratio ranged from 20% to 40% with steps of 10%. Therefore, there are 5×3×4=60 data points for the EGR cases (including the baseline) and 5×3×3=45 data points for the R-EGR cases. The relative heat transfer and Otto MEP were calculated for the resulting 105 points, and the relationship between these parameters was plotted in Figure 4.7. The absolute heat transfer increases; however, the relative heat transfer decreases as load increases in both cases [149]. As can be seen, the R-EGR case has higher relative heat loss due to the increase in the post-combustion temperature.

The impact of friction was estimated by evaluating the friction mean effective pressure (FMEP) following the Chen and Flynn expression [48], see equation 1.11. Engine speed is set at 1500 rpm, giving a mean piston speed of 4.07 m/s. The P_{max} from the Otto cycle (without heat transfer) was used; therefore, the calculated FMEP is higher than in practice. FMEP decreases as the combustion duration increases.

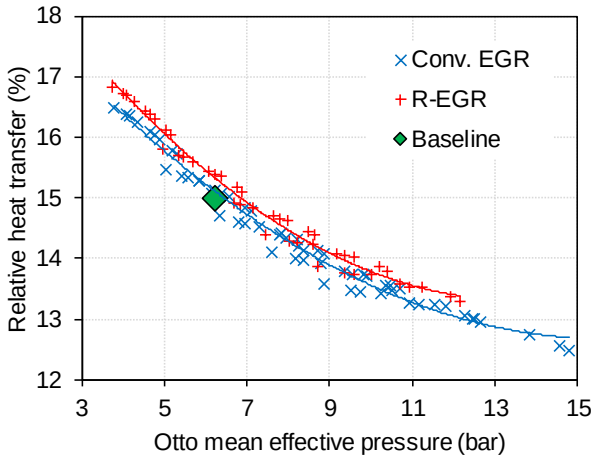

Figure 4.7: The relative heat transfer as a function of the Otto MEP.

The last key loss is the pumping work. In the Otto cycle, the pumping mean effective pressure (PMEP) equals the difference in the intake and exhaust pressures. Due to the lack of exhaust pressure, the impact of PMEP is ignored, thus the gross BTE will be used to present the efficiency of the engine.

4.3.2 Results

Figure 4.8 shows the efficiency losses as functions of EGR ratio. The uppermost solid line represents the Otto cycle efficiency, without heat losses (adiabatic case). The efficiency increases as EGR ratio improves. Lower efficiency lines result from adding losses such as combustion duration (20 CAD duration), heat transfer, and friction losses. The second line shows the Otto efficiency with a combustion duration of 20 CAD. The third line presents the gross indicated thermal efficiency (ITE), i.e. accounting for heat losses, with the same combustion duration as in the second line. The pumping loss is neglected, so the lowest line, which includes frictional losses, represents the gross BTE curve. The results of R-EGR cases with the reforming fraction of 20 % are also added in this Figure (dashed lines with symbols), with the EGR ratio ranging from 20 to 40%.

Figure 4.8a illustrates the efficiency with a constant initial pressure, P_0 of 1 bar. After increasing the combustion duration from 0 CAD to 20 CAD, the absolute efficiency drops by ~3-5%. If the heat loss is taken into account, the efficiency significantly decreases to the gross ITE. Before adding the heat loss, the efficiency of the R-EGR case is a bit higher than the conventional EGR. However, there is

almost no difference in the gross ITE between the two cases. The improvement in the Otto cycle efficiency is transferred to the heat loss. After adding the friction loss, the efficiency in the R-EGR cases is slightly lower than the conventional EGR because of the increase in the relative friction loss. Although the post-combustion pressure is lower than the EGR cases (see Figure 4.2), the relative friction loss increases because of a reduction in inlet energy for the R-EGR cases. In both cases, the relative friction energy increases as the EGR ratio increases.

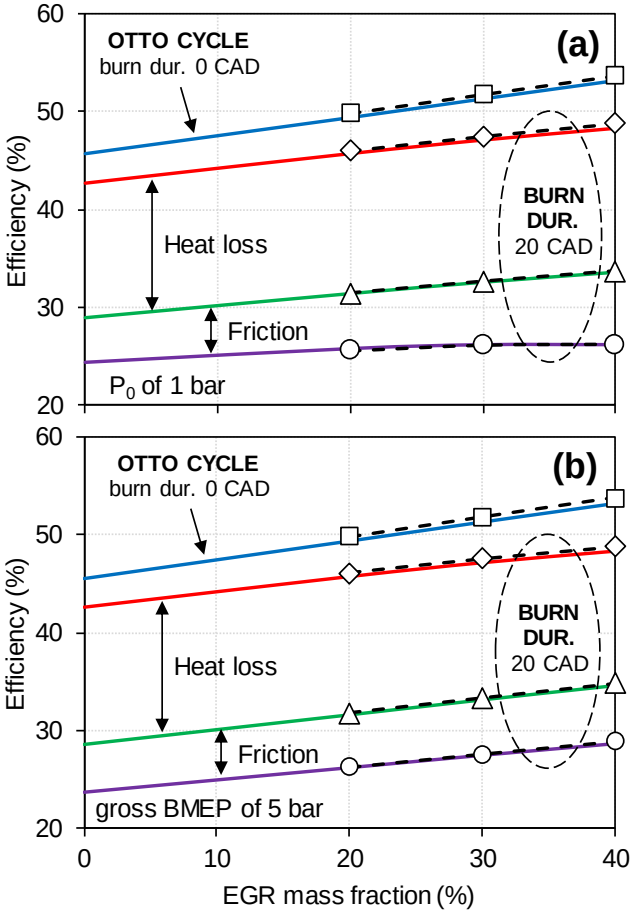

Figure 4.8: Key efficiency losses as a function of EGR ratio. Solid lines: conventional EGR, dashed lines with symbols: R-EGR with reforming fraction of 20%. (a) at P_0 of 1 bar, (b) at gross BMEP of 5 bar.

Figure 4.8b shows the efficiency losses at a constant gross BMEP of 5 bar. The initial pressure is now controlled to maintain the gross BMEP of 5 bar for different EGR ratios and combustion duration. The peak pressure (P_2) increases and the

maximum temperature (T_2) decreases as EGR ratio increases. In the conventional EGR cases (combustion duration of 20 CAD), the relative heat transfer slightly decreases when the EGR ratio increases from 20% to 40%. The reduction in relative heat transfer is more obvious if a longer combustion duration was applied for a highly EGR diluted case. Due to the increase of peak pressure, the friction work increases slightly. After adding these losses, the gross ITE and gross BTE as a function of EGR ratio were presented in Figure 4.8b.

Similar to the analysis at same initial pressure P_0 (Figure 4.8a), the difference in the gross ITE and the gross BTE is almost trivial for the two types of EGR. The absolute difference between the conventional EGR and the R-EGR in the gross BTE is around 0.1 to 0.2%. Because the gross BMEP is identical, the exhaust pressure can be assumed as similar between the two cases. Therefore, the absolute difference in PMEP equals the absolute difference in P_0. In the R-EGR case, P_0 increases to maintain the gross BMEP. The relative improvement by reducing PMEP can thus be calculated. Together with the difference in the gross BMEP, the absolute increase in the BTE can then be estimated.

Figure 4.9 shows the absolute efficiency improvement (in percentage point) in the predicted BTE, the gross ITE and the Otto cycle efficiency as functions of EGR ratio at gross BMEPs of 5 bar and 7 bar. At higher load, the absolute enhancement is higher; however, the relative improvement is lower. As can be seen, the difference in the gross ITE is less than the predicted BTE due to the contribution of PMEP. The absolute difference from the Otto cycle efficiency calculation and the predicted BTE is comparable, the maximum absolute difference between the two efficiencies is about 0.1%. The comparison in the predicted BTE is done at the same combustion duration. With a faster LBV of syngas (see Chapter 5), a shorter combustion duration is expected in the R-EGR cases. The absolute gain in BTE would then be closer to the change in the Otto cycle efficiency. It thus seems that the Otto cycle efficiency can be used to predict the absolute improvement in BTE between the two cases.

The calculations described in this part help to predict the trend of engine efficiency with the R-EGR concept. However, they are not able to predict the real efficiency. A more complete picture can be obtained by using a gas-dynamic engine code to evaluate the potential of fuel reforming for increased efficiency, which will be presented in Chapter 7.

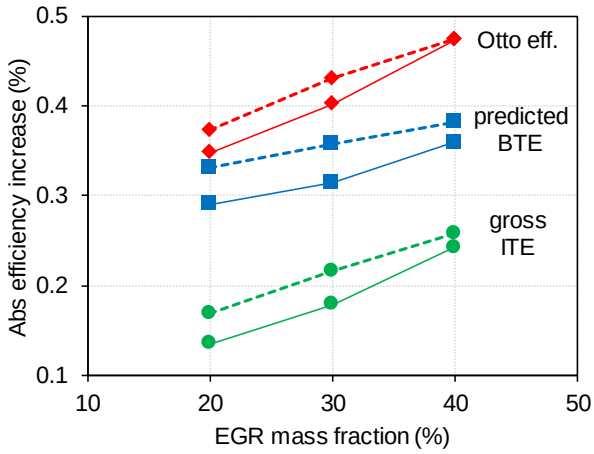

Figure 4.9: The absolute difference of the Otto cycle efficiency, the gross ITE and the predicted BTE between the R-EGR and the conventional EGR cases. Solid lines: gross BMEP of 5 bar; dashed lines: gross BMEP of 7 bar.

4.4 Fuel effects

Methanol is the most promising e-fuel and it is easy to reform. However, only a small increase in reformate exergy results in a limited relative increase in engine efficiency. Fuels which have higher exergy increase in the reforming products such as ethanol and iso-octane (gasoline surrogate) seem to have more potential. Chakravarthy et al. [150] analyzed the fundamental thermodynamics of thermochemical recuperation for a range of fuels. They concluded that the relative improvement of the cycle work of methanol reforming is less than ethanol and iso-octane at the same reforming fraction, ~95%. However, the absolute efficiency of the system and the difficulty of fuel reforming were not considered in that research. This section will analyze the theoretical efficiency with the R-EGR engine concept for three fuels (methanol, ethanol, and iso-octane). The comparison was performed at the same degree of reforming first. A fuel conversion of 100% was employed for all fuels to see the impact of reformate exergy on the efficiency improvement. Later on, the comparison at the same combustion stability limit and the same catalyst temperature will be compared.

4.4.1 Comparison with the same degree of reforming, 100%

This section focuses on the maximum efficiency of the R-EGR concept that can be achieved for different fuels. Table 4.1 shows the theoretical reforming reactions of three fuels with the enthalpy of formation, the LHV increase and the exergy increase of the reforming products. Again, similar to the calculation in Chapter 3, the enthalpy of formation here was calculated with the fuel and the water in the gas phase, the required enthalpy for vaporization was neglected.

Table 4.1: Fuel reforming reactions, enthalpy of formation, LHV and exergy gain

Reaction	Δh_f (kJ/mol)	LHV gain	Exergy gain	Name
$CH_3OH+CO_2 \leftrightarrow 2CO+H_2+H_2O$	+131	+26%	+9.3%	MeOH-Dry
$CH_3OH+H_2O \leftrightarrow CO_2+3H_2$	+49	+13%	+1%	Methanol
$C_2H_5OH+CO_2 \leftrightarrow 3CO+3H_2$	+297	+27%	+11%	EtOH-Dry
$C_2H_5OH+H_2O \leftrightarrow 2CO+4H_2$	+256	+23.5%	+8.8%	EtOH-CO
$C_2H_5OH+3H_2O \leftrightarrow 2CO_2+6H_2$	+173	+16.5%	+4.25%	EtOH-CO2
$C_8H_{18}+8CO_2 \leftrightarrow 16CO+9H_2$	+1588	+31.8%	+17.8%	Octane-Dry
$C_8H_{18}+8H_2O \leftrightarrow 8CO+17H_2$	+1259	+25%	+13.2%	Octane-CO
$C_8H_{18}+16H_2O \leftrightarrow 8CO_2+25H_2$	+930	+18.3%	+8.6%	Octane-CO2

The engine exhaust includes H_2O and CO_2 which can react with the fuel to produce syngas through steam reforming or dry reforming. Similar to the previous chapter, the effect of CO_2 on the reforming process was neglected, only steam reforming was considered. There are two possibilities of steam reforming of ethanol and iso-octane, the product can be a mixture of H_2/CO or H_2/CO_2. These reactions were named depending on the input fuel (EtOH stands for ethanol) and the second product (CO or CO_2). To produce a mixture of H_2 and CO_2, less energy is required. This leads to a reduction in LHV and exergy for the reactions which have CO_2 in the reforming products. The combustion reactions for four cases (two for ethanol and two for iso-octane) were calculated, similar to the methanol calculation (reaction R4.1) in the previous part. Less water is required to reform the fuel into CO. Reactions in detail and coefficients can be found in Appendix B. Byproducts like CH_4 were not considered in this research. The reaction between H_2 and CO_2 through the r-WGS reaction was ignored as well. Similar to the work on methanol, the reforming starts at EGR ratio $\geqslant$ 20%. Similar to the previous calculation, the same compression ratio (9:1), initial pressure (1 bar) and initial temperature (343 K) were used.

Figure 4.10a illustrates the Otto cycle efficiency of the R-EGR engine with different fuels as a function of the reforming fraction at 20% EGR. The reforming

fraction is limited in some cases because of the lack of water vapour. As seen in the Table 4.1, to reform one mole of fuel, one mole of water is needed to reform methanol and reform ethanol to H_2/CO mixture (EtOH-CO). Therefore, the reforming fraction in these cases can be increased to 50%. The EtOH-CO2, Octane-CO and Octane-CO2 cases require respectively 3 moles, 8 moles and 16 moles of water to reform one mole of fuel, so the reforming fraction of these three cases are limited.

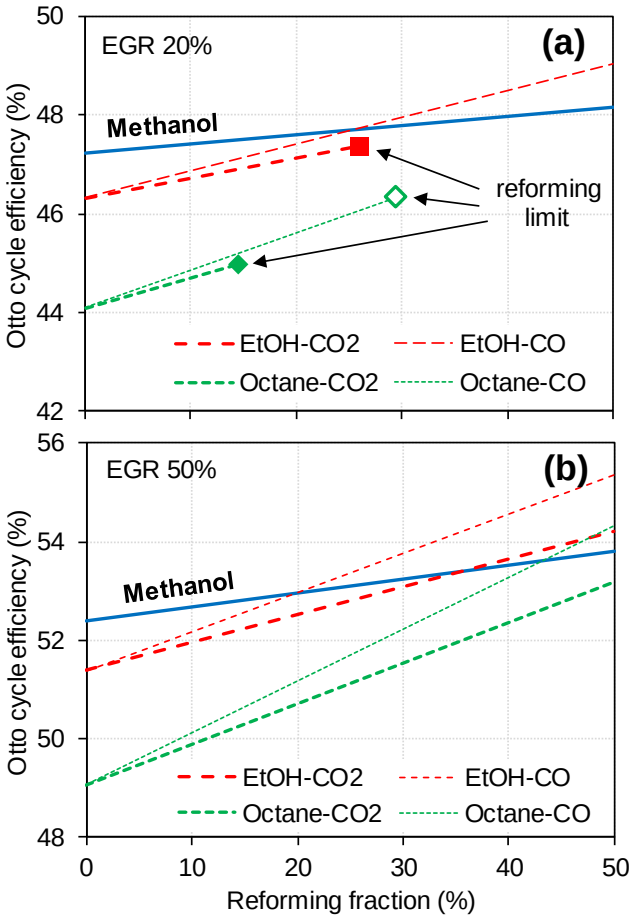

Figure 4.10: The Otto cycle efficiency of methanol, ethanol and iso-octane engines as a function of reforming fraction. (a) Comparison at 20% EGR, (b) comparison at 50% EGR.

Without reforming, the efficiency of methanol is the highest because methanol has the highest exergy-to-energy ratio [22]. However, the efficiency increases slowly with higher reforming fractions. Ethanol and especially iso-octane have a better improvement rate, represented by the slope of the lines. The case which

has a higher exergy increase (see Table 4.1) will have a higher relative efficiency improvement. Because of the water limit at an EGR ratio of 20%, the comparison at 50% EGR was added. At 50% EGR, there is enough water to reform up to 50% ethanol and iso-octane, see Figure 4.10b. Although the original efficiency of ethanol and iso-octane is lower than methanol, the efficiency of EtOH-CO, EtOH-CO2 and Octane-CO becomes higher than methanol at reforming fractions of 50%. This is due to the significant improvement of reformate exergy. Depending on the reforming product (or CO selectivity), ethanol engines could have a higher efficiency than methanol engines if more than 20-35% of the fuel would be fully reformed (at 50% EGR).

4.4.2 Comparison at the same combustion stability limit

In order to compare the maximum efficiency that can be achieved with the R-EGR engine concept, ethanol cases were selected to be compared with methanol. Previously, the comparison was done at the same EGR ratio and the same reforming fraction, i.e. the combustion stability limit was not considered. To determine the combustion stability limit, a constant laminar burning velocity is used [94]. In Chapter 7, the limit for total burned gas mass fraction is 29% (CoV_{imep} of 5%). With 4% residual in this calculation, the external EGR limit is 25%. The laminar burning velocity of the methanol-air flames at 25% EGR at ignition timing (as in Chapter 2) condition (P_1 and T_1 from the Otto cycle) is employed to set the limit of LBV. The LBV is calculated using the CHEM1D code [151] at that condition using Li's mechanism [70], and equals 36 cm/s. For the ethanol cases, the laminar burning velocity was calculated using a different mechanism which was developed by the same group [152]. The LBV limit decreases as a higher value of CoV_{imep} is used, such as 10%. Figure 4.11 shows the EGR limit, defined in this way, of the methanol, EtOH-CO2 and EtOH-CO cases versus the reforming fraction.

For the methanol case, the EGR limit is 25% without reforming, and it increases up to ~35.7% at a reforming fraction of 50%. This is due to a faster LBV of syngas versus methanol (see Chapter 5). As seen in this Figure, at the reforming fraction of 20%, the EGR limit for the R-EGR case is around 29%, close to the external EGR limit estimation (30%) in Chapter 7. Ethanol has a slower LBV compared to methanol [153], thus the dilution limit is lower, around 20% EGR without reforming. At increased reforming fraction, the EGR limit enhances significantly and reaches a higher dilution limit than methanol (~36.7% versus 35.7% for methanol) at the reforming fraction of 50%. The EGR limit in the two ethanol cases overlap each other because the LBV of the syngas is almost

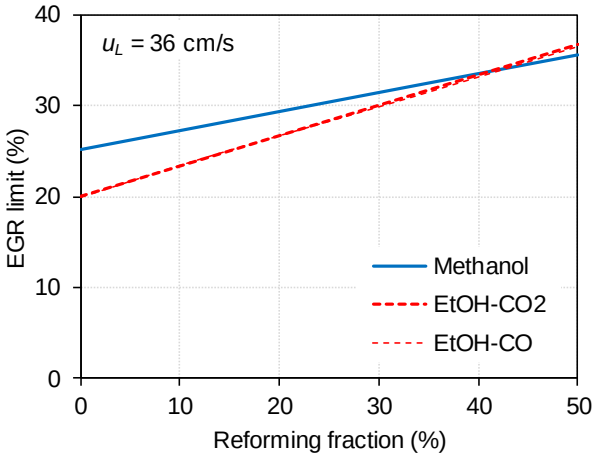

Figure 4.11: The EGR limit of Methanol, EtOH-CO2 and EtOH-CO versus reforming fraction (same laminar burning velocity of 36 cm/s).

independent of the CO selectivity (see Figure 7.5). Ethanol reforming produces approximately double the amount of syngas versus methanol (see Table 4.1), so the syngas/fuel molar ratio in the ethanol cases is higher at the same reforming fraction. This leads to a sharper boost in the dilution limit.

Figure 4.12 shows the maximum Otto cycle efficiency of the methanol, EtOH-CO2 and EtOH-CO cases at the combustion stability limit against the reforming fraction. Although the two ethanol cases have the same dilution limit, the maximum efficiency in the EtOH-CO case is higher due to the increase of LHV with a CO selectivity of 100%. Without reforming and without EGR, there is a small difference in Otto cycle efficiency between methanol and ethanol, 43.77% versus 42.86%. The maximum efficiency increases up to 48.12% for methanol and 46.28% for ethanol without reforming. The efficiency can be improved to 51.12%, 52.57% and 51.45% for methanol, EtOH-CO2 and EtOH-CO respectively if 50% of fuel is fully reformed. Higher efficiency can be observed with ethanol if the catalyst can reform over ~30% and ~40% of fuel to an H_2-CO and H_2-CO_2 mixture, respectively. The efficiency of an R-EGR ethanol engine is somewhere between the two dashed lines, since it depends on the CO selectivity.

4.4.3 Comparison at the same catalyst temperature

As presented in Chapter 3, the steam reforming of methanol takes place at a lower temperature compared to ethanol and iso-octane. The calculation of the Otto

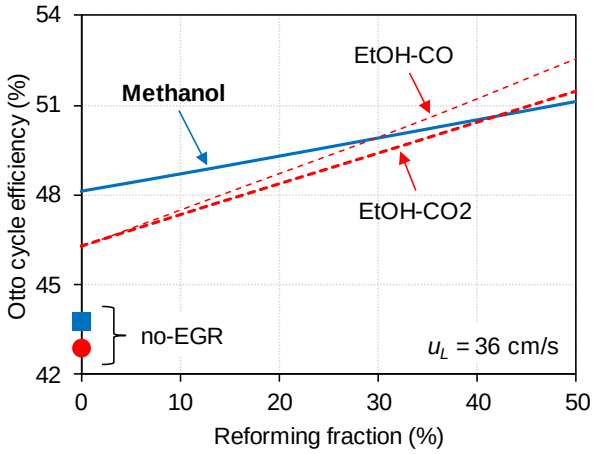

Figure 4.12: The maximum Otto cycle efficiency of Methanol, EtOH-CO2 and EtOH-CO reforming at the same combustion stability limit of 5% CoV_{imep}.

efficiency for these fuels was also performed at the same catalyst temperature and the results are presented in this section. The reforming products were predicted using ASPEN PLUS with the reactant being a mixture of fuel and combustion products at 25% EGR. The mass fraction of fuel for reforming was 20% and 33%, i.e. X_{fuel} equals 0.25 and 0.5, respectively. As can be seen in Figure 4.11, the combustion is stable at this EGR ratio for both methanol and ethanol for a reforming fraction larger than 20%. The calculation of the molar fraction of the combustion products are presented in Appendix B.

The simulation using ASPEN was performed at four reactor temperatures, 100 °C to 400 °C with steps of 100 °C. Because ASPEN PLUS uses an infinite volume reactor, the temperature to achieve the same fuel conversion is much lower than what would be possible in experiments. Therefore, a temperature increase should be used (section 3.2.2). If a temperature increase of 260 °C was employed, the simulation was performed with a catalyst temperature range of 360 °C - 660 °C. The impact of the fuel's HoV on the catalyst temperature was neglected. In practice, the injection of liquid fuel upstream the catalyst causes a decrease in the inlet gas temperature of the catalyst due to the evaporation of the fuel, leading to a reduction in the catalyst temperature.

Figure 4.13 presents the fuel conversion as a function of catalyst temperature for three fuels and two inlet conditions (20% and 33% fuel for reforming) for each fuel. As can be seen, almost 100% methanol was reformed with a catalyst temperature greater than 100 °C for both inlet conditions. Therefore, the impact

of catalyst temperature and inlet conditions on fuel conversion of methanol is invisible with catalyst temperature > 100 °C. Ethanol and iso-octane require a higher temperature for reforming, so the effect of catalyst temperature and inlet conditions on fuel conversion of these two fuels is clearly presented in this figure. Higher catalyst temperature results in an increase in fuel conversion. However, a higher fuel fraction (33%) causes a lower conversion. This can be explained by the reduction of the water/fuel molar ratio and the reduction of diluted gas fraction. The converted fuel mass is calculated by multiplying inlet fuel mass and fuel conversion. Thus a lower fuel conversion in the case of 33% fuel in the EGR system might result in a higher mass of converted fuel.

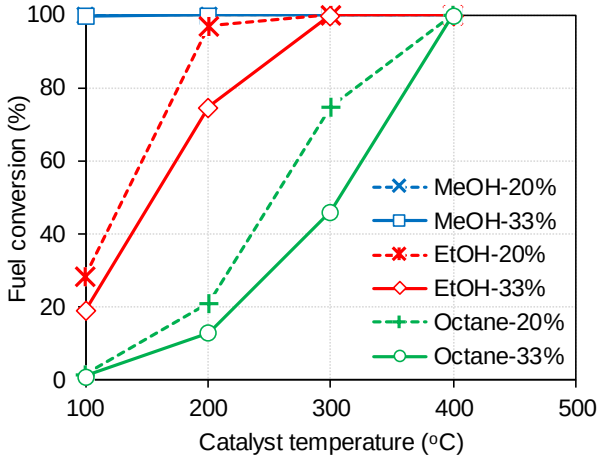

Figure 4.13: Fuel conversion as a function of temperature at EGR ratio of 25%. Dashed lines: 20% fuel in the EGR system, solid lines: 33% fuel in the EGR system.

The molar concentration (excluding N_2) of the R-EGR mixture as a function of catalyst temperature for ethanol and iso-octane are presented in Figures 4.14 and 4.15. The molar fraction of the R-EGR mixture for methanol is not presented because the fuel conversion is ~100%, so the temperature only affects the r-WGS reaction. A slight increase in the concentration of CO and H_2O as well as a small reduction in the molar fraction of H_2 and CO_2 can then be predicted. As can clearly be seen in Figures 4.14 and 4.15, the molar fraction of fuel decreases as temperature increases. The H_2O concentration decreases and then increases due to the reforming of water through the r-WGS reaction at high temperature. The inverse behavior was detected for CO_2 and H_2; they increase and then decrease with increased temperature. For ethanol, the molar fraction of CO_2 reaches a peak at a temperature of 200 °C. At a higher temperature, the r-WGS reaction takes place, so CO_2 in the products becomes a reactant to produce CO. Therefore, CO_2 starts to decrease at the temperature where CO starts to increase. For H_2, the

concentration reaches its peak where almost 100% fuel is reformed. At higher temperatures, H_2 is consumed by the initiation of the r-WGS reaction.

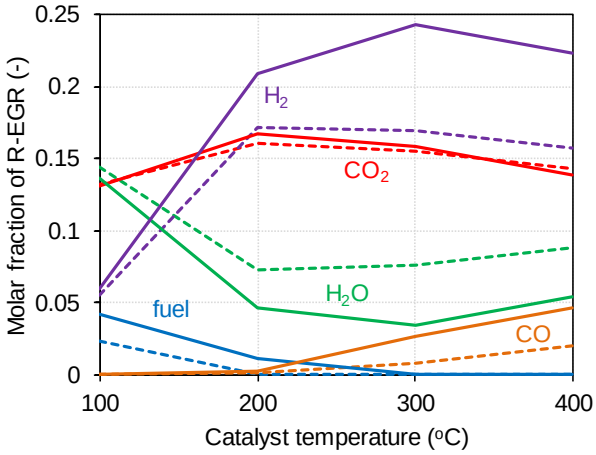

Figure 4.14: The molar fraction of the R-EGR mixture as a function of temperature for ethanol engines. Dashed lines: 20% fuel in the EGR system, solid lines: 33% fuel in the EGR system.

A similar behavior was found for the change of the species' concentration in the R-EGR mixture for iso-octane. However, it shifts to a higher catalyst temperature. The molar concentration of all species (excluding the fuel) is identical between the two cases for a temperature range of 100 - 300 °C. Although the fuel conversion is lower in the case which has 33% fuel in the EGR system, the amount of reformed fuel is the same thanks to a higher inlet fraction of iso-octane. The molar fractions of all species overlap each other for the two cases. At 400 °C, the fuel conversion is the same, so the difference in molar fraction is obvious.

The Otto cycle efficiency at an EGR ratio of 25% for two different fuel masses in the EGR system is presented in Figure 4.16. As can be seen, the efficiency of methanol is higher than ethanol and iso-octane at low temperature. This can be explained by two main reasons: higher exergy-to-energy ratio and higher reformed fuel fraction. The difference in efficiency at low temperature is larger than at high temperature due to the impact of fuel conversion. The efficiency increases as temperature increases for all fuels. The efficiency for methanol increases slightly with increased catalyst temperature. Because the methanol conversion was ~100% at a temperature of 100 °C, the reason for that improvement is the formation of CO in the R-EGR mixture through the r-WGS reaction at high temperature. However, for ethanol and iso-octane, the efficiency increases significantly before reaching a fuel conversion of ~100%. After reaching that fuel conversion, the efficiency

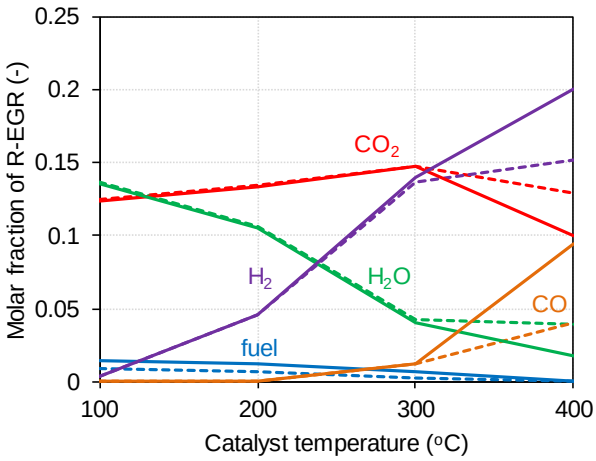

Figure 4.15: The molar fraction of the R-EGR mixture as a function of temperature for octane engines. Dashed lines: 20% fuel in the EGR system, solid lines: 33% fuel in the EGR system.

improvement rate decreases. It can clearly be seen in the change of the efficiency for ethanol as a function of temperature. With 20% fuel in the EGR system, the fuel conversion reaches ~100% at 200 °C (see Figure 4.13). The improvement rate of efficiency for ethanol is higher at temperatures ≤ 200 °C. At a higher temperature (> 200 °C), the improvement rate is very small. Similar behavior is found for the case of 33% fuel in the EGR system, the efficiency improvement rate with temperature > 300 °C is smaller. Because the simulation was limited to a temperature range of 100 - 400 °C, the efficiency improvement with temperatures > 400 °C for iso-octane cannot be seen.

Because the fuel fraction for reforming and the catalyst temperature were limited at 33% and 400 °C, the maximum efficiency of ethanol engines was lower than that of methanol engines. A higher reformed fuel fraction and a higher catalyst temperature cause an increase in efficiency for ethanol. The required reforming fraction of ethanol is between 30% to 40%, which is not easy to achieve with normal temperatures of the engine exhaust gases, especially at low loads. Furthermore, high catalyst temperature is also not easy to achieve with more fuel in the EGR system (HoV effect). Another factor is the compression ratio. Methanol has a better knock resistance than ethanol [154], together with a higher HoV, so the compression ratio of a methanol engine can be increased to a higher value than for an ethanol engine. If the CR was optimized for methanol and ethanol engines, the efficiency of the methanol engine should be highest even at high reforming fraction.

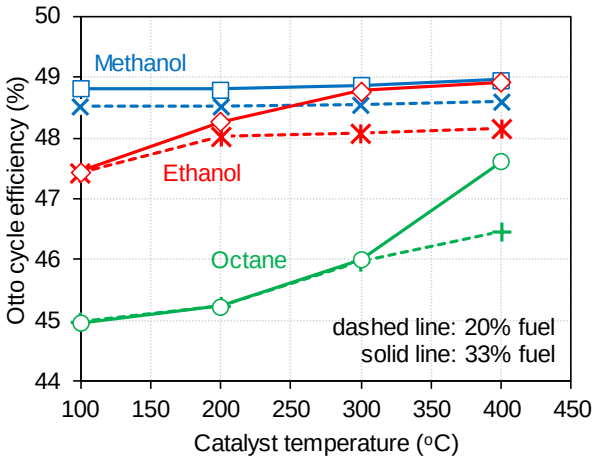

Figure 4.16: Otto cycle efficiency as a function of temperature at EGR ratio of 25%. Dashed lines: 20% fuel in the EGR system, solid lines: 33% fuel in the EGR system.

4.5 Closure

Theoretical studies have been carried out to evaluate the potential of the reformed-exhaust gas recirculation (R-EGR) concept for achieving high fuel economy with methanol SI engines. An Otto cycle calculation was used first. Then the Otto cycle efficiency was also extended with a simple analysis of energy losses, performed to predict the change in engine brake thermal efficiency using specifications of a Volvo T3 engine. The fuel effects were also studied at the same degree of reforming (100%), same combustion stability limit, and same catalyst temperature. Based on the results, the following conclusions can be drawn.

- Combustion in the R-EGR cases produced higher temperatures and lower pressures than conventional EGR with an identical initial pressure. Raising EGR levels and reforming fractions caused a decline in the cycle work.

- For a given EGR ratio, the reforming fraction did not have a significant impact on the efficiency. The improvement was larger at higher EGR ratios. This was due to the reduction of molar expansion ratio with the reforming products in the reactant. The decline in molar expansion ratio at high EGR ratios was less than at low EGR levels.

- The R-EGR case had higher relative heat loss than the conventional EGR. There was almost no difference in the gross ITE between the R-EGR and

conventional EGR. The improvement in BTE in the R-EGR concept is more obvious due the reduction of PMEP.

- Ethanol and iso-octane had a larger relative improvement in the efficiency at the same reforming fraction versus methanol. High reforming fractions (30 - 40%) of ethanol were required to achieve a similar efficiency as methanol.
- At high catalyst temperatures, the formation of CO through the r-WGS reaction caused a slight increase in efficiency. The methanol engine (R-EGR concept) would be able to produce a higher efficiency than the ethanol engine if the optimal CR was used.
- A more detailed engine gas-dynamic simulation is needed to understand the impact of all parameters on the final efficiency.

5

Laminar burning velocity

5.1 Introduction

As mentioned in Chapter 1, laminar burning velocity (LBV or u_L) is an important parameter for a highly efficient SI engine. A faster burning velocity helps to increase combustion phasing efficiency, η_{glh}. In the previous Chapter, the efficiency comparison was performed at the same combustion duration; the impact of hydrogen in the reactants on the combustion process was ignored. In order to predict the real combustion behavior, the LBV has to be investigated. Hydrogen has a very high LBV, much faster than other fuels, as shown in Table 1.1. Furthermore, a faster burning velocity helps to stabilize highly diluted combustion (see Chapter 2 and Chapter 4). This chapter focuses on the LBV of a methanol-syngas blend. A LBV correlation will be developed. This chapter is based on the published papers by the author [93, 155, 156]. In the two conference papers [155, 156], the author Duc-Khanh Nguyen did chemical kinetic simulation, subsequent analysis, developed a correlation, wrote the papers, and prepared all figures and tables. The author Sebastian Verhelst contributed corrections, discussions and proof-reading. The universal dilution term section was presented in the Fuel journal paper [93], the authors' contributions are explained in the previous Chapter.

5.2 Simulation code and mechanism selection

The laminar burning velocity was calculated using a one-dimensional flame code - CHEM1D [151], similar to previous Chapters. This was developed by the Combustion Technology group at Eindhoven University of Technology. It solves the conservation equations of mass, momentum, species and enthalpy [157] and uses the EGLIB complex transport model [158]. In each case, a stationary simulation was performed with an exponential differential scheme and free flame type using 200 grid points. Figure 5.1 shows the validation of simulated laminar burning velocities of methanol and H_2/CO blends (50%-50% by mole) in air using Li's mechanism [70] and the USC-II 2007 mechanism [159], versus experiments from literature (see Appendix A).

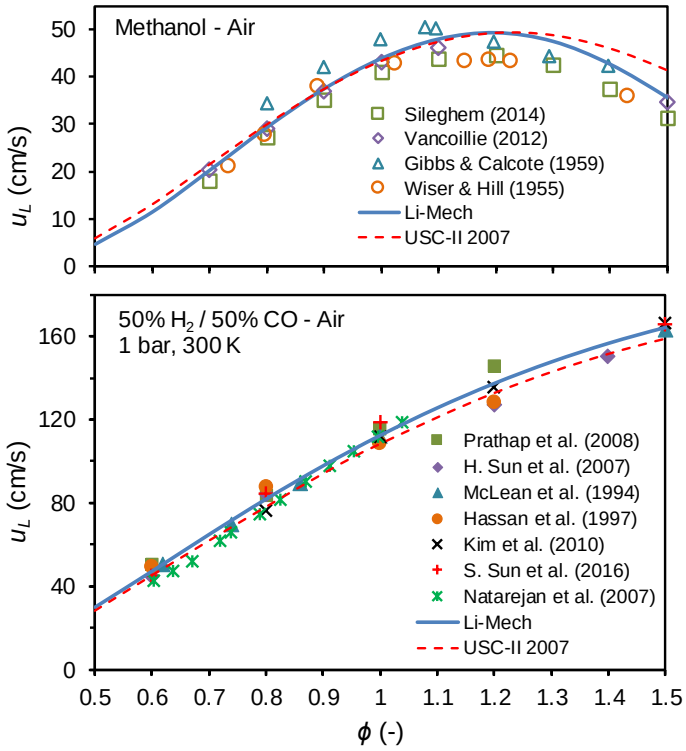

Figure 5.1: Validation of Li's and USC-II mechanisms for the u_L prediction of methanol (upper) and CO/H_2 blend (50/50 by mole) (lower) in air at 1 bar, 300 K. The experimental data of methanol-air flames is from [153, 160–162], H_2/CO-air flames from [163–169].

Li's mechanism [70] is a skeletal and accurate chemical kinetic mechanism for the simulations of both methanol and syngas. It is updated from a methanol oxidation

mechanism [170] to be able to simulate the combustion of $CO/H_2/H_2O/O_2$ and CH_2O. According to Olm et al. [171], it is ranked 5th in the prediction of laminar burning velocities of syngas. In the top four best mechanisms, only the USC-II 2007 mechanism [159] (ranked 2nd) is eligible to simulate the combustion of methanol. Therefore, these two mechanisms were employed to validate against the experiments. It is clearly seen that the two mechanisms have the same performance for the prediction of laminar burning velocity of methanol-air flames for equivalence ratios less than 1.2. At richer conditions, the calculated data using the USC-II 2007 mechanism over-predicts the experimental data. A small difference is found between the USC-II 2007 and Li's mechanism in the prediction of the laminar burning velocity of H_2/CO blends. Furthermore, USC-II 2007 consists of 111 species and 784 reactions. The number of species and reactions of Li's mechanism is only 21 and 93, respectively. Therefore, the simulation time with Li's mechanism is significantly faster than that with the USC-II 2007 mechanism. For these reasons, the mechanism developed by Li et al. is selected for this research.

5.3 Laminar burning velocity of methanol-syngas blends

Five fuels (methanol, SG25, SG50, SG75, and syngas) were tested in this study. The "SG" designates syngas and the number next to "SG" designates the percentage by volume of syngas in the fuel blends. Assuming the fuel conversion is 100%, there are three main products of methanol steam-reforming, after condensation (CO, CO_2 and H_2). However, their concentrations vary for different conditions. Their ratio is a function of the CO selectivity (as shown in Figure 3.10). In this part, syngas was simplified to a mixture of only two components, hydrogen and carbon monoxide. The selected syngas has a ratio by mole of H_2/CO of 50/50. This syngas has a lower heating value (LHV) similar to that of an $H_2/CO/CO_2$ mixture with CO selectivity of 50%. Furthermore, experimental LBV data of that mixture in air is available for the validation of CHEM1D simulation results at different equivalence ratios (Figure 5.1). The volume fractions of the three components of the five tested fuels and their LHVs are plotted in Figure 5.2.

The studied range of equivalence ratio was 0.5 - 2.0 with $\Delta\phi$ = 0.1, and unburned gas temperature was 300 K - 900 K (ΔT = 50 K) at 1 bar. In total, 1040 independent simulations were performed.

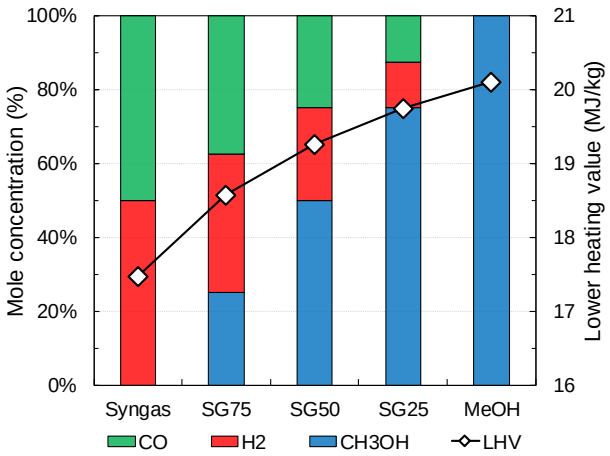

Figure 5.2: The components of the tested fuels, their concentrations by mole and lower heating values.

5.3.1 Evaluation of mixing rules

For the fuel blends, it is essential to know how the laminar burning velocity varies when the blend ratios are changed. However, most of the current reaction mechanisms were developed and validated for a single fuel. Developing a comprehensive mechanism for a mixture of several fuels requires a lot of work and computation time. Knowledge of that behavior without time-consuming chemical kinetic calculations could allow faster simulation of the engine operation. In order to find a mixing rule to predict the laminar burning velocity of methanol-syngas blends, an examination of existing mixing rules was done. Five mixing rules are evaluated in this study, including mole fraction, mass fraction, energy fraction [172], Le Chatelier's [173] and Hirasawa's mixing rules [174].

To predict the LBV of fuel blends ($u_{L,blend}$), the LBV of each component ($u_{L,i}$) is needed. The first three mixing rules are based on the mole fraction, mass fraction and energy fraction of fuel components to calculate the LBV of blends. Therefore, the LBV changes proportionally to a change in the mole, mass and energy fraction. Le Chatelier's mixing rule uses the mole fraction (x_i) of fuel's components to predict the LBV of fuel blends as in equation 5.1.

$$u_{L,blend} = \frac{1}{\sum_{i=1}^{n} \frac{x_i}{u_{L,i}}} \tag{5.1}$$

Hirashawa's mixing rule predicts $u_{L,blend}$ as a function of "activation temperature" and the adiabatic flame temperature of the fuel blend. The adiabatic flame temperature is calculated based on the heat release, the number of moles of the products, and the mean molar specific heat of the products. The "activation temperature" is estimated by the mole fraction, number of moles of the products, adiabatic flame temperature and LBV of each fuel's components. More information about this mixing rule can be found in [172, 174].

According to Sileghem et al. [172], the energy fraction mixing rule, the mixing rule developed by Hirasawa et al., and the Le Chatelier's rule performed very well for blends of hydrocarbons and ethanol. However, these mixing rules did not work for hydrogen-methane blends because of the strong reactivity of hydrogen. In the discussion below, these mixing rules have been appraised for the blends of methanol and syngas.

As shown in Figure 5.1, the LBV of syngas is much higher than methanol. Hence, LBV of the blend increases as syngas molar fraction increases. However, it does not increase linearly with the increase of syngas molar fraction. Figure 5.3 displays the improvement of LBV with respect to pure methanol as a function of syngas content at four equivalence ratios and two unburned temperatures, 300 K and 600 K. It can be seen that the improvement in LBV is larger at high syngas ratios. The syngas addition and unburned temperatures have lower influence at stoichiometric conditions. This explains why the effect of hydrogen addition on engine performance is most obvious at lean conditions [175].

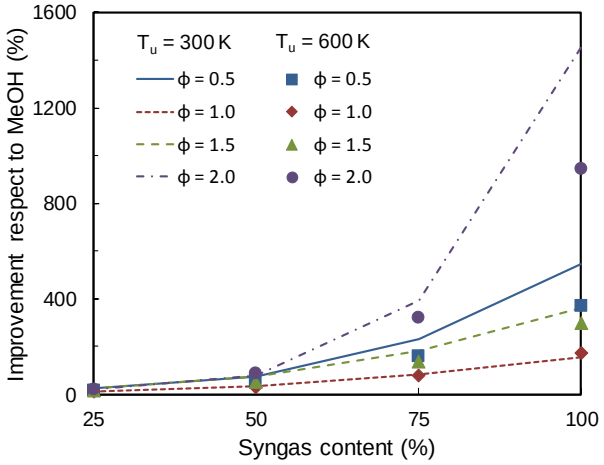

Figure 5.3: Relative improvement of LBV with respect to methanol as a function of syngas molar fraction at 1 bar.

The data of SG50-air flames then were compared to the calculated values using different mixing rules, as shown in Figure 5.4. It is clear that mole, mass and energy fraction mixing rules were unable to accurately predict the laminar flame speed of the methanol-syngas blend accurately, especially at rich conditions. This is due to the fact that the peak burning velocities of methanol and syngas occur at different ϕ. The fastest laminar burning velocity of methanol-air was observed at ϕ = 1.2, whereas the equivalence ratio for the peak burning velocity of syngas-air is 2.0. This difference results from the high thermal and mass diffusivities of hydrogen compared to normal liquid fuels.

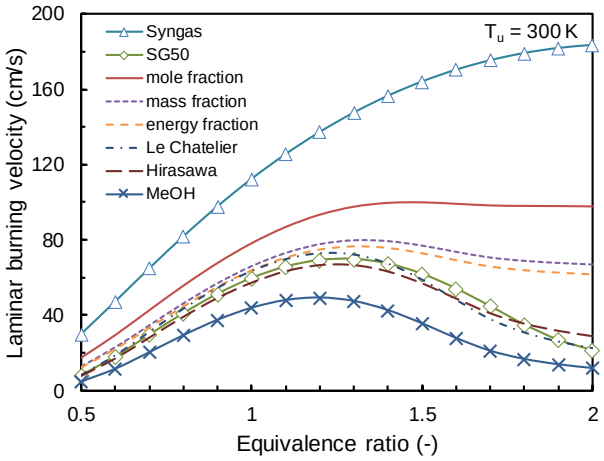

Figure 5.4: Simulated LBV and calculated LBV of SG50-air mixture using different mixing rules as a function of ϕ at 1 bar, 300 K.

Le Chatelier's and Hirasawa's mixing rules predict the burning velocity of methanol-syngas blends well. In general, the Hirasawa's mixing rule provides better results than the Le Chatelier's rule. Especially, at unburned gas temperature of 600 K, the data from the calculation with Hirasawa's mixing rule shows a perfect fit with the simulated results. Figure 5.5 indicates the comparison of laminar burning velocities which were calculated using Le Chatelier and Hirasawa mixing rules versus the kinetic simulation results at two temperatures, 300 K and 600 K. It is clearly seen that the Le Chatelier and Hirasawa mixing rules are only predictive for the mixture with syngas ratios less than or equal to 50%. If the allowable deviation is 10%, the Hirasawa mixing rule is preferred to predict the flame speed of methanol-syngas blends at high temperature, and for lean and stoichiometric mixtures at low temperature. However, Le Chatelier's mixing rule is recommended for the prediction of the flame speed of mixtures with a high syngas content (75%) at lean and stoichiometric conditions.

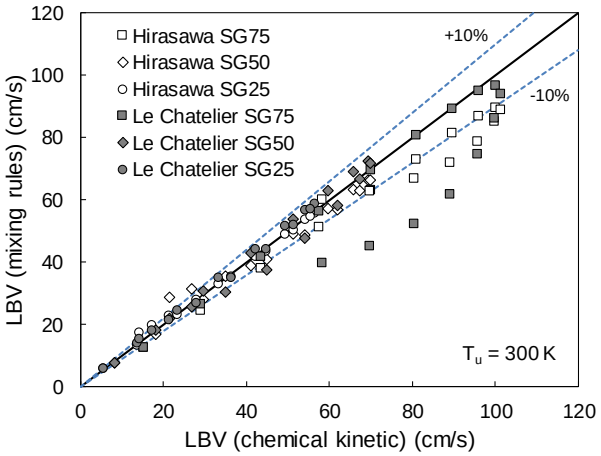

Figure 5.5: LBV of methanol-syngas blends at 300 K: mixing rules versus kinetic calculation at all equivalence ratios.

Table 5.1 displays the root-mean-square-error (RMSE) of the two mixing rules compared to the data from the chemical kinetic calculations. The data in the brackets is the RMSE for lean and stoichiometric mixtures. There is a trend that the RMSE becomes larger with more syngas (less methanol) content for both mixing rules, which is due to the kinetic interactions having a larger influence on the flame speed. Because no mixing rule is outperforming the other in the prediction of LBV for methanol/syngas blends for a wide range of ϕ, a LBV correlation will be developed for methanol/syngas blends in section 5.4, i.e. these mixing rules will not be employed.

Table 5.1: RMSE of the different mixing rules. The data in brackets presents the RMSE for $\phi \leq 1$ (cm/s)

Mixture	T_u = 300 K		T_u = 600 K	
	Le Chatelier	Hirashawa	Le Chatelier	Hirashawa
SG75	14.19 (1.72)	10.18 (5.91)	30.5 (8.18)	19.89 (12.75)
SG50	3.35 (2.09)	3.59 (1.66)	12.52 (12.98)	4.56 (1.19)
SG25	1.39 (1.41)	1.24 (0.37)	6.51 (7.04)	2.48 (0.42)

5.3.2 Effect of unburned gas temperature

Unburned gas temperature has a strong impact on LBV. Normally, LBV is calculated as a function of unburned temperature T_u, reference laminar burning

velocity $u_{L,0}$ at reference temperature T_0, and temperature power exponent α using the correlation in equation 5.2. In order to have a better prediction of LBV under engine-like conditions, α is an important parameter in the LBV correlation. The α was normally determined by the slope of the linear fitting line in the $\log(u_L)$-$\log(T_u)$ plot [153, 160, 176].

$$u_L = u_{L,0}\left(\frac{T_u}{T_0}\right)^{\alpha} \tag{5.2}$$

Figure 5.6 shows the calculated α based on the correlation in equation 5.2 for the SG50-air mixture. It is clearly seen that for a certain equivalence ratio, a single value of α is not able to present the influence of unburnt temperature on the flame speed. The α derived from the slope of linear fitting line in the $\log(u_L)$-$\log(T_u)$ plot is equal to the calculated α at maximum temperature. The laminar burning velocity at lower temperatures calculated with that α is higher than the observed value. For this reason, the averaged α was used to represent the temperature power exponent.

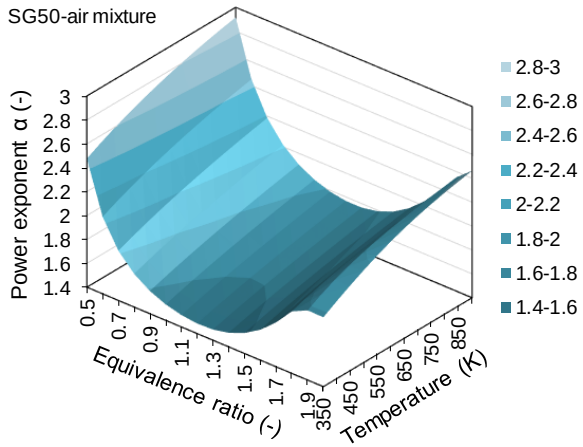

Figure 5.6: The map of power exponent α of SG50-air mixture as a function of ϕ and T_u at 1 bar.

The averaged α values of all fuels are plotted together with data from other research in Figure 5.7. There is no significant difference between the α of methanol and methanol-syngas blends at $0.5 \leq \phi \leq 1.5$. It is also clearly seen that the well-known correlations for methanol-air flames such as Metghalchi and Keck [177], Liao [178] and Saeed [179] are not able to predict the laminar burning velocities at high temperatures. The Gülder model [180] is only predictive for

mixtures at the stoichiometric condition. The α from the correlation developed by Vancoillie et al. [181] is over-predicting because the α was determined by the slope of the linear fitting line in the $\log(u_L)$-$\log(T_u)$ plot. Fanelli et al. [182] developed a correlation for the laminar flame speed of syngas, but their α is only acceptable for mixtures which are close to the stoichiometric condition. Therefore, there is a need for the development of a new laminar burning velocity correlation for methanol and methanol-syngas blends to implement it into the engine simulation tool.

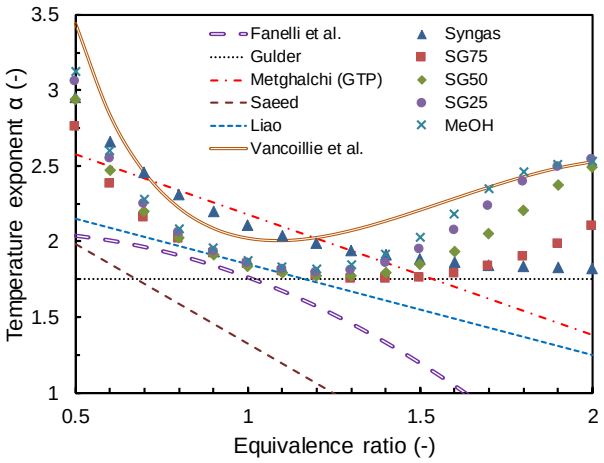

Figure 5.7: Comparison between temperature exponent α from simulation (symbols) and α from published correlations (lines).

5.4 Laminar burning velocity correlation

To design and optimize the engine and reformer system based on simulations, the laminar burning velocity of mixtures containing reformed fuel needs to be known as a function of the in-cylinder conditions, as this is a base parameter for any predictive engine combustion model. Therefore, in this section an accurate laminar burning velocity correlation is derived first. The laminar burning velocity of mixtures in two engine concepts (EFR and R-EGR, which were presented in section 3.4) were calculated using CHEM1D at engine-like conditions. Then the correlation is developed based on the calculated data and then compared to the existing correlations. Finally, the developed correlation is analyzed to compare different dilution methods and reforming concepts.

5.4.1 Overview

Before developing the correlation, several laminar burning velocity correlations of methanol-air flames at elevated pressures have been reviewed. The list of existing correlations is shown in Table 5.2. The early works, including those of Ryan and Lestz [183], Metghalchi and Keck [177], Gülder [180], developed the correlation based on their experiments using a constant volume chamber (CVC). However, they did not account for the effects of stretch or hydrodynamic instabilities on flame propagation, therefore these correlations are not expected to give reliable results [184].

Table 5.2: Existing laminar burning velocity correlations of methanol-air flames at elevated pressure

References	Method	ϕ	p (bar)	T_u (K)
Ryan and Lestz [183]	CVC	1.0	0.4-18	470-600
Metghalchi and Kech [177]	CVC	0.8-1.5	0.4-40	298-700
Gülder [180]	CVC	0.7-1.4	1-8	298-800
Saeed and Stone [179]	CVC	0.7-1.5	0.5-13.5	295-650
Müller et al. [185]	Numerical	0.6-1.0	1-40	298-800
Vancoillie et al. [181]	Numerical	0.5-2.0	5-85	298-900
Liu et al. [186]	Calculation	0.6-1.5	1-50	400-2600

Müller et al. [185] used a two-equation asymptotic fit to correlate the steady laminar burning velocity data from numerical calculations using an elementary reaction mechanism. The correlation is developed for undiluted combustion of lean and stoichiometric mixtures. Also using the data form chemical kinetic simulations, Vancoillie et al. [181] developed a correlation for methanol-air combustion with fitting coefficients for polynomial functions determined using the Levenberg-Marquardt method. As showed in Figure 5.7, Vancoillie's correlation seems to over predict slightly the temperature power exponent. However, that comparison was done at 1 bar, and the combustion in engines takes place at higher pressure. The predictability of this correlation at engine-like conditions needs to be evaluated.

Liu et al. [186] built a correlation for methanol-hydrogen blends using the form of Metghalchi's formula, with a first order function for the influence of residual gas fraction. They used a similar method to Vancoillie et al., finding the fitting coefficients of second and third order polynomial functions using the Levenberg-Marquardt algorithm. The correlation was developed based on a data set which was calculated using flame-temperature mixing rules with a wide range of ϕ, p, T_u, hydrogen ratio and residual gas mass fractions. There are 72,600

data points in total which are correlated in a formula with 42 fitting coefficients. Because methanol reformate contains not only H_2 but also CO and CO_2, a new correlation is needed.

5.4.2 Development methodology

Engine-like conditions

In order to predict the combustion under SI-engine-like conditions, the simulation is performed at elevated pressures (p) and unburned gas temperatures (T_u) ranging respectively from 10 to 85 bar and 550 to 800 K. Recent SI engines have a compression ratio above 9:1 and are equipped with a boosting system, therefore the in-cylinder pressure when the spark ignites is greater than 10 bar. The minimum temperature is calculated starting from the pressure using the isentropic compression equation. The syngas ratios in the fuel blend, fuel-air equivalence ratios, and EGR ratios are varied in a range from 0% to 50% by volume (X_{SG} = 0-0.5), 0.5 to 1.5 (ϕ = 0.5-1.5), and 0% to 30% (Y_{EGR} = 0-0.3), respectively. The blend of syngas-methanol with syngas molar ratio of 0%, 10%, 20%, 30%, 40% and 50% by volume is designated as MeOH, SG10, SG20, SG30, SG40 and SG50, respectively.

Reactant compositions

After selecting the conditions, the concentration of reactant components is another parameter for the simulation. In this study, syngas is a mixture of H_2, CO and CO_2 with a CO selectivity of 6.5%, which is the product of methanol steam reforming over a Cu-Mn-O/Al foam catalyst, with a water to methanol molar ratio of 1.5 and a catalyst temperature of ~320 ^{o}C [109]. As the temperature of exhaust gas is much higher than that value, we assume that the fuel conversion is 100% in this study, so there is no methanol left in the product. The CO selectivity is defined as the molar ratio of CO produced to the sum of CO and CO_2 in the product. The reforming reaction with different CO selectivity has been presented in section 3.5. In this case, X_{CO} equals 0.065.

To identify the reactants in the EFR and R-EGR concepts (see section 3.4), assume that the combustion is complete to produce CO_2, H_2O and N_2. For rich combustion, the fuel left in the exhaust gases is kept in its original form. The reactions for lean and stoichiometric conditions ($\phi \leq 1.0$), and for rich mixtures ($\phi > 1.0$), in case of the EFR concept, are presented respectively in Appendix B. For the R-EGR

concept, due to the reduction of energy ratio and LBV of methanol reformates with the presence of O_2 in the exhaust (see reaction R3.9), only stoichiometric combustion is considered. For methanol, to form one mole of CO_2, one mole of steam is needed. Therefore, the sum of CO_2 produced in the syngas and H_2O left after the reformer equals the moles of steam in the inlet EGR mixture. All combustion reactions are shown in Appendix B.

Figure 5.8 shows the mole fraction of reactants for the EFR concept as a function of Y_{EGR} at $\phi = 1$. With $X_{SG} = 0$ (neat methanol, top graph), the reactant includes only CH_3OH, CO_2, H_2O, O_2 and N_2, the mole fraction of H_2 and CO equals 0. The concentration of combustion products like CO_2 and H_2O increases with a rising EGR ratio, whereas, the mole fraction of CH_3OH and O_2 decreases. In the case of 50% syngas in the fuel blend ($X_{SG} = 0.5$, bottom graph), at $Y_{EGR} = 0$, the total mole fraction of H_2, CO_2 and CO equals that of CH_3OH. When $Y_{EGR} > 0$, CO_2 from the combustion products is recirculated to the reactant, therefore the total mole fraction of H_2, CO_2 and CO is greater than that of CH_3OH. The concentration of N_2 in the mixture is almost constant for all EGR ratios.

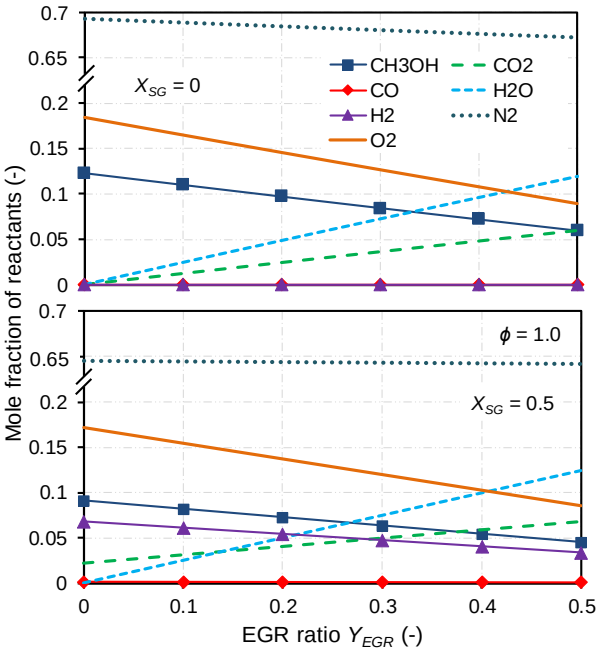

Figure 5.8: Molar fraction of reactant species in the EFR concept as a function of Y_{EGR} at $\phi = 1$.

Figure 5.9 presents the reactant mole fraction as a function of Y_{EGR} for the

R-EGR concept at $\phi = 1$. The Y_{EGR} is limited at 0.428 due to the fact that the water/methanol molar fraction is maintained at 1.5. At this limit, 100% methanol is injected into the EGR system and reformed completely. Thanks to the consumption of water vapour during the fuel reforming process, the mole fraction of H_2O left in the combustion chamber is much smaller than is the case for the EFR concept (as shown in Figure 5.8). The mole fractions of H_2 and CO_2 significantly increase with a rising EGR ratio. The concentration of N_2 decreases dramatically due to the expansion in volume of the reforming products.

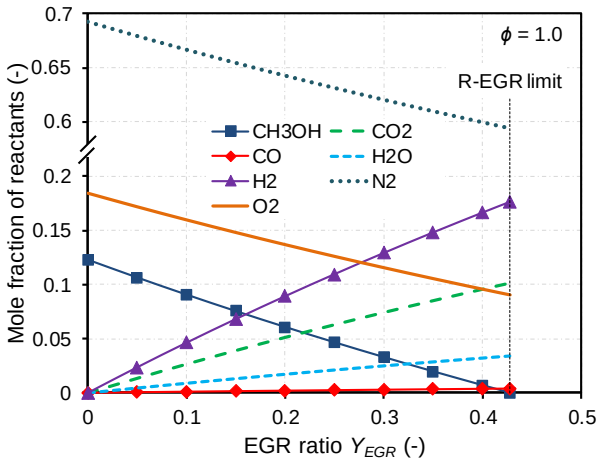

Figure 5.9: Molar fraction of reactant species in the R-EGR concept as a function of Y_{EGR} at $\phi = 1$.

5.4.3 Combustion without EGR dilution

After reviewing the developed correlations, a new correlation for methanol/syngas blends has been developed based on burning velocity computations using CHEM1D. Equation 5.3 shows the general form of the correlation for the undiluted combustion of methanol/syngas blends; it is similar to the correlation developed by Liu et al. [186]. The reference velocity is a function of equivalence ratio and syngas ratio in the blend. The pressure power exponent β depends on three variables: equivalence ratio, unburned temperature and syngas ratio. However, the temperature power exponent α is a function of only equivalence ratio because the influence of syngas ratio on the change of α is very small (see section 5.3.2), so it can be neglected. The detailed formulae for reference velocity, α and β are presented in Appendix C.

$$u_L = u_{L,0}(\phi, X_{SG}).\left(\frac{T_u}{T_0}\right)^{\alpha(\phi)}.\left(\frac{p}{p_0}\right)^{\beta(\phi,T_u,X_{SG})} \tag{5.3}$$

Figure 5.10 shows the comparison of predicted laminar burning velocities using equation 5.3 and the simulated data from CHEM1D. There are 1,056 data points for each fuel composition (pure methanol, MeOH, to methanol with 50% syngas, SG50), so 6,336 data points in total. The standard deviation ±10% is also added. It can be seen that most of the points are within the standard error limit.

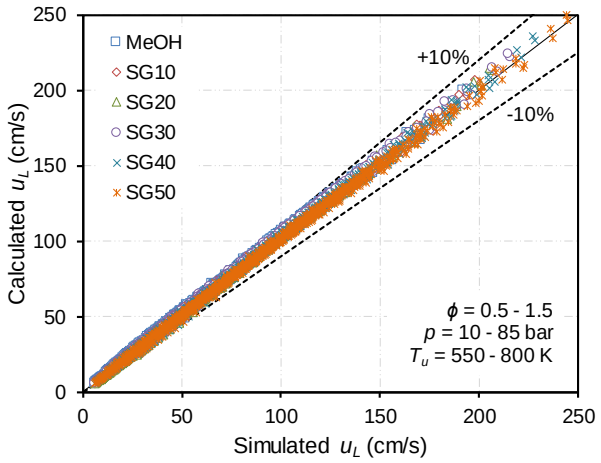

Figure 5.10: Comparison between calculated u_L using equation 5.3 and simulated u_L from CHEM1D of undiluted flames for the EFR concept.

The quality of the fit for methanol-syngas-air mixtures including average relative residual (equation 5.4), average absolute relative residual (equation 5.5), minimum and maximum residuals, and the percentage of data within ±10%, are provided in Table 5.3. As can be seen, there is a good agreement between predicted and simulated values. Almost 100% of data points for each fuel blend have an error less than 10% compared to the data from CHEM1D.

$$\text{Average relative residual} = \frac{1}{N}\sum_{n=1}^{N}\frac{u_{L,calculated} - u_{L,simulated}}{u_{L,simulated}} \tag{5.4}$$

$$\text{Average absolute relative residual} = \frac{1}{N}\sum_{n=1}^{N}\frac{|u_{L,calculated} - u_{L,simulated}|}{u_{L,simulated}} \tag{5.5}$$

Table 5.3: Fitting statistics of undiluted methanol/syngas combustion

Fuel	Ave. rel. residual	Ave. abs. residual	Minimum error	Maximum error	Data within ±10%
MeOH	2.47%	3.61%	-9.27%	10.1%	99.6%
SG10	2.71%	3.72%	-9.05%	10.2%	99.7%
SG20	2.76%	3.7%	-9.21%	9.81%	100%
SG30	2.56%	3.5%	-9.64%	9.62%	100%
SG40	1.98%	3.03%	-10.46%	8.94%	99.9%
SG50	0.83%	2.35%	-11.93%	7.53%	99.5%

5.4.4 Combustion with (R-)EGR dilution

For the influence of EGR dilution, most of the existing correlations employed a first order equation. This is simple, however, since it is only predictive for limited cases. In order to have a better prediction of LBV with the (R-)EGR dilution, a different dilution term was developed. For EGR dilution, an exponential function of equivalence ratio, unburned gas temperature and EGR ratio is used. The influences of pressure and syngas ratio are neglected. The formula of the full correlation is illustrated in equation 5.6. The detailed equation of ε is presented in Appendix C. To reduce the number of simulation points of diluted combustion, we chose five levels of equivalence ratio (ϕ = 0.6, 0.8, 1.0, 1.2 and 1.4), three levels of pressure (p = 10, 50 and 85 bar) and unburned gas temperature (T_u = 550, 700 and 800 K), and seven levels of EGR ratio (Y_{EGR} = 0, 0.05, 0.1, 0.15, 0.2, 0.25 and 0.3). Therefore, there are 315 conditions for each fuel. Figure 5.11 displays the comparison of predicted LBV using equation 5.6 and the simulated data.

$$u_L = u_{L,0} \cdot \left(\frac{T_u}{T_0}\right)^{\alpha} \cdot \left(\frac{p}{p_0}\right)^{\beta} .exp(\varepsilon) \tag{5.6}$$

Equation 5.7 illustrates the formula of the developed laminar burning velocity correlation at ϕ = 1.0 for the R-EGR concept. In this concept, the influence of the EGR ratio is determined by an exponential function of unburned temperature, EGR ratio and pressure. The detailed formula of ε' is displayed in Appendix C. Figure 5.12 presents the comparison between predicted data using equation 5.7 and simulated results from CHEM1D.

$$u_L = u_{L,0} \cdot \left(\frac{T_u}{T_0}\right)^{\alpha} \cdot \left(\frac{p}{p_0}\right)^{\beta} .exp(\varepsilon') \tag{5.7}$$

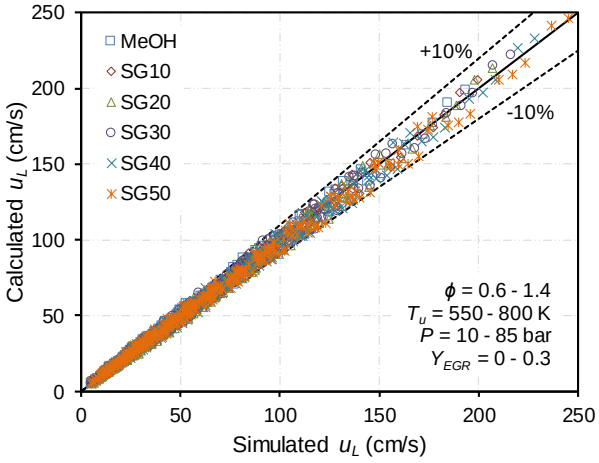

Figure 5.11: Comparison between calculated u_L using equation 5.6 and simulated u_L from CHEM1D of undiluted flames for the EFR concept.

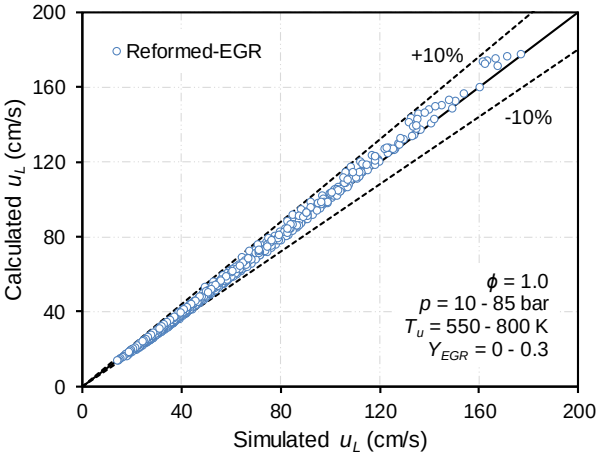

Figure 5.12: Comparison between calculated u_L using equation 5.7 and simulated u_L from CHEM1D of undiluted flames for the R-EGR concept.

The fitting statistics of diluted combustion of methanol/syngas blends as well as R-EGR are presented together in Table 5.4. Because the correction term is simplified to reduce the complexity of the full correlation, the error is increased with the dilution of EGR mixtures. The maximum error is around 18% compared to the simulated data. However, over 99% of data points are within a standard deviation of ±15%.

Table 5.4: Fitting statistics of EGR diluted methanol/syngas and R-EGR combustion

Fuel	Ave. rel. residual	Ave. abs. residual	Minimum error	Maximum error	Data within ±15%
MeOH	-1.80%	4.03%	-14.73%	11.22%	100%
SG10	-1.14%	3.85%	-13.91%	12.55%	100%
SG20	-0.60%	3.76%	-13.17%	13.87%	100%
SG30	-0.20%	3.76%	-12.53%	15.19%	99.68%
SG40	-0.02%	3.79%	-12.07%	16.60%	99.68%
SG50	-0.22%	3.95%	-11.90%	17.92%	99.37%
R-EGR	-1.63%	3.12%	-11.06%	7.88%	100%

5.4.5 Performance of developed correlation

Compared to existing correlations

Due to the lack of measured LBV data at engine-like conditions and no existing correlation for methanol/syngas blends, the performance of the newly developed correlations is evaluated by comparing the calculated LBV to the LBV data from existing correlations for methanol. Figure 5.13 compares the predicted u_L using equation 5.3 and the calculated data from published correlations at engine-like condition, p = 20 bar, T_u = 650 K. It is clearly seen that the predicted u_L using equation 5.3 agrees well with the data from the correlations developed by Vancoillie et al. [181] and Liu et al. [186]. The other kinetic-based correlation, developed by Müller et al. [185], has the same performance at ϕ = 0.9-1.0. However, the experimental-based correlations developed by Metghalchi and Keck [177], Gülder [180] and Saeed and Stone [179] are not predictive. The dilution term for methanol-air flames at T_u = 650 K and p = 20 bar is compared to published correlations in Figure 5.14. The dilution term in this study agrees well with the data from the work of Vancoillie et al. [181].

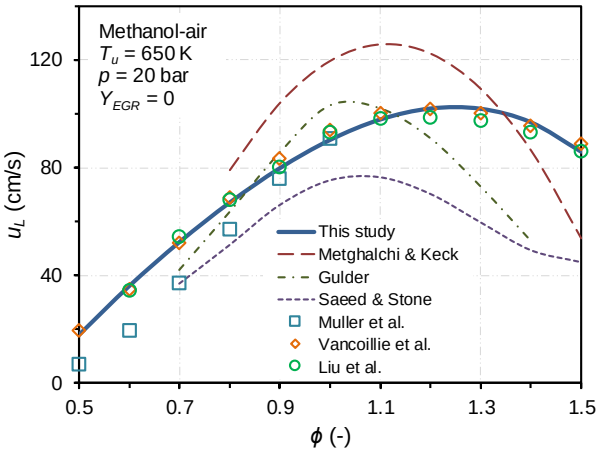

Figure 5.13: Comparison of the calculated u_L using equation 5.3 and existing correlations for undiluted methanol-air flames at 20 bar, 650 K.

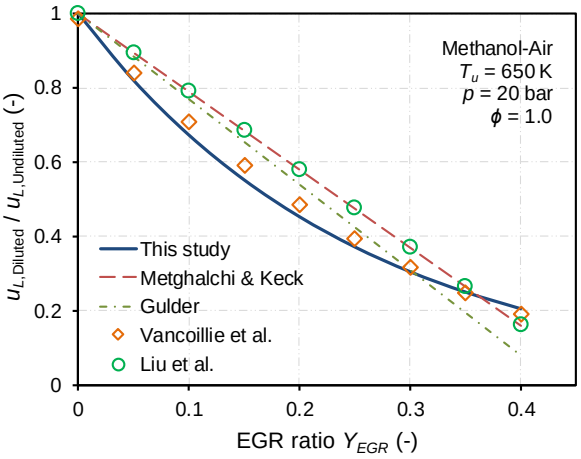

Figure 5.14: Comparison of the dilution term in equation 5.6 and existing correlations for methanol-air flames at 20 bar, 650 K.

Compared to Hirasawa's mixing rule

In order to evaluate the predictability of the developed correlation for the laminar burning velocity of methanol/syngas blends, the predicted u_L of methanol/syngas blends are now compared to the calculated u_L using Hirasawa's mixing rule [174], as presented in Figure 5.15. For the calculation of u_L using the mixing rule, the u_L data of 100% syngas and neat methanol are from the kinetic simulations using CHEM1D. It can be seen that Hirasawa's mixing rule is only predictive for the blends with low syngas concentration. The error increases with rising syngas content in the fuel mixtures, similar to the conclusion in section 5.3.1.

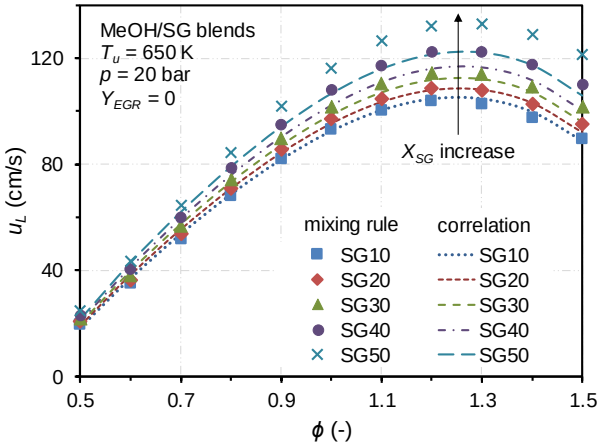

Figure 5.15: Comparison of the calculated u_L using equation 5.3 (dashed lines) and the Hirasawa mixing rule (symbols) of methanol/syngas blends at 20 bar, 650 K.

5.4.6 Influence of dilution method

As mentioned in Chapter 2, lean operation (diluted by air) and/or EGR dilution are among the key techniques to increase the engine efficiency. The laminar burning velocity of a fuel-oxidizer mixture strongly depends on the quantity of air and/or EGR ratio [187]. In order to better understand the effect of dilution methods, lean mixtures are compared to a stoichiometric mixture diluted with burned gases using the developed correlations. To indicate the dilution of air, EGR and R-EGR mixtures, the fuel-to-charge equivalence ratio ϕ' is used, as in equation 2.8.

Figure 5.16 shows the u_L of methanol and the SG50 blend, when they are diluted by air or EGR mixtures, as well as methanol-air combustion diluted by R-EGR

mixture. This illustration is for a pressure of 20 bar and an unburned temperature of 650 K. For both fuels, MeOH and SG50, the u_L for air dilution exceeds that of the EGR diluted mixture because the u_L is related to the mixture O_2 concentration as well as the reaction front temperature [188]. The heat capacity of the burned gases (including CO_2, N_2 and water vapour) is higher than that of air, which leads to a stronger decrease of the reaction front temperature for the EGR dilution. However, for the dilution with the R-EGR mixture, the laminar burning velocity is faster than that of air-diluted methanol combustion when ϕ' drops below 0.75 (corresponding to $Y_{EGR} > 0.25$ in the R-EGR concept). The necessary T_u as a function of ϕ' to maintain constant u_L at 100 cm/s is presented in Figure 5.17 (again for 20 bar). As can be seen, the required T_u increases slightly when diluting with R-EGR mixtures for lower ϕ'. In contrast, the required T_u to maintain constant u_L for the air and EGR diluted cases increases dramatically. The ΔT_u between EGR diluted MeOH and SG50 combustion is almost constant at 44 K.

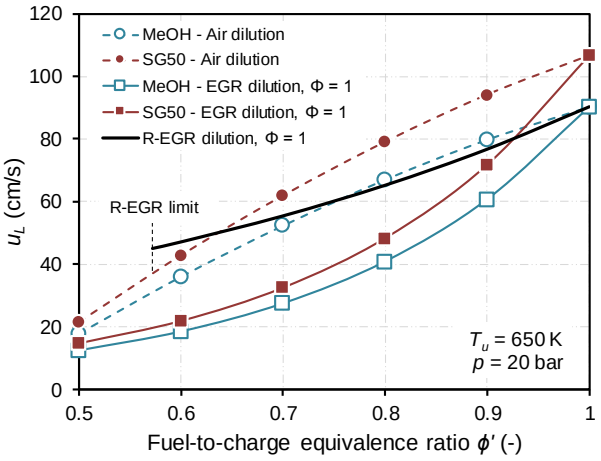

Figure 5.16: u_L as a function of overall dilution ϕ' at 20 bar, 650 K.

Based on the required moles of methanol to generate one mole of syngas with reaction R3.9, the molar/mass fraction of methanol supplied from the second injector (to the reformer catalyst) has been calculated for different syngas blend ratios. The mass fraction of methanol used for the reforming reaction, $Y_{MeOH,catalyst}$ is the ratio of mass flow rate of methanol to the catalyst to the total mass flow rate, as follows:

$$Y_{MeOH,catalyst} = \frac{\dot{m}_{MeOH,catalyst}}{\dot{m}_{MeOH,engine} + \dot{m}_{MeOH,catalyst}} \tag{5.8}$$

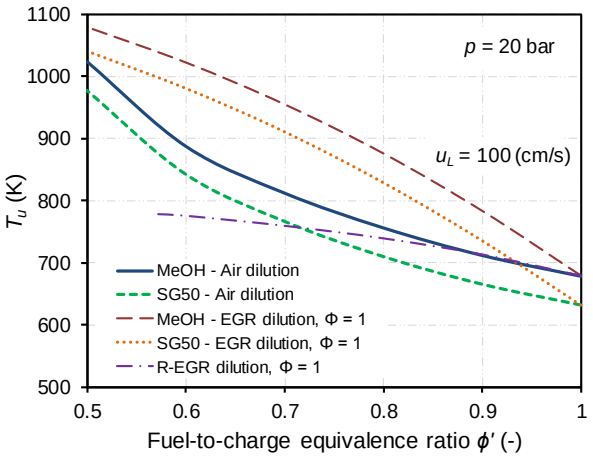

Figure 5.17: Required T_u as a function of overall dilution ϕ' to maintain u_L = 100 (cm/s) at 20 bar.

In the R-EGR concept, the mass flow rate of methanol to the catalyst is determined by the water concentration in the EGR gases. The ratio of water to methanol is kept at a constant value, 1.5 as in the previous section. Therefore, $Y_{MeOH,catalyst}$ increases with rising EGR levels (decreasing ϕ'). $Y_{MeOH,catalyst}$ reaches 1 at an EGR ratio of 42.8%, thus constituting the R-EGR limit. The relationship between $Y_{MeOH,catalyst}$ and ϕ' is illustrated in the lower graph of Figure 5.18. For the syngas blends, horizontal lines result, as the dilution can be set independently from the fuel composition. For example, to produce the SG50 blend, a blend with 50 vol% methanol and 50 vol% syngas, around 20% of the total methanol mass is injected into the catalyst, and 80% is supplied directly to the engine. For the R-EGR, there is a fixed relation between $Y_{MeOH,catalyst}$ and ϕ'. Taking the SG50 case as an example, with the same $Y_{MeOH,catalyst}$, the EGR ratio in the R-EGR concept is ~13% ($\phi' = 0.87$).

The top graph of Figure 5.18 plots the ratios of $u_{L,R-EGR}/u_{L,Air}$ and $u_{L,EGR}/u_{L,Air}$ as a function of ϕ' to compare the two engine concepts. The $u_{L,R-EGR}$ and $u_{L,EGR}$ indicate the u_L of the mixture diluted by R-EGR and EGR at $\phi = 1$, respectively. The $u_{L,Air}$ indicates the u_L when diluted with air (lean operation). For the EGR and air dilution cases, six fuel mixtures are plotted: MeOH to SG50. Because in the developed correlation, the influence of X_{SG} on the dilution term is neglected, the $u_{L,EGR}/u_{L,Air}$ ratio versus ϕ' is independent of the syngas ratio. Therefore, only one curve of $u_{L,EGR}/u_{L,Air}$ is plotted in the top graph of Figure 5.18. Because the denominator, $u_{L,Air}$ of methanol/syngas blends, improves (increases) with increasing syngas ratio (as shown in Figure 5.15) and there is only one value

of $u_{L,R-EGR}$ at each ϕ' (numerator), the $u_{L,R-EGR}/u_{L,Air}$ ratio decreases with the higher content of syngas in the blends. Six curves of $u_{L,R-EGR}/u_{L,Air}$ vs. ϕ' are illustrated for different syngas ratios, with ϕ' being confined by the R-EGR limit. The ratio $u_{L,R-EGR}/u_{L,Air}$ at $\phi' = 1$ respectively equals 1, 0.975, 0.947, 0.917, 0.884 and 0.847 for X_{SG} increasing from 0, 0.1 to 0.5.

At the same ϕ' (Y_{EGR}) and the same $Y_{MeOH,catalyst}$, the combustion diluted by R-EGR mixtures is faster than that of normal EGR dilution. For instance, the $u_{L,EGR}/u_{L,Air}$ equals ~0.7 and the $u_{L,R-EGR}/u_{L,Air}$ equals ~0.81 for SG50 at a ϕ' of 0.87. This means LBV in the R-EGR concept is faster than in the EFR concept with the same $Y_{MeOH,catalyst}$ and EGR ratio. A similar trend is found for other syngas molar fractions. This can be explained by the increase of hydrogen concentration and the reduction of water vapour in the reactants, which is shown in Figure 5.9.

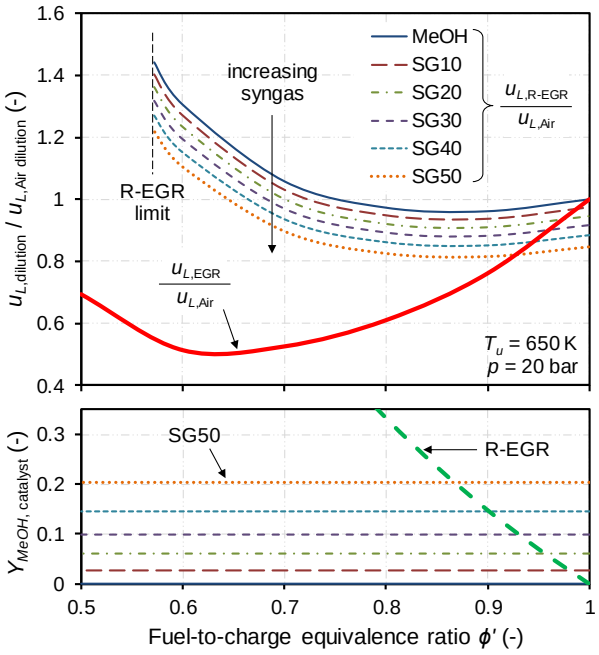

Figure 5.18: Ratio of u_L at 20 bar, 650 K for different dilution methods, EGR relative to air, and mass fraction of methanol delivered to reformer catalyst as a function of ϕ'.

If NO_x emissions are not considered, dilution with air is preferable because it produces a faster laminar burning velocity if a small amount of burned gases (less than 25%) is recirculated to the intake. As can be seen in Figure 5.18, the $u_{L,R-EGR}/u_{L,Air}$ ratio is greater than 1 when ϕ' is smaller than 0.744, 0.722, 0.7,

0.682, 0.659 and 0.643 (corresponding to EGR ratios greater than 25.6%, 27.8%, 30%, 31.8%, 34.1% and 35.7%, respectively) for a syngas ratio X_{SG} of 0, 0.1, 0.2, 0.3, 0.4 and 0.5, respectively.

Figure 5.19 compares the u_L of an undiluted methanol-air mixture at $\phi = 1$ to four diluted mixtures at constant dilution factor, $\phi' = 0.87$, for an isentropic compression starting from atmospheric conditions ($\gamma = 1.35$). Compared to other diluted mixtures, the air dilution case (lean operation at $\phi = 0.87$) offers the fastest burning velocity. Comparing the other dilution methods (at $\phi = 1$), it can be seen that the EGR diluted SG50 and R-EGR diluted case have an increased u_L compared to normal EGR dilution due to the combustion of hydrogen-rich mixtures. In both cases (SG50 and R-EGR), the same $X_{MeOH,catalyst}$ and Y_{EGR} are used, 0.2 and 0.13 respectively. Although it is not possible to recover the same u_L as without EGR, the R-EGR concept provides faster burning velocities than the EFR concept. Additionally, the required volume of the vehicle's fuel tank in the R-EGR concept is much smaller than that of the EFR one (as there is no need for a water tank) [189]. For these reasons, the R-EGR concept is recommended for supporting high dilution levels when an SI engine is operated with a stoichiometric mixture.

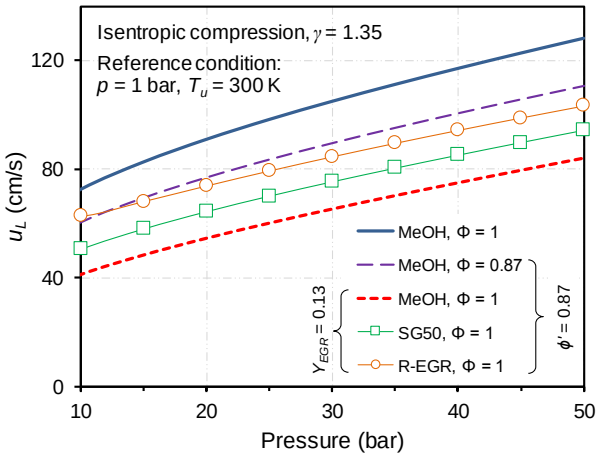

Figure 5.19: u_L as a function of pressure under isentropic compression.

5.5 Universal dilution term

In the R-EGR case, the LBV is expected to be higher than for conventional EGR at the same EGR ratio because of the presence of H_2 in the reactant. Therefore, the dilution term (ratio of diluted LBV to non-diluted LBV) in the two cases will

be different. In this part, a new dilution term correlation is proposed based on the reactant molar concentrations, which is applicable to both conventional EGR and R-EGR dilutions. The change in mixture concentration with different EGR ratio and reforming fraction can be presented by the variety of CO_2, CO and H_2O concentrations. Therefore, a new parameter is defined, $X_{dilution} = X_{CO_2} + X_{CO} + 3X_{H_2O}$. In which, X_{CO_2}, X_{CO} and X_{H_2O} is the molar fraction of CO_2, CO and H_2O in the reactant, respectively.

Figure 5.20 presents the molar fraction of all species which were derived from GT-Power. The molar fraction of N_2 is the largest, around 0.64 - 0.69. The molar fraction of other species is small, so the Y-axis was scaled down to 0.4. The first 8 cases are the reactants for different EGR ratio (no reforming), cases 9 - 13 represent the mixture for a fixed mass fraction of fuel for reforming (20%) and varied EGR ratios, cases 14-16 illustrate the mixture in the combustion chamber for a fixed EGR ratio (25%) and varied reforming fraction.

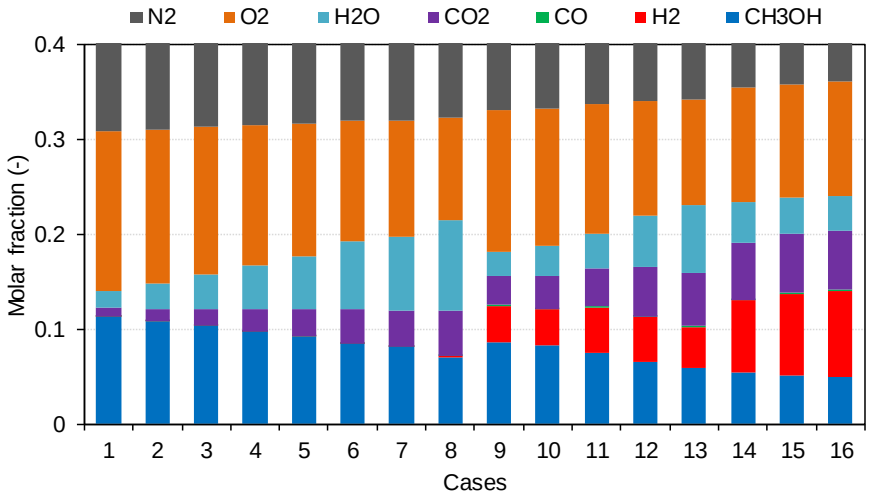

Figure 5.20: Molar fraction of all species in the combustion chamber with EGR dilution (cases 1-8), R-EGR with varied EGR ratio and 20% fuel for reforming (cases 9-13), and with fixed EGR ratio at 25% and varied reforming fraction (cases 14-16).

The dilution term is calculated as in equation 5.9, where the coefficients, a_1 and a_2, are a function of unburned gas temperature and pressure to fit the results from CHEM1D simulations [151] with the mechanism developed by Li et al. [70]. Figure 5.21 compares the calculated u_L using equation 5.3 together with equation 5.9 and the simulated u_L using CHEM1D for different pressure and unburned gas temperature. As can be seen, most of the points are within the standard deviation of ±10%. This dilution term will be employed with equation 5.3 for the cycle

engine simulation in Chapter 7.

$$f(dilution)_{new} = a_1 X_{dilution}^2 + a_2 X_{dilution} + 1 \tag{5.9}$$

$$a_1 = -0.0105(T_u - 600) + (-0.00222P^2 + 0.200943P + 0.218925) \tag{5.10}$$

$$a_2 = 0.0045(T_u - 600) + (0.000842P^2 - 0.07263P - 2.55193) \tag{5.11}$$

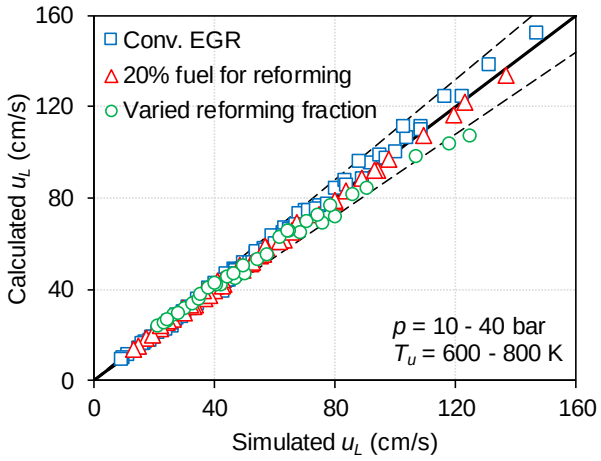

Figure 5.21: Comparison of u_L for the 16 cases shown in Figure 5.20 at different pressures and temperatures.

5.6 Closure

This Chapter presented laminar burning velocity studies, including the effect of syngas addition, evaluation of existing mixing rules, unburned gas temperature effects, development of a LBV correlation and a universal dilution term. The influence of unburned temperatures on the flame speed of methanol-syngas blends in air at atmospheric pressure was investigated first using CHEM1D. The calculations were performed over a wide range of equivalence ratios (0.5-2.0), and temperatures (300 K-900 K) at atmospheric pressure. The simulation showed that the laminar burning velocity of fuel blends increased dramatically with higher syngas contents. The influence of the syngas ratio became less important at stoichiometric conditions and at higher temperature. Several mixing rules were

examined for the prediction of laminar burning velocities of methanol-syngas blends in air. The mass fraction, mole fraction and energy fraction rules showed a worse prediction compared to the Le Chatelier and Hirasawa rules. However, no mixing rule outperforms the others. The averaged power exponents α at each equivalence ratio were calculated and compared with other α from developed correlations. Only a few correlations are predictive for mixtures close to the stoichiometric condition. The difference in α for methanol/syngas blends is very small with ϕ in the range of 0.5 - 1.5.

The laminar burning velocity correlations for engine simulations for the EFR and R-EGR concepts were then developed based on the simulation results. The simulation was performed over syngas ratios, fuel-air equivalence ratios, temperatures, pressures and EGR levels ranging from 0% to 50% by volume, 0.5 to 1.5, 550 to 800 K, 10 to 85 bar, and 0% to 30% by mass, respectively. The correlations were developed from the simulated data, and consist of 30 constants with a maximum error of 18%. The predicted u_L of methanol-air flames using the correlation in this study agreed well with the recent kinetic-based correlations. The predicted u_L of methanol/syngas in air fitted well with the calculated u_L using Hirasawa's mixing rule with a syngas content below 30%. A correlation for the reformed-EGR engine concept is also developed, at stoichiometric condition, with an averaged absolute error of 3.12%.

Based on the developed correlations, the required unburned gas temperature and equivalence ratio to meet a desired laminar burning velocity have been presented. The influence of dilution methods, EGR, R-EGR and air, is also investigated in this study. The diluted combustion with EGR was noted to produce lower laminar burning velocity than air diluted combustion. This is due to the reduction of O_2 concentration in the reactant and high heat capacity of EGR mixtures compared to air. With dilution using R-EGR, the laminar burning velocities increase with the mass fraction of methanol delivered to the catalyst and the same EGR ratio. With faster laminar burning velocities, the R-EGR technology is a promising approach to support high levels of EGR dilution in advanced SI engines for increased thermal efficiency. Finally, a universal dilution term was developed as a function of CO, CO_2 and H_2O molar concentration in the reactants. The developed dilution term is applicable to both conventional EGR and R-EGR dilution.

6

Reaction front properties

This chapter including all figures and tables was previously published in the Energy & Fuels journal [94]. The author Duc-Khanh Nguyen ran all simulations, did all calculations, wrote the paper and generated all figures and tables. The author Sebastian Verhelst contributed corrections, discussions and proof-reading.

6.1 Introduction

As explained in the previous chapter, in order to make a mixture of methanol-syngas with a 50%-50% ratio by mole (in the EFR concept), around 20% of the fuel mass needs to be supplied to the catalyst (with the remainder being injected directly into the combustion chambers). In the R-EGR concept, the amount of methanol that is injected into the EGR system is constrained by the concentration of water vapour in the exhaust gas. Around 20% of the fuel mass can be injected into the EGR system if the EGR ratio is 13% (to have water/methanol molar ratio of 1.5). The previous chapter showed that at stoichiometric conditions, with the same EGR ratio of 13% and mass fraction of methanol supplied to the catalyst (around 20% by mass), the laminar burning velocity in the R-EGR concept is faster than that of the EFR concept. The laminar burning velocity correlations for methanol-air mixtures enriched by syngas were also developed for both the

EFR and R-EGR concepts. However, the properties of the flame front like the knock behavior and flame structure at auto-ignition, and lower flammability limit have not yet been studied. The primary objective of this chapter is to analyze the reaction front characteristics of diluted methanol-air flames with the addition of fuel reforming products. The stable combustion regime, knock and flame limit of diluted methanol-syngas-air flames will be discussed. In this chapter knock is defined as the auto-ignition of the end gas after spark ignition, i.e. it is not pre-ignition.

6.2 Methodology

In order to analyze the flame structures, chemical kinetic calculations were performed using CHEM1D. CHEM1D was also used to calculate the flame thickness (δ_F) which was determined based on the temperature profile [190]. For analyzing the stable combustion regime with different dilution methods, the auto-ignition delay time (IDT or τ_{ID}) is needed. The ignition delay time was calculated using Cantera [69] as in Chapter 2. All the simulations were performed with the kinetic mechanism developed by Li et al. [70]. In the previous chapter, Li's mechanism was considered to be the best mechanism to predict the laminar burning velocity of methanol-syngas blends. A comparison of the ignition delay of methanol and syngas between simulation and experiments is presented in Figure 6.1. The ignition delays of both methanol and syngas were measured at the National University of Ireland - Galway, in the studies of Burke et al. [191] and Kéromnès et al. [192] respectively. As can be seen in this figure, the ignition delay of methanol is predicted almost perfectly with Li's mechanism. For syngas, the simulated data does not fit that well with the measured data, especially at low temperatures. However, according to Olm et al. [171], Li's mechanism predicts the ignition delay of syngas better than the USC-II 2007 mechanism (the second best mechanism to predict the laminar burning velocity of methanol-syngas blends). Therefore, this mechanism is employed in this investigation.

In the first parts of this chapter, all simulations are performed at a constant pressure of 40 bar, similar to previous studies [184, 188]. This is close to the end of compression pressure of a stoichiometric methanol-air mixture corresponding to an end gas temperature of 850 K if the pressure and temperature of the initial mixture are 1 bar and 343 K respectively. The temperature, equivalence ratio and EGR rate have been varied in a range of 600 - 1000 K, 0.6 - 1.0, and 0 - 40% by mass respectively. The impact of the gas properties is analyzed separately in section 6.3.4, as the end gas pressure and temperature after compression will change for different mixtures or dilution ratio. Two assumptions of the initial

mixture condition at intake valve closure were assumed, leading to a significant change in the end gas state, which will be explained later. To compare air and EGR dilution, the fuel-to-charge equivalence ratio ϕ' is used, see equation 2.8 (page 50).

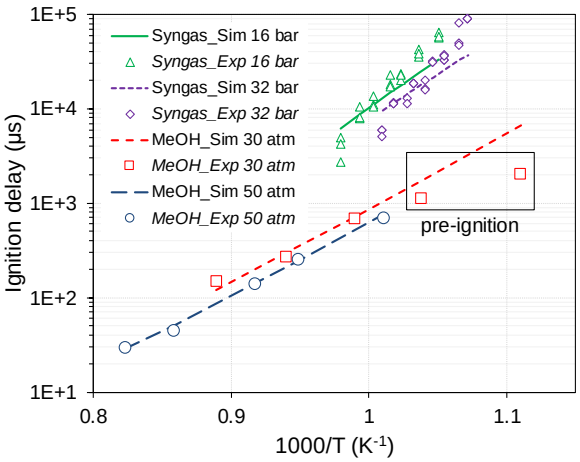

Figure 6.1: Comparison of ignition delay of methanol and syngas from experimental studies (symbols) of methanol [191] and syngas [192] versus simulated data (lines).

The flame structure analyses were performed at a constant fuel-to-charge equivalence ratio, $\phi' = 0.87$. Five mixtures were investigated, MeOH-Air, MeOH-EGR, SG50-Air, SG50-EGR and R-EGR. Methanol and methanol-syngas blend (50% - 50% by volume) is designated respectively as MeOH and SG50. The following characters, Air and EGR, are used for air and EGR dilution, respectively. In the air dilution cases, it is a lean combustion without EGR, so $\phi = \phi' = 0.87$. In contrast, the EGR dilution is done at stoichiometric condition only, which is the preferred operating condition in SI engines to achieve the highest conversion efficiency of the three-way catalyst. In the R-EGR case, because of the complexity of the reforming process in the presence of oxygen left in the exhaust gas when the engine is operated under lean combustion, this concept is also investigated at stoichiometric conditions only.

6.3 Results

6.3.1 Stable regime of diluted combustion

In the research of Lavoie et al. [99], a multi-mode combustion diagram was proposed, based on the constraints of each region. For instance, the SI region is restricted at $\phi' \leq 1$, by the flame and knock limits. The flame limit is a constant flame speed contour that passes through T_b = 1900 K, based on findings from experimental engine data of Flynn et al. [193]. That limiting temperature is associated with the reaction rate balance within the flame front, which is driven by fundamental hydrocarbon kinetics, presenting a boundary for a sufficiently fast combustion [193]. When T_b falls below 1900 K, flame quenching or local quenching will occur. This value for T_b was observed with hydrocarbon fuels, and most likely does not represent the lower limit for the combustion of oxygenated fuels like methanol and a non-carbon fuel like hydrogen. Therefore, different T_b values should be used for each mixture, requiring fundamental studies for these fuels. For simplicity, instead of a lower temperature limit, a lower limit for laminar burning velocity u_L is assumed here. A value of u_L between 10 - 15 cm/s is considered as the flame limit for iso-octane [99]. With the faster laminar burning velocity of methanol compared to iso-octane [153, 176], a constant value of laminar burning velocity u_L = 15 cm/s is employed to represent the lower limit of the SI region for methanol.

For the upper limit of the SI region, a knock limit line is defined, as the temperature of unburned gas reaches ~1000 K [99]. That temperature is considered as the knock limit of gasoline (iso-octane), and that value will also be changed when a new fuel is used. Other research used the residence time, τ_{RES}, as an indicator of knock occurrence. If $\tau_{ID} < \tau_{RES}$, the end gas auto-ignites before the flame fully consumes the charge [81]. This is a very rough approach to define the knock limit in SI engines, as knock is strongly influenced by the end gas pressure, temperature, and mixture composition but is used here for its simplicity. The residence time is a function of engine speed and residence period in crank angle degrees, and it was defined in Chapter 2 (see equation 2.6). The residence time is 1.125 ms at an engine speed of 2000 rpm. This value is in the range of ignition delay when knock occurs, as in the research of Kalghatgi et al. [194]. Therefore, this value of ignition delay will be used here as the upper boundary for the SI region.

Figure 6.2 shows the simulated ignition delay τ_{ID} of five mixtures versus ϕ' at 40 bar and T_b = 850 K. The unburned temperature of 850 K is selected because that value is the minimum temperature to initiate auto-ignition of methanol [195]. The calculated ignition delay of iso-octane (iC8H18) and ethanol (EtOH) at lean

conditions, using Arrhenius type correlations [196, 197], were also plotted in the figure. The trends of τ_{ID} of iso-octane and ethanol which are calculated using Arrhenius correlations are similar to the simulated data of methanol and SG50, i.e. a longer ignition delay with a leaner mixture. The ignition delay in the EGR diluted cases also present a similar trend, the ignition delay increases with rising EGR ratio [198]. Only the R-EGR mixture shows a significant improvement of τ_{ID} with a reduction of ϕ' due to the important growth of the H_2 mole fraction in the reactant. SG50 has a longer τ_{ID} than that of MeOH because of the presence of H_2 in the reactant and a lower O_2 concentration. Compared to the air diluted cases at the same ϕ', the τ_{ID} of EGR diluted mixtures are slightly shorter with both MeOH and SG50 fuels.

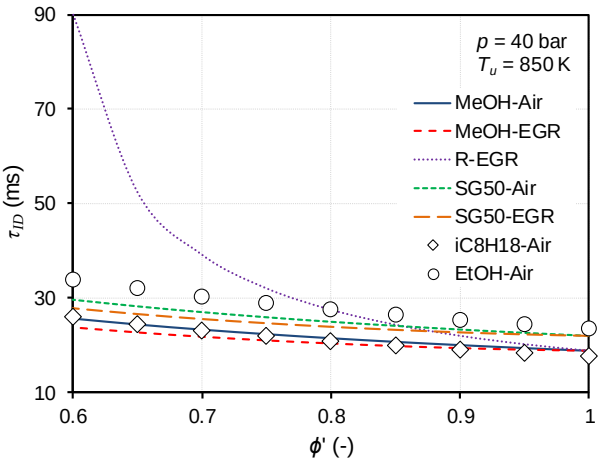

Figure 6.2: τ_{ID} versus ϕ' at p = 40 bar, T_u = 850 K. Simulated data with Li's mechanism 51 (lines) vs. calculated ignition delay of iso-octane and ethanol at lean conditions using Arrhenius correlations [196, 197] (symbols).

Based on the relationship of τ_{ID} and T_u, the required T_u to achieve the desired τ_{ID} = 1.125 ms is found at each ϕ'. Figure 6.3 presents the contours of constant τ_{ID} (the upper limit) and laminar burning velocity, which is derived from the developed correlation (the lower limit) in Section 5.4 in the T_u-ϕ' domain at 40 bar. Five mixtures were compared. As can be seen in this figure, there is one trend that was observed for all mixtures: the knock limit is extended to a higher value of T_u when increasing the dilution level, therefore the auto-ignition of the end gas is inhibited with a diluted mixture at the same pressure. This can be explained by the increase of τ_{ID} when ϕ' decreases, as shown in Figure 6.2. Higher temperature leads to a reduction of ignition delay. Therefore, the fuel which has a longer ignition delay can cope with a higher temperature before reaching the same value of ignition delay compared to high reactivity fuels. With the addition of syngas, the upper

limit is also extended to a higher value of T_u. In the R-EGR case, at a higher EGR rate, the upper T_u limit can be increased significantly. Therefore, at a higher dilution level, R-EGR seems to be a promising concept to decrease the knock tendency.

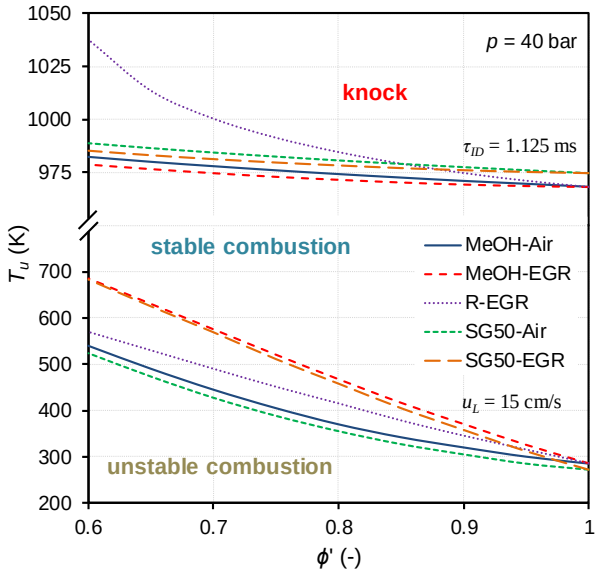

Figure 6.3: Stable combustion diagram of five mixtures in T_u-ϕ' domain at 40 bar. The upper limit lines separate knock and normal combustion, and the lower limit lines separate stable (normal) and unstable combustion (quenching).

Looking at the lower limit of the stable combustion regime, at low dilution levels, unstable combustion is no issue with a homogeneous charge because the combustion only becomes unstable at a very low T_u. That temperature is almost impossible to reach when the charge is compressed to 40 bar. If the dilution level is larger, the T_u to achieve a stable flame propagation needs to be increased. Therefore, to avoid quenching or partial combustion during cold starts, it is recommended that the engine initially operates at stoichiometric condition without EGR. Furthermore, if the engine is operated with a stratified mixture and temperature inhomogeneities, there are unwanted phenomena at the locations which have a high dilution level or low local temperature. Therefore, if an EGR system is applied to turbocharged SI engines to dilute the combustion, low pressure loop EGR is recommended for a better mixing to avoid abnormal combustion during the flame propagation.

As can be seen from the lower and upper limits, air dilution has a wider range for T_u to achieve a stable flame propagation than EGR dilution. With air dilution, stable

combustion can be observed at a higher dilution rate (smaller ϕ'), therefore air dilution is favored. If NO_x emissions are considered, operation at stoichiometric condition with EGR-type dilution is preferred to achieve a higher conversion efficiency of the TWC. In that case, R-EGR is a promising approach to extend the dilution limit of the engine to get a higher fuel efficiency.

6.3.2 Knock behavior at the upper limit

In order to analyze the heat release at the knock limit, the ratio of ignition delay to reaction front time τ_{ID}/τ_F when knock occurs is used. The reaction front time τ_F (or chemical time scale) is the time during which the flame propagates by a distance of once its flame thickness, and is calculated as

$$\tau_F = \frac{\delta_F}{u_L} \tag{6.1}$$

where δ_F is the flame thickness, which is calculated using CHEM1D based on the flame temperature profile [190]. The laminar burning velocity is derived from the developed correlation in the previous chapter. This ratio presents the chemical time scale, i.e. a large τ_F value means a slow chemical reaction. As the chemical time scale increases, the flame front moves slower when crossing the flame thickness which separates the burned zone from the unburned zone [199].

Schmid et al. [200] concluded that the turbulent burning velocity could be related to the molecular diffusivity a_0 of the mixture and the chemical time scale as in equation 6.2. In this research, the impact of turbulent combustion is not considered, therefore this parameter is used as a metric to present the speed of combustion for each mixture at different ϕ'.

$$u_t = 1.2\sqrt{\frac{a_0}{\tau_F}} \tag{6.2}$$

Figure 6.4 shows the τ_{ID}/τ_F ratio (or τ_{RES}/τ_F ratio) at the knock limit, $\tau_{RES} = 1.125$ ms. The ratio also presents the number of flame thicknesses over which the flame passed. A higher τ_{ID}/τ_F ratio means the residence time is long enough for the flame development. Because τ_{ID} is a constant, a lower value of τ_F increases the τ_{ID}/τ_F ratio. Schmid et al. [200] assumed that the rate of heat release is proportional to the inverse of τ_F, so more heat is released by the flame with a lower τ_F mixture (or higher τ_{ID}/τ_F ratio). As can be seen in the Figure, when auto-ignition occurs,

the τ_{ID}/τ_F ratio for the air dilution cases is larger than for the EGR dilution cases. When the dilution level increases, the ratio decreases. Therefore, more fuel energy is consumed by the flame and less energy is released by the auto-ignition for air dilution. The fraction of heat release by auto-ignition increases with the decrease of ϕ'. When the end-gas spontaneously auto-ignites, a rapid release of the remaining fuel energy will generate high-amplitude pressure waves. Because the mixture energy is not identical between the cases, one cannot conclude that the ringing intensity increases for a higher fraction of the auto-ignition heat release. In the final part of this chapter, a comparison at the same energy content is performed to compare the ringing intensity.

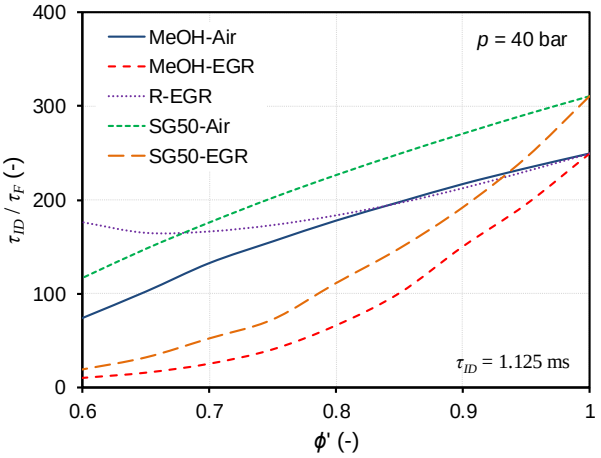

Figure 6.4: τ_{ID}/τ_F ratio versus ϕ' when knock occurs (τ_{ID} = 1.125 ms) at 40 bar.

6.3.3 Flame structures at the lower limit

In this section, the flame structure at the flammability limit (u_L = 15 cm/s) was analyzed. The simulation was performed at p = 40 bar, ϕ' = 0.87, and a T_u which was adjusted to ensure a resulting flame speed of 15 cm/s (as shown in Figure 6.3). The required T_u to achieve a laminar flame speed of 15 cm/s for MeOH-Air, MeOH-EGR, R-EGR, SG50-Air and SG50-EGR cases respectively is 333 K, 398 K, 365 K, 317 K and 385 K. Figure 6.5 shows the temperature profile of the five mixtures as a function of the axial distance. The burned temperature T_b of the five mixtures is around 2120 - 2160 K. In the research of Flynn et al. [193], the end of combustion flame temperature is estimated using a constant pressure, adiabatic condition, at the point where 95% of the total heat release has occurred. The flame temperature at the point where 95% of the total heat released is calculated, was

around 1983 K, 1952 K, 1942 K, 1965 K and 1936 K for MeOH-Air, MeOH-EGR, R-EGR, SG50-Air and SG50-EGR, respectively (see symbols in Figure 6.5).

The flame temperature is lower with the dilution of EGR (same fuel) because of a higher heat capacity of the burned gases. These temperatures are similar to the data cloud in the research of Flynn et al. [193]. As can be seen, there is a very small difference between the temperature profiles of MeOH and SG50. Compared to the EGR-type dilution cases (R-EGR, MeOH-EGR and SG50-EGR), although the unburned gas temperature is lower, the air dilution cases have a higher burned gas temperature. The T_b of the R-EGR mixture is higher than that of the normal EGR dilution (MeOH-EGR and SG50-EGR) and lower than the air dilution cases. This can be explained by the concentration of burned products like carbon dioxide (CO_2) and water vapour (H_2O), species which have higher heat capacity values. In the air dilution cases, because no combustion products are present and there is a greater oxygen concentration, T_b is higher than for the EGR-type dilution cases. Compared to normal EGR dilution, the R-EGR case has a higher T_b due to a smaller concentration of water vapour in the reactant because it was consumed partly for the reforming.

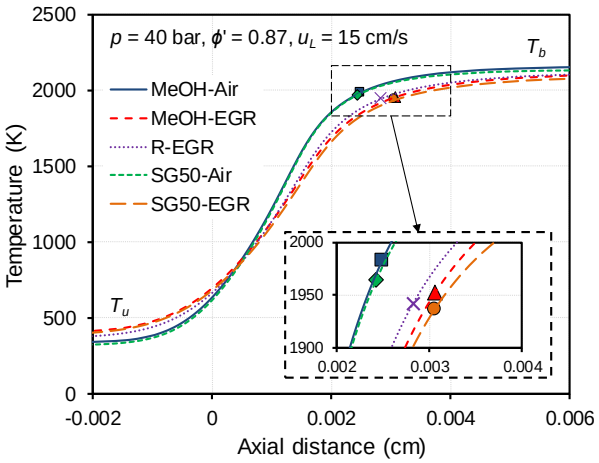

Figure 6.5: Temperature profiles at lower flammability limit, p = 40 bar and $\phi' = 0.87$. Symbols: the flame temperature and location where 95% total heat release occurred.

The concentrations of four main species (CH_3OH, O_2, CO_2 and H_2O) are compared between MeOH-Air and SG50-Air in Figure 6.6. Because of its replacement by syngas, the mole fraction of CH_3OH in the unburned zone of the SG50-Air case is obviously smaller than for the MeOH-Air case. The stoichiometric air to fuel ratio (by mole) of syngas is much smaller than that of methanol (~1.81 compared to 7.14), so the required amount of O_2 to have the same $\phi = 0.87$ when syngas is

added is lower than for pure methanol combustion. However, CH_3OH is almost consumed at the same location. CO_2 is a product of the fuel reforming process, so the initial CO_2 concentration is higher with the addition of syngas. In this study, syngas is a product of steam reforming, therefore the mole fraction of H_2O increases faster to a higher concentration for the enrichment with syngas. With a higher heat capacity of H_2O, the combustion temperature of SG50 is lower than methanol if EGR is used to dilute the combustion, as can be seen in Figure 6.5.

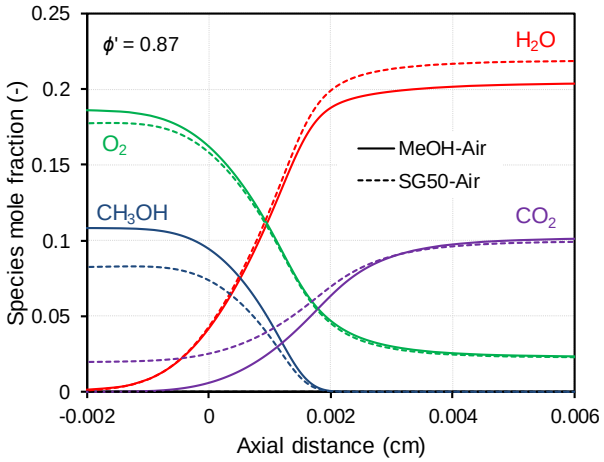

Figure 6.6: Comparison of species mole fraction between MeOH-Air and SG50-Air cases at $\phi' = 0.87$.

To compare the air and EGR dilution, the mole fraction of the mentioned species of the SG50-Air case was plotted together with the SG50-EGR case, as shown in Figure 6.7. In the EGR dilution case, the mole fraction of O_2 in the unburned region is much lower than for the air dilution case. Although the simulation is carried out at a similar ϕ', the mixture for the EGR dilution cases is stoichiometric ($\phi = 1$), so the O_2 in the burned zone is almost completely consumed. The combustion products concentrations, CO_2 and H_2O, are higher in both the unburned and burned zones, leading to a lower combustion temperature.

The SG50-EGR case is then compared to the R-EGR one in Figure 6.8. At $\phi' = 0.87$, the mass fraction of methanol for fuel reforming and the EGR ratio for the SG50-EGR and R-EGR cases are identical. Therefore as can be seen in Figure 6.8, the molar concentrations of CH_3OH, O_2 and CO_2 are related for these two cases. In the SG50-EGR case, a slightly lower concentration of CH_3OH and O_2 can be observed in the unburned mixture because of their displacement by H_2O, which is not partly consumed for the fuel reforming as in the R-EGR concept. The H_2O concentration is smaller in the R-EGR case both in the unburned and burned

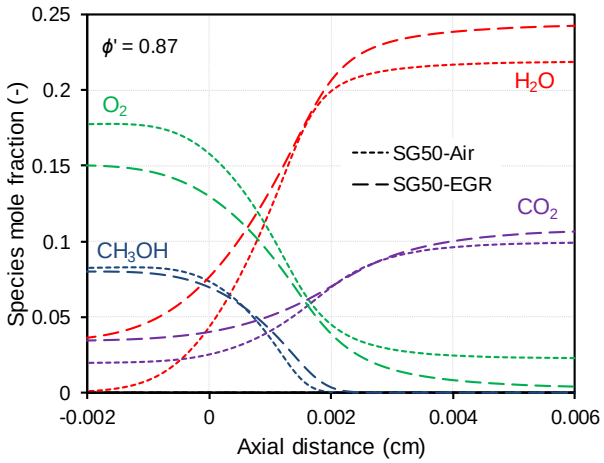

Figure 6.7: Comparison of species mole fraction between SG50-Air and SG50-EGR cases at $\phi' = 0.87$.

zones because the water vapour in the EGR mixture is consumed partly for the steam reforming of methanol. The higher H_2O concentration in the SG50-EGR case leads to a decrease in the burned temperature (see Figure 6.5).

Figure 6.9 shows the mole fraction of H_2 and CO, two components of syngas, as a function of axial distance through the flame. In the combustion of methanol (MeOH-Air and MeOH-EGR cases), hydrogen only appears as an intermediate species. In these cases, the hydrogen concentration grows and reaches its peak at around the flame layer position. With the dilution of EGR-type mixture, the hydrogen concentration increases faster and reaches a peak at a higher concentration. The H_2 mole fraction in the burned zone is also higher because the H atom is less consumed by H-abstraction reactions at a lower combustion temperature [201]. In the R-EGR and SG50 cases, H_2 is present as a fuel component, so going from left to right, its concentration falls and almost equals the concentration in the combustion of methanol. Three EGR-type dilution cases (R-EGR, MeOH-EGR and SG50-EGR) have a higher H_2 concentration in the burned zone. As can be seen, the consumption rate of H_2 in the R-EGR case is a bit faster than that of the SG50-EGR case, which might be due to a smaller concentration of water vapour in the reactant.

The CO concentration is also plotted in Figure 6.9. Although CO is a component of the methanol steam reforming product, CO is still an intermediate species in the R-EGR and SG50 cases. Compared to the EGR-type dilution cases, the air dilution cases have a lower CO concentration, which agrees with the typical trend of CO

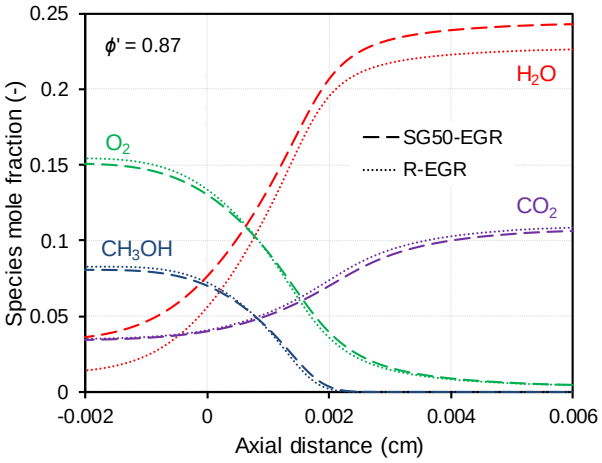

Figure 6.8: Comparison of species mole fraction between SG50-EGR and R-EGR cases at $\phi' = 0.87$.

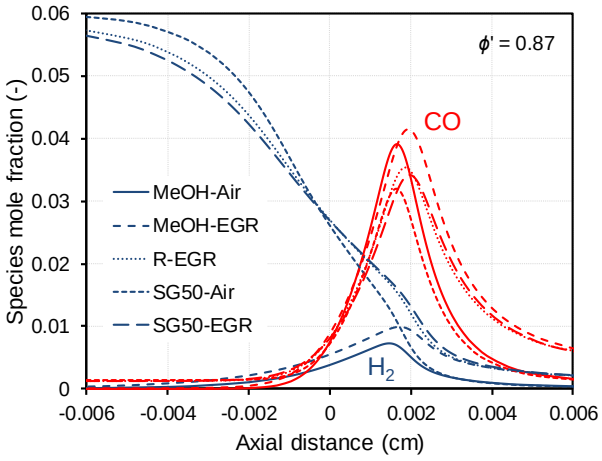

Figure 6.9: Comparison of H_2 and CO mole fraction between five cases at $\phi' = 0.87$.

emission with lambda. The difference in CO mole fraction is very small between methanol and SG50, in both the air and EGR dilution cases. This can be explained as follows. First, the higher gas temperature promotes the CO oxidation, so the case which has a lower T_b results in a higher concentration of CO. The burned temperature of methanol and SG50 are similar, so the CO emission is almost the same between the two fuels. Second, the ratio of hydrogen to methanol (or H/C ratio) increases when syngas is added, leading to the decrease of carbon-related emissions like CO [202]. This is similar to the observation in the research of Han et al. [203], where the CO concentration in exhaust gases was higher with EGR dilution compared to air dilution (at the same $\phi' = 0.8$), and there was no clear change in CO emissions with varied syngas fraction.

6.3.4 Influence of gas properties

In the previous parts, the comparison was conducted at a constant pressure. However, this is not a good basis for the comparison of different mixtures in real engines. In this part, to simulate the condition of the end gas after compression in SI engines, the influence of gas properties is considered. Two scenarios for the intake charge condition at intake valve closure (IVC) were considered in this study: the first case is the same initial pressure and temperature, a pressure of 1 bar and a temperature of 343 K, for all mixtures (constant inlet pressure scenario), the second one is the same initial temperature (343 K) and the same energy content (constant inlet energy scenario). In the first scenario, because the energy content varies with different mixtures as well as ϕ', there is a penalty on engine performance when it works with a diluted mixture. In the second scenario, the initial pressure of the diluted mixtures at IVC was increased to result in the same amount of energy as for the undiluted mixture. The reference pressure is 1 bar for the stoichiometric methanol-air case without EGR.

The specific heat ratio γ as a function of temperature for each mixture at different ϕ' were calculated using NASA polynomial coefficients. Assuming the compression is adiabatic, the maximum compression is assumed to be reached when the end gas temperature reaches the auto-ignition temperature of a methanol-air mixture. With the auto-ignition temperature of methanol being 850 K [63], this "compression ratio" is then calculated, using the specific heat ratio γ of a stoichiometric methanol-air mixture at 850 K, as follows

$$CR = \sqrt[\gamma-1]{\frac{T_{end}}{T_{IVC}}} = 17.74 \tag{6.3}$$

This compression ratio is used for all mixtures to calculate the end gas temperature and pressure using the γ value at the end of compression (γ at T_{end}, as shown in Figure 6.10). As can be seen in this figure, γ decreases with the increase of the EGR ratio in two normal EGR dilution cases (MeOH-EGR and SG50-EGR). Although the mass fraction of methanol (which has the lowest γ) reduced with the increase of EGR ratio, the oxygen mass fraction is also decreased. Therefore, the overall γ of the mixture declines with a higher dilution ratio. This shows a different trend compared to the research of Alger et al. [204], where the cycle-averaged γ is used to compare different EGR ratios. Due to a lower combustion temperature with EGR dilution, the cycle-averaged γ is increased with increasing EGR ratio. Here, the impact of combustion temperature is neglected, so that γ is a function of only compression temperature and mixture composition. The end gas temperature and pressure calculated from isentropic compression were then used as the initial conditions for the ignition delay prediction. In both scenarios, because the initial temperature and the compression ratio are the same, there is no difference in end gas temperature after compression.

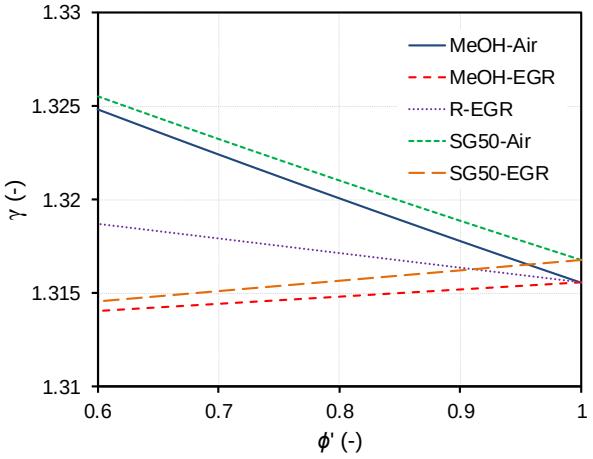

Figure 6.10: Specific heat ratios as a function of ϕ' of five mixtures after compression. The initial gas temperature is 343 K and compression ratio is 17.74.

In the constant inlet pressure scenario, the end gas pressure follows the trend of γ: decreasing in the two normal EGR dilution cases (MeOH-EGR and SG50-EGR), and increasing in the air dilution and R-EGR cases with the reduction of ϕ'. However, in the constant inlet energy scenario, due to the difference in initial pressure, the end gas pressure increases with the increase in dilution ratio. At $\phi' = 0.6$, the maximum difference between the five mixtures in pressure and temperature is around 6 bar and 35 K respectively. Because of a higher end gas pressure in the second scenario with $\phi' < 1$, the ignition delay is shorter compared

to the first scenario, as can be seen in Figure 6.11. However, the trend is similar in both scenarios: the ignition delay is shorter with lower ϕ' in the two air dilution cases (MeOH-Air and SG50-Air) and vice versa in the three EGR type dilution cases (MeOH-EGR, R-EGR and SG50-EGR). The trends in the two air dilution cases are reversed versus the trends observed in Figure 6.2: the ignition delay decreases instead of increases with a smaller value of ϕ'. This can be explained by the increase of end gas temperature after compression with a leaner mixture, which is not a constant temperature like was assumed for Figure 6.2. Based on the ignition delay trends, we can conclude that the knock tendency decreases with EGR type dilution, with R-EGR having a lower knock tendency compared to the SG50-EGR case for $\phi' \leq$~0.85. However, the knock tendency increases with a leaner mixture.

For the constant inlet energy scenario, this is similar to the conclusion of Topinka et al. [205], however it is opposite to the findings with a constant inlet pressure scenario. There, this can be explained by a lower peak combustion pressure due to a lower energy content, so the end gas temperature is lower in that scenario. Therefore a longer ignition delay will be observed, and the knock tendency decreases with lean operation [205]. As in this research, since the impact of flame propagation is neglected, the decrease of the peak pressure (as well as the end gas temperature) cannot be captured. Therefore the increase of ignition delay for a lean mixture is not predictable in the constant inlet pressure scenario. For the constant inlet energy scenario, the effect of flame propagation on peak combustion pressure can be accounted for. The peak combustion pressure is dependent on the pressure at ignition timing as well as on the combustion speed. A diluted mixture has a higher pressure at spark timing and a slower burning velocity, based on this trade-off and the same indicated mean effective pressure (due to the same energy content), and we can assume that the peak combustion pressure is similar in all cases. Therefore, the next analyses will be done for the constant inlet energy scenario.

Assuming the compression of the unburned gas (or end gas) is adiabatic, Figure 6.12 illustrates the end gas temperature versus end gas pressure at different ϕ' and dilution methods (air vs. EGR) for the constant inlet energy scenario. Ignoring the change of γ during the compression, a specific value of γ for each mixture at 850 K was used to calculate the end gas conditions. Because the energy content of the diluted mixtures is less than of the undiluted one, a higher initial pressure needs to be introduced, leading to a higher end gas pressure. However, the end gas temperature is dependent on only compression ratio, γ and initial temperature, so the difference in end gas temperature is much smaller than the difference in end gas pressure. Furthermore, since the energy content of the EGR diluted mixture is lower than of the air diluted one (at the same ϕ'), the initial pressure of the

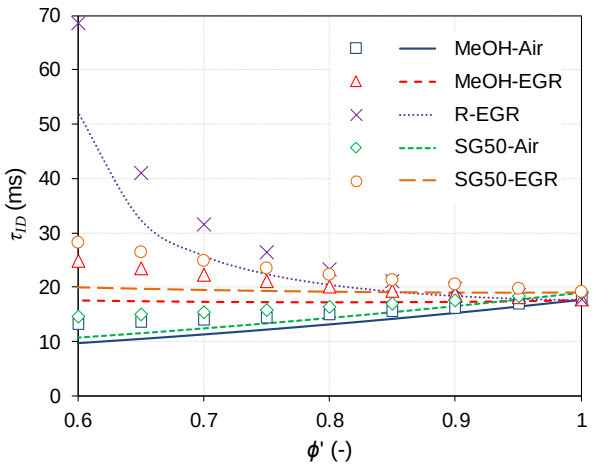

Figure 6.11: Influence of gas properties on the ignition delay in two cases. Case 1: similar initial pressure of 1 bar (symbols) vs. case 2: similar energy content (lines).

EGR diluted mixture needs to be higher, so the end gas pressure increases further. Therefore, at a given pressure, the end gas temperature is lower with a higher dilution ratio (lower ϕ') and the end gas temperature for the EGR dilution cases is lower than for the air dilution ones (same ϕ').

Figure 6.13 shows the pressure and temperature of the end gas when knock occurs (τ_{ID} = 1.125 ms) with ϕ' varying from 1 to 0.6 ($\Delta\phi'$ = 0.05 for each step) for the five mixtures in the constant inlet energy scenario. As can be seen in the figure, the case of methanol at ϕ = 1 experiences knock when the end gas is compressed to a pressure of ~72 bar and a temperature of ~955 K. For the stoichiometric SG50-air mixture this is ~73 bar and ~962 K, respectively. As the increase of end gas pressure is more significant than of the end gas temperature for an EGR diluted mixture, that mixture can be auto-ignited at a lower temperature and higher pressure compared to an undiluted one, as can be seen in Figure 6.13. In the two air (MeOH-Air and SG50-Air) and the two EGR dilution cases (MeOH-EGR and SG50-EGR), the auto-ignition of the end gas is almost independent of the temperature, with only a very small change in the end gas temperature with a diluted mixture, at ~955±5 K and ~962±5 K respectively. Knock for the R-EGR case is only experienced at a higher end gas pressure and temperature when ϕ' decreases, which is mainly due to the increase of the hydrogen concentration with increasing EGR ratio, which is a chemical effect.

Figure 6.14 shows the τ_{ID}/τ_F ratio at the end gas conditions which were presented in Figure 6.13. The trend is similar to the comparison at 40 bar (see Figure 6.4),

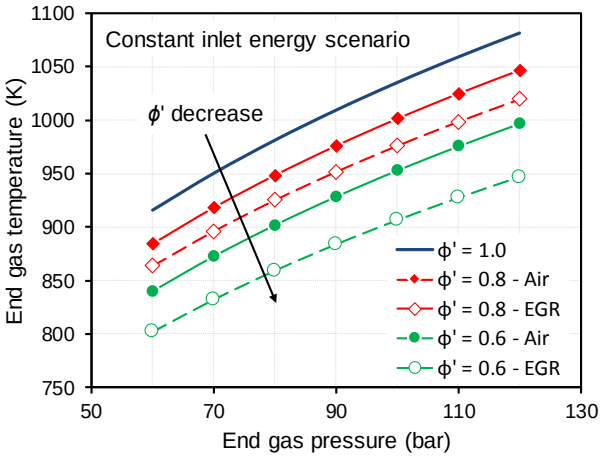

Figure 6.12: End gas temperature versus end gas pressure for different ϕ' and dilution methods for the constant inlet energy scenario. Trajectories represent the end gas conditions when knock occurs.

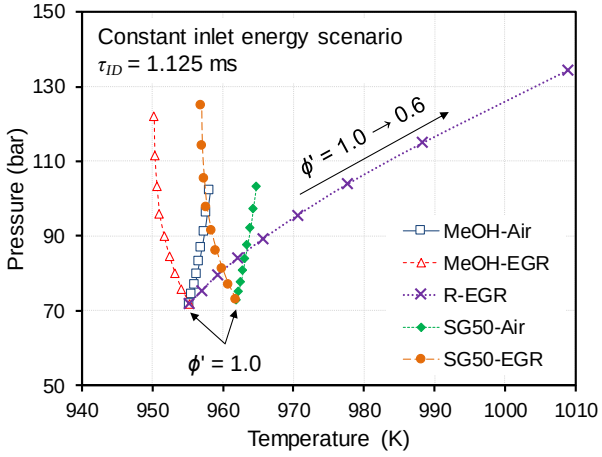

Figure 6.13: End gas conditions when knock occurs (τ_{ID} = 1.125 ms) for the constant inlet energy scenario.

i.e. the ratio decreases with increasing dilution ratio (reducing ϕ'). In this scenario, the energy is similar for all mixtures, therefore knocking can be compared between the different fuels. The amount of heat released by auto-ignition reduces for a fuel which has a higher τ_{ID}/τ_F ratio, therefore the knock intensity reduces. As can be seen, at $\phi' = 0.87$ (in this case, the SG50-EGR and R-EGR cases have the same mass fraction of methanol fed to the catalyst and the same EGR ratio), the τ_{ID}/τ_F ratio of the R-EGR mixture is higher than of the SG50-EGR mixture, therefore the pressure oscillation due to knock is reduced for the R-EGR case. At $0.9 \leq \phi' \leq 1.0$, the SG50-EGR case is better than R-EGR in terms of ringing intensity.

Compared to lean combustion of methanol, dilution with an R-EGR mixture can reduce the ringing intensity. Air dilution has a larger amount of fuel energy consumed by the flame and less energy released by the auto-ignition than for dilution by EGR. Although the knock tendency for the air dilution case is higher, when the knock occurs, the EGR dilution case has a higher ringing intensity [206]. The phenomenon is similar to what happens in SACI (spark assisted compression ignition) engines, it is more SI-like combustion with air dilution and more HCCI-like combustion with EGR dilution. When diluted with an R-EGR mixture, it is more SI-like combustion than other EGR dilution cases and the mixture is stoichiometric, so this strategy is recommended for the SI engines to enable an increase in dilution ratios as well as to achieve a high conversion efficiency of the three-way catalyst. Because SI engines have a higher specific energy content of the charge (ϕ') than SACI engines ($0.65 \leq \phi'_{SI} \leq 1$ instead of $0.45 \leq \phi'_{SACI} \leq 0.65$) [46], once knock develops, very strong knock will be observed.

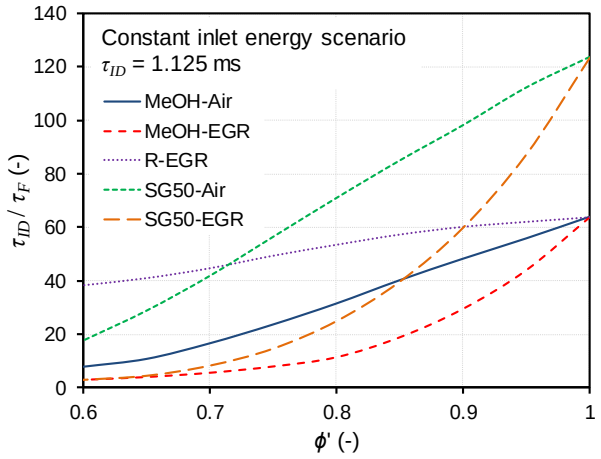

Figure 6.14: τ_{ID}/τ_F ratio versus ϕ' when knock occurs (τ_{ID} = 1.125 ms) for the constant inlet energy scenario.

6.4 Closure

This chapter presented fundamental investigations of the flame front properties for diluted methanol/air combustion. The simulation was performed at engine-like conditions to gain insight into the stable combustion regime, flame structures, and knocking behavior with different kinds of dilution. Note that the conclusions of this chapter do not correspond directly to the engine efficiency. However, the change of the flame front properties could be used to predict the engine behavior with these dilutions.

The simulation showed that the upper limit of the unburned gas temperature is extended with higher dilution levels, especially in the case of the R-EGR mixture. At that limit, the fraction of auto-ignition heat release is lower with the dilution by air. The knock propensity is reduced with the addition of syngas. At the flammability limit, compared to EGR dilution, the air dilution cases have a lower T_u limit to get a stable flame. The limit is also extended to a lower value of T_u when syngas is added. The engines are able to operate at higher dilution ratio and higher compression ratio with R-EGR dilution compared to the conventional EGR dilution. This causes an increase in engine efficiency.

With the addition of syngas, the concentration of water vapour in the burned zone increases. It is further improved when EGR mixture is used to dilute the combustion. If the mixture is diluted by R-EGR mixture, the water vapour is reduced in both unburned and burned zones due to the consumption of part of the water for the fuel reforming. This results in a higher combustion temperature and more heat losses to the walls compared to conventional EGR dilution. The concentration of H_2 and CO in the combustion product when using EGR-type dilution is higher than for the air dilution cases, this means combustion efficiency decreases.

The influence of gas properties was also investigated for a constant inlet energy scenario. After compression, the end gas condition is significantly changed between the five mixtures, especially at low ϕ', resulting in a shorter ignition delay for a leaner mixture and a longer one for higher EGR rates. Therefore, the knock tendency increases with the decrease of equivalence ratio and it decreases with the increase of EGR ratio. In the R-EGR case, knock occurs at a higher pressure and temperature when ϕ' decreases from 1 to 0.6. Compared to the EGR dilution cases, air dilution has a higher knock tendency. However, the ringing intensity decreases for the dilution with air. At a higher dilution ratio ($\phi' \leq 0.85$), R-EGR has a lower ringing intensity compared to the two normal EGR dilution cases and a lower knock tendency compared to the two air dilution cases.

7 Engine simulation

7.1 Introduction

In Chapter 4, the R-EGR concept showed a small improvement in the Otto cycle efficiency with fuel reforming. After taking the heat loss into account, the difference in gross indicated thermal efficiency between R-EGR and conventional EGR dilution is almost negligible. However, this comparison was performed with the same combustion duration and a simple estimation of relative heat loss. The impact of changes to the laminar burning velocity, gas exchange, turbulence, etc. have not been considered. In this Chapter, a gas-dynamic engine cycle simulation was performed using GT-Power. This work has previously been published in the Fuel journal [93]. The authors' contributions are presented in previous chapters. Figures were updated with the most recent results.

7.2 Methodology

A commercial one-dimensional engine code, GT-Power from Gamma Technologies, was used. The full engine model includes two main parts: engine and fuel reformer. The engine model was built and calibrated first. The

R-EGR system was then added into the model with the fuel reforming reaction mechanism which was modified and calibrated with experimental data. The Volvo T3 engine was selected as a case study. This engine was mentioned previously and the engine specifications are listed in Table 2.1. More information about the engine and the experimental setup can be found in Chapter 2. The experimental results were used to validate the base model.

7.2.1 Building of engine model

Figure 7.1 shows the model of the Volvo T3 engine in GT-Power. The baseline engine does not include the EGR system. The engine model was built step-by-step. First, the cylinder was constructed with a user-combustion model. A burn rate from the TPA simulation at full load (see Chapter 2) was implemented. The intake and exhaust systems were then added with correct dimensions, materials and friction coefficients. The pressure loss connection was used to simulate the K & N air filter with the pressure drop table from the flow bench test results. The pressure drop over the TWC was adjusted to have the same averaged exhaust pressure as in the experiments. The gas dynamic model of the engine was calibrated based on the intake and exhaust pressure profiles from experiments.

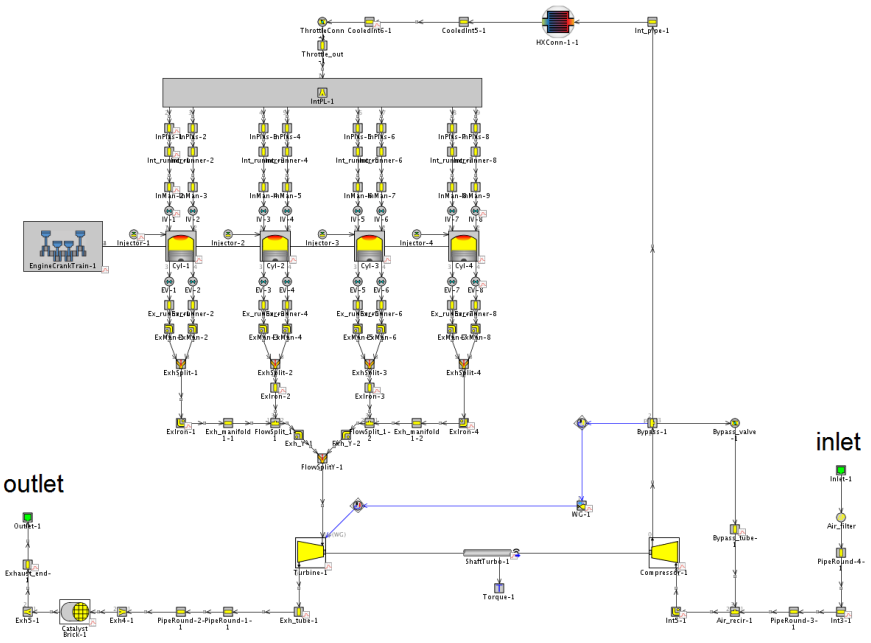

Figure 7.1: GT-Power model of Volvo T3 engine.

After the gas-dynamic model was calibrated, the combustion model was shifted to a predictive turbulent combustion model, *SITurb*, in GT-Power. The developed LBV correlation for the non-EGR case and the universal dilution term were used to calculate the LBV (see Chapter 5). Similar to the previous work of Nguyen et al. [74], the initial flame kernel size was calibrated to match the ignition delay (CA0-2) to the experiments. An initial flame kernel size of 2.6 mm was used in all simulations. The standard turbulent combustion model from GT-Power was employed. The *Turbulent Kernel Growth Multiplier* and *Taylor Length Scale Multiplier* were set equal to 1 (standard settings), the *Turbulent Flame Speed Multiplier* was changed to 1.05. Heat transfer (model of Morel et al. [47], heat transfer multiplier table for methanol, and wall temperature estimation) and fuel spray settings were set similar to the TPA simulation in Chapter 2.

Figure 7.2 compares the intake and cylinder pressures from simulation and experiment for methanol at the same engine speed (1500 rpm), same ignition timing (12 CAD bTDC$_f$), same throttle angle (11.4%) and same valve timing (standard). As can be seen, the simulation is in good agreement with the experiment. The model is ready for the addition of the R-EGR system.

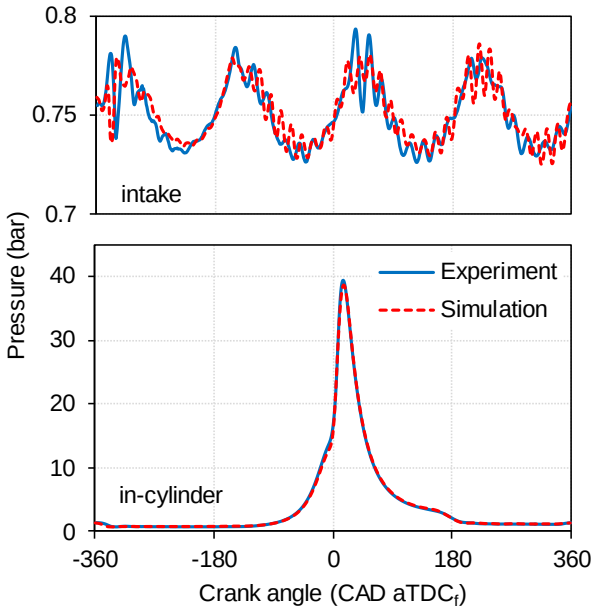

Figure 7.2: The comparison of the intake and the in-cylinder pressures between simulation and experiment for methanol at a throttle angle of 11.4%, ignition timing of 12 CAD bTDC$_f$, standard valve timing, and engine speed of 1500 rpm.

7.2.2 Building of R-EGR system

Before adding the R-EGR system into the full engine model, the surface reaction mechanism was modified and calibrated. A simple surface reaction mechanism was used, which includes three main reactions: methanol steam reforming (MSR), reverse-water gas shift (r-WGS) and water gas shift (WGS) reactions. Similar work was done in GT-Power to simulate a $CuO/ZnO/Al_2O_3$ catalyst [207] using the power-law reaction rates developed by Purnama et al. [208] and Lee et al. [209]. As mentioned in Section 3.5, a Cu-Mn-O metal-foam based catalyst is used in the present work. Unfortunately, no mechanism has been developed for this particular catalyst material. A model with similar settings as in the experiment [109] was built in GT-Power, with the pre-exponential multiplier of the three reactions calibrated to fit the experimental data. Figure 7.3 presents the model in GT-Power for the calibration. The conditions were set exactly as per the experiments [109].

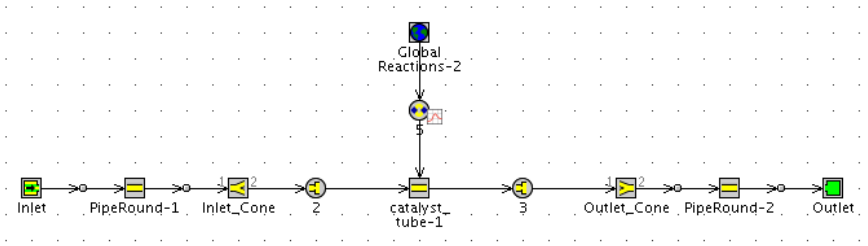

Figure 7.3: Reforming model in GT-Power for the calibration.

The rate of the three reactions was modified as follows:

$$r_{MSR} = 6E5.exp\left(\frac{-103[kJ/mol]}{R.T}\right).P_{CH_3OH}{}^{0.564}.\left(P_{H_2}+11.6\right)^{-0647}\left[\frac{mol}{s.kg_{cat}}\right] \quad (7.1)$$

$$r_{rWGS} = 9.3E5.exp\left(\frac{-108[kJ/mol]}{R.T}\right).P_{CO_2}.P_{H_2}\left[\frac{mol}{s.kg_{cat}}\right] \quad (7.2)$$

$$r_{WGS} = 2E4.exp\left(\frac{-67[kJ/mol]}{R.T}\right).P_{H_2O}.P_{CO}\left[\frac{mol}{s.kg_{cat}}\right] \quad (7.3)$$

where P_{CH_3OH}, P_{H_2}, P_{CO_2}, P_{H_2O}, and P_{CO} are the partial pressures of CH_3OH, H_2, CO_2, H_2O, and CO in the reactant (in kPa).

Figure 7.4a presents the simulated and the measured fuel conversion as a function of the catalyst temperature. The simulation agrees well with the experiment. A higher catalyst temperature results in an increase in fuel conversion. In this simulation, the remaining fuel (fuel conversion < 100%) will remain in the original chemical formula (CH_3OH), and does not convert to byproducts like CH_4 or HCOOH. The reforming products include H_2, CO, CO_2, water vapour and unreacted methanol. Figure 7.4b compares the CO selectivity from simulation and experiment. The simulation is not in perfect agreement with the experiment. However, both experiment and simulation have a very small CO selectivity (less than 5%), so the difference in the energy of the reforming product can be neglected.

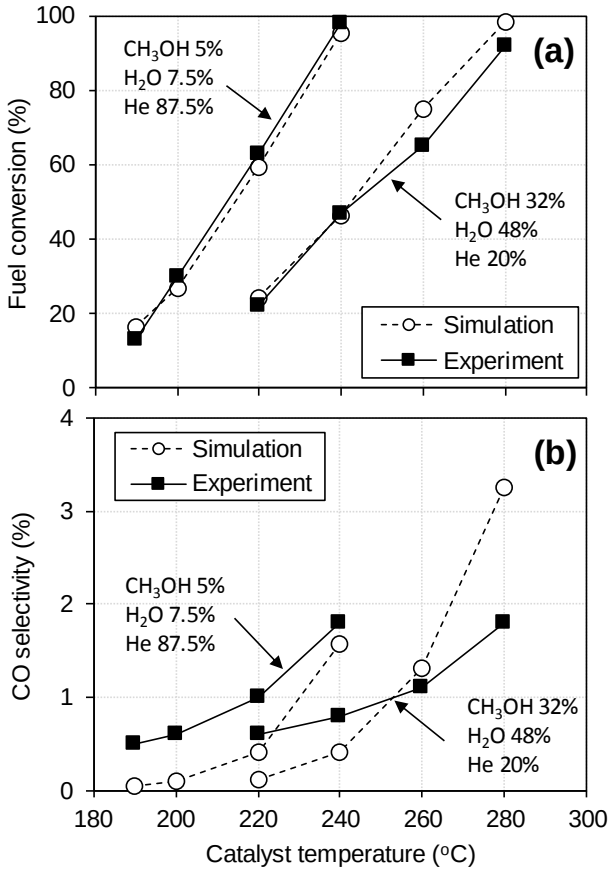

Figure 7.4: Comparison of (a) fuel conversion and (b) CO selectivity of methanol steam reforming over Cu-Mn-O metal-foam based catalyst. Simulation: GT-Power with the updated mechanism, experiment: from [109].

The laminar burning velocity is another important parameter. The impact of

CO selectivity on the LBV of syngas at stoichiometric conditions was studied and is presented in Figure 7.5. Because the reforming of methanol and ethanol produces similar products (CO_2/H_2 molar ratio of 1/3 in the CO_2/H_2 mixture and CO/H_2 molar ratio of 1/2 in the CO/H_2 mixture), the data in Figure 7.5 is also representative for the LBV of ethanol steam reforming products. The simulation was performed using the one-dimensional chemical kinetics CHEM1D code [151] with Li's mechanism [70] and Davis's mechanism [210], and then validated with experiment [211]. The Davis mechanism was considered to be the most accurate mechanism to predict the LBV of syngas [171]. From the simulations, the LBV increases slightly as CO selectivity rises. The experiment on the other hand shows a different trend. The Davis mechanism predicts LBV better than Li's mechanism at high CO selectivity. The comparison of syngas mechanisms [171] was constructed for a mixture of H_2 and CO. For this mixture, Davis's mechanism is better, whereas for a H_2/CO_2 mixture, Li's mechanism is preferred. However, the impact of CO selectivity is clearly trivial, which means the updated reaction mechanism can be used with only a very small influence on the laminar burning velocity.

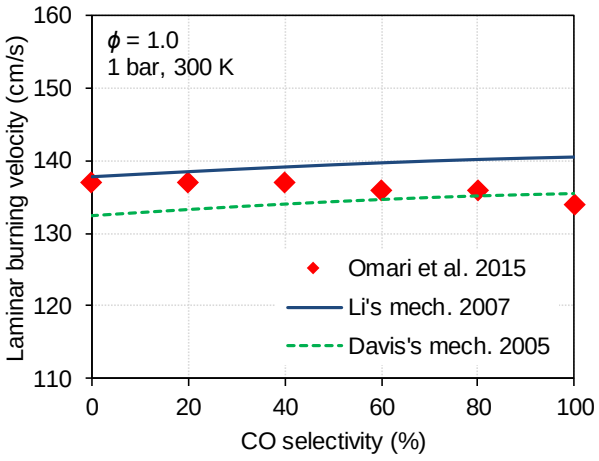

Figure 7.5: Influence of CO selectivity on the LBV of methanol/ethanol steam reforming products. Symbols: experiment [211], solid line: simulation with Li's mechanism [70], dashed line: simulation with Davis's mechanism [210].

A high pressure (HP) EGR loop then was added in the calibrated engine model. HP-EGR was selected because it provides a higher EGR gas temperature. The reformer catalyst was located inside the EGR loop. The pressure drop over the metal-foam based catalyst was calculated as a function of mass flow rate as in literature [212]. The catalyst surface temperature is assumed to be identical to the gas temperature. The gas temperature drops after the catalyst; therefore, an

averaged value of the gas temperature before and after the catalyst was used to represent the catalyst temperature. Three reaction rates in equations 7.1-7.3 were employed. The catalyst has a volume of 0.7 litre. A low pressure injector (the fifth injector) was added to the EGR loop, 300 mm upstream of the reformer. This injector was synchronized with the injector of cylinder 4 (for ease of implementation). The (inner) wall temperature of the R-EGR system (from the EGR inlet to the outlet of the reformer) was set constant, at 550 K. In practice, this value depends on the engine load, EGR ratio, thickness of thermal insulation, insulation material properties like thermal conductivity, thermal resistance, etc. A higher EGR wall temperature causes higher fuel conversion and/or higher produced CO fraction. Higher fuel conversion means more air is replaced by the reformates, so that the engine needs a larger throttle angle to maintain the work output. If the temperature is sufficient for ~100% fuel conversion, a higher wall temperature causes a higher CO rate in the reformates. Therefore, the engine work increases. This would mean the engine needs a smaller throttle angle to keep the output constant. In this thesis, the EGR wall temperature was kept at 550 K for simplicity.

7.2.3 Engine conditions

The simulations with the conventional EGR and the R-EGR concept were carried out at the same BMEP and engine speed of 7 bar and 1500 rpm respectively. As recommended in Chapter 4, the comparison between conventional EGR and R-EGR should be done at mid load. At a higher load, the engine is unable to maintain the output with high EGR ratio. At a lower load, the engine output is very sensitive with a small change of throttle angle, so the error is relatively larger. Low engine speed is preferred to decrease the catalyst space velocity, so the fuel conversion increases. Therefore, the simulations were performed at only one load (mid-load) and one speed (low speed). The throttle opening had to be increased to maintain the load when diluting with EGR and especially with the R-EGR mixtures. The BMEP was controlled with a maximum absolute error of 0.06 bar. The minimum advance for maximum brake torque (MBT) ignition timing was used for all cases using an optimization function in GT-Power. All simulations were performed at lambda one, and valve timing was maintained as standard, i.e. valve overlap of -30 CAD.

In this work, the fifth injector (R-EGR injector) delivers a similar amount of fuel as each of the other injectors. This means the fraction of supplied fuel to the reformer is 20%. If the fuel conversion is 80%, the reforming fraction then is 0.8×20% = 16%. In theory, a higher fuel fraction could improve the efficiency. However, the

fuel conversion decreases due to the increase of space velocity and the reduction of catalyst temperature (HoV effect), thus the reforming fraction does not improve much. In practice, the fuel conversion is influenced by the catalyst temperature, water-to-fuel molar ratio, and space velocity (ratio of inlet volumetric flow rate to the catalyst volume). Fuel conversion increases as catalyst temperature and water-to-fuel molar ratio increase, and as space velocity decreases. To maintain the water-to-fuel molar ratio with a higher delivered rate of fuel, the engine needs to operate at a higher EGR ratio. The catalyst volume then also needs to increase in order to maintain the space velocity. To reduce the pressure drop over the catalyst, a bigger cross section area catalyst (with a shorter length) can be used. If the space is limited, a longer catalyst has to be used, thus the pressure drop over the catalyst would increase; therefore, a higher exhaust pressure would be required. If a back pressure valve is installed in the exhaust pipe, the PMEP increases. Therefore, the fuel fraction for reforming is maintained at 20% in the present study.

For the conventional EGR cases, the fifth injector does not deliver any fuel to the system. The reformer catalyst is still located inside the EGR loop without reforming reactions and the pressure drop is the same as in the R-EGR simulation. The EGR ratio is determined by the ratio of mass flow rate of EGR (upstream of the EGR injector) to the total mass flow rate of the exhaust gases.

7.3 Results

7.3.1 Catalyst characteristics

In the R-EGR cases, 20% of fuel was supplied to the reformer, so the water-to-methanol (W/M) molar ratio changes with varying EGR ratio. Figure 7.6 shows the W/M molar ratio against the EGR ratio. The W/M ratio was calculated based on the cycle averaged molar fraction of H_2O and CH_3OH at the reformer inlet. As can be seen, the W/M molar ratio increases as EGR ratio increases, which supports an increase of fuel conversion. At low EGR ratio (6.5%), the W/M ratio is less than unity, which causes a higher CO fraction in the products. High CO fraction is good for engine performance, but this is not recommended in practice due to possible deactivation of the catalyst. The catalyst temperature (mean value of upstream and downstream gas temperature) is also presented in this Figure. The catalyst temperature increases as EGR increases due to the increase of EGR mass flow rate and the relative reduction of injected methanol mass upstream (less HoV effect). The fuel conversion and the CO selectivity are also shown. The fuel conversion was calculated based on the mass fraction of methanol upstream and

downstream of the catalyst. Because CO and CO_2 are present in the catalyst inlet, the difference in mass fraction (ΔY) between inlet and outlet is used to calculate the CO selectivity, as in Equation 7.4.

$$X_{CO} = \frac{\frac{\Delta Y_{CO}}{MW_{CO}}}{\frac{\Delta Y_{CO}}{MW_{CO}} + \frac{\Delta Y_{CO_2}}{MW_{CO_2}}} \times 100\% \tag{7.4}$$

where ΔY_{CO} and ΔY_{CO_2} are the difference in the mass fraction of CO and CO_2 between inlet and outlet, respectively, and MW is the molecular weight.

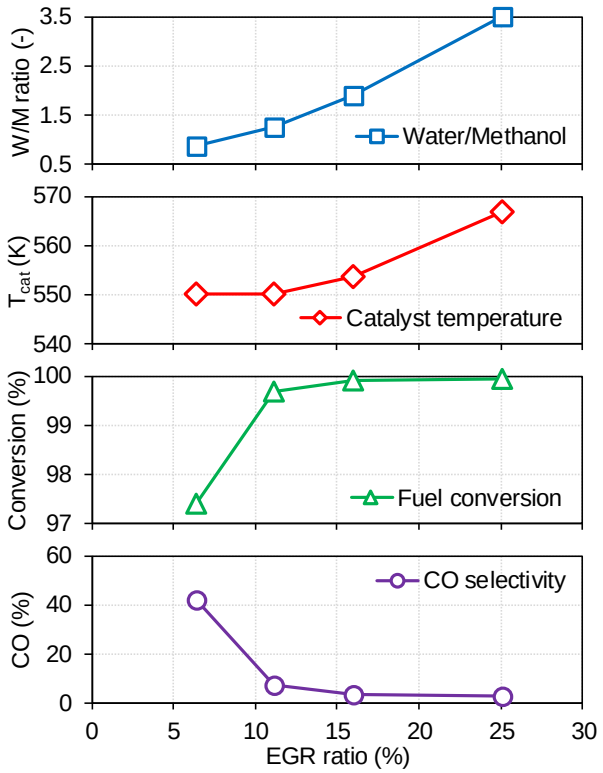

Figure 7.6: The water/methanol molar ratio, catalyst temperature, fuel conversion and CO selectivity as a function of EGR ratio.

Fuel conversion increases as EGR ratio increases. Although the W/M ratio is less than unity, the fuel conversion reaches over 97% at an EGR ratio of 6.5% thanks to a high catalyst temperature. Because of low W/M ratio at this EGR ratio, the

CO selectivity is high, over 40%. With increased EGR ratio, the CO selectivity decreases.

7.3.2 Engine characteristics

Figure 7.7 shows the molar fraction of key species of the unburned gas in the combustion chamber as a function of EGR ratio for both conventional EGR and R-EGR cases. As can clearly be seen, the concentration of H_2 and CO is very small in the conventional EGR cases (top graph). The molar fraction of methanol decreases and molar concentration of CO_2 and H_2O increases as EGR ratio increases. Due to the presence of in-cylinder residuals, the molar fraction of CO_2 and H_2O does not equal 0 at an EGR ratio of 0%.

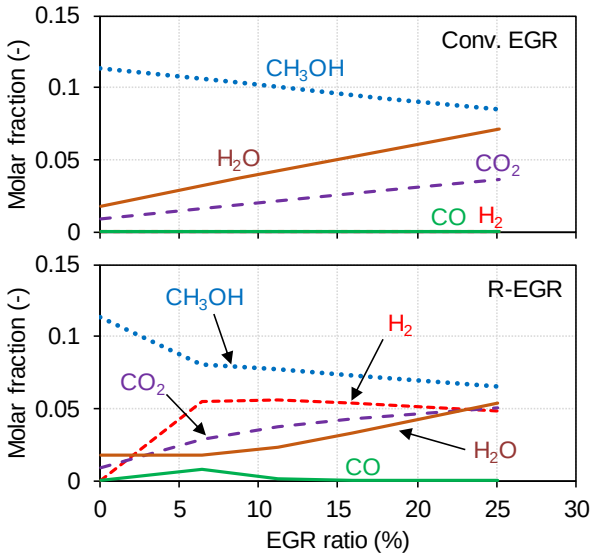

Figure 7.7: Molar fraction of in-cylinder reactants as a function of EGR ratio.

For the R-EGR cases (bottom graph), the molar fractions of H_2 and CO do not equal 0 beyond 6.5% EGR rate. The molar fraction of H_2 equals ~0.05 for different EGR ratios. At an EGR ratio of 6.5%, the CO molar fraction equals ~0.0075, higher than for the other cases due to a high CO selectivity (see Figure 7.6). The molar fraction of water at this EGR ratio is similar to the case without dilution (0% EGR), i.e. it is due to internal EGR. This means 100% of the water in the EGR loop was consumed by the steam reforming process. Compared to the case without dilution, the molar fraction of water slightly decreases due to the reduction of residual mass fraction with a larger throttle position.

Thanks to the presence of H_2 in the reactants, the combustion efficiency increases. Figure 7.8 illustrates the combustion efficiency for two cases against the EGR ratio. The combustion efficiency was predicted using energy left at EVO (from unburned fuel, H_2 and CO) and the inlet fuel energy. The fraction of unburned fuel, H_2 and CO was calculated using the equilibrium method developed by Olikara and Borman [213]. As can be seen, the combustion efficiency in the R-EGR cases is higher than in the conventional EGR cases, especially at high EGR ratio. Also thanks to the formation of H_2 with fuel reforming, LBV increases in the R-EGR cases. This causes a difference in the MBT ignition timing between the two cases. Figure 7.9 presents the ignition timing for the two cases as a function of EGR ratio. As can clearly be seen, the R-EGR cases have a later ignition timing than the conventional EGR cases.

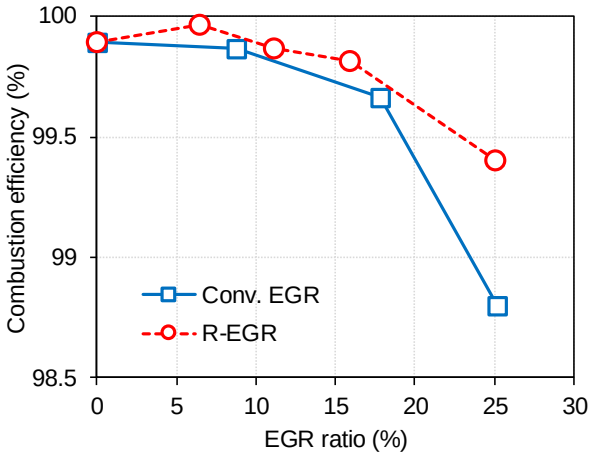

Figure 7.8: Combustion efficiency.

With the presence of H_2, the LBV increases which leads to a change in the flame development period (CA0-10) and the combustion duration (CA10-90). Figure 7.10 shows the CA0-10 (top graph) and CA10-90 (bottom graph) as a function of EGR ratio for both conventional EGR and R-EGR cases. CA0-10 and CA10-90 of the R-EGR cases are shorter than the conventional EGR cases, especially the flame development period. This is due to the increase in LBV. There are two main reasons for the increase of LBV: the presence of H_2 and a later ignition timing (higher unburned gas temperature). In SI engines, the combustion is first initiated by a laminar flame before it is wrinkled by the in-cylinder turbulence to form a turbulent flame. Therefore, the impact of a difference in LBV on CA0-10 is considerable. The CA10-90 is strongly influenced by the total (turbulent plus laminar) flame speed.

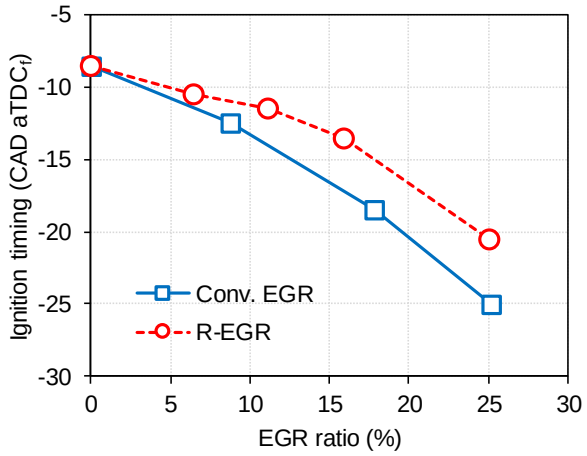

Figure 7.9: MBT ignition timing for two cases as a function of EGR ratio.

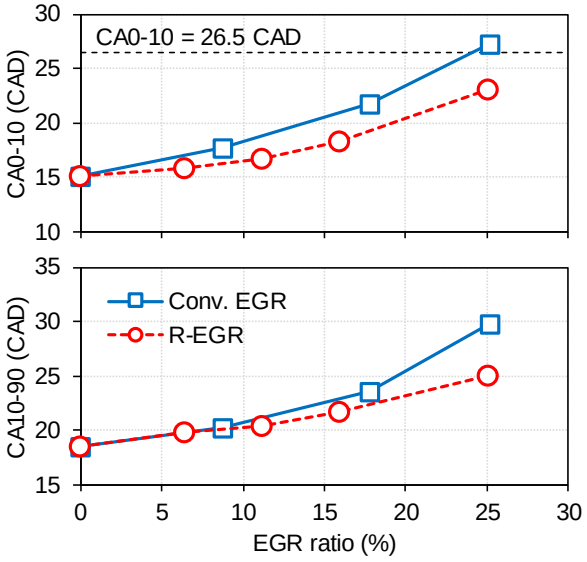

Figure 7.10: Comparison of flame development period (CA0-10) and combustion duration (CA10-90) between the conventional EGR and the R-EGR at a BMEP of 7 bar, 1500 rpm.

To define the combustion stability limit, a CA0-10 limit of 26.5 CAD was applied (see Chapter 2). This corresponds to 5% coefficient of variance of IMEP (CoV_{imep}). As shown in Figure 7.10, the EGR limit for the conventional EGR is ~24% and ~30% for the R-EGR (CA0-10 of 26.5 CAD at these EGR ratios). Note that the combustion becomes unstable not only due to the presence of external EGR gases but also because of the presence of internal residual. At this EGR ratio, the residual mass fraction equals ~5% (in the conventional EGR cases). Thus the total burned gas mass fraction is ~29% for the EGR case.

The relationship between gross ITE and BTE with the change of EGR ratio in the conventional EGR and the R-EGR cases is presented in Figure 7.11. As can be seen in the top graph, the BTE in the R-EGR cases is higher. The absolute difference in BTE between the two cases becomes larger with increased EGR ratio, except for the case with EGR ratio of 6.5%. At this EGR ratio, the CO selectivity is high (see Figure 7.6). Higher CO fraction leads to an increase in the engine efficiency. At higher EGR ratios, the absolute difference is small, around 0.3%. At an EGR ratio of 25%, the difference is larger, ~0.7%. As explained in section 4.2.2, the improvement increases as EGR increases due to a smaller reduction of molar expansion ratio. Furthermore, the BTE decreases with an EGR ratio > 25% due to increased combustion duration. Thanks to a shorter combustion duration (see Figure 7.10), the BTE of the R-EGR cases keeps increasing continuously, so the absolute difference between the two cases will be larger at high dilution rates.

The bottom graph compares the gross ITE of the two cases. As concluded in Section 4.3, the difference in gross ITE between the two cases is trivial. At EGR ratios of 6.5% and 25%, the difference is larger. As explained previously, high CO selectivity is the main reason for the behavior at an EGR ratio of 6.5%. At 25% EGR, the gross ITE decreases with conventional EGR dilution due to a significant enhancement of pumping work (decrease of absolute PMEP) or gross IMEP (see Figure 7.12). The reduction of gross IMEP is more obvious than the decrease of injected fuel. The reduction rate of injected fuel decreases as EGR ratio increases. Therefore, the gross ITE decreases at 25% EGR. The increase of BTE is further attributed to the reduction of pumping work. The pumping work decreases as EGR ratio increases, so the absolute difference between gross ITE and BTE becomes smaller at high EGR ratios.

In the conventional EGR cases, the BTE increases by around 1.3% points with 25% EGR. The R-EGR concept got a slightly higher efficiency versus the conventional EGR, with the absolute difference being larger at higher EGR ratios. Similar to the results of the Otto cycle efficiency calculation (see Figure 4.4), the efficiency increases little with fuel reforming (versus EGR diluted combustion) and the improvement is more obvious at a higher EGR ratios. This can be explained

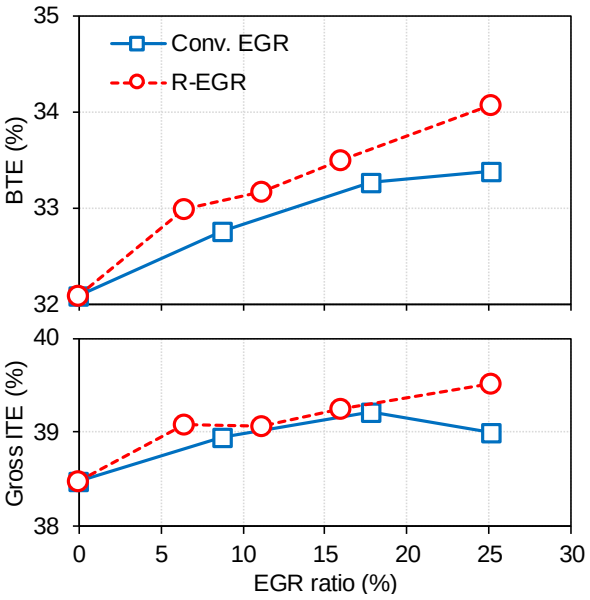

Figure 7.11: The influence of EGR ratio on the gross indicated thermal efficiency and brake thermal efficiency of the conventional EGR and the R-EGR cases at a BMEP of 7 bar, 1500 rpm.

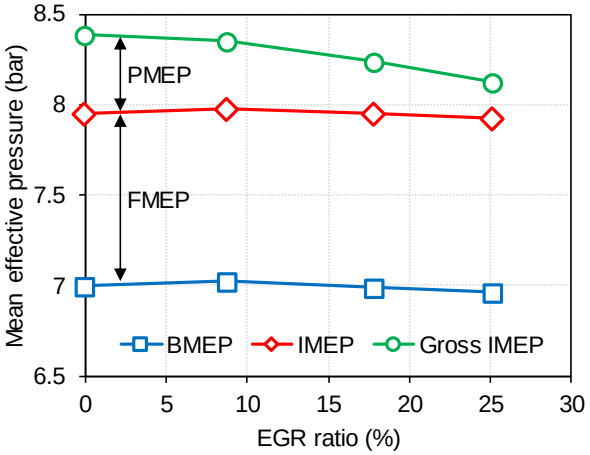

Figure 7.12: Mean effective pressures as a function of EGR ratio for conventional EGR cases.

by a small enhancement of the reformate exergy compared to methanol and the reduction in the MER being less significant at high EGR ratios. Compared to the baseline (no dilution), BTE increases 4.04% with EGR and 6.15% with R-EGR at an EGR ratio of 25%. Because the EGR limit for the conventional EGR cases was estimated to be 24%, the efficiency improvement is slightly less. The estimated BTE at EGR ratio of 30% in the R-EGR case is ~34.3% (at the dilution limit). The relative increase in BTE is 6.9% against the baseline, higher than ~4% improvement with the EGR dilution at the same combustion stability.

Figure 7.13 shows an example of the fuel energy distribution at an EGR ratio of 15% in the two cases, conventional EGR and R-EGR. The fuel energy is distributed in 6 parts: combustion loss, heat loss, exhaust loss, pumping loss, friction loss and brake work. The combustion loss represents the unreleased chemical energy in the exhaust gas at EVO (exhaust valve opening). The combustion loss is very small and the difference is almost invisible in the Figure. As in the previous prediction, a larger amount of heat is lost through the cylinder walls in the R-EGR cases. In this simulation, the heat loss increases from 14% to 15.1% with fuel reforming. The absolute difference in the gross ITE of conventional EGR and R-EGR is very small, 0.1%. It is less than the difference in the BTE, which increases by ~0.3%. The absolute difference in friction loss is negligible. This means the improvement of BTE is mainly attributed to the reduction of pumping work. The trend and the absolute change of engine efficiency is similar to the findings in the previous analyses.

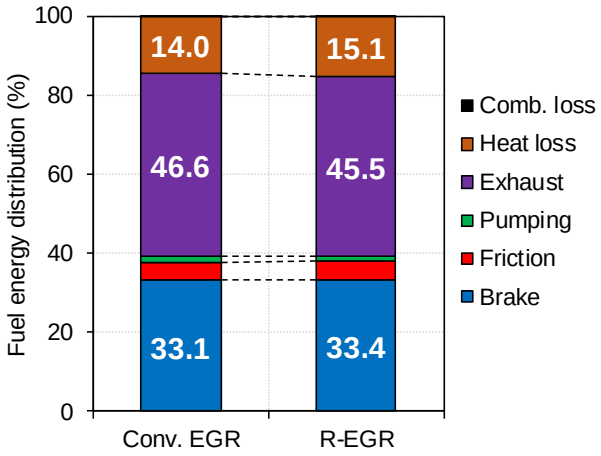

Figure 7.13: The fuel energy distribution of the conventional EGR and the R-EGR cases at an EGR ratio of 15%, BMEP of 7 bar, and 1500 rpm.

Figure 7.14 presents the in-cylinder pressure of the conventional EGR and R-EGR

cases at an EGR ratio of 15%. The pressure profiles were plotted in the log(P)-log(V) diagram, so the difference in the pumping work area can clearly be seen. The two cases have a similar exhaust pressure, however, the pressure during the intake stroke of the R-EGR is higher (larger throttle opening). Thus, the pumping work in the R-EGR cases is smaller. Higher intake pressure causes a higher pressure during the compression stroke, thus the compression work increases. Although the MER decreases with fuel reforming, thanks to a higher initial pressure (pre-combustion pressure) and a shorter combustion (see Figure 7.10), the peak pressure in the R-EGR case is slightly higher. This results in a marginal increase of friction work.

In order to further clarify the impact on burning velocities, Figure 7.15 presents the laminar and turbulent flame speeds for the conventional EGR and R-EGR cases at the same EGR ratio (15%). It is clear that the LBV in the R-EGR case is higher than for the conventional EGR case. Thanks to a higher LBV in the R-EGR cases, the flame development period (CA0-10) is shorter, thus the MBT ignition timing is later. Furthermore, the dilution limit was extended to ~30% instead of 24% as for the conventional EGR dilution cases. Due to a late ignition timing in the R-EGR case, the turbulent burning velocity is slower in the beginning. Then, the turbulent burning velocity increases and reaches a peak before decreasing. The maximum turbulent burning velocity in the R-EGR case is identical to the conventional EGR case.

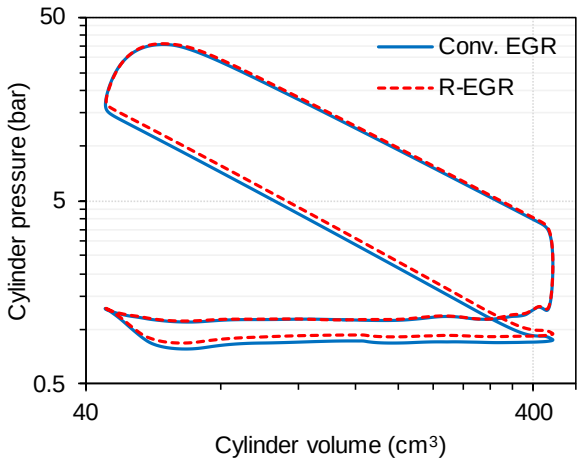

Figure 7.14: Cylinder pressure in the conventional EGR and the R-EGR cases at an EGR ratio of 15%, BMEP of 7 bar, and 1500 rpm.

The turbulent flame speed depends strongly on the turbulent intensity (u') in the combustion chamber [45]. Figure 7.16 shows the comparison of in-cylinder

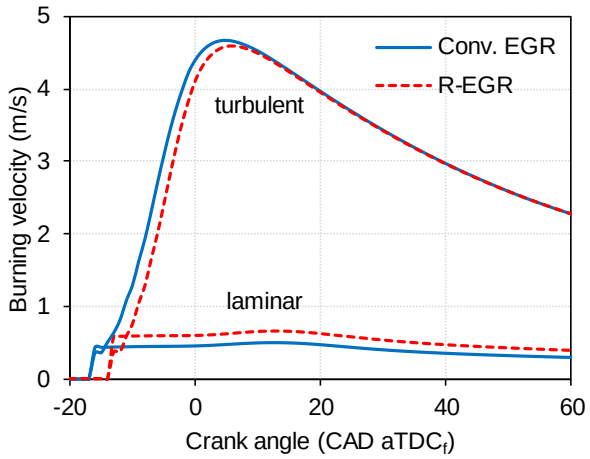

Figure 7.15: The instantaneous burning velocities in the conventional EGR and the R-EGR cases at an EGR ratio of 15%, BMEP of 7 bar, and 1500 rpm.

turbulent intensity during the intake and compression strokes. The timing of IVO, start of injection (SOI), and IVC are also presented in this Figure. After the intake valves open, turbulent intensity increases. The fuel injection contributes a significant increase in u'. Thanks to a longer injection period in the conventional EGR case, the peak u' is higher in this case. However, the difference in u' is trivial after closing of the intake valves, causing an identical turbulent burning velocity. Therefore, the absolute difference in total burning velocity is similar to the difference in LBV. The relative change in the total burning velocity with the addition of syngas decreases, which explains the slight shortening in CA10-90 at low EGR ratios (see Figure 7.10). As presented in Figure 7.16, the fuel fraction of the main injection has a small impact on the final u'. If a double injection strategy is applied, with a late injection during the compression stroke, the u' before ignition could be increased [214–216].

Figure 7.17 compares the in-cylinder cumulative heat release at an EGR ratio of 15% between the two cases. Although the total amount of fuel decreases, total heat release improves in the R-EGR case. Due to the increased LHV of the reforming products, the combustion releases more heat than the conventional one. This leads to an increase in the burned gas temperature (T_b), see Figure 7.18. The combustion starts later in the R-EGR case (later MBT ignition timing) and the burned zone temperature is higher. There are two reasons for this: more heat is released during the combustion and there is a higher initial temperature (see unburned gas temperature T_u). The increase in T_u in the R-EGR cases can be explained by a higher γ during the compression stroke.

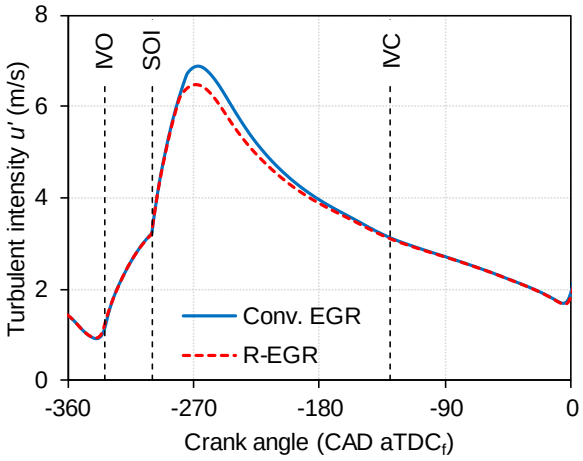

Figure 7.16: In-cylinder turbulent intensity during intake and compression strokes at an EGR ratio of 15%, BMEP of 7 bar, and 1500 rpm.

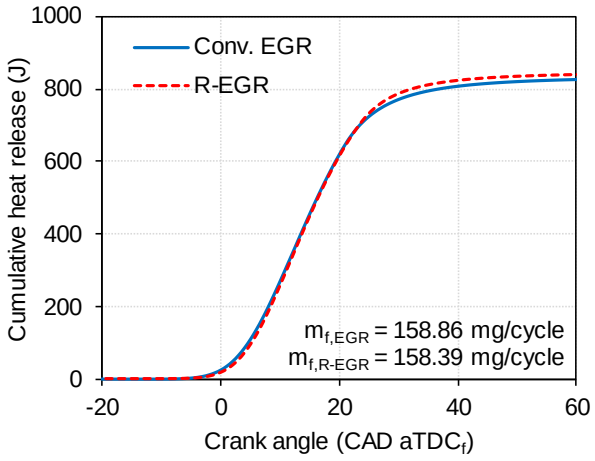

Figure 7.17: The cumulative heat release of the conventional EGR and the R-EGR cases at an EGR ratio of 15%, BMEP of 7 bar, and 1500 rpm.

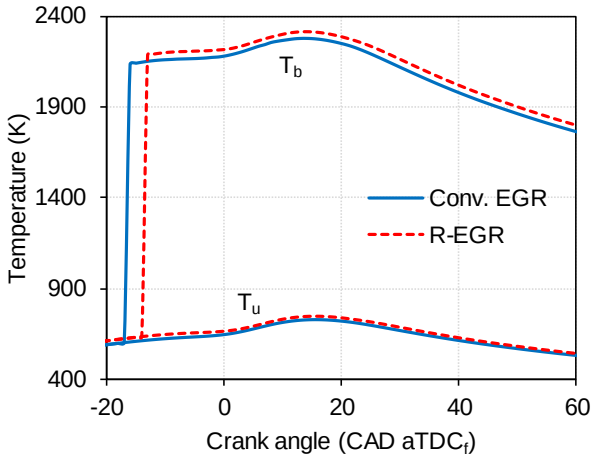

Figure 7.18: The burned and unburned gas temperatures of the conventional EGR and the R-EGR cases at an EGR ratio of 15%, BMEP of 7 bar, and 1500 rpm.

Figure 7.19 shows the in-cylinder γ in the conventional EGR and the R-EGR cases versus crank angle at the same EGR ratio of 15%. At the beginning, γ increases during the intake stroke. Before SOI, the R-EGR case has a slightly higher γ than conventional EGR due to the presence of H_2 and the reduction of H_2O in the inlet. After injection, γ decreases significantly because of a high specific heat C_p of the liquid fuel. Thanks to the cooling effect, γ improves again after the end of injection. Less fuel is injected directly to the cylinder in the R-EGR cases (~80%), this clarifies a higher γ. The unburned gas temperature and pressure after the compression are higher with fuel reforming. After the ignition, γ decreases sharply because of high combustion temperatures. As shown in Figure 7.18, the combustion temperature increases in the R-EGR case, thus that case has (slightly) lower γ values during the expansion and the exhaust strokes. The increase of combustion temperature explains the increase in relative heat transfer.

Although there are some uncertainties in the full engine simulation such as the turbulence, combustion, heat transfer, and so on, the full engine simulation results further confirm the conclusion from the Otto cycle calculation. The limited increase in exergy of the reformate is the key reason for the small improvement in BTE versus the use of conventional EGR.

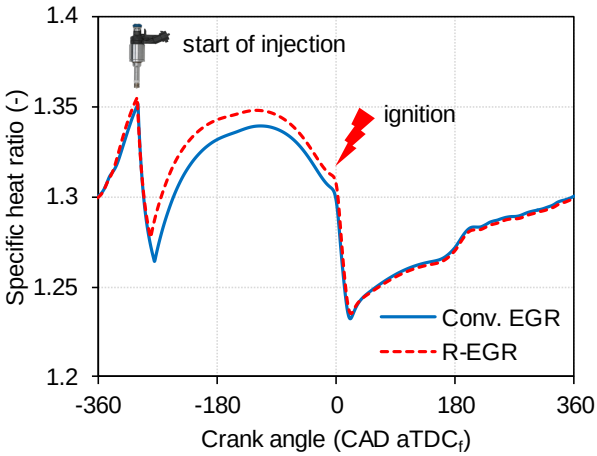

Figure 7.19: The in-cylinder specific heat ratio of the conventional EGR and the R-EGR cases at an EGR ratio of 15%, BMEP of 7 bar, and 1500 rpm.

7.4 Closure

The potential of the R-EGR concept for increased efficiency was evaluated through a gas-dynamic engine simulation using GT-Power. This was an extension of Chapter 4, and the effects of laminar burning velocity, turbulence, pumping work, etc. were taken into account. A HP-EGR loop was constructed in the engine model with a reformer catalyst inside to simulate the R-EGR engine concept. The fuel fraction for reforming was fixed at 20% in the R-EGR cases. The comparison between conventional EGR and R-EGR dilution was performed at a fixed BMEP of 7 bar and an engine speed of 1500 rpm. Based on the results, the following conclusions can be made.

- The water/methanol molar ratio increases as EGR ratio increases, causing an increase in fuel conversion and a decrease in CO selectivity.
- Thanks to the presence of H_2 in the reactants, combustion efficiency increases and MBT ignition timing was retarded in the R-EGR cases.
- The flame development period (CA0-10) and combustion duration (CA10-90) reduce with the presence of H_2 in the EGR mixture. The external EGR limit was 24% and 30% for conventional EGR and R-EGR cases, respectively.
- A small increase in BTE was found. The main contributor for the increase of BTE of the R-EGR concept relative to conventional EGR is the reduction

of pumping work. The BTE increases by ~0.3% absolute compared to the conventional EGR at an EGR ratio of 15%.

- A CA0-10 of 25 CAD is used as the combustion limit, which corresponds with a CoV_{imep} of 5%. At the EGR limits, BTE relatively increases ~4% and 6.9% compared to the baseline with the dilution by EGR and R-EGR mixture, respectively.
- The combustion in the R-EGR case releases more heat than the conventional EGR. Therefore, the combustion temperature is higher in the R-EGR cases, leading to a higher heat loss to the walls.
- The specific heat ratio rises in the R-EGR case due to the presence of H_2 in the reactant and less liquid fuel being injected during the intake stroke.

8

Conclusions

8.1 Conclusions of this work

This work started with the reasons why spark-ignition engines are preferred for passenger cars in the near future. The methodologies for CO_2 emissions reduction were discussed. Fuel properties play an important role for the reduction of CO_2 emissions, both in the carbon intensity and the engine thermal efficiency. Methanol is the liquid fuel which has the lowest carbon intensity (from a stoichiometric combustion). A liquid fuel is preferred because of its high energy density, ease of storage and distribution using current infrastructures. The fuel properties for a highly efficient SI engine were then analyzed. A fuel with high Research Octane Number, high octane sensitivity, high laminar burning velocity, high heat of vaporization, high oxygen mass fraction, low catalyst light-off temperature and low particle matter index is recommended. Thanks to its interesting properties, methanol seems the most promising fuel. However, the challenge of methanol includes cold start behavior and long warm-up duration of the aftertreament system. The molar expansion ratio (MER) was also studied, an increase of 1% in efficiency with molar expansion ratio increase of 0.02 was found. Additionally, methanol is the most simple type of liquid synthetic fuel, so it has an advantage in production compared to other complex fuels. The well-to-wheel efficiency of methanol is the highest compared to other liquid synthetic fuels.

The potential of methanol was evaluated by measurements in a direct-injection spark-ignition engine. The capacity of methanol for engine downsizing and lean burn extension was analyzed. The engine can be downsized by around 10% compared to operation on gasoline. At the same load (maximum load for gasoline), higher efficiency and lower emissions (CO, CO_2, NO_x) were achieved with methanol. The lean-burn limit was also extended for methanol compared to gasoline. The engine operated smoothly with lambda up to 1.5 at wide open throttle. The engine efficiency reached a peak with a λ of ~1.2-1.4, at around 41%. Compared to the maximum efficiency for gasoline, ~ 34%, the efficiency on methanol thus increased 20% relative to gasoline. From literature analyses and measurement results, methanol was considered the most promising fuel for future SI engines.

The efficiency of methanol engines can be further improved by recovering exhaust waste heat. A brief overview of different exhaust heat recovering systems was performed. The conversion of exhaust energy into chemical energy by means of thermochemical recuperation was then selected. Methanol reforming requires a lower catalyst temperature than other fuels, so it is easier to reform into hydrogen-rich gas. Steam reforming of methanol was chosen thanks to a faster reaction rate and for having less propensity for coke formation compared to methanol thermal decomposition. The reformed-exhaust gas recirculation (R-EGR) concept was then selected to investigate the potential of fuel reforming for increased efficiency of methanol fueled SI engines.

The potential of the R-EGR concept for increased efficiency of methanol engines was first assessed theoretically. An Otto cycle calculation was employed to predict the maximum efficiency of methanol engines with the R-EGR concept. The calculation showed that there is a small increase in Otto cycle efficiency with R-EGR dilution compared to conventional EGR dilution. Although the lower heating value increases significantly as the reforming fraction increases, the reduction of the MER is the key reason for the limited enhancement of efficiency. Hydrogen has a MER of ~0.85, much lower than methanol, ~1.06. Thus, the improvement in lower heating value has to compensate for the reduction of MER. The addition of energy losses such as heat transfer, combustion duration, and friction were also investigated. After taking heat transfer into account, there was almost no difference in the gross indicated thermal efficiency between R-EGR and conventional EGR. The heat transfer increased in the R-EGR concept due to a higher combustion temperature. Compared to ethanol and iso-octane (gasoline surrogate), methanol had a higher efficiency using dilution with conventional EGR due to a higher theoretical efficiency and higher EGR limit. However, at a higher reforming fraction, the efficiency of ethanol engines was higher due to a significant increase in the LHV of ethanol's reforming products, although, a

reforming fraction of 30-40% is needed for an ethanol engine to have a higher efficiency than methanol engines, which is hard to achieve.

The LBV of methanol and methanol-syngas blends were calculated using the CHEM1D code. A LBV correlation was developed to fit the simulated data at engine-like conditions. The developed correlation agreed well with recent correlations for methanol. At the same EGR ratio and reforming fraction, the R-EGR concept has a faster LBV. A universal dilution term was derived for both R-EGR and conventional EGR dilution. The reaction front properties were also investigated fundamentally. The flame limit and the knock limit were extended with the use of reforming products. The concentration of H_2 and CO in the combustion products when using EGR-type dilution is higher than other air-diluted cases.

A full cycle engine simulation was ultimately performed on the chosen engine using GT-Power. The results confirmed there being almost no difference between the gross indicated thermal efficiency for R-EGR dilution and conventional EGR dilution. The increase in brake thermal efficiency is mainly attributed to the reduction of pumping work. Therefore, there is a small difference between R-EGR and conventional EGR dilution at the same EGR ratio (absolute 0.3% at 15% EGR). However, the dilution limit can be extended using dilution with the R-EGR mixture, to ~30%, compared to 24% with conventional EGR. The brake thermal efficiency then increases ~6.9% for R-EGR dilution against the baseline, versus ~4.0% with conventional EGR.

8.2 Recommendations for future work

The original purpose of this work was to achieve very high efficiency with a fuel reforming concept [217]. The potential of fuel reforming to increase engine efficiency was predicted through calculation and simulation in this work. Engine experiments are needed to evaluate the capacity of the R-EGR concept to improve fuel economy, especially as an extension of the dilution limit. The combustion stability limit is a challenge for engine simulation, which is why the experiment is necessary to fully discover the potential of this technology. Computational fluid dynamics (CFD) could be used to investigate the mixture formation, turbulence, and combustion in the cylinder to have a better understanding about this concept. However, the fuel reforming product cannot deliver such a large improvement in engine output/efficiency as is promised by the increase in lower heating value. The engine needs high pressure and low temperature from the combustion, for high efficiency. The fuel reforming products are simple molecules, so the combustion

of reformates produces less pressure than complex fuels.

Another application of fuel reformates is through the electrochemical process, or fuel cell. Recently, Fyffe et al. [218], Oh and Song [219], Chuachy and Kokjohn [220] have investigated the potential of combustion engine-fuel cell hybrid systems to achieve very high system efficiency (~70%). The engine can be located downstream of a fuel cell to consume unreacted fuel or located upstream of a fuel cell and work as a fuel reformer. In the former case, the engine operates with a low quality fuel under lean condition. Therefore, the exergy destruction with combustion is large. In the latter case, the engine operates with a rich mixture, so the exergy destruction during combustion is small. The exhaust contains a significant amount of fuel energy at high temperature. It includes H_2 and CO, which will be consumed in a high temperature solid-oxide fuel cell (SOFC). The SOFC has advantages of high efficiency, use of cheap materials, long-term stability, and fuel flexibility. The disadvantage of this type of fuel cell is longer starting period. Therefore, Fyffe et al. [218] used engine exhaust to heat up a SOFC before shifting to rich combustion.

Figure 8.1 presents a diagram for such a combustion engine-fuel cell hybrid system. The engine is operated with a rich mixture and the exhaust feeds into the anode side of the SOFC. Thanks to the rich combustion, the exhaust temperature is sufficient for high temperature operation of SOFC (~700 - 1000 °C). The outlet temperature of the fuel cell is high, therefore a heat exchanger/reformer is installed to reform a part of the fuel at high pressure. The syngas can be injected upstream of the SOFC or into the intake manifold to increase the combustion stability as well as combustion temperature. This concept seems unlikely for vehicle applications but might be possible for stationary applications.

It would be better for energy/exergy gain if thermal decomposition was used. To avoid coke formation, materials such as Pt or Rh should be used. If steam reforming was chosen, addition of water is needed. With the presence of a heat exchanger, the inlet temperature of the turbine decreases to protect the blades. Additional waste heat recovery systems such as turbo-compounding, Rankine cycle, etc. can be employed to further increase the system efficiency. Thanks to the movement of oxygen ions through the electrolyte from cathode to anode, the SOFC works as an oxidation catalyst. The exhaust lambda is controlled depending on the fuel conversion efficiency of the SOFC.

Because the SOFC requires high operating temperatures, port fuel injection of methanol is employed. There is no inter-cooler, and the intake air is cooled by the injected fuel. Thanks to a high LBV of methanol, the combustion is stable in the SI mode. However, the H_2 and CO concentrations are not as high as

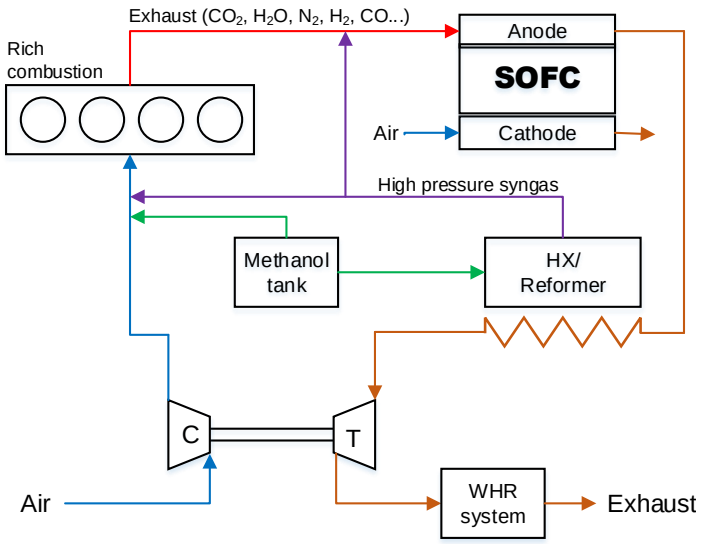

Figure 8.1: System diagram of combustion-electrochemical hybrid system.

under homogeneous charge compression ignition (HCCI) mode [111]. One of the main reasons is that HCCI operates at a richer condition. Figure 8.2 shows the equilibrium combustion products of methanol as a function of ϕ. The results from an ASPEN PLUS simulation at a pressure of 80 bar and a temperature of 2500 K were used to simulate the combustion products. Because of a small fraction of CH_4, CH_3OH, and O_2, only H_2, CO, CO_2, H_2O and N_2 were present. As can be seen, the molar fraction of H_2 and CO increases as ϕ increases. In practice, however, the fraction of fuel and O_2 increases as ϕ increases because of crevice and wall-quenching, which cannot be predicted from this simulation [111].

The efficiency of methanol engines can be further improved without fuel reforming by extending the expansion stroke with an Atkinson/Miller type cycle. A test on a high geometric compression ratio with variable inlet valve closure (IVC) to provide a differential effective compression ratio engine can evaluate the potential of a Miller-type cycle for increased efficiency. The potential of load control by varying IVC timing without a throttle then can be investigated. The IVC can be early or late to have a lower effective compression ratio. With a late IVC, the pumping work increases, therefore, early IVC is preferred. The main challenge for early IVC is the reduction of in-cylinder tumble ratio, which leads to a decrease in combustion speed and combustion efficiency. Methanol has high LBV and high oxygen concentration, so the combustion speed and combustion efficiency increase compared to gasoline. The optimum geometric compression ratio for

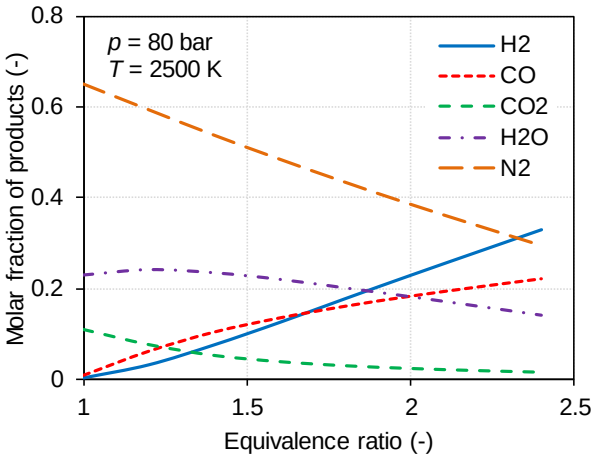

Figure 8.2: Simulated equilibrium combustion products of methanol at different ϕ.

methanol is still unknown. Higher geometric compression ratio causes an increase in the expansion ratio, so the engine can achieve a higher efficiency. However, higher compression ratio also leads to a higher heat loss due to the increase of the surface area/volume ratio of the combustion chamber at top dead center. Methanol has a high heat of vaporization, which might lead to a higher optimum geometric compression ratio compared to gasoline through reduced cycle temperatures.

Osborne et al. [221] have chosen a geometric compression ratio of 13:1 for their Magma engine concept to deliver maximum benefit from increased expansion work before the negative effect of heat transfer begins to dominate. For methanol, the optimum geometric compression ratio could be increased, to 14:1 or 15:1. The effective expansion ratio is limited by the geometric compression ratio. Therefore, the exhaust valve should open around the bottom dead centre. As mentioned previously, early IVC is preferred to control the effective compression ratio, and the normal tumble ratio decreases. Most of recent SI engines have two inlet valves and a symmetric intake port, so the swirl ratio is almost negligible. If two valves are able to control independently, the asynchronous valve timing could be used to increase the swirl ratio and side-way tumble ratio [222].

At low load, one valve might close to generate a strong swirl motion for a certain mass flow rate of air. In order to support the swirl flow motion, a high bore-to-stroke ratio is preferred. With higher bore-to-stroke ratio, the specific area of the combustion chamber at TDC increases, so heat transfer increases. If the swept volume is maintained, higher bore-to-stroke ratio results in a shorter stroke, thus mean piston speed decreases. With a lower mean piston speed, the

heat transfer decreases [223]. The relative heat transfer also is influenced by the intake boost pressure, so the vane position in variable geometry turbine (VGT) turbocharger has a strong impact on heat transfer. In conclusion, the trade-off between geometric compression ratio, IVC timing, swirl ratio, bore-to-stroke ratio, vane position and heat transfer needs to be investigated through 1D/3D simulation as well as through engine experiments to design a highly efficient stoichiometric methanol engine.

List of Appendices

A

Laminar burning velocity data

Table A.1: Laminar burning velocities (cm/s) of methanol-air flames at ~300 K

Wiser (1955) [162]		Gibbs (1959) [161]		Vancoillie (2012) [160]		Sileghem (2014) [153]	
ϕ	u_L	ϕ	u_L	ϕ	u_L	ϕ	u_L
0.731	21.4945	0.8008	34.4873	0.7	20.5	0.7	18.2
0.7943	28.0052	0.8989	42.0719	0.8	29.2	0.8	27.3
0.8865	38.2628	0.9989	48.0377	0.9	37.1	0.9	35.1
1.0215	43.1899	1.0774	50.4715	1.0	43.2	1.0	41.1
1.1442	43.6742	1.0958	50.2695	1.1	46.3	1.1	44.0
1.1864	43.9066	1.1969	47.5739	1.5	34.6	1.2	44.7
1.2249	43.5739	1.2944	44.4539			1.3	42.6
1.4292	36.2119	1.3973	42.3226			1.4	37.6
						1.5	31.3

Table A.2: Laminar burning velocities (cm/s) of syngas-air flames at ~300 K

McLean (1994) [165]		Hasan (1997) [166]		Natarejan (2007) [169]	
ϕ	u_L	ϕ	u_L	ϕ	u_L
0.62	50.52632	0.6	49.46619	0.6	42.73
0.74	69.89474	0.8	87.54448	0.64	47.27
0.86	89.68421	1.0	108.8968	0.67	52.12
1	112	1.2	128.4698	0.72	62.12
1.5	162.9474	1.6	164.0569	0.74	65.76
1.9	180.6316	2.0	172.9537	0.79	74.85
2.15	181.8947	2.4	169.3950	0.83	81.52
2.4	177.6842	2.8	151.6014	0.87	90.30
3.05	154.9474	3.0	136.2989	0.91	98.18
3.4437	137.2632	3.5	106.7616	0.95	105.15
4.4261	88.84211	4.0	87.54448	1.0	112.12
		4.5	55.51601	1.04	119.09

H. Sun (2007) [164]		Prathap (2008) [163]		Kim (2010) [167]		S. Sun (2016) [168]	
ϕ	u_L	ϕ	u_L	ϕ	u_L	ϕ	u_L
0.6	44.83986	0.6	50.8	0.8	76.26	0.6	45.37
0.8	84.34164	0.8	80.3	1.0	111.99	0.8	84.73
1.2	127.4021	1.0	115.6	1.2	135.70	1.0	118.68
1.4	150.1779	1.2	145.9	1.5	166.32	1.5	165.9
1.6	162.6335	1.6	172.2	1.8	178.84	2.0	182.19
2.0	172.9537	2.0	181.5	2.0	184.40	2.5	172.15
3.0	145.5516	2.4	177.5	2.5	176.44	3.0	155.19
3.5	130.6050	2.8	154.8	3.0	155.93	3.5	126.78
4.0	105.6940	3.5	125.6			4.0	106.61

B

Combustion reactions

For combustion reaction of a "general fuel" $C_xH_yO_z$, only conventional EGR and lean combustion are considered. The combustion reactions were balanced with varied equivalence ratio ϕ and EGR mass fraction Y_{EGR}. For methanol fueled SI engines with fuel reforming, the syngas molar fraction in the blends X_{SG}, CO selectivity X_{CO}, and water-to-methanol molar ratio $R_{W/M}$ (W/M ratio in the text) were added.

B.1 General combustion reaction

Assuming the fuel is completely burned. The air left from a lean combustion is recirculated back to the reactant:

$$C_xH_yO_z + \frac{d}{\phi}\left(O_2 + 3.76\,N_2\right) + Y_{EGR}\left[aCO_2 + bH_2O + cN_2 + d\left(\frac{1}{\phi} - 1\right)O_2\right]$$

$$\longrightarrow aCO_2 + bH_2O + cN_2 + d\left(\frac{1}{\phi} - 1\right)O_2$$

After balancing the reaction, coefficients a, b, c, and d are calculated as:

$$a = \frac{x}{1 - Y_{EGR}} \tag{B.1}$$

$$b = \frac{y}{2(1 - Y_{EGR})} \tag{B.2}$$

$$c = \frac{3.76\left(x + \frac{y}{4} - \frac{z}{2}\right)}{(1 - Y_{EGR})(\phi + Y_{EGR} - \phi Y_{EGR})} \tag{B.3}$$

$$d = \frac{\phi\left(x + \frac{y}{4} - \frac{z}{2}\right)}{\phi + Y_{EGR} - \phi Y_{EGR}} \tag{B.4}$$

B.2 Combustion reaction in EFR concept

B.2.1 Lean and stoichiometric combustion

Similar to the global reaction, the impact of syngas molar fraction (X_{SG}) and CO selectivity (X_{CO}) were added.

$$\mathrm{CH_3OH} + \frac{d}{\phi}\left(\mathrm{O_2} + 3.76\,\mathrm{N_2}\right) + Y_{\mathrm{EGR}}\left[a\mathrm{CO_2} + b\mathrm{H_2} + c\mathrm{N_2} + d\left(\frac{1}{\phi} - 1\right)\mathrm{O_2}\right]$$

$$+ \frac{X_{SG}}{1-X_{SG}}\left[\frac{X_{CO}}{4-X_{CO}}\mathrm{CO} + \frac{1-X_{CO}}{4-X_{CO}}\mathrm{CO_2} + \frac{3-X_{CO}}{4-X_{CO}}\mathrm{H_2}\right]$$

$$\longrightarrow a\mathrm{CO_2} + b\mathrm{H_2O} + c\mathrm{N_2} + d\left(\frac{1}{\phi} - 1\right)\mathrm{O_2}$$

After balancing the reaction, coefficients a, b, c, and d are calculated as::

$$a = \frac{1 + \dfrac{X_{SG}}{1-X_{SG}}\dfrac{1}{4-X_{CO}}}{1-Y_{EGR}} \tag{B.5}$$

$$b = \frac{2 + \dfrac{X_{SG}}{1-X_{SG}}\dfrac{3-X_{CO}}{4-X_{CO}}}{1-Y_{EGR}} \tag{B.6}$$

$$c = \frac{3.76d}{\phi(1-Y_{EGR})} \tag{B.7}$$

$$d = \frac{(2a+b)(1-Y_{EGR}) - \dfrac{X_{SG}}{1-X_{SG}}\dfrac{2-X_{CO}}{4-X_{CO}} - 1}{2Y_{EGR}\left(\dfrac{1}{\phi} - 1\right) + 2} \tag{B.8}$$

B.2.2 Rich combustion

The unburned fuel after the combustion is kept in its original form, do not converted to another species or radicals. The ratio between methanol and syngas left in the product is fixed as in the reactant.

$$\phi CH_3OH + d\left(O_2 + 3.76N_2\right) + \phi\frac{X_{SG}}{1-X_{SG}}\left[\frac{X_{CO}}{4-X_{CO}}CO + \frac{1-X_{CO}}{4-X_{CO}}CO_2 + \frac{3-X_{CO}}{4-X_{CO}}H_2\right]$$

$$+ Y_{EGR}\left(aCO_2 + bH_2O + cN_2\right)$$

$$+ Y_{EGR}\left\{\left(\phi - 1\right)CH_3OH + \left(\phi - 1\right)\left[\frac{X_{CO}}{1-X_{CO}}CO + \frac{1-X_{CO}}{4-X_{CO}}CO_2 + \frac{3-X_{CO}}{4-X_{CO}}H_2\right]\right\}$$

$$\longrightarrow aCO_2 + bH_2O + cN_2$$

$$+ \left(\phi - 1\right)CH_3OH + \left(\phi - 1\right)\left[\frac{X_{CO}}{1-X_{CO}}CO + \frac{1-X_{CO}}{4-X_{CO}}CO_2 + \frac{3-X_{CO}}{4-X_{CO}}H_2\right]$$

After balancing the reaction, coefficients a, b, c, and d are calculated as:

$$a = \frac{\left(1 + \frac{X_{SG}}{1-X_{SG}}\frac{1}{4-X_{CO}}\right)\left[Y_{EGR}\left(\phi - 1\right) + 1\right]}{1 - Y_{EGR}} \tag{B.9}$$

$$b = \frac{\left(2 + \frac{X_{SG}}{1-X_{SG}}\frac{3-X_{CO}}{4-X_{CO}}\right)\left[Y_{EGR}\left(\phi - 1\right) + 1\right]}{1 - Y_{EGR}} \tag{B.10}$$

$$c = \frac{3.76d}{1 - Y_{EGR}} \tag{B.11}$$

$$d = \frac{\left(2a + b\right)\left(1 - Y_{EGR}\right) - \left(1 + \frac{X_{SG}}{1-X_{SG}}\frac{2-X_{CO}}{4-X_{CO}}\right)\left[Y_{EGR}\left(\phi - 1\right) + 1\right]}{2} \tag{B.12}$$

B.3 R-EGR engine combustion

The total mole of water left in the reactant and produced CO_2 in the syngas equals the moles of water in EGR in the case without reforming. Based on the moles of water in the product, the moles of water in the EGR system is bY_{EGR}. Therefore, the number of moles of methanol which are injected upstream the catalyst is $bY_{EGR}/R_{W/M}$. With the molar ratio of methanol and water in R3.10, the moles of consumed water for fuel reforming is $(1-X_{CO})bY_{EGR}/R_{W/M}$. We can easily calculate the moles of water left downstream the catalyst: $bY_{EGR}[1-(1-X_{CO})/R_{W/M}]$ and produced CO_2 in the syngas: $bY_{EGR}(1-X_{CO})/R_{W/M}$.

$$\mathrm{CH_3OH} + d\left(\mathrm{O_2} + 3.76\mathrm{N_2}\right) + Y_{EGR}\left(a\mathrm{CO_2} + b\mathrm{H_2O} + c\mathrm{N_2}\right) - bY_{EGR}\frac{1-X_{CO}}{R_{W/M}}\mathrm{H_2O}$$

$$+ bY_{EGR}\frac{4-X_{CO}}{R_{W/M}}\left[\frac{X_{CO}}{4-X_{CO}}\mathrm{CO} + \frac{1-X_{CO}}{4-X_{CO}}\mathrm{CO_2} + \frac{3-X_{CO}}{4-X_{CO}}\mathrm{H_2}\right]$$

$$\longrightarrow a\mathrm{CO_2} + b\mathrm{H_2O} + c\mathrm{N_2}$$

After balancing the reaction, coefficients a, b, c, and d are calculated as:

$$a = \frac{1 + \dfrac{bY_{EGR}}{R_{W/M}}}{1-Y_{EGR}} \tag{B.13}$$

$$b = \frac{2}{1 - Y_{EGR}\dfrac{2+R_{W/M}}{R_{W/M}}} \tag{B.14}$$

$$c = \frac{3.76a\left(1-Y_{EGR}\right) + 1.88b\left(1 - Y_{EGR}\dfrac{1+R_{W/M}}{R_{W/M}}\right) - 1.88}{1-Y_{EGR}} \tag{B.15}$$

$$d = \frac{a\left(1-Y_{EGR}\right)}{3.76} \tag{B.16}$$

B.4 R-EGR engine combustion for different fuels

B.4.1 Methanol

Assuming methanol is fully reformed to a mixture of H_2/CO_2.

$CH_3OH + H_2O \longrightarrow CO_2 + 3H_2$

Therefore, the combustion reaction will be:

$CH_3OH + d\left(O_2 + 3.76N_2\right) + \left(Y_{res} + Y_{EGR}\right)\left(aCO_2 + bH_2O + cN_2\right)$

$- X_{fuel}H_2O + X_{fuel}CO_2 + 3X_{fuel}H_2 \longrightarrow aCO_2 + bH_2O + cN_2$

After balancing the reaction:

$$a = \frac{1 + X_{fuel}}{1 - Y_{res} - Y_{EGR}} \tag{B.17}$$

$$b = \frac{2\left(1 + X_{fuel}\right)}{1 - Y_{res} - Y_{EGR}} \tag{B.18}$$

$$c = \frac{3.76d}{1 - Y_{res} - Y_{EGR}} \tag{B.19}$$

$$d = \frac{\left(2a + b\right)\left(1 - Y_{res} - Y_{EGR}\right) - X_{fuel} - 1}{2} \tag{B.20}$$

B.4.2 Ethanol

Reactions

Ethanol steam reforming reactions:

$C_2H_5OH + 3H_2O \longrightarrow 2CO_2 + 6H_2$

$C_2H_5OH + H_2O \longrightarrow 2CO + 4H_2$

The combustion reactions:

Reforming product: CO_2/H_2 blend

$C_2H_5OH + d\left(O_2 + 3.76N_2\right) + \left(Y_{res} + Y_{EGR}\right)\left(aCO_2 + bH_2O + cN_2\right)$

$- 3X_{fuel}H_2O + 2X_{fuel}CO_2 + 6X_{fuel}H_2 \longrightarrow aCO_2 + bH_2O + cN_2$

Reforming product: CO/H_2 blend

$C_2H_5OH + d\left(O_2 + 3.76N_2\right) + \left(Y_{res} + Y_{EGR}\right)\left(aCO_2 + bH_2O + cN_2\right)$

$- X_{fuel}H_2O + 2X_{fuel}CO + 4X_{fuel}H_2 \longrightarrow aCO_2 + bH_2O + cN_2$

Coefficients

$$a = \frac{2\left(1 + X_{fuel}\right)}{1 - Y_{res} - Y_{EGR}} \tag{B.21}$$

$$b = \frac{3\left(1 + X_{fuel}\right)}{1 - Y_{res} - Y_{EGR}} \tag{B.22}$$

$$c = \frac{3.76d}{1 - Y_{res} - Y_{EGR}} \tag{B.23}$$

$$d = \frac{\left(2a + b\right)\left(1 - Y_{res} - Y_{EGR}\right) - X_{fuel} - 1}{2} \tag{B.24}$$

B.4.3 Iso-octane

Reactions

Iso-octane steam reforming reactions:

$C_8H_{18} + 16H_2O \longrightarrow 8CO_2 + 25H_2$

$C_8H_{18} + 8H_2O \longrightarrow 8CO + 17H_2$

The combustion reaction:

Reforming product: CO_2/H_2 blend

$C_8H_{18} + d\left(O_2 + 3.76N_2\right) + \left(Y_{res} + Y_{EGR}\right)\left(aCO_2 + bH_2O + cN_2\right)$

$- 16X_{fuel}H_2O + 8X_{fuel}CO_2 + 25X_{fuel}H_2 \longrightarrow aCO_2 + bH_2O + cN_2$

Reforming product: CO/H_2 blend

$C_8H_{18} + d\left(O_2 + 3.76N_2\right) + \left(Y_{res} + Y_{EGR}\right)\left(aCO_2 + bH_2O + cN_2\right)$

$- 8X_{fuel}H_2O + 8X_{fuel}CO + 17X_{fuel}H_2 \longrightarrow aCO_2 + bH_2O + cN_2$

Coefficients

$$a = \frac{8\left(1 + X_{fuel}\right)}{1 - Y_{res} - Y_{EGR}} \tag{B.25}$$

$$b = \frac{9\left(1 + X_{fuel}\right)}{1 - Y_{res} - Y_{EGR}} \tag{B.26}$$

$$c = \frac{3.76d}{1 - Y_{res} - Y_{EGR}} \tag{B.27}$$

$$d = \frac{\left(2a + b\right)\left(1 - Y_{res} - Y_{EGR}\right)}{2} \tag{B.28}$$

C

Laminar burning velocity correlations

The correlation were developed for a fixed water-to-methanol molar ratio ($R_{W/M}$ = 1.5) and a fixed CO selectivity (X_{CO} = 0.065). The fitting coefficients were found for syngas in the molar ratio range of 0 to 0.5, for an EGR mass fraction range of 0 to 0.3.

$$u_L = u_{L,0}\left(\frac{T_u}{T_0}\right)^{\alpha}\left(\frac{p}{p_0}\right)^{\beta}.exp(\varepsilon)$$

For the R-EGR case, the ε' will be used instead of ε for the conventional EGR dilution in the EFR concept.

C.1 EFR concept

The reference velocity $u_{L,0}$, at p_0 = 10 bar, T_0 = 550 K

$$u_{L,0} = \left(-101\phi^3 + 164\phi^2 + 54.4\phi - 43.2\right)\left(1 - X_{SG}\right)^{-0.267\phi^2 + 0.521\phi - 0.548} \tag{C.1}$$

Temperature power exponent:

$$\alpha = -2.683\phi^3 + 11\phi^2 - 14.494\phi + 8.5 \tag{C.2}$$

Pressure power exponent:

$$\beta = \beta_1\left(1 - X_{SG}\right)^{\beta_2} + 2\times 10^{-7}\left(T_u - T_0\right)^2 + 8\times 10^{-5}\left(T_u - T_0\right) - 5\times 10^{-4} \tag{C.3}$$

where

$$\beta_1 = 0.771\phi^4 - 2.7773\phi^3 + 3.485\phi^2 - 1.677\phi - 0.089 \tag{C.4}$$

$$\beta_2 = -0.1812\phi^3 + 0.0873\phi^2 + 0.4288\phi - 0.583 \tag{C.5}$$

The power of the exponential function in the correction term:

$$\varepsilon = \varepsilon_1\left[1 + \varepsilon_2\left(T_u - T_0\right)\right] \tag{C.6}$$

where

$$\varepsilon_1 = -8.7\phi^3 + 30.6\phi^2 - 34.8\phi + 8.55 \tag{C.7}$$

$$\varepsilon_2 = -6\times 10^{-4}\phi^2 + 1.5\times 10^{-3}\phi - 1.8\times 10^{-3} \tag{C.8}$$

C.2 R-EGR concept

$$\varepsilon' = \left(11.5p^{-0.472} - 5\right)\left[1 - 0.0104p^{-0.46}\left(T_u - T_0\right)\right] \tag{C.9}$$

D

Flow discharge coefficients

The flow discharge coefficient was calculated based on the measured data from a master's thesis which was advised by the author [224]. It was calculated with a constant reference diameter, 24 mm for the intake and 19 mm for the exhaust.

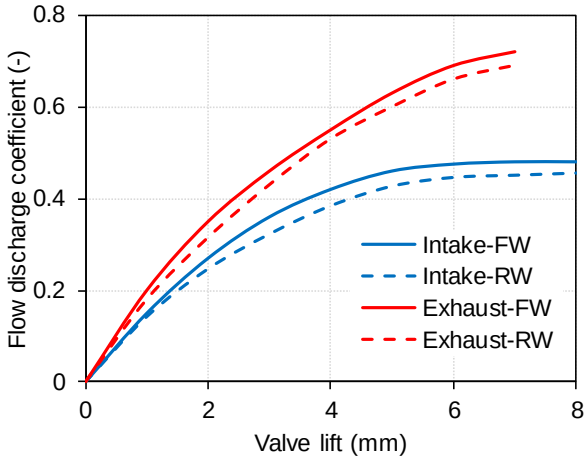

Figure D.1: The flow discharge coefficients of intake and exhaust valves as a function of valve lift. FW: forward flow, RW: reverse flow.

References

[1] Rolf D Reitz. *Grand challenges in engine and automotive engineering*. Frontiers in Mechanical Engineering, 1:1, 2015.

[2] Jamie Condliffe. *Four Huge Cities Are Banning Diesel Cars*. https://www.technologyreview.com/s/603026/four-huge-cities-are-banning-diesel-cars/, 2016.

[3] Michael Reilly. *Global Air Pollution Is Getting Worse, but Removing It Could Worsen Climate Change*. https://www.technologyreview.com/s/601455/global-air-pollution-is-getting-worse-but-removing-it-could-worsen-climate-change/, 2016.

[4] Transport and Environment. *Diesel: the true (dirty) story*. https://www.transportenvironment.org/publications/diesel-true-dirty-story, 2017.

[5] Matteo De Cesare, Nicolo Cavina, and Luigi Paiano. *Technology Comparison for Spark Ignition Engines of New Generation*. SAE International Journal of Engines, 10(5):2513–2534, 2017.

[6] Tom McCarthy. *Reduce, Reuse and Recycle: Energy Management in Future Automotive Applications*. In SAE-Waste Heat Recovery Symposium, 2018.

[7] Börje Grandin and Hans-Erik Ångström. *Replacing fuel enrichment in a turbo charged SI engine: lean burn or cooled EGR*. SAE Technical Paper 1999-01-3505, 1999.

[8] Jerald A Caton. *A Comparison of Lean Operation and Exhaust Gas Recirculation: Thermodynamic Reasons for the Increases of Efficiency*. SAE Technical Paper 2013-01-0266, 2013.

[9] S. Verhelst. *A study of the combustion in hydrogen-fuelled internal combustion engines.* PhD thesis, Ghent University, 2005.

[10] Sebastian Verhelst and Thomas Wallner. *Hydrogen-fueled internal combustion engines*. Progress in Energy and Combustion Science, 35(6):490–527, 2009.

[11] J. Vancoillie. *Modeling the combustion of light alcohols in spark-ignition engines.* PhD thesis, Ghent University, 2013.

[12] L. Sileghem. *A Study of the Combustion of Alcohol-Gasoline Blends in Internal Combustion Engines.* PhD thesis, Ghent University, 2015.

[13] R. J. Pearson, J. W. G. Turner, and A. J. Peck. *Gasoline-ethanol-methanol tri-fuel vehicle development and its role in expediting sustainable organic fuels for transport*. In IMechE Low Carbon Vehicles Conference, pages 1–21, London, UK, 2009.

[14] Andy Yates, Arthur Bell, and Andre Swarts. *Insights relating to the autoignition characteristics of alcohol fuels*. Fuel, 89(1):83–93, 2010.

[15] Chongming Wang, Hongming Xu, Ritchie Daniel, Akbar Ghafourian, Jose Martin Herreros, Shijin Shuai, and Xiao Ma. *Combustion characteristics and emissions of 2-methylfuran compared to 2, 5-dimethylfuran, gasoline and ethanol in a DISI engine*. Fuel, 103:200–211, 2013.

[16] Matthias Thewes, Martin Muether, Stefan Pischinger, Matthias Budde, André Brunn, Andreas Sehr, Philipp Adomeit, and Juergen Klankermayer. *Analysis of the impact of 2-methylfuran on mixture formation and combustion in a direct-injection spark-ignition engine*. Energy & Fuels, 25(12):5549–5561, 2011.

[17] Haiqiao Wei, Dengquan Feng, Gequn Shu, Mingzhang Pan, Yubin Guo, Dongzhi Gao, and Wei Li. *Experimental investigation on the combustion and emissions characteristics of 2-methylfuran gasoline blend fuel in spark-ignition engine*. Applied Energy, 132:317–324, 2014.

[18] Fabian Hoppe, Ultan Burke, Matthias Thewes, Alexander Heufer, Florian Kremer, and Stefan Pischinger. *Tailor-Made Fuels from Biomass: Potentials of 2-butanone and 2-methylfuran in direct injection spark ignition engines*. Fuel, 167:106–117, 2016.

[19] Martin Härtl, Andreas Stadler, Fabian Backes, Georg Wachtmeister, and Eberhard Jacob. *Potentially CO_2–neutral Fuels for Clean SI Engines*. MTZ Worldwide, 78(7-8):76–83, 2017.

[20] Kieran P Somers, John M Simmie, Fiona Gillespie, Ultan Burke, Jessica Connolly, Wayne K Metcalfe, Frédérique Battin-Leclerc, Patricia

Dirrenberger, Olivier Herbinet, P-A Glaude, et al. *A high temperature and atmospheric pressure experimental and detailed chemical kinetic modelling study of 2–methyl furan oxidation*. Proceedings of the Combustion Institute, 34(1):225–232, 2013.

[21] Maxim E Bardin, Evgenii V Ivanov, Elna JK Nilsson, Vladimir A Vinokurov, and Alexander A Konnov. *Laminar burning velocities of dimethyl carbonate with air*. Energy & Fuels, 27(9):5513–5517, 2013.

[22] James P. Szybist, Kalyana Chakravathy, and C. Stuart Daw. *Analysis of the Impact of Selected Fuel Thermochemical Properties on Internal Combustion Engine Efficiency*. Energy & Fuels, 26(5):2798–2810, 2012.

[23] John Farrell. *US DOE Co-Optimization of Fuels and Engines (Co-Optima) Initiative: Recent progress on light-duty boosted spark-ignition*. In ERC - Symposium, 2017.

[24] Michael D Boot, Miao Tian, Emiel JM Hensen, and S Mani Sarathy. *Impact of fuel molecular structure on auto-ignition behavior–Design rules for future high performance gasolines*. Progress in Energy and Combustion Science, 60:1–25, 2017.

[25] SM Remmert, RF Cracknell, R Head, A Schuetze, S Akehurst, JWG Turner, and A Popplewell. *Octane response in a downsized, highly boosted direct injection spark ignition engine*. SAE International Journal of Fuels and Lubricants, 7(1):131–143, 2014.

[26] Gautam Kalghatgi and Richard Stone. *Fuel requirements of spark ignition engines*. Proceedings of the Institution of Mechanical Engineers, Part D: Journal of Automobile Engineering, 232(1):22–35, 2018.

[27] Arjun Prakash, Chongming Wang, Andreas Janssen, Allen Aradi, and Roger Cracknell. *Impact of Fuel Sensitivity (RON-MON) on Engine Efficiency*. SAE International Journal of Fuels and Lubricants, 10(1):115–125, 2017.

[28] Chongming Wang, Arjun Prakash, Allen Aradi, Roger Cracknell, and Hongming Xu. *Significance of RON and MON to a modern DISI engine*. Fuel, 209:172–183, 2017.

[29] James P Szybist and Derek A Splitter. *Pressure and temperature effects on fuels with varying octane sensitivity at high load in SI engines*. Combustion and Flame, 177:49–66, 2017.

[30] GT Kalghatgi. *Fuel anti-knock quality–Part I. Engine studies*. SAE Technical Paper 2001-01-3584, 2001.

[31] JE Anderson, U Kramer, SA Mueller, and TJ Wallington. *Octane numbers of ethanol–and methanol–gasoline blends estimated from molar concentrations*. Energy & Fuels, 24(12):6576–6585, 2010.

[32] James P Szybist and Derek A Splitter. *Understanding chemistry–specific fuel differences at a constant RON in a boosted SI engine*. Fuel, 217:370–381, 2018.

[33] Matthew A Ratcliff, Jonathan Burton, Petr Sindler, Earl Christensen, Lisa Fouts, and Robert L McCormick. *Effects of Heat of Vaporization and Octane Sensitivity on Knock-Limited Spark Ignition Engine Performance*. SAE Technical Paper 2018-01-0218, 2018.

[34] Eshan Singh, Ponnya Hlaing, Hao Shi, and Robert Dibble. *Effect of Different Fluids on Injection Strategies to Suppress Pre-Ignition*. SAE Technical Paper 2019-01-0257, 2019.

[35] Chongming Wang, Andreas Janssen, Arjun Prakash, Roger Cracknell, and Hongming Xu. *Splash blended ethanol in a spark ignition engine–Effect of RON, octane sensitivity and charge cooling*. Fuel, 196:21–31, 2017.

[36] Ritchie Daniel, Chongming Wang, Hongming Xu, Guohong Tian, and Dave Richardson. *Dual-injection as a knock mitigation strategy using pure ethanol and methanol*. SAE International Journal of Fuels and Lubricants, 5(2):772–784, 2012.

[37] Chongming Wang, Soheil Zeraati-Rezaei, Liming Xiang, and Hongming Xu. *Ethanol blends in spark ignition engines: RON, octane-added value, cooling effect, compression ratio, and potential engine efficiency gain*. Applied Energy, 191:603–619, 2017.

[38] Christopher P Kolodziej, Michael Pamminger, James Sevik, Thomas Wallner, Scott W Wagnon, and William J Pitz. *Effects of fuel laminar flame speed compared to engine tumble ratio, ignition energy, and injection strategy on lean and EGR dilute spark ignition combustion*. SAE International Journal of Fuels and Lubricants, 10(1):82–94, 2018.

[39] Muharrem Eyidogan, Ahmet Necati Ozsezen, Mustafa Canakci, and Ali Turkcan. *Impact of alcohol–gasoline fuel blends on the performance and combustion characteristics of an SI engine*. Fuel, 89(10):2713–2720, 2010.

[40] Hosuk H Jung, Michael H Shelby, Charles E Newman, and Robert A Stein. *Effect of Ethanol on Part Load Thermal Efficiency and CO_2 Emissions of SI Engines*. SAE International Journal of Engines, 6(1):456–469, 2013.

[41] Koichiro Aikawa, Takayuki Sakurai, and Jeff J Jetter. *Development of a predictive model for gasoline vehicle particulate matter emissions*. SAE International Journal of Fuels and Lubricants, 3(2):610–622, 2010.

[42] Paul Miles. *Efficiency Merit Function for Spark Ignition Engines: Revisions and Improvements Based on FY16–17 Research*. Technical report, U.S. Department of Energy, DOE/GO-102018-5041, 2018.

[43] Eshan Singh, Vijai Shankar Bhavani Shankar, Rupali Tripathi, Heinz Pitsch, and S Mani Sarathy. *2–Methylfuran: A bio-derived octane booster for spark-ignition engines*. Fuel, 225:349–357, 2018.

[44] J Farrell, R Wagner, J Holladay, and C Moen. *Co-Optimization of Fuels & Engines–FY17 Year in Review*. Golden, National Renewable Energy Laboratory, 2017.

[45] Gamma Technologies. *GT-Suite Version 7.5 User's Manual*. Gamma Technologies, Westmont, IL, USA, 2015.

[46] George A Lavoie, Elliott Ortiz-Soto, Aristotelis Babajimopoulos, Jason B Martz, and Dennis N Assanis. *Thermodynamic sweet spot for high-efficiency, dilute, boosted gasoline engines*. International Journal of Engine Research, 14(3):260–278, 2013.

[47] Thomas Morel and Rifat Keribar. *A model for predicting spatially and time resolved convective heat transfer in bowl-in-piston combustion chambers*. SAE Technical Paper 850204, 1985.

[48] Simon K Chen and Patrick F Flynn. *Development of a single cylinder compression ignition research engine*. SAE Technical Paper 650733, 1965.

[49] Martin L Wissink, Derek A Splitter, Adam B Dempsey, Scott J Curran, Brian C Kaul, and Jim P Szybist. *An assessment of thermodynamic merits for current and potential future engine operating strategies*. International Journal of Engine Research, 18(1-2):155–169, 2017.

[50] Richard Backhaus. *Alternative Fuels CO_2–neutral into the Future*. MTZ Worldwide, 78(6):8–13, 2017.

[51] Agora Verkehrswende and Agora Energiewende. *The Future Cost of Electricity-Based Synthetic Fuels: Conclusions Drawn by Agora Verkehrswende and Agora Energiewende*. In Agora Verkehrswende, Agora Energiewende and Frontier Economics (2018): The Future Cost of Electricity-Based Synthetic Fuels, 2018.

[52] Alexander Tremel, Peter Wasserscheid, Manfred Baldauf, and Thomas Hammer. *Techno–economic analysis for the synthesis of liquid and gaseous fuels based on hydrogen production via electrolysis*. International Journal of Hydrogen Energy, 40(35):11457–11464, 2015.

[53] Dominik Bongartz, Larissa Doré, Katharina Eichler, Thomas Grube, Benedikt Heuser, Laura E Hombach, Martin Robinius, Stefan Pischinger, Detlef Stolten, Grit Walther, et al. *Comparison of light-duty transportation fuels produced from renewable hydrogen and green carbon dioxide*. Applied Energy, 231:757–767, 2018.

[54] Carl Berninghausen. *Is hydrogen and carbon dioxide a perfect wedding?* In The future of e–Fuels in Europe, 2018.

[55] Kostiantyn Turcheniuk, Dmitry Bondarev, Vinod Singhal, and Gleb Yushin. *Ten years left to redesign lithium-ion batteries*. https://www.nature.com/articles/d41586-018-05752-3, 2018.

[56] Sarah J Jones. *If electric cars are the answer, what was the question?* British medical bulletin, 129(1):13–23, 2019.

[57] J. Vancoillie, J. Demuynck, L. Sileghem, M. Van De Ginste, S. Verhelst, L. Brabant, and L. Van Hoorebeke. *The potential of methanol as a fuel for flex-fuel and dedicated spark-ignition engines*. Applied Energy, 102:140 – 149, 2013.

[58] J. Vancoillie, J. Demuynck, L. Sileghem, M. Van De Ginste, and S. Verhelst. *Comparison of the renewable transportation fuels, hydrogen and methanol formed from hydrogen, with gasoline - Engine efficiency study*. International Journal of Hydrogen Energy, 37(12):9914 – 9924, 2012.

[59] Louis Sileghem, Andrew Ickes, Thomas Wallner, and Sebastian Verhelst. *Experimental investigation of a DISI production engine fuelled with methanol, ethanol, butanol and iso-stoichiometric alcohol blends*. SAE Technical Paper 2015-01-0768, 2015.

[60] Jeroen Vancoillie, Louis Sileghem, Maarten Van de Ginste, Joachim Demuynck, Jonas Galle, and Sebastian Verhelst. *Experimental evaluation of lean-burn and EGR as load control strategies for methanol engines*. SAE Technical Paper 2012-01-1283, 2012.

[61] Mustafa Kemal Balki and Cenk Sayin. *The effect of compression ratio on the performance, emissions and combustion of an SI (spark ignition) engine fueled with pure ethanol, methanol and unleaded gasoline*. Energy, 71:194–201, 2014.

[62] Mustafa Kemal Balki, Cenk Sayin, and Mustafa Canakci. *The effect of different alcohol fuels on the performance, emission and combustion characteristics of a gasoline engine*. Fuel, 115:901–906, 2014.

[63] Duc-Khanh Nguyen, Tim Van Craeynest, Thomas Pillu, Jakob Coulier, and Sebastian Verhelst. *Downsizing Potential of Methanol Fueled DISI Engine with Variable Valve Timing and Boost Control*. SAE Technical Paper 2018-01-0918, 2018.

[64] Duc-Khanh Nguyen, Bram Stepman, Viktor Vergote, Louis Sileghem, and Sebastian Verhelst. *Combustion Characterization of Methanol in a Lean-burn Direct Injection Spark Ignition (DISI) Engine*. SAE Technical Paper 2019-01-0566, 2019.

[65] Tim Van Craeynest and Thomas Pillu. *Assessing performance and emissions of methanol in a downsized DISI engine at high loads*. Master's thesis, Ghent University, Belgium, 2017.

[66] Bram Stepman and Viktor Vergote. *Diluted combustion and fuel reforming in methanol-fuelled spark ignition engines*. Master's thesis, Ghent University, Belgium, 2018.

[67] JWG Turner, A Popplewell, R Patel, TR Johnson, NJ Darnton, S Richardson, SW Bredda, RJ Tudor, CI Bithell, R Jackson, et al. *Ultra boost for economy: extending the limits of extreme engine downsizing*. SAE International Journal of Engines, 7(1):387–417, 2014.

[68] Pierre Leduc, Benjamin Dubar, Alain Ranini, and Gaëtan Monnier. *Downsizing of gasoline engine: an efficient way to reduce CO_2 emissions*. Oil & Gas Science and Technology, 58(1):115–127, 2003.

[69] David G Goodwin, Harry K Moffat, and Raymond L Speth. *Cantera: An object-oriented software toolkit for chemical kinetics, thermodynamics, and transport processes*. Caltech, Pasadena, CA, 2009.

[70] Juan Li, Zhenwei Zhao, Andrei Kazakov, Marcos Chaos, Frederick L Dryer, and James J Scire. *A comprehensive kinetic mechanism for CO, CH_2O, and CH_3OH combustion*. International Journal of Chemical Kinetics, 39(3):109–136, 2007.

[71] Marco Mehl, William J Pitz, Charles K Westbrook, and Henry J Curran. *Kinetic modeling of gasoline surrogate components and mixtures under engine conditions*. Proceedings of the Combustion Institute, 33(1):193–200, 2011.

[72] Gautam Kalghatgi, Hassan Babiker, and Jihad Badra. *A simple method to predict knock using toluene, n–heptane and iso–octane blends (TPRF) as gasoline surrogates*. SAE International Journal of Engines, 8(2):505–519, 2015.

[73] Seungmok Choi, Christopher P Kolodziej, Alexander Hoth, and Thomas Wallner. *Development and Validation of a Three Pressure Analysis (TPA) GT-Power Model of the CFR F1/F2 Engine for Estimating Cylinder Conditions*. SAE Technical Paper 2018-01-0848, 2018.

[74] Duc-Khanh Nguyen, Louis Sileghem, and Sebastian Verhelst. *A quasi–dimensional combustion model for spark ignition engines fueled with gasoline–methanol blends*. Proceedings of the Institution of Mechanical Engineers, Part D: Journal of Automobile Engineering, 232(1):57–74, 2018.

[75] Huayang Zhu, Yuyin Zhang, Min Xu, and Robert J Kee. *Droplet vaporization characteristics of multicomponent mixtures of methanol and gasoline surrogate in opposed stagnation flows*. Proceedings of the Combustion Institute, 34(1):1545–1552, 2013.

[76] Hiroshi Miyagawa, Makoto Nagaoka, Katsuyuki Ohsawa, and Toshio Yamada. *Spray vaporization model for multi-component gasoline*. JSAE review, 19(4):299–304, 1998.

[77] A Lee and CK Law. *An experimental investigation on the vaporization and combustion of methanol and ethanol droplets*. Combustion Science and Technology, 86(1-6):253–265, 1992.

[78] S Richard, S Bougrine, G Font, F-A Lafossas, and F Le Berr. *On the reduction of a 3D CFD combustion model to build a physical 0D model for simulating heat release, knock and pollutants in SI engines*. Oil & Gas Science and Technology-Rev. IFP, 64(3):223–242, 2009.

[79] Joachim Demuynck. *A fuel independent heat transfer correlation for premixed spark ignition engines*. PhD thesis, Ghent University, 2012.

[80] Bertrand Lecointe and Gaëtan Monnier. *Downsizing a gasoline engine using turbocharging with direct injection*. SAE Technical Paper 2003-01-0542, 2003.

[81] Anne Lewis, Elliott Ortiz-Soto, George Lavoie, and Dennis N Assanis. *Scaling and dimensional methods to incorporate knock and flammability limits in models of high-efficiency gasoline and ethanol engines*. International Journal of Engine Research, 16(2):181–196, 2015.

[82] James P Szybist, Scott W Wagnon, Derek Splitter, William J Pitz, and Marco Mehl. *The Reduced Effectiveness of EGR to Mitigate Knock at High Loads in Boosted SI Engines*. SAE International Journal of Engines, 10(5):2305–2318, 2017.

[83] Sunyoup Lee, Seunghyun Park, Changgi Kim, Young-Min Kim, Yongrae Kim, and Cheolwoong Park. *Comparative study on EGR and lean burn strategies employed in an SI engine fueled by low calorific gas*. Applied Energy, 129:10–16, 2014.

[84] Philipp Adomeit, Johannes Scharf, Matthias Thewes, Bastian Morcinkowski, Patrick Hoppe, Stefania Esposito, and Marius Böhmer. *Extreme lean gasoline technology–best efficiency and lowest emission powertrains*. In Internationaler Motorenkongress 2017, pages 101–122. Springer, 2017.

[85] W Strehlau, J Leyrer, ES Lox, T Kreuzer, M Hori, and M Hoffmann. *New developments in lean NOx catalysis for gasoline fueled passenger cars in Europe*. SAE Technical Paper 962047, 1996.

[86] B Morcinkowski, P Hoppe, F Hoppe, M Mally, P Adomeit, T Uhlmann, M Thewes, J Scharf, and H Baumgarten. *Simulating Extreme Lean Gasoline Combustion–Flow Effects on Ignition*. In International Conference on Ignition Systems for Gasoline Engines, pages 87–105. Springer, 2016.

[87] Dongwon Jung, Kosaku Sasaki, and Norimasa Iida. *Effects of increased spark discharge energy and enhanced in-cylinder turbulence level on lean limits and cycle-to-cycle variations of combustion for SI engine operation*. Applied Energy, 205:1467–1477, 2017.

[88] Yasushi Yoshihara, Koichi Nakata, Daishi Takahashi, Tetsuo Omura, and Atsuharu Ota. *Development of High Tumble Intake-Port for High Thermal Efficiency Engines*. SAE Technical Paper 2016-0-0692, 2016.

[89] Joonsik Hwang, Wooyeong Kim, Choongsik Bae, Wonho Choe, Jeonghwa Cha, and Soohyung Woo. *Application of a novel microwave-assisted plasma ignition system in a direct injection gasoline engine*. Applied Energy, 205:562–576, 2017.

[90] Dongwon Jung and Norimasa Iida. *An investigation of multiple spark discharge using multi-coil ignition system for improving thermal efficiency of lean SI engine operation*. Applied Energy, 212:322–332, 2018.

[91] Srinivas Padala, Shashank Nagaraja, Yuji Ikeda, and Minh Khoi Le. *Extension of Dilution Limit in Propane-Air Mixtures Using Microwave Discharge Igniter*. SAE Technical Paper 2017-24-0148, 2017.

[92] Yan Chang, James P. Szybist, Josh A. Pihl, and D. William Brookshear. *Catalytic Exhaust Gas Recirculation-Loop Reforming for High Efficiency in a Stoichiometric Spark-Ignited Engine through Thermochemical Recuperation and Dilution Limit Extension, Part 2: Engine Performance*. Energy & Fuels, 32(2):2257–2266, 2018.

[93] Duc-Khanh Nguyen, Louis Sileghem, and Sebastian Verhelst. *Exploring the potential of reformed-exhaust gas recirculation (R-EGR) for increased efficiency of methanol fueled SI engines*. Fuel, 236:778–791, 2019.

[94] Duc-Khanh Nguyen and Sebastian Verhelst. *Computational Study of the Laminar Reaction Front Properties of Diluted Methanol-Air Flames Enriched by the Fuel Reforming Product*. Energy & Fuels, 31(9):9991–10002, 2017.

[95] L Tartakovsky and M Sheintuch. *Fuel reforming in internal combustion engines*. Progress in Energy and Combustion Science, 67:88–114, 2018.

[96] Roger Cracknell, Arjun Prakash, and Robert Head. *Influence of laminar burning velocity on performance of gasoline engines*. SAE Technical Paper 2012-01-1742, 2012.

[97] James P Szybist and Derek Splitter. *Effects of fuel composition on EGR dilution tolerance in spark ignited engines*. SAE International Journal of Engines, 9(2):819–831, 2016.

[98] Kazunori Yamaji, Makoto Tomimatsu, Isao Takagi, Akihiko Higuchi, Takashi Yoshida, and Eiji Murase. *New 2.0 L I4 Gasoline Direct Injection Engine with Toyota New Global Architecture Concept*. SAE Technical Paper 2018-01-0370, 2018.

[99] George A Lavoie, J Martz, M Wooldridge, and D Assanis. *A multi-mode combustion diagram for spark assisted compression ignition*. Combustion and Flame, 157(6):1106–1110, 2010.

[100] TK Lee, RG Prucka, and ZS Filipi. *Real-time estimation of combustion variability for model-based control and optimal calibration of spark ignition engines*. Proceedings of the Institution of Mechanical Engineers, Part D: Journal of Automobile Engineering, 223(11):1361–1372, 2009.

[101] Philipp Schiffmann, David L Reuss, and Volker Sick. *Empirical investigation of spark-ignited flame-initiation cycle-to-cycle variability in a homogeneous charge reciprocating engine*. International Journal of Engine Research, 19(5):491–508, 2018.

[102] James C Conklin and James P Szybist. *A highly efficient six-stroke internal combustion engine cycle with water injection for in-cylinder exhaust heat recovery*. Energy, 35(4):1658–1664, 2010.

[103] EA Ibrahim, James P Szybist, and JE Parks. *Enhancement of automotive exhaust heat recovery by thermoelectric devices*. Proceedings of the Institution of Mechanical Engineers, Part D: Journal of Automobile Engineering, 224(8):1097–1111, 2010.

[104] Charles Sprouse III and Christopher Depcik. *Review of organic Rankine cycles for internal combustion engine exhaust waste heat recovery*. Applied Thermal Engineering, 51(1-2):711–722, 2013.

[105] Lee F Brown. *A comparative study of fuels for on-board hydrogen production for fuel-cell-powered automobiles*. International Journal of Hydrogen Energy, 26(4):381–397, 2001.

[106] Stephen R Turns. *An Introduction to Combustion: Concepts and Applications, Third Edition*. McGraw-Hill New York, 2012.

[107] Leonid Tartakovsky, Vladimir Baibikov, and Mark Veinblat. *Modeling Methanol Steam Reforming for Internal Combustion Engine*. Energy and Power, 4(1A):50–56, 2014.

[108] Daniel R Palo, Robert A Dagle, and Jamie D Holladay. *Methanol steam reforming for hydrogen production*. Chemical Reviews, 107(10):3992–4021, 2007.

[109] Joan Papavasiliou, George Avgouropoulos, and Theophilos Ioannides. *In situ combustion synthesis of structured Cu-Ce-O and Cu-Mn-O catalysts for the production and purification of hydrogen*. Applied Catalysis B: Environmental, 66(3-4):168–174, 2006.

[110] Emmanuel G Lim, Enoch E Dames, Kevin D Cedrone, Angela J Acocella, Thomas R Needham, Andrea Arce, Daniel R Cohn, Leslie Bromberg, Wai K Cheng, and William H Green. *The engine reformer: Syngas production in an engine for compact gas-to-liquids synthesis*. The Canadian Journal of Chemical Engineering, 94(4):623–635, 2016.

[111] Sebastian Wiemann, Robert Hegner, Burak Atakan, Christof Schulz, and Sebastian A Kaiser. *Combined production of power and syngas in an internal combustion engine–Experiments and simulations in SI and HCCI mode*. Fuel, 215:40–45, 2018.

[112] Terry Alger and Barrett Mangold. *Dedicated EGR: a new concept in high efficiency engines*. SAE International Journal of Engines, 2(1):620–631, 2009.

[113] Eric Randolph, Raphael Gukelberger, Terrence Alger, Thomas Briggs, Christopher Chadwell, and Antonio Bosquez Jr. *Methanol Fuel Testing on Port Fuel Injected Internal-Only EGR, HPL-EGR and D-EGR® Engine Configurations*. SAE International Journal of Fuels and Lubricants, 10(3):718–727, 2017.

[114] A Poran, A Thawko, A Eyal, and L Tartakovsky. *Direct injection internal combustion engine with high-pressure thermochemical recuperation–Experimental study of the first prototype*. International Journal of Hydrogen Energy, 43:11969–11980, 2018.

[115] Leonid Tartakovsky, Ran Amiel, V Baibikov, R Fleischman, M Gutman, A Poran, and M Veinblat. *SI engine with direct injection of methanol reforming products-first experimental results*. SAE Technical Paper 2015-32-0712, 2015.

[116] A Poran and L Tartakovsky. *Performance and emissions of a direct injection internal combustion engine devised for joint operation with a high-pressure thermochemical recuperation system*. Energy, 124:214–226, 2017.

[117] A Poran and L Tartakovsky. *Influence of methanol reformate injection strategy on performance, available exhaust gas enthalpy and emissions of a direct-injection spark ignition engine*. International Journal of Hydrogen Energy, 42(23):15652–15668, 2017.

[118] Yan Chang, James P. Szybist, Josh A. Pihl, and D. William Brookshear. *Catalytic Exhaust Gas Recirculation-Loop Reforming for High Efficiency in a Stoichiometric Spark-Ignited Engine through Thermochemical Recuperation and Dilution Limit Extension, Part 1: Catalyst Performance*. Energy & Fuels, 32(2):2245–2256, 2018.

[119] James P Szybist, Josh Pihl, Shean Huff, and Brian Kaul. *High Load Expansion of Catalytic EGR–Loop Reforming under Stoichiometric Conditions for Increased Efficiency in Spark Ignition Engines*. SAE Technical Paper 2019-01-0244, 2019.

[120] Joseph G Finegold and J Thomas McKinnon. *Dissociated methanol test results*. In Biomass to Methanol Workshop, 1982.

[121] E. Anthonissen and J.S. Wallace. *Dissociated methanol engine testing results using H_2/CO mixtures*. In Intersociety Energy Conversion Engineering Conference, 1983.

[122] Joseph G Finegold. *Dissociated methanol vehicle test results*. In VI International Symposium on Alcohol Fuels Technology, 1984.

[123] Norman D Brinkman and Russell F Stebar. *A Comparison of Methanol and Dissociated Methanol Illustrating Effects of Fuel Properties on Engine Efficiency–Experiments and Thermodynamic Analyses*. SAE Technical Paper 850217, 1985.

[124] Bengt Lindner and Krister Sjöström. *Operation of an internal combustion engine: lean conditions with hydrogen produced in an onboard methanol reforming unit*. Fuel, 63(11):1485–1490, 1984.

[125] Lars Pettersson and Krister Sjöström. *An experimental and theoretical evaluation of the onboard decomposed methanol spark-ignition engine*. Combustion Science and Technology, 71(1-3):129–143, 1990.

[126] Brant A Peppley, John C Amphlett, Lyn M Kearns, and Ronald F Mann. *Methanol–steam reforming on Cu/ZnO/Al_2O_3. Part 1: the reaction network*. Applied Catalysis A: General, 179(1-2):21–29, 1999.

[127] Martyn V Twigg and Michael S Spencer. *Deactivation of copper metal catalysts for methanol decomposition, methanol steam reforming and methanol synthesis*. Topics in Catalysis, 22(3-4):191–203, 2003.

[128] Y Jamal and ML Wyszynski. *On-board generation of hydrogen-rich gaseous fuels–a review*. International Journal of Hydrogen Energy, 19(7):557–572, 1994.

[129] Lars Pettersson and Krister Sjöström. *Decomposed Methanol as a Fuel–A review*. Combustion Science and Technology, 80(4-6):265–303, 1991.

[130] James W G Turner. *Processing of fuel and recirculated exhaust gas*. UK Patent GB2484495, 2012.

[131] Perry Leung, Athanasios Tsolakis, José Rodríguez-Fernández, and Stan Golunski. *Raising the fuel heating value and recovering exhaust heat by onboard oxidative reforming of bioethanol*. Energy & Environmental Science, 3(6):780–788, 2010.

[132] S Rijo Gomes, N Bion, G Blanchard, S Rousseau, D Duprez, and F Epron. *Study of the main reactions involved in reforming of exhaust gas recirculation (REGR) in gasoline engines*. RSC Advances, 1(1):109–116, 2011.

[133] Daniel Fennell, Jose Herreros, and Athanasios Tsolakis. *Improving gasoline direct injection (GDI) engine efficiency and emissions with hydrogen from exhaust gas fuel reforming*. International Journal of Hydrogen Energy, 39(10):5153–5162, 2014.

[134] S Rijo Gomes, N Bion, G Blanchard, S Rousseau, V Bellière-Baca, V Harlé, D Duprez, and F Epron. *Thermodynamic and experimental studies of catalytic reforming of exhaust gas recirculation in gasoline engines*. Applied Catalysis B: Environmental, 102(1-2):44–53, 2011.

[135] Zhaolei Zheng, Chuntao Liu, and Xiaoyu Zhang. *Numerical study of effects of reformed exhaust gas recirculation (REGR) on dimethyl ether HCCI combustion*. International Journal of Hydrogen Energy, 39(15):8106–8117, 2014.

[136] Koichi Ashida, Hirofumi Maeda, Takashi Araki, Maki Hoshino, Koji Hiraya, Takao Izumi, and Masayuki Yasuoka. *Study of an on–board fuel reformer and hydrogen-added EGR combustion in a gasoline engine*. SAE International Journal of Fuels and Lubricants, 8(2):358–366, 2015.

[137] Athanasios Tsolakis, A Megaritis, D Yap, and A Abu-Jrai. *Combustion characteristics and exhaust gas emissions of a diesel engine supplied with reformed EGR*. SAE Technical Paper 2005-01-2087, 2005.

[138] A Abu-Jrai, J Rodríguez-Fernández, A Tsolakis, A Megaritis, K Theinnoi, RF Cracknell, and RH Clark. *Performance, combustion and emissions of a diesel engine operated with reformed EGR. Comparison of diesel and GTL fuelling*. Fuel, 88(6):1031–1041, 2009.

[139] A Tsolakis, A Megaritis, and ML Wyszynski. *Application of exhaust gas fuel reforming in compression ignition engines fueled by diesel and biodiesel fuel mixtures*. Energy & Fuels, 17(6):1464–1473, 2003.

[140] J Rodríguez-Fernández, A Tsolakis, RF Cracknell, and RH Clark. *Combining GTL fuel, reformed EGR and HC-SCR aftertreatment system to reduce diesel NOx emissions. A statistical approach*. International Journal of Hydrogen Energy, 34(6):2789–2799, 2009.

[141] Y Jamal, T Wagner, and ML Wyszynski. *Exhaust gas reforming of gasoline at moderate temperatures*. International Journal of Hydrogen Energy, 21(6):507–519, 1996.

[142] Prakash D Vaidya and Alirio E Rodrigues. *Insight into steam reforming of ethanol to produce hydrogen for fuel cells*. Chemical Engineering Journal, 117(1):39–49, 2006.

[143] RR Davda, JW Shabaker, GW Huber, RD Cortright, and James A Dumesic. *Aqueous-phase reforming of ethylene glycol on silica-supported metal catalysts*. Applied Catalysis B: Environmental, 43(1):13–26, 2003.

[144] Francesco Lucci, Augusto Della Torre, Gianluca Montenegro, and Panayotis Dimopoulos Eggenschwiler. *On the catalytic performance of open cell structures versus honeycombs*. Chemical Engineering Journal, 264:514–521, 2015.

[145] Stijn Broekaert, Michel De Paepe, and Sebastian Verhelst. *A Heat Transfer Model for Low Temperature Combustion Engines*. SAE Technical Paper 2018-01-1662, 2018.

[146] Günter F Hohenberg. *Advanced approaches for heat transfer calculations*. SAE Technical Paper 790825, 1979.

[147] Jerald A Caton. *Maximum efficiencies for internal combustion engines: Thermodynamic limitations*. International Journal of Engine Research, 19(10):1005–1023, 2018.

[148] Thomas De Cuyper, Stijn Broekaert, Duc-Khanh Nguyen, Kam Chana, Michel De Paepe, and Sebastian Verhelst. *Studying the effect of the flame passage on the convective heat transfer in a SI engine*. SAE Technical Paper 2017-01-0515, 2017.

[149] JA Caton. *First and second law implications of fuel selection for an SI engine*. In 2010 Spring Technical Meeting of the Central States Section of the Combustion Institute, 2010.

[150] V. Kalyana Chakravarthy, C. Stuart Daw, Josh A. Pihl, and James C. Conklin. *Study of the Theoretical Potential of Thermochemical Exhaust Heat Recuperation for Internal Combustion Engines*. Energy & Fuels, 24(3):1529–1537, 2010.

[151] CHEM1D. *A one-dimensional laminar flame code, Eindhoven University of Technology*. https://www.tue.nl/en/university/departments/mechanical-engineering/research/research-groups/multiphase-and-reactive-flows/our-expertise/research-topics/chem1d/, 2016.

[152] Juan Li, Andrei Kazakov, M Chaos, and FL Dryer. *Chemical kinetics of ethanol oxidation*. In 5th US combustion meeting, pages 25–28, 2007.

[153] L. Sileghem, V.A. Alekseev, J. Vancoillie, E.J.K. Nilsson, S. Verhelst, and A.A. Konnov. *Laminar burning velocities of primary reference fuels and simple alcohols*. Fuel, 115:32 – 40, 2014.

[154] Kai Morganti, Yoann Viollet, Robert Head, Gautam Kalghatgi, Marwan Al-Abdullah, and Abdullah Alzubail. *Maximizing the benefits of high octane fuels in spark-ignition engines*. Fuel, 207:470–487, 2017.

[155] Duc-Khanh Nguyen and Sebastian Verhelst. *The temperature dependence of laminar burning velocities of methanol-syngas-air flames*. In FISITA 2016 World Automotive Congress, 2016.

[156] Duc-Khanh Nguyen and Sebastian Verhelst. *Development of laminar burning velocity correlation for the simulation of methanol fueled SI engines operated with onboard fuel reformer*. SAE Technical Paper 2017-01-0539, 2017.

[157] Roy Theodorus Elisabeth Hermanns. *Laminar burning velocities of methane-hydrogen-air mixtures*. PhD thesis, Technische Universitat Eindhoven, 2007.

[158] Alexandre Ern and Vincent Giovangigli. *EGLIB: A Multicomponent Transport Software for Fast and Accurate Evaluation Algorithms*. http://www.cmap.polytechnique.fr/www.eglib/, 2004.

[159] Hai Wang, Xiaoqing You, Ameya V Joshi, Scott G Davis, Alexander Laskin, Fokion Egolfopoulos, and Chung K Law. *USC Mech Version II. High-Temperature Combustion Reaction Model of H_2/CO/C1-C4 Compounds*, 2007.

[160] Jeroen Vancoillie, Moah Christensen, EJK Nilsson, Sebastian Verhelst, and AA Konnov. *Temperature dependence of the laminar burning velocity of methanol flames*. Energy & Fuels, 26(3):1557–1564, 2012.

[161] GJ Gibbs and HF Calcote. *Effect of molecular structure on burning velocity.* Journal of Chemical and Engineering Data, 4(3):226–237, 1959.

[162] Wendell H Wiser and George Richard Hill. *A kinetic comparison of the combustion of methyl alcohol and methane*. Symposium (International) on Combustion, 5(1):553–558, 1955.

[163] C Prathap, Anjan Ray, and MR Ravi. *Investigation of nitrogen dilution effects on the laminar burning velocity and flame stability of syngas fuel at atmospheric condition*. Combustion and Flame, 155(1-2):145–160, 2008.

[164] Hongyan Sun, SI Yang, Grunde Jomaas, and CK Law. *High-pressure laminar flame speeds and kinetic modeling of carbon monoxide/hydrogen combustion*. Proceedings of the Combustion Institute, 31(1):439–446, 2007.

[165] Ian C McLean, David B Smith, and Simon C Taylor. *The use of carbon monoxide/hydrogen burning velocities to examine the rate of the CO+OH reaction*. Proceedings of the Combustion Institute, 25(1):749–757, 1994.

[166] MI Hassan, KT Aung, and GM Faeth. *Properties of laminar premixed CO/H/air flames at various pressures*. Journal of Propulsion and Power, 13(2):239–245, 1997.

[167] Jeong Soo Kim, Jeong Park, Dae Seok Bae, Tran Manh Vu, Ji Soo Ha, and Tae Kwon Kim. *A study on methane–air premixed flames interacting with syngas–air premixed flames*. International Journal of Hydrogen Energy, 35(3):1390–1400, 2010.

[168] Shaozeng Sun, Shun Meng, Yijun Zhao, Huanhuan Xu, Yangzhou Guo, and Yukun Qin. *Experimental and theoretical studies of laminar flame speed of CO/H_2 in O_2/H_2O atmosphere*. International Journal of Hydrogen Energy, 41(4):3272–3283, 2016.

[169] J Natarajan, T Lieuwen, and J Seitzman. *Laminar flame speeds of H_2/CO mixtures: effect of CO_2 dilution, preheat temperature, and pressure*. Combustion and Flame, 151(1-2):104–119, 2007.

[170] Timothy J Held and Frederick L Dryer. *A comprehensive mechanism for methanol oxidation*. International Journal of Chemical Kinetics, 30(11):805–830, 1998.

[171] Carsten Olm, István Gy Zsély, Tamás Varga, Henry J Curran, and Tamás Turányi. *Comparison of the performance of several recent syngas combustion mechanisms*. Combustion and Flame, 162(5):1793–1812, 2015.

[172] Louis Sileghem, Jeroen Vancoillie, Joachim Demuynck, Jonas Galle, and Sebastian Verhelst. *Alternative fuels for spark-ignition engines: mixing rules for the laminar burning velocity of gasoline–alcohol blends*. Energy & Fuels, 26(8):4721–4727, 2012.

[173] V Di Sarli and A Di Benedetto. *Laminar burning velocity of hydrogen–methane/air premixed flames*. International Journal of Hydrogen Energy, 32(5):637–646, 2007.

[174] T Hirasawa, CJ Sung, A Joshi, Z Yang, H Wang, and CK Law. *Determination of laminar flame speeds using digital particle image velocimetry: binary fuel blends of ethylene, n-butane, and toluene*. Proceedings of the Combustion Institute, 29(2):1427–1434, 2002.

[175] Changwei Ji, Bo Zhang, and Shuofeng Wang. *Enhancing the performance of a spark-ignition methanol engine with hydrogen addition*. International Journal of Hydrogen Energy, 38(18):7490–7498, 2013.

[176] L. Sileghem, V.A. Alekseev, J. Vancoillie, K.M. Van Geem, E.J.K. Nilsson, S. Verhelst, and A.A. Konnov. *Laminar burning velocity of gasoline and the gasoline surrogate components iso-octane, n-heptane and toluene*. Fuel, 112:355 – 365, 2013.

[177] Mohamad Metghalchi and James C Keck. *Burning velocities of mixtures of air with methanol, isooctane, and indolene at high pressure and temperature*. Combustion and Flame, 48:191–210, 1982.

[178] SY Liao, DM Jiang, ZH Huang, WD Shen, C Yuan, and Q Cheng. *Laminar burning velocities for mixtures of methanol and air at elevated temperatures*. Energy Conversion and Management, 48(3):857–863, 2007.

[179] Khizer Saeed and CR Stone. *Measurements of the laminar burning velocity for mixtures of methanol and air from a constant-volume vessel using a multizone model*. Combustion and Flame, 139(1-2):152–166, 2004.

[180] Ömer L Gülder. *Laminar burning velocities of methanol, ethanol and isooctane-air mixtures*. Proceedings of the Combustion Institute, 19(1):275–281, 1982.

[181] Jeroen Vancoillie, Sebastian Verhelst, and Joachim Demuynck. *Laminar burning velocity correlations for methanol-air and ethanol-air mixtures valid at SI engine conditions*. SAE Technical Paper 2011-01-0846, 2011.

[182] Emanuele Fanelli, Annarita Viggiano, Giacobbe Braccio, and Vinicio Magi. *On laminar flame speed correlations for H_2/CO combustion in premixed spark ignition engines*. Applied Energy, 130:166–180, 2014.

[183] Thomas W Ryan and Samuel S Lestz. *The laminar burning velocity of isooctane, n-heptane, methanol, methane, and propane at elevated temperature and pressures in the presence of a diluent*. SAE Technical Paper 800103, 1980.

[184] JB Martz, RJ Middleton, GA Lavoie, A Babajimopoulos, and DN Assanis. *A computational study and correlation of premixed isooctane–air laminar reaction front properties under spark ignited and spark assisted compression ignition engine conditions*. Combustion and Flame, 158(6):1089–1096, 2011.

[185] UC Müller, M Bollig, and N Peters. *Approximations for burning velocities and Markstein numbers for lean hydrocarbon and methanol flames*. Combustion and Flame, 108(3):349–356, 1997.

[186] Xiaolong Liu, Changwei Ji, Binbin Gao, Shuofeng Wang, Chen Liang, and Jinxin Yang. *A laminar flame speed correlation of hydrogen–methanol blends valid at engine-like conditions*. International Journal of Hydrogen Energy, 38(35):15500–15509, 2013.

[187] Chung K Law. *Combustion physics*. Cambridge University Press, 2010.

[188] Robert J Middleton, Jason B Martz, George A Lavoie, Aristotelis Babajimopoulos, and Dennis N Assanis. *A computational study and correlation of premixed isooctane air laminar reaction fronts diluted with EGR*. Combustion and Flame, 159(10):3146–3157, 2012.

[189] Leonid Tartakovsky, Vladimir Baibikov, and Mark Veinblat. *Comparative performance analysis of SI engine fed by ethanol and methanol reforming products*. SAE Technical Paper 2013-01-2617, 2013.

[190] Jozef Jarosinski. *The thickness of laminar flames*. Combustion and Flame, 56(3):337 – 342, 1984.

[191] Ultan Burke, Wayne K Metcalfe, Sinead M Burke, K Alexander Heufer, Philippe Dagaut, and Henry J Curran. *A detailed chemical kinetic modeling, ignition delay time and jet-stirred reactor study of methanol oxidation*. Combustion and Flame, 165:125–136, 2016.

[192] Alan Kéromnès, Wayne K Metcalfe, Karl A Heufer, Nicola Donohoe, Apurba K Das, Chih-Jen Sung, Jürgen Herzler, Clemens Naumann, Peter Griebel, Olivier Mathieu, et al. *An experimental and detailed chemical kinetic modeling study of hydrogen and syngas mixture oxidation at elevated pressures*. Combustion and Flame, 160(6):995–1011, 2013.

[193] Patrick F Flynn, Gary L Hunter, Russell P Durrett, Lisa A Farrell, and Wole C Akinyemi. *Minimum engine flame temperature impacts on diesel and spark-ignition engine NOx production*. SAE Technical Paper 2000-01-1177, 2000.

[194] Gautam Kalghatgi, Ibrahim Algunaibet, and Kai Morganti. *On knock intensity and superknock in SI engines*. SAE International Journal of Engines, 10(3):1051–1063, 2017.

[195] Kamal Kumar and Chih-Jen Sung. *Autoignition of methanol: experiments and computations*. International Journal of Chemical Kinetics, 43(4):175–184, 2011.

[196] X He, MT Donovan, BT Zigler, TR Palmer, SM Walton, MS Wooldridge, and A Atreya. *An experimental and modeling study of iso-octane ignition*

delay times under homogeneous charge compression ignition conditions. Combustion and Flame, 142(3):266–275, 2005.

[197] Andy Yates, Arthur Bell, and Andre Swarts. *Insights relating to the autoignition characteristics of alcohol fuels*. Fuel, 89(1):83–93, 2010.

[198] BM Gauthier, David F Davidson, and Ronald K Hanson. *Shock tube determination of ignition delay times in full-blend and surrogate fuel mixtures*. Combustion and Flame, 139(4):300–311, 2004.

[199] Camille Strozzi, Arnaud Mura, Julien Sotton, and Marc Bellenoue. *Experimental analysis of propagation regimes during the autoignition of a fully premixed methane–air mixture in the presence of temperature inhomogeneities*. Combustion and Flame, 159(11):3323–3341, 2012.

[200] Hans-Peter Schmid, Peter Habisreuther, and Wolfgang Leuckel. *A model for calculating heat release in premixed turbulent flames*. Combustion and Flame, 113(1-2):79–91, 1998.

[201] Xiaolei Gu, Zuohua Huang, Jian Cai, Jing Gong, Xuesong Wu, and Chia-fon Lee. *Emission characteristics of a spark-ignition engine fuelled with gasoline-n-butanol blends in combination with EGR*. Fuel, 93:611–617, 2012.

[202] Erjiang Hu, Zuohua Huang, Bing Liu, Jianjun Zheng, Xiaolei Gu, and Bin Huang. *Experimental investigation on performance and emissions of a spark-ignition engine fuelled with natural gas–hydrogen blends combined with EGR*. International Journal of Hydrogen Energy, 34(1):528–539, 2009.

[203] Taehoon Han, George Lavoie, Margaret Wooldridge, and André Boehman. *Effect of Syngas (H_2/CO) on SI Engine Knock under Boosted EGR and Lean Conditions*. SAE International Journal of Engines, 10(3):959–969, 2017.

[204] T Alger, J Gingrich, C Roberts, and B Mangold. *Cooled exhaust-gas recirculation for fuel economy and emissions improvement in gasoline engines*. International Journal of Engine Research, 12(3):252–264, 2011.

[205] Jennifer A Topinka, Michael D Gerty, John B Heywood, and James C Keck. *Knock behavior of a lean-burn, H_2 and CO enhanced, SI gasoline engine concept*. SAE Technical Paper 2001-01-0975, 2004.

[206] Laura Manofsky Olesky, Jason B Martz, George A Lavoie, Jiri Vavra, Dennis N Assanis, and Aristotelis Babajimopoulos. *The effects of spark timing, unburned gas temperature, and negative valve overlap on the rates of stoichiometric spark assisted compression ignition combustion*. Applied Energy, 105:407–417, 2013.

[207] Arnon Poran, Moris Artoul, Moshe Sheintuch, and Leonid Tartakovsky. *Modeling internal combustion engine with thermo-chemical recuperation of the waste heat by methanol steam reforming*. SAE International Journal of Engines, 7(1):234–242, 2014.

[208] Herry Purnama, Thorsten Ressler, Rolf E Jentoft, Hary Soerijanto, Robert Schlögl, and Reinhard Schomäcker. *CO formation/selectivity for steam reforming of methanol with a commercial $CuO/ZnO/Al_2O_3$ catalyst*. Applied Catalysis A: General, 259(1):83–94, 2004.

[209] Jin Kyung Lee, Jung Bong Ko, and Dong Hyun Kim. *Methanol steam reforming over $Cu/ZnO/Al_2O_3$ catalyst: kinetics and effectiveness factor*. Applied Catalysis A: General, 278(1):25–35, 2004.

[210] Scott G Davis, Ameya V Joshi, Hai Wang, and Fokion Egolfopoulos. *An optimized kinetic model of H_2/CO combustion*. Proceedings of the Combustion Institute, 30(1):1283–1292, 2005.

[211] Ahmad Omari, Michael Shapiro, and Leonid Tartakovsky. *Laminar burning velocity of alcohol reforming products and effects of cellularity on flame propagation*. SAE Technical Paper 2015-01-0775, 2015.

[212] Simone Mancin, Claudio Zilio, Andrea Diani, and Luisa Rossetto. *Experimental air heat transfer and pressure drop through copper foams*. Experimental Thermal and Fluid Science, 36:224–232, 2012.

[213] Cherian Olikara and Gary L Borman. *A computer program for calculating properties of equilibrium combustion products with some applications to IC engines*. SAE Technical Paper 750468, 1975.

[214] Jingeun Song, Taehoon Kim, Jihwan Jang, and Sungwook Park. *Effects of the injection strategy on the mixture formation and combustion characteristics in a DISI (direct injection spark ignition) optical engine*. Energy, 93:1758–1768, 2015.

[215] Taehoon Kim, Jingeun Song, and Sungwook Park. *Effects of turbulence enhancement on combustion process using a double injection strategy in direct-injection spark-ignition (DISI) gasoline engines*. International Journal of Heat and Fluid Flow, 56:124–136, 2015.

[216] Lewis Gene Clark, Sanghoon Kook, Qing Nian Chan, and Evatt Hawkes. *The Effect of Fuel-Injection Timing on In-cylinder Flow and Combustion Performance in a Spark-Ignition Direct-Injection (SIDI) Engine Using Particle Image Velocimetry (PIV)*. Flow, Turbulence and Combustion, pages 1–28, 2018.

[217] Leslie Bromberg and Daniel R Cohn. *Ultra-high efficiency alcohol engines using optimized exhaust heat recovery*. US Patent 9,234,482, 2016.

[218] John R Fyffe, Mark A Donohue, Maria C Regalbuto, and Chris F Edwards. *Mixed combustion–electrochemical energy conversion for high-efficiency, transportation–scale engines*. International Journal of Engine Research, 18(7):701–716, 2017.

[219] Sechul Oh and Han Ho Song. *Exergy analysis on non–catalyzed partial oxidation reforming using homogeneous charge compression ignition engine in a solid oxide fuel cell system*. International Journal of Hydrogen Energy, 43(5):2943–2960, 2018.

[220] Flavio DF Chuahy and Sage L Kokjohn. *Solid oxide fuel cell and advanced combustion engine combined cycle: A pathway to 70% electrical efficiency*. Applied Energy, 235:391–408, 2019.

[221] Richard Osborne, Ken Pendlebury, T Downes, and Simon O'Brien. *A Miller cycle engine without compromise–The Magma concept*. In 17th Internationales Stuttgarter Symposium, pages 1507–1529. Springer, 2017.

[222] Duc-Khanh Nguyen. *Numerical study on the dynamics of in-cylinder flow under the influence of asynchronous valve timing*. Master's thesis, National Cheng Kung University, Taiwan ROC, 2015.

[223] Sechul Oh, Seokwon Cho, Eunsu Seol, Chiheon Song, Woojae Shin, Kyoungdoug Min, Han Ho Song, Byeongsoek Lee, Son Jinwook, and Soo Hyung Woo. *An Experimental Study on the Effect of Stroke–to–Bore Ratio of Atkinson DISI Engines with Variable Valve Timing*. SAE International Journal of Engines, 11(6):1183–1193, 2018.

[224] Pieter-Jan Bulcke. *Implementation and validation of a downsized engine model for engine control simulation purposes*. Master's thesis, Ghent University, Belgium, 2017.